Investigating Exciton Dynamics by Photoluminescence Quenching Experiments in Metal-Organic Frameworks and Thermally Activated Delayed Fluorescence Emitters

Zur Erlangung des akademischen Grades eines

Doktor-Ingenieurs

von der KIT-Fakultät für Elektrotechnik und Informationstechnik
des Karlsruher Instituts für Technologie (KIT)

genehmigte

Dissertation

von

Marius Felix Jakoby, M. Sc.
geboren in Heidelberg

Tag der mündlichen Prüfung:	08.03.2021
Hauptreferent:	Prof. Dr. Bryce S. Richards
Korreferent:	Prof. Dr. Anna Köhler

"*Continuous improvement is better than delayed perfection.*"

Mark Twain

Table of Contents

Kurzfassung vii

Abstract xi

Acknowledgments xv

List of Publications xvii

List of Abbreviations xxiii

1 Introduction 1

2 Theoretical Background 13
2.1 Introduction to Organic Semiconductors 14
2.1.1 Molecular Orbitals 14
2.1.2 Excited States 17
2.1.3 Spin States 18
2.1.4 Intramolecular Excited-State Processes 20
2.1.5 Electronic Coupling Between Molecules 25
2.2 Exciton Transport in Organic Semiconductors 28
2.2.1 Förster Resonance Energy Transfer 29
2.2.2 Dexter Energy Transfer 30
2.2.3 Exciton Diffusion 31

2.3 Thermally Activated Delayed Fluorescence 33
2.3.1 Overview 33
2.3.2 Reaction-Diffusion Equations of TADF Emitters . . . 38
2.3.3 Hyperfluorescence 42
2.4 Metal-Organic Frameworks 44

3 Methods **47**
3.1 Sample Preparation 48
3.1.1 TADF Emitter in Degassed Solution 48
3.1.2 Spin Coating of TADF Thin-Films 48
3.1.3 Spin Coating of SURMOF Thin-Films 49
3.2 Steady-State Spectroscopy Methods 51
3.2.1 Emission and Excitation Spectra 51
3.2.2 Photoluminescence Quantum Yield Measurements . . 51
3.2.3 Ultraviolet-Visible Spectroscopy 54
3.3 Time-Resolved Spectroscopy Methods 55
3.3.1 Streak Camera 55
3.3.2 Time-Correlated Single Photon Counting 58
3.3.3 Intensified Charge-Coupled Device 60
3.3.4 Transient Absorption Spectroscopy 62
Ground State Bleach 64
Stimulated Emission 65
Photoinduced Absorption 66
3.4 Stern-Volmer Analysis 66
3.5 Monte Carlo Simulation 70
3.5.1 Simulation Method for TADF Molecules 70
3.5.2 Monte Carlo Step 72
3.5.3 Verification 72

4 Increasing the Absorption Cross-Section of TADF Emitters **75**
4.1 Energy Transfer within TADF-Oligomer Conjugates 77
4.2 Impact of the Oligomer on the RISC Rate 80
4.3 Impact of the Oligomer on the CT-LE Resonance 85
4.4 Conclusion 92

5 Exciton Motion between TADF Emitters **95**
5.1 Method for Determination of Singlet and Triplet Diffusion Lengths 98
5.2 Alternative Approach Based on Quenching of Delayed Decay Rate . . . 103
5.3 Verification of the Method . . . 104
5.3.1 Monte Carlo Simulation . . . 104
5.3.2 Analytic Approach . . . 108
5.4 Experimental Study of Exciton Motion . . . 111
5.5 Verification by Density-Functional Simulations . . . 116
5.6 Discussion . . . 120
5.7 Implications for an Hyperfluorescence OLED . . . 123
5.8 Conclusion . . . 128

6 Exciton Transport in Zn-ADB-SURMOF-2 **129**
6.1 Excited States in Zn-ADB-SURMOF-2 . . . 132
6.1.1 Impact of the Rotational Motion of ADB Linkers on the Photo-Excited States . . . 132
6.1.2 Monomer and Excimer Excitonic State Dynamics . . . 134
6.2 Design of a Donor-Acceptor SURMOF . . . 140
6.2.1 Energy Transfer between ADB and DPP . . . 141
6.2.2 Energy Transfer Efficiencies of Excimer and Excited Monomer State to DPP . . . 144
6.2.3 FRET Radii of Excimer and Excited Monomer . . . 149
6.3 Exciton Dynamics in Zn-ADB SURMOF . . . 150
6.3.1 Stern-Volmer Analysis and Exciton Motion Scenarios 151
6.3.2 Anisotropic Motion of Excimer State . . . 155
6.4 Conclusion . . . 160

7 Conclusion and Outlook **161**
7.1 Towards Background-Free Photonic Markers . . . 162
7.2 Towards Hyperfluorescence OLEDs . . . 165
7.3 Towards SURMOF-Based Solar Cells . . . 168

References **172**

Kurzfassung

Emittermoleküle mit thermisch aktivierter verzögerter Fluoreszenz (TADF) haben in letzter Zeit im Zusammenhang mit organischen Leuchtdioden (OLEDs) große Aufmerksamkeit erregt, da sie sowohl Singulett- als auch Triplett-Exzitonen in den Lichtemissionsprozess einbeziehen. Dies ist eine wesentliche Eigenschaft für effiziente OLED-Emitter, da drei von vier Ladungsrekombinationsereignissen zu Triplett-Exzitonen führen und deren Übergang zurück in den Grundzustand für Standardfluoreszenzemitter normalerweise nichtradiativ erfolgt. In TADF-Molekülen hingegen haben die ersten angeregten Singulett- und Triplett-Spin-Zustände ähnliche Energien und sind zudem gekoppelt. Folglich kann jedes Exziton mehrfach die Singulett- und Triplett-Spin-Konfigurationen durchlaufen. Dies hat eine interessante Auswirkung auf die Exzitonenbewegung in diesen Materialien. Da sich die Mechanismen der Bewegung von Singulett- und Triplett-Exzitonen stark voneinander unterscheiden, hängt die durchschnittliche Geschwindigkeit der Exzitonenbewegung zu einem bestimmten Zeitpunkt vom Anteil der Population der angeregten Zustände ab, die zu diesem Zeitpunkt den Singulett- und Triplett-Zustand durchlaufen, sowie von den Transferraten für Singulett- und Triplett-Exzitonen. Für die Optimierung von TADF-basierten OLEDs ist es essentiell, die Diffusionslängen der Singulett- und Triplett-Exzitonen unabhängig voneinander experimentell bestimmen zu können. Diese Arbeit konzentriert sich auf die Verwendung von Fluoreszenzlöschexperimenten zur Bestimmung von Diffusionskoeffizienten (und -längen) der Exzitonen. Hierbei ist der zentrale Beitrag dieser Arbeit die Demonstration, wie trotz der Koexistenz von Triplett- und Singulett-Exzitonen die individuellen Diffusionslängen beider Zustände in organischen TADF-Molekülen bestimmt werden können.

Praktisch zeigt diese Arbeit durch Monte-Carlo-Modellierung, dass TADF-Moleküle mit vernachlässigbarer Triplett-Diffusionslänge von besonderem Interesse für das Design von OLED-Aktivschichten sind, in denen TADF-Moleküle als Hilfsdotierstoffe verwendet werden, um die schmalbandige Emission eines Fluoreszenzakzeptors zu sensibilisieren, sogenannte *hyperfluoreszierende Systeme*. In diesem Zusammenhang kann ein schlechter Triplett- in Verbindung

mit einem guten Singulett-Transport zwischen TADF-Molekülen bereits für eine effiziente Hyperfluoreszenz sorgen. Darüber hinaus zeigen diese Simulationen, wie die in dieser Arbeit entwickelte Methode zum Erfassen der Triplett-Diffusion in TADF-Molekülen eine genaue physikalische Modellierung von TADF-basierten OLED-Aktivschichten ermöglichen kann.

Des Weiteren werden die Singulett- und Triplett-Diffusionslängen verschiedener TADF-Moleküle, die in einer Wirtsmatrix aus 1,3-Bis(N-carbazolyl)benzol (mCP) dispergiert sind, experimentell bestimmt. Hierbei werden einerseits TADF-Moleküle, die auf benachbarten Donor-Akzeptor-Einheiten basieren, wie 2,4,5,6-Tetra(9H-carbazol-9-yl)isophthalonitril (4CzIPN) und 2,3,5,6-Tetrakis(3, 6-Di-tert.-butyl-9H-carbazol-9-yl)-benzonitril (4TCzBN) und andererseits Molekülarchitekturen, die auf Elektronenresonanzeffekten beruhen, wie Uinolino[3,2,1-de]acridin-5,9-dion (DiKTa), untersucht. In den Benchmark-Materialien 4CzIPN und 4TCzB sind die extrahierten Singulett-Diffusionslängen $(9,1 \pm 0,2)$ und $(12,8 \pm 0,3)$ nm (bei 20 wt% in mCP), während die Triplett-Diffusionslängen vernachlässigbar sind, und definitiv kleiner als 1,0 bzw. 1,2 nm. Dichtefunktionaltheorieberechnungen bestätigen, dass die fehlende Überlappung zwischen den abgeschirmten niedrigsten unbesetzten Molekülorbitalen (LUMOs) die Triplett-Bewegung zwischen TADF-Chromophoren in diesen Molekülarchitekturen behindert. Obwohl diese Ursache für die Unterdrückung der Triplett-Bewegung für das Molekül DiKTa nicht auftritt, ist die Triplett-Diffusionslänge immer noch vernachlässigbar, wenn DiKTa in einer ausreichend niedrigen Konzentration dispergiert wird, um Aggregation zu verhindern (1 wt% in mCP). Zusammenfassend deuten diese Ergebnisse darauf hin, dass es möglich ist, auf eine geringe Beweglichkeit der Triplett- im Vergleich zu den Singulett-Exzitonen zu setzen, um effiziente hyperfluoreszierende Gerätearchitekturen zu realisieren.

Über ihre Anwendung in aktiven Schichten von OLEDs hinaus, sind TADF-Materialien auch vielversprechende Kandidaten für den Einsatz als photonische Marker. Hier ermöglicht die lange Lebensdauer der verzögerten Lumineszenz eine hintergrundfreie Detektion durch zeitaufgelöste Messungen im Mikrosekundenbereich. Allerdings basiert die niederenergetischste Absorptionsbande von TADF-Molekülen in der Regel auf einem Ladungstransfer-Zustand, welcher nur einen kleinen Absorptionsquerschnitt besitzt und damit die Anwendung

von TADF-Molekülen als photonische Marker erschwert. Mit dem übergeordneten Ziel den Absorptionsquerschnitt von TADF-Molekülen zu erhöhen, wird in dieser Arbeit die Photophysik von TADF-Oligomerkonjugaten untersucht, in welchen das Oligomer als Antenne fungiert, die dem TADF-Kern Energie zuführt. Diese Studien zeigen, dass, obwohl der Energietransfer zwischen Oligomer und TADF-Kern prinzipiell eine gute Effizienz hat, bei längerer Antenne die verzögerte Fluoreszenz abgeschaltet wird. Interessanterweise ist dies auf eine Abnahme der reverse Interkombinationsrate (RISC-Rate) zurückzuführen und nicht auf einen Triplett-Exziton-Transfer vom TADF-Kern in den energetisch tiefer liegenden Triplett-Zustand des Oligomers. Obwohl das Ergebnis des Ausschaltens der verzögerten Fluoreszenz durch die Oligomere die Verwendung der untersuchten Systeme als photonische Marker ausschließt, ist der unterdrückte Triplett-Transfer zwischen dem TADF-Kern und der Antenne dennoch ein ermutigendes Ergebnis für zukünftige Forschung in diese Richtung.

Zusätzlich wird in dieser Arbeit die Exzitonenbewegung in oberflächenverankerten metallorganischen Gerüsten (SURMOFs) untersucht, die ein großes Potenzial haben in Zukunft effiziente Lichtsammelplattformen zu bilden. SURMOFs sind mikroporöse und oft kristalline Systeme, die aus anorganischen Baueinheiten (Metallkomplexe) sowie zu deren Vernetzung aus organischen Molekülen (Linkern) zusammengesetzt sind. Diese Arbeit untersucht die Exzitonendiffusion und Energietransferprozesse in SURMOF-Heterostrukturen bestehend aus Zink-basierten Metallkomplexen, sowie aus Anthracen- (ADB) und Diketopyrrolopyrrol-basierten (DPP) Linkern. Interessanterweise besitzt der reine Zn-ADB-SURMOF bereits zwei verschiedene emittierende angeregte Zustände: i) einen angeregten Singulett-Monomerzustand und ii) einen energetisch niedriger liegenden Excimer-ähnlichen Zustand, welcher mindestens über zwei Linker delokalisiert ist. Dieser delokalisierte Zustand lässt sich auf die Rotationsfreiheit der Anthracen-Einheit der Linker und die daraus resultierende Änderung der Kopplung benachbarter Moleküle zurückführen. Ausgehend von den beiden angeregten Zuständen von Zn-ADB wird der Förster-Resonanzenergietransfer (FRET) zwischen Donatoren (ADB) und Akzeptoren (DPP) für zwei verschiedene Architekturen untersucht: i) eine Doppelschicht-Struktur, in welcher Zn-ADB in verschiedenen Schichtdicken epitaxial auf Zn-DPP aufgebracht wird und ii) ein SURMOF mit gemischten Linkern, in welcher die Konzentration von DPP relativ zu ADB variiert wird. Während

der Monomerzustand in beiden Architekturen effizient übertragen wird, ist der Transfer des Excimer-ähnliche Zustands lediglich für die Struktur mit gemischten Linkern effizient. Darauf basierend kann durch die Kombination von zeitaufgelösten Photolumineszenzmessungen mit Monte-Carlo-Simulationen gezeigt werden, dass die Bewegung des Excimer-ähnlichen Zustands in einer der Vorzugsrichtungen des SURMOFs mit einer abgeschätzten Diffusionlänge von 49 nm reduziert ist. Insbesondere der Umstand, dass der Excimer-ähnliche Zustand aufgrund des verschwindenden Absorptionsquerschnitts nicht über Dipol-Dipol-Wechselwirkungen zwischen ADB-Linkern diffundieren kann, sondern seine Bewegung auf der Überlappung von Wellenfunktionen beruhen muss (Dexter-Energietransfer), macht dieses Ergebnis besonders interessant für weitere Forschung in diese Richtung. Dies liegt insbesondere darin begründet, dass FRET-basierte Diffusion maximal Diffusionslängen bis 230 nm erreichen kann, während für Dexter-basierte Diffusion kein fundamentales Limit existiert.

Abstract

Thermally activated delayed fluorescence (TADF) molecules continue to attract attention for organic light-emitting diode (OLED) applications. TADF materials can harvest both the singlet and triplet excitons created by charge carrier recombination because the singlet and triplet spin-state manifolds are of similar energies and coupled. Consequently, each exciton can pass multiple times through singlet and triplet spin configurations. This has an interesting implication for understanding the exciton motion in these materials. Because the motion of singlets and triplets varies significantly in mechanism, the average speed of exciton motion at any given time depends on fraction of the excited-state population cycling through the singlet and triplet state at that moment, as well as the transfer rates for singlets and triplets. For the optimization of TADF-based OLEDs, it is essential to be able to experimentally determine the diffusion lengths of a singlet state and a triplet state uniquely. This thesis focuses on using quenching experiments to determine exciton diffusion coefficients (and lengths). Its key contribution is the demonstration of how, despite the coexistence of triplets and singlets, the individual singlet and triplet state diffusion lengths can be determined in TADF molecules.

Practically, this thesis demonstrates by Monte Carlo (MC) modeling that TADF molecules with negligible triplet diffusion length are of particular interest for the design of OLED active layers, in which TADF molecules are employed as assistant dopants to sensitize emission of a narrow bandwidth fluorescence acceptor, so-called *hyperfluorescence systems*. In this context, poor triplet transport but good singlet transport between TADF molecules can already ensure efficient hyperfluorescence. Moreover, these simulations indicate how the novel and accurate method for understanding triplet diffusion in TADF molecules developed in this work can enable accurate physical modeling of TADF-based OLED emitter layers.

The singlet and triplet exciton diffusion lengths of various TADF molecules dispersed in a host matrix of 1,3-bis(N-carbazolyl)benzene (mCP) are experimentally determined. TADF molecules based on adjacent donor-acceptor moieties, such as 2,4,5,6-tetra(9H-carbazol-9-yl)isophthalonitrile (4CzIPN) and 2,3,5,6-tetrakis(3,6-di-tert-butyl-9H-carbazol-9-yl)benzonitrile (4TCzBN) and,

second, molecular architectures that rely on electron resonance effects, such as uinolino[3,2,1-de]acridine-5,9-dione (DiKTa) are examined. In the benchmark materials 4CzIPN and 4TCzB, the extracted singlet diffusion length are (9.1 ± 0.2) and (12.8 ± 0.3) nm (at 20 wt% in mCP), while the triplet diffusion lengths are negligible, and certainly less than 1.0 and 1.2 nm, respectively. Density functional theory calculations confirm that the lack of overlap between the shielded lowest unoccupied molecular orbitals (LUMOs) hinders triplet motion between TADF chromophores in these molecular architectures. While this cause for the suppression of triplet motion does not occur for the molecule DiKTa, the triplet diffusion length is still negligible when DiKTa is dispersed at a sufficiently low concentration to prevent aggregation (1 wt% in mCP). These findings suggest that poor triplet motion but good singlet motion could underpin efficient hyperflourescent device architectures.

Beyond their application in active layers of OLEDs, TADF molecules are also promising candidates to act as photonic markers. Here, the long lifetime of the delayed luminescence allows background-free detection by time-gated measurements in the microsecond range. However, due to the charge-transfer (CT) nature of their absorption band, TADF molecules usually possess only a small absorption cross-section, conflicting with the desired application. This thesis establishes the photophysics of TADF-oligomer conjugates, where the oligomer acts as an antenna that feeds energy to the TADF core. The studies show that even though the energy-transfer between the oligomer and TADF core has in principle good efficiency, the delayed fluorescence is turned off for longer antennae. Interestingly, this latter effect is attributed to a decrease in the RISC rate and not to a triplet exciton transfer from the TADF to the energetically lower-lying triplet state of the oligomer. Although this result excludes the use of the investigated systems as photonic markers, suppressed triplet transfer between TADF core and the antenna is nevertheless an encouraging finding for future research in this direction.

This thesis also investigates exciton motion in surface anchored metal-organic frameworks (SURMOFs), which have great potential to form efficient light-harvesting platforms in the future. SURMOFs are microporous and often crystalline systems that are composed of inorganic building units and organic molecules linking the inorganic building blocks. This thesis investigates exciton diffusion and energy transfer processes in SURMOF heterostructures consisting

of zinc (Zn) based metal centers, anthracene based linkers (ADB) as Förster resonant energy transfer (FRET) donors, and diketopyrrolopyrrole based linkers (DPP) as FRET acceptors. Interestingly, the pristine Zn-ADB SURMOF already exhibits two distinct emitting species, a singlet excited state of a single ADB linker (monomer) and a lower-energy excimer-like state. The excimer-like is attributed to the rotational freedom of the anthracene unit of the linkers and a resulting change in the coupling of neighboring molecules subsequent to excitation. On the basis of these two excited states of Zn-ADB, the energy transfer between donors (ADB) and acceptors (DPP) is investigated for two different architectures: i) a bilayer structure in which Zn-ADB is epitaxially deposited on top of Zn-DPP with different layer thicknesses; ii) a mixed linker SURMOF in which the concentration of DPP is varied relative to ADB. While the monomer state is efficiently quenched in both architectures, the excimer-like state is quenched only in the mixed linker structure. By combining time-resolved photoluminescence measurements with MC simulations, it can be shown that the motion of the excimer-like state is reduced to the [010] direction of the SURMOF with an estimated diffusion length of 49 nm. This finding is particularly interesting in light of the fact that the excimer-like state's motion must be based on Dexter-type energy transfer due to its vanishing absorption cross-section. Since FRET-based diffusion is fundamentally limited to distances below 230 nm, this is a promising finding for the design of long-range singlet exciton diffusion in the future.

Acknowledgements

I would like to express my profound gratitude to Dr. Ian Howard for his continuous support in all aspects of this work. His extensive knowledge, creativity along with his strong experimental skill set have made the time at the Institute of Microstructure Technology (IMT) particularly instructive for me and were of indispensable help in the making of this thesis. Along these lines, I would like to thank Prof. Dr. Bryce Richards for giving me the opportunity to pursue my PhD in the "Advanced Materials and Optical Spectroscopy" group of the IMT and for creating a pleasant and productive working environment throughout the institute. Furthermore, I would like to thank Prof. Dr. Anna Köhler for sparking my interest in photophysics during my master studies and for agreeing to be the second reviewer of my dissertation.

Special thanks go to the Karlsruhe School of Optics and Photonics for funding my first two years and my summer-school stay in the French alps within the framework of a doctoral scholarship, as well as for enabling me to expand my skillset for example in the MBA-fundamentals program. Along this line, I would like to thank the SFB "Molecular Structuring of Soft Matter" for financial support of my Conference stay in Boulder, USA, and the organization of multiple great workshops with inspiring talks.

My publications and this work would have not been possible without many collaboration partners at other institutes of the KIT and beyond. I am very grateful for the support received by Dr. Ritesh Haldar and Prof. Dr. Christof Wöll from the Institute of Functional Interfaces, Lorenz Graf von Reventlow and Prof. Dr. Uli Lemmer from the Light Technology Institute (LTI), Shahriar Moritz Heidrich and Prof. Dr. Wolfgang Wenzel from the Institute of Nanotechnology, Prof. Dr. Michael Seitz from the Institute of Inorganic Chemistry at the University of Tübingen, as well as Dr. Subeesh Suresh and Prof. Dr. Zysman-Colman from the University of St Andrews, UK.

As already indicated, parts of this work were carried out in between two institutes that are at least 31 light-microseconds apart. Therefore, I would like to thank Isabel Allegro for reducing the number of times I had to overcome this distance and always being helpful during my LTI excursions.

Further, I would like to thank all my colleagues and new friends I met at IMT. Here, special thanks go to the people from the Taskforce Perovskite Photovoltaics lead by Dr. Uli Paetzold, the people from Spectral Conversion Materials group lead by Dr. Andrey Turshatov as well as to the people from the Advanced Materials and Optical Spectroscopy group lead by Dr. Ian Howard. Furthermore, I am pleased to have spent my time with Dr. Nicolò Baroni, Dr. Michael Oldenburg, and Dr. Michael Adams who quickly accepted me into their illustrious circle and introduced me, among others, into the fascinating world of SURMOFs. Here, special credit goes to Dr. Michael Adams who laid out the foundations in the fastlab ("TrALaLa") that this work is partly based on, including the sophisticated Labview programs and the SurfaceExplorer. In a similar vein, I want to thank Dr. Dmitry Busko for his helping hand when building new optical setups and the well-maintained "archive lab". In addition, I am grateful to Milian Kaiser and Jan Christoph Fischer who frequently joined me during long evenings in the optical lab, as well as for the organization of after-hour meetings including cold hypertonic beverages in the second half of my PhD. Last but not least, I would like to thank my long-term office mate Dr. Malte Langenhorst for all the shared laughter and the perfectly timed passes on the soccer field which certainly played their part in keeping up my spirits.

Ein besonderer Dank geht natürlich an meine Familie. Insbesondere hervorheben möchte ich hier einerseits meine Eltern, welche mich immer bedingungslos unterstützt haben und damit einen unschätzbaren Anteil an meinem Werdegang besitzen und andererseits meine bezaubernde Frau Andrea, welche sich stets liebevoll um mich gekümmert hat und so die auch intensiven Zeiten dieser Arbeit erträglich machte. Diese Arbeit ist für euch.

List of Publications

Peer-Reviewed Journals

During the cause of this work, four publications as first author (including one joint-first-authored paper, denoted by [1]) and 19 co-author publications were published in peer-reviewed scientific journals and are listed in the following. The publications can be further categorised by the targeted application: lasing[L], photon-upconversion[PU], photovoltaik[PV], light-emitting diodes[LED], photonic marker[PM] and ferroelectric materials[FM].

First Author Publications

1. M. Jakoby, C. Beil, P. Nazari, B. S. Richards, M. Seitz, A. Turshatov, and I. A. Howard, "Rare-earth coordination polymers with multimodal luminescence on the nano-, micro-, and milli-second time scales," *iScience*, vol. 24, no. 3, 102207, 2021.[PM]

2. M. Jakoby, S. Heidrich, L. Graf von Reventlow, C. Degitz, S. Madayanad Suresh, E. Zysman-Colman, W. Wenzel, B. S. Richards, and I. A. Howard, "Method for accurate experimental determination of singlet and triplet exciton diffusion between thermally activated delayed fluorescence molecules," *Chem. Sci.*, vol. 12, pp. 1121–1125, 2021.[LED]

3. M. Jakoby, B. S. Richards, U. Lemmer, and I. A. Howard, "Investigations of singlet and triplet diffusion in thermally activated delayed-fluorescence emitters: Implications for hyperfluorescence," *Phys. Rev. B*, vol. 100, 045303, 2019.[LED]

4. R. Haldar[1], M. Jakoby[1], A. Mazel, Q. Zhang, A. Welle, T. Mohamed, P. Krolla, W. Wenzel, S. Diring, F. Odobel, B. S. Richards, I. A. Howard, and C. Wöll, "Anisotropic energy transfer in crystalline chromophore assemblies," *Nat. Commun.*, vol. 9, no. 1, 4332, 2018.[PV]

Co-Author Publications

Publications on Thermally Activated Delayed Fluorescence Molecules

5. O. Franco, M. Jakoby, R. V. Schneider, F. Hundemer, D. Hahn, B. S. Richards, S. Bräse, M. A. R. Meier, U. Lemmer, and I. A. Howard, "Sensitizing TADF absorption using variable length oligo(phenylene ethynylene)antennae," *Front. Chem.*, vol. 8, 126, 2020.[PM]

6. R. Haldar, M. Jakoby, M. Kozlowska, M. R. Khan, H. Chen, Y. Pramudya, B. S. Richards, L. Heinke, W. Wenzel, F. Odobel, S. Diring, I. A. Howard, U. Lemmer, and C. Wöll, "Tuning optical properties by controlled aggregation: Electroluminescence assisted by thermally-activated delayed fluorescence from thin films of crystalline chromophores," *Chem. Eur. J.*, vol. 26, no. 71, pp. 17016–17020, 2020.[LED]

Publications on Metal-Organic Frameworks

7. R. Haldar, M. Kozlowska, M. Ganschow, S. Ghosh, M. Jakoby, H. Chen, F. Ghalami, W. Xie, S. Heidrich, Y. Tsutsui, J. Freudenberg, S. Seki, I. A. Howard, B. S. Richards, U. Bunz, M. Elstner, W. Wenzel, C. Wöll, "Interplay of structural dynamics and electronic effects in an engineered assembly of pentacene in a metal-organic framework," *Chem. Sci.*, vol. 12, pp. 4477-4483, 2021.[PV]

[1] authors contributed equally

8. M. Kozlowska, Y. Pramudya, M. Jakoby, S. Heidrich, L. Pan, B. S. Richards, I. A. Howard, C. Wöll, R. Haldar, and W. Wenzel, "Crystalline assembly of perylene in metal–organic framework thin film: J-aggregate or excimer? insight into the electronic structure," *J. Condens. Matter Phys.*, vol. 33, no. 3, 034001, 2020.[LED,PV]

9. R. Haldar, A. Mazel, M. Krstic, Q. Zhang, M. Jakoby, I. A. Howard, B. S. Richards, N. Jung, D. Jacquemin, S. Diring, W. Wenzel, F. Odobel, and C. Wöll, "A de novo strategy for predictive crystal engineering to tune excitonic coupling," *Nat. Commun.*, vol. 10, no. 1, 2048, 2019.[LED]

10. S. Hamer, F. Röhricht, M. Jakoby, I. A. Howard, X. Zhang, C. Näther, and R. Herges, "Synthesis of dipolar molecular rotors as linkers for metal-organic frameworks," *Beilstein J. Org. Chem.*, vol. 15, pp. 1331–1338, 2019.[FM]

11. M. Oldenburg, A. Turshatov, D. Busko, M. Jakoby, R. Haldar, K. Chen, G. Emandi, M. O. Senge, C. Wöll, J. M. Hodgkiss, B. S. Richards, and I. A. Howard, "Enhancing the photoluminescence of surface anchored metal–organic frameworks: mixed linkers and efficient acceptors," *Phys. Chem. Chem. Phys.*, vol. 20, pp. 11 564–11 576, 2018.[PU,LED]

Publications on Organic–Inorganic Lead Halide Perovskites

12. M. Kaiser, Y. Li, J. Schwenzer, M. Jakoby, M. Gerhard M. Koch, B. S. Richards, J. V. Milic, U. Paetzold, and I. A. Howard, "How free exciton-exciton annihilation lets bound exciton emission dominate the photoluminescence of 2D-perovskites under high-fluence pulsed excitation at cryogenic temperatures," *J. Appl. Phys.*, vol. 129, no. 12, 123101, 2021.[PV]

13. S. Moghadamzadeh, I. M. Hossain, M. Jakoby, B. Abdollahi Nejand, D. Rueda-Delgado, J. A. Schwenzer, S. Gharibzadeh, T. Abzieher, M. R. Khan, A. A. Haghighirad, I. A. Howard, B. S. Richards, U. Lemmer, and U. W. Paetzold, "Spontaneous enhancement of the stable power conversion efficiency in perovskite solar cells," *J. Mater. Chem. A*, vol. 8, pp. 670–682, 2020.[PV]

14. B. Abdollahi Nejand, I. M. Hossain, M. Jakoby, S. Moghadamzadeh, T. Abzieher, S. Gharibzadeh, J. A. Schwenzer, P. Nazari, F. Schackmar, D. Hauschild, L. Weinhardt, U. Lemmer, B. S. Richards, I. A. Howard, and U. W. Paetzold, "Vacuum-assisted growth of low-bandgap thin films ($FA_{0.8}MA_{0.2}Sn_{0.5}Pb_{0.5}I_3$) for all-perovskite tandem solar cells," *Adv. Energy Mater.*, vol. 10, no. 5, 1902583, 2020.[PV]

15. M. Payandeh, V. Ahmadi, F. Arabpour Roghabadi, P. Nazari, F. Ansari, P. Brenner, R. Baeuerle, M. Jakoby, U. Lemmer, I. A. Howard, B. S. Richards, U. W. Paetzold, and B. Abdollahi Nejand, "High-brightness perovskite light-emitting diodes using a printable silver micro-flake contact," *ACS Appl. Mater. Interfaces*, vol. 12, no. 10, pp. 11428-11437, 2020.[LED]

16. P. Brenner, O. Bar-On, M. Jakoby, I. Allegro, B. S. Richards, U. W. Paetzold, I. A. Howard, J. Scheuer, and U. Lemmer, "Continuous wave amplified spontaneous emission in phase-stable lead halide perovskites," *Nat. Commun.*, vol. 10, no. 1, 988, 2019.[L]

17. D. Rueda-Delgado, I. M. Hossain, M. Jakoby, J. A. Schwenzer, T. Abzieher, I. A. Howard, B. S. Richards, U. Lemmer, and U. W. Paetzold, "Solution-processed and evaporated C_{60} interlayers for improved charge transport in perovskite photovoltaics," *Org. Electron.*, 105526, 2019.[PV]

18. S. Gharibzadeh, B. Abdollahi Nejand, M. Jakoby, T. Abzieher, D. Hauschild, S. Moghadamzadeh, J. A. Schwenzer, P. Brenner, R. Schmager, A. A. Haghighirad, L. Weinhardt, U. Lemmer, B. S. Richards, I. A. Howard, and U. W. Paetzold, "Record open-circuit voltage wide-bandgap perovskite solar cells utilizing 2d/3d perovskite heterostructure," *Adv. Energy Mater.*, vol. 9, no. 21, 1803699, 2019.[PV]

19. P. Brenner, T. Glöckler, D. Rueda-Delgado, T. Abzieher, M. Jakoby, B. S. Richards, U. W. Paetzold, I. A. Howard, and U. Lemmer, "Triple cation mixed-halide perovskites for tunable lasers," *Opt. Mater. Express*, vol. 7, no. 11, pp. 4082–4094, 2017.[L]

Other Publications

20. D. Beri, M. Jakoby, I. A. Howard, D. Busko, B. S. Richards, and A. Turshatov, "Improved photon absorption in dye-functionalized silicon nanocrystals synthesized via microwave-assisted hydrosilylation," *Dalton Trans.*, vol. 49, pp. 2290–2299, 2020.[PM]

21. D. Beri, M. Jakoby, D. Busko, B. S. Richards, and A. Turshatov, "Enhancing singlet oxygen generation in conjugates of silicon nanocrystals and organic photosensitizers," *Front. Chem.*, vol. 8, 567, 2020.[PM]

22. J. Kurpiers, T. Ferron, S. Roland, M. Jakoby, T. Thiede, F. Jaiser, S. Albrecht, S. Janietz, B. A. Collins, I. A. Howard, and D. Neher, "Probing the pathways of free charge generation in organic bulk hetero-junction solar cells," *Nat. Commun.*, vol. 9, no. 1, 2038, 2018.[PV]

23. N. Kiseleva, M. A. Filatov, M. Oldenburg, D. Busko, M. Jakoby, I. A. Howard, B. S. Richards, M. O. Senge, S. M. Borisov, and A. Turshatov, "The janus-faced chromophore: a donor–acceptor dyad with dual performance in photon up-conversion," *Chem. Commun.*, vol. 54, pp. 1607–1610, 2018.[PU]

Conference and Summer School Contributions

Parts of this thesis have been presented at scientific conferences, workshops, and summer schools.

Oral Presentations

- M. Jakoby, B. S. Richards, U. Lemmer, and I. A. Howard, "Investigations of singlet and triplet diffusion in thermally activated delayed-fluorescence emitters: Implications for hyperfluorescence," International Conference on Photochemistry, Boulder (Colorado), July 23, 2019.

- M. Jakoby, F. Hundemer, O. Franco, D. Hahn, S. Bräse, M. Meier, U. Lemmer, and I. A. Howard, "Tailor-made sequence-controlled polymer-dye conjugates for controlling exciton dynamics," DFG Sonderforschungsbereich 1176 Workshop, Speyer, March 06, 2019.

Poster Presentations

- M. Jakoby, B. S. Richards, U. Lemmer, and I. A. Howard, "Investigations of Singlet and Triplet Diffusion in Thermally-Activated Delayed-Fluorescence Emitters: Implications for Hyperfluorescence," KSOP Days of Optics and Photonics, Karlsruhe, Germany, September 9, 2019.
- M. Jakoby, R. Haldar, C. Wöll, B. S. Richards and I. A. Howard, "Anisotropic Energy Transport in Metal-Organic Thin Film," KSOP Summer School Optical Technologies, Bad Herrenalb, September 5, 2018.
- M. Jakoby, R. Haldar, C. Wöll, B. S. Richards and I. A. Howard, "Anisotropic Energy Transport in Metal-Organic Thin Film," Symposium on Porous Coordination Polymers and Metal-Organic Frameworks, Raitenhaslach, Germany, May 1, 2018.
- M. Jakoby, R. Haldar, C. Wöll, B. S. Richards and I. A. Howard, "Crystalline Chromophore Assemblies Render Anisotropic Energy Transfer in Metal-Organic Thin Film," International Thematic School on Excitonics for Photonic Applications, Ecole de Physique des Houches, April 20, 2018.
- M. Jakoby, R. Haldar, C. Wöll, B. S. Richards and I. A. Howard, "Exciton transport in surface–anchored metal-organic frameworks," KSOP Days of Optics and Photonics, Karlsruhe, Germany, September 7, 2017.

List of Abbreviations

4CzIPN	2,4,5,6-tetra(9*H*-carbazol-9-yl)isophthalonitrile
4TCzBN	2,3,5,6-tetrakis(3,6-di-*tert*-butyl-9*H*-carbazol-9-yl)benzonitrile
ADB	ditopic carboxylate 4,4'-(anthracene-9,10-diyl)dibenzoate
CCD	charge coupled device
CT	charge-transfer
CW	continuous wave
Cz	carbazole
DCM	dichloromethane
DET	Dexter electron transfer
DFT	density-functional theory
DiKTa	quinolino[3,2,1-de]acridine-5,9-dione
DPP	((2,5-bis(butyl)-3,6-bis(4-carboxylicphneyl-4-yl)-2,5-dihydropyrrolo[3,4-c]pyrrole-1,4-dione
ET	electron transfer
F-dopant	fluorescent dopant

FRET	Förster resonance energy transfer
HATCN	hexacarbonitrile
HOMO	highest occupied molecular orbital
ICBA	indene-C60 bisadduct
ICCD	intensified charge-coupled device
ICT	intramolecular charge-transfer
IQE	internal quantum efficiency
IRF	instrumental response function
ISC	intersystem crossing
ITO	indium tin oxide
LBO	lithium triborate
LE	local excitation
LED	light emitting diode
LUMO	lowest unoccupied molecular orbital
MC	Monte Carlo
MCP	microchannel plate
mCP	1,3-bis(*N*-carbazolyl)benzene
MLCT	metal-to-ligand charge-transfer
MOF	metal-organic framework
OLED	organic light emitting diode
OPE	oligo(phenylene ethynylene)
OPO	optical parametric oscillator
OPV	organic photovoltaic
OSC	organic solar cell
PCBM	[6,6]-Phenyl-C61-butyric acid methyl ester
PIA	photo-induced absorption

PL	photoluminescence
PLQY	photoluminescence quantum yield
PMT	photomultiplier tube
QE	quenching efficiency
RISC	reverse intersystem crossing
RMS	root mean square
SAM	self-assembled monolayer
SHG	second-harmonic generation
SOC	spin-orbit coupling
SURMOF	surface-anchored metal-organic framework
SV	Stern-Volmer
T-oligomer	TADF-oligomer conjugate
TADF	thermally activated delayed fluorescence
TAS	transient absorption spectroscopy
TCSPC	time-correlated single-photon counting
THF	tetrahydrofuran
TTA	triplet-triplet annihilation
TTL	transistor-transistor logic
UV-Vis	ultraviolet–visible spectroscopy
WLG	white-light continuum generation
Zn-ADB	Zn-ADB-SURMOF-2
Zn-DPP	Zn-DPP-SURMOF-2

1

Introduction

In sophisticated light-harvesting and light-emitting systems, a chain of specialized components performs the higher-level task of converting photons into electronic charges or vice versa. Usually, these components are separated from each other in the nano- to micro-meter range, and for efficient devices, it is crucial that energy is transported over these distances with minimal loss. In order to optimize device structures with respect to such efficient transport, the underlying loss mechanisms, as well as their scaling with excitation density, must be understood in detail. Figure 1.1 illustrates the most common decay mechanisms for organic semiconductors, that is, monomolecular processes that are independent of the excitation density and motion of the particles (charges and excitons) and bimolecular processes that depend on both aspects. A very good example to illustrate the subtle interplay of these processes and also to get

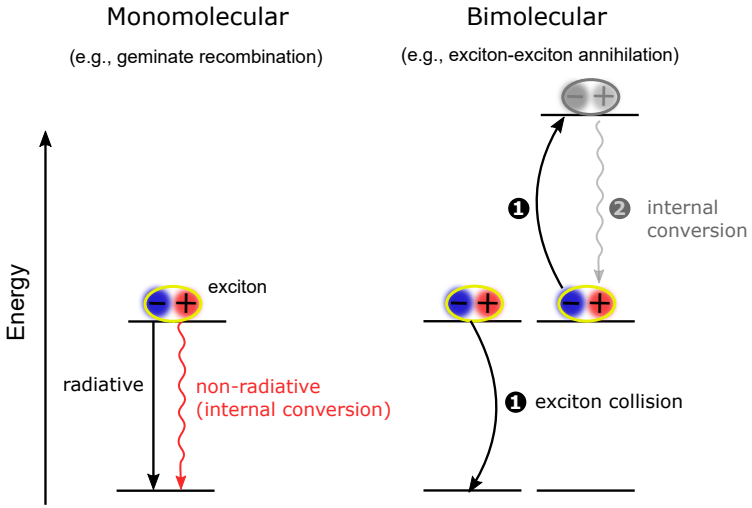

FIGURE 1.1: Scheme of a monomolecular (first-order) and bimolecular (second-order) process in an organic semiconductor. Importantly only the second-order process is dependent on the particle concentration(s) and requires movement of the particles. In a light-harvesting device, both types of exciton decay mechanisms are considered as undesired losses, while in a light-emitting diode the radiative monomolecular decay on the emitter molecule is a desired mechanism. Please note, if the preceding exciton formation from electron and hole is the rate determining process the light emission in a diode is a bimolecular process.

a perspective on how they can be managed to an efficient device is provided by nature in the context of photosynthesis.

Nature employs well-organized photosynthetic units (PU), where the underlying molecular framework along with the energy transport between chromophores have been optimized over three billion years. PUs are comprised of many light-harvesting complexes (LHCs) that transport their collected energy, often with negligible losses, to a charge-separating reaction center (RC) [1]. Depending on the organism, two to three different types of LHCs are typically found in each PU, distinguished by their structure and specific absorption spectrum. These different types of LHCs are usually labeled by Roman numeral from I to III. However, before turning to a concrete example with the well-studied PU of purple bacteria, some further general remarks are made as to why it is so beneficial to have components with specialized responsibilities, such as LHC and RC, that together perform the superordinate task of converting photons into electric charges.

The high number of LHCs that can be associated with a single RC effectively increases the absorption cross-section (typically by a factor of $\sim$200) of each RC and therefore also the exciton flow towards it [2]. Naturally, under average sunlight, this exactly synchronizes the mean time interval between two collected excitons and the RC's turnover time for charge separation ($\sim 10\,\mathrm{ms}$), making the PU work at its full potential [3]. Moreover, to achieve this optimal situation for a wide-range of average sunlight conditions, light-harvesting organisms can adjust the ratio between LHCs and RCs [2]. Thus, on the one hand, PUs can operate efficiently under reduced sunlight (e.g., due to constant shading) while under bright conditions potential second-order loss processes resulting from exciton-exciton interactions can be suppressed. Indeed, PUs are typically well optimized to avoid second-order processes, which is not only important with respect to efficiency but also to prevent photo-degradation [4]. For example, PUs usually contain carotenoid pigments which are efficient triplet exciton quencher due to their high internal-conversion rates. These triplet managers become important once the RC is saturated. Here, the increased lifetime of the excitons enhances the probability, on the one hand, of second-order processes and, on the other hand, of intersystem crossings and thus the yield of triplet excitons. The carotenoids significantly reduce triplet exciton lifetimes and consequently suppress: i) exciton-exciton annihilation and the subsequent formation of a

highly excited transient state; ii) reaction with oxygen to form the very reactive singlet oxygen. Those are both processes that accelerate the degradation of the PU. Furthermore, LHCs can undergo a state transition under intense sunlight which effectively reduces the antenna size and with it the absorption cross-section. This protects the PU from second-order processes and thereby also from photo-degradation [4, 5]. Now that some general aspects of photosynthesis related to energy transport have been discussed, a specific example of exciton motion within a PU will be given.

LHCs are usually cylindrical-shaped protein scaffolds that hold light-harvesting antennae (pigments) in specific positions in order to optimize their interaction and funnel energy towards a reaction center. A well-studied PU with energy transfer efficiencies exceeding 95 % can be found in purple bacteria [6] and is depicted in Figure 1.2. Here, the PU consists of two types of highly-symmetrical light-harvesting complexes. The larger light-harvesting complex *LH-I* surrounds the reaction center and is in turn surrounded by peripheral antenna complexes called *LH-II*. The high transfer efficiencies between those units is a consequence of a combination between coherent transport, i.e., delocalization of excitons over strongly-coupled pigment rings like the one formed by B850 pigments, and directed hops to energetically lower-lying antenna complexes [10]. An important consequence of the delocalization of excitons is a significantly increased oscillator strength, which, in turn, leads to enhanced transfer rates between LHCs [7]. Moreover, a gradually increasing resonance wavelength of the coupled antennas with decreasing separation from the reaction center leads to the aforementioned energy funneling and is concomitant with an increase of the absorption bandwidth. These are both important aspects of a sensitive sunlight response. Along these lines, the ultra-fast transfer rates mentioned in Figure 1.2A, which result from the perfectly attuned components, lead to an exciton trapping time on the reaction center that is more than an order of magnitude lower than the typical exciton lifetime ($\sim 1\,\mathrm{ns}$) on the PU [2]. The ultra-fast trapping on the reaction center is a key to suppressing undesired first- and second-order exciton decay mechanisms. Consequently, this underlines the high energy transfer efficiencies reached by purple bacteria.

The elaborate design of such PUs has inspired scientists for a long time, thereby contributing to the ongoing success story of organic electronics. From a device perspective, this story started in the 1950s with preliminary investigations

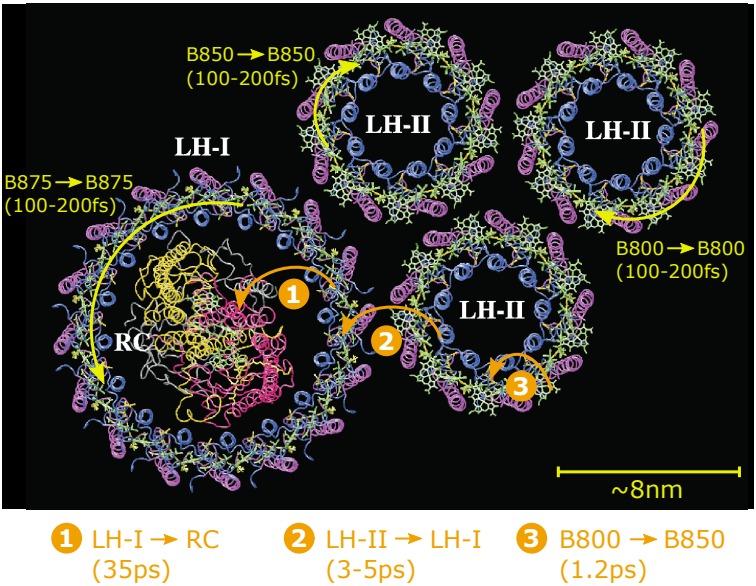

FIGURE 1.2: PU of purple bacteria (view along the direction of incoming light). LH-II is comprised of two rings of pigments with resonant wavelengths at 800 nm and 850 nm. They are therefore termed *B800* and *B850*, respectively. The B850 ring lies closer to the viewer on the cylindrically shaped LH-II. The transfer times between the subunits are taken from Mirkovic *et. al.* [7], and the scale bar from Oda *et al.* [8]. Adapted with permission from Hu *et al.* [9]. Copyright (1998) National Academy of Sciences, U.S.A.

towards organic light emitting diodes (OLEDs) by Bernanose *et al.* [11] and the construction of the first organic solar cell (OSC) by Kearns and Calvin [12]. These early devices still exhibited negligible conversion efficiencies ($\ll 1\,\%$) and it required multiple breakthroughs to reach the fine-tuned devices that are built today. The early organic photovoltaics (OPVs) were constructed as Schottky diodes between inevitably oxygen p-doped organic films and a low work-function metal [13]. In 1986, an important milestone was reached by Tang [14]. He introduced the first donor-acceptor stack, which facilitated splitting the strongly-bound excitons. Consequently, device efficiencies reached $1\,\%$. However, due to the small exciton diffusion lengths ($< 20\,\mathrm{nm}$) in the amorphous films, only a small fraction of the exciton could actually reach the donor-acceptor interface, which prevented higher efficiencies in these planar devices. In 1995, this led to the invention of the device architecture that is still predominantly used today, in which the active layer consists of a phase-separated donor-acceptor mixture and was termed *bulk heterojunction* [15]. As shown in Figure 1.3A, such a device structure significantly decreases the distances excitons must overcome by diffusion within their lifetime in order to reach a donor-acceptor interface. Soon after its introduction, considerable efforts were put into optimizing the bulk heterojunction, which lead to a steady increase in device efficiencies with recent records of $15.9\,\%$ for a single junction [16] and $17.3\,\%$ in a tandem (organic-organic) device [17]. Even though these are impressive results for OPV devices, their efficiency is still lacking behind by about $10\,\%$ (and more when comparing larger areas $\ll 1\,\mathrm{cm}^2$) in comparison to the record efficiencies of other photovoltaic platforms [18]. These include for example silicon (Si), copper indium gallium selenide, or the emerging metal-organic hybrid perovskite materials. However, the favorable properties of OPVs such as, non-toxicity, low weight, and flexibility make them still promising candidates for next-generation device platforms [19, 20]. Fundamental reasons for the reduced efficiencies in OPVs are the low charge mobilities as well as the already mentioned low exciton diffusion lengths, both of which result from a large degree of disorder in the amorphous active layers [21, 22]. As a consequence, even for the bulk heterojunction, the thickness of the active layers has to be chosen thinner than it would be desired for complete absorption of the visible sun spectrum. This inevitably leads to reduced external device efficiencies.

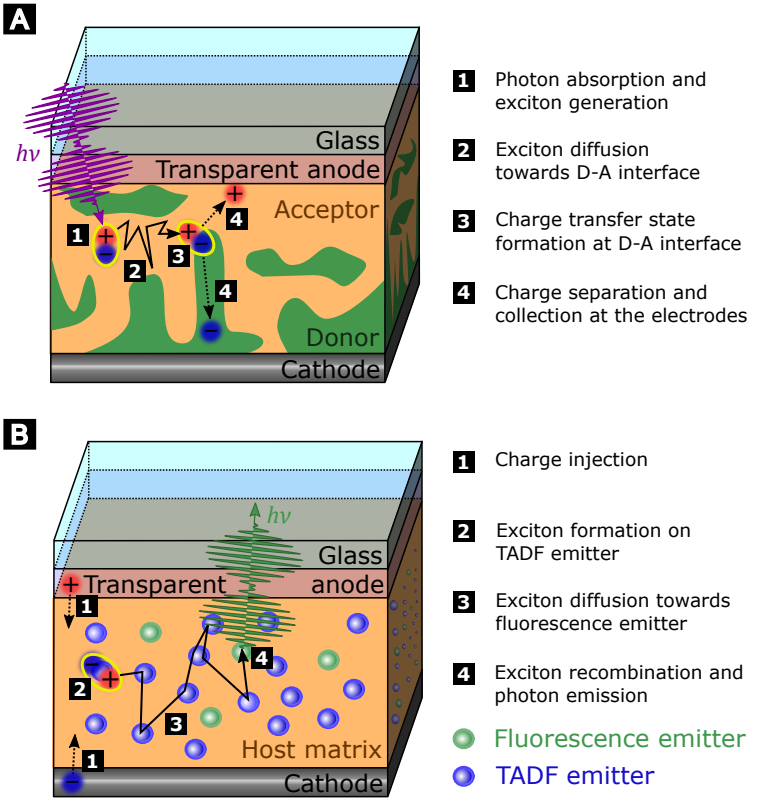

FIGURE 1.3: (A) Schematic of a bulk heterojunction OSC. (B) Schematic of a thermally activated delayed fluorescence (TADF) OLED with additional doping of fluorescence emitters in order to increase color purity, as well as the net radiative decay rate. Please note that in both cases the anode and cathode are usually comprised of multiple layers. In the case of the OSC, these layers are used to efficiently extract electrons and holes while trapping excitons in the active layer. For OLEDs, these layers are chosen to efficiently inject charges and trap them together with the excitons inside the active layer.

A material class with the potential of overcoming the aforementioned problems is surface-anchored metal-organic frameworks (SURMOFs). These crystalline materials built from metal-based nodes and linked by organic ligands and can be directly deposited on a substrate from solution due to a self-assembly process. The relative ease in tuning their functionalities allows the precise selection of ligands with an optimized intermolecular coupling that promotes long-range exciton transport. Indeed, Adams *et al.* demonstrated that one-dimensional triplet diffusion lengths in a zinc-palladium-porphyrin-based SURMOF can reach several micrometers if crystal grain sizes are sufficiently large [23]. Based on this excellent pioneer study, this thesis investigates the singlet exciton motion in SURMOFs that are comprised of zinc-based (Zn) nodes, as well as anthracene-based (ADB) and diketopyrrolopyrrole-based (DPP) linkers. This mixed-linker SURMOF forms an efficient energy harvesting network, in which the ADB linker (donor) transfers its absorbed energy to DPP (acceptor). Here, the energy transfer is based on electric dipole-dipole interactions and is also referred to as *Förster resonance energy transfer (FRET)*. The energy transfer efficiency from donor to acceptor is compared for different architectures: i) a stacked SURMOF architecture, where the donor Zn-ADB-SURMOF is epitaxially grown on top of the acceptor Zn-DPP-SURMOF; ii) a SURMOF comprised of intermixed DPP and ADB linkers. This comparison enabled the study of the exciton motion in different crystal directions of the ADB SURMOF and it allows the detection of an anistropy in the exciton motion. Interestingly, already two distinct excited states are present in ADB SURMOF, a localized monomer-related excited state, and a delocalized excimer-related state. While the monomer state diffuses rather isotropically the motion of the excimer is restricted to a single axis of the SURMOF with an estimated diffusion length of about 49 nm.

These initial results are certainly positive with regard to potential application in light-harvesting devices. Here, the following aspects underline this assertion. First of all, the excimer's motion is based on electron exchange between adjacent linkers, i.e., Dexter electron transfer (DET), and does not rely on dipole-dipole (FRET) coupling. In the latter case, the exciton diffusion length would be fundamentally restricted to values below 230 nm [24]. Given that the studied spin-coated films still possess small crystal grain sizes [23], a better control of the long-range order of SURMOF films might allow increased singlet diffusion lengths based on Dexter transfer in the future. An additional advantage in the

design of the long-range exciton transfer based on the Dexter type is that it leads to a simultaneous increase in charge mobilities, since the underlying electron transfer mechanisms are directly related. Last but not least, the entry of metal-organic frameworks (MOFs) into photovoltaic applications is also very well reflected by the recent publication of Wu *et al.*, where a zirconium-thiol-decked MOF was employed as electron-extraction layer in a perovskite solar cell [25]. This incorporation of a MOF boosted device efficiency from 19 % to 22 % along with a significant increase in device stability.

Now that the research conducted on SURMOFs in this thesis has been placed in a historical context, the following section turns to the investigations of OLEDs. Beyond the important contributions of Tang to OPV research, he also played an important role in the development of OLEDs. In 1987, he and VanSlyke demonstrated the first OLED with bright emission (exceeding $1000\,\mathrm{cd/m^2}$) at driving voltages below 10 V [26]. In these early devices, Tang and VanSlyke already introduced two innovative technologies that are still used in devices. One was employing very thin organic layer thicknesses ($\ll 150\,\mathrm{nm}$) and the other was using a bilayer stack in between the electrodes [27]. This bilayer stack consisted of a hole transporting layer and a combined electron-transporting and emitting layer. As a result, charge carriers and excitons are trapped inside the active layer until spontaneous emission occurs, which substantially increased device efficiency. Even though these new innovations attracted considerable attention from the research community the external device efficiencies were still restricted to about 1 % [27]. A fundamental reason for the low efficiencies in these devices was that only singlet excitons were included in the light-emitting process. However, since three out of four charge recombination events lead to a triplet exciton, devices that solely rely on singlet excitons are limited to an internal quantum efficiency of 25 %. This fundamental problem of OLEDs was first solved by Baldo *et al.* with the demonstration of a phosphorescence-based device [28]. Here, a high degree of spin-orbit coupling between singlet and triplet states is introduced by heavy-metal doping, allowing singlet states to efficiently transfer to the energetically lower-lying triplet state from which emission takes place. With this concept, red and green OLEDs quickly reached internal quantum efficiencies of virtually 100 % [29]. However, to reach this high efficiency while maintaining sufficient stability for lighting and display applications, usually noble metals (mainly iridium and platinum) are used as

dopants [30]. Unfortunately, both iridium and platinum belong to the ten most scarce naturally occurring elements on earth and it is, therefore, unsustainable to base such large-scale industries on these resources [31]. Another drawback is that wide gamut displays require deep blue pixels. However, phosphorescent emitters in this wavelength range are particularly unstable due to at room temperature thermally accessible dissociative states (from the high-lying first excited triplet state) [32].

An alternative approach in harvesting both singlet and triplet excitons in an OLED is to rely on thermally activated delayed fluorescence (TADF) emitters. These emitters are usually purely organic or hybrid copper-organic complexes and are characterized by a singlet-triplet gap that is comparable to the available thermal energy at room temperature. This allows the electrically generated triplet excitons to populate the emissive singlet state by a thermally activated transition. In TADF-based devices, internal quantum efficiencies of nearly 100 % have already been demonstrated [33], as well as an impressive external quantum efficiency of 37 % for a sky-blue (peak emission wavelengths 480 nm) TADF OLED [34]. Furthermore, deep-blue (peak emission wavelengths 450 nm) TADF based devices already reached an external quantum efficiency of 20 % [35]. These results highlight the huge potential of TADF based OLEDs. However, despite all these achievements, some undesirable aspects of TADF emitters still need to be addressed to make them market-ready. These include, for example, the often severe efficiency roll-off at high driving voltages, which is connected to the relatively long turnover times from exciton formation to photon emission (in the microsecond range), favoring second-order loss processes [36]. As mentioned before, these second-order processes also play a crucial role in device degradation and therefore should be suppressed. Here, a promising concept that can also further reduce emission bandwidth of TADF-based OLEDs (desired for display applications) at the same time are *hyperfluorescence* OLEDs [37]. Figure 1.3B illustrates such a device structure, where the active layer consists of a matrix doped with TADF molecules and "standard" fluorescence emitters. The absorption of the fluorescent dopant (F-dopant) is chosen to be in resonance with the emission of the TADF emitter in order to promote efficient singlet transfer between the two components, while triplet transfer needs to be suppressed. In practice, this is done by choosing a substantially lower F-dopants concentration in comparison to the TADF emitter

concentration. However, a judicious choice of relative doping concentrations requires precise knowledge of singlet and triplet diffusion lengths in the active layer. Unfortunately, due to the strongly coupled singlet and triplet states in TADF molecules, it is not straightforward to determine both diffusion lengths experimentally and a method to address this problem is therefore required. For purely organic TADF molecules, such a method is developed as part of this work. Consequently, not only scientific curiosity but also the further development of hyperfluorescence OLEDs was an important driving force to investigate the unique exciton motion between TADF emitters.

Outline

Now that a brief introduction of exciton motion in OLEDs and OPVs was given, Chapter 2 presents the theoretical background of this work. This includes an introduction to organic semiconductors and a brief overview of the relevant literature for TADF emitters and metal-organic frameworks.

In Chapter 3, the experimental setups and methods used throughout this thesis are summarized. This includes also the discussion of the frequently employed Stern-Volmer analysis, as well as a stochastic approach in simulating exciton diffusion, a Monte Carlo simulation.

The findings of this thesis are presented in Chapters 4 to 6. First, in Chapter 4 the photophysics of TADF-oligomer conjugates are established. Inspired by these results of negligible triplet transport between the TADF core of the molecule and the oligomer antenna, the triplet motion between TADF emitters is investigated, and presented in Chapter 5. The last results part, Chapter 6, turns to the investigation of excited state processes in the anthracene- and diketopyrrolopyrrole-based SURMOFs.

To conclude, Chapter 7 summarizes the findings of this thesis and gives an outlook about potential future work.

2

Theoretical Background

This chapter gives an overview of the fundamental concepts used within this work. It starts with a brief introduction of the photophysics of organic semiconductors, followed by the presentation of the two specific material classes studied throughout this thesis. These are TADF molecules which are especially useful for light-emitting devices and SURMOFs, crystalline structures that can promote long-range exciton transport, interesting for optoelectronic applications.

2.1 Introduction to Organic Semiconductors

Organic semiconductors are carbon-based molecular materials that are characterized by a vanishing density of states around the Fermi energy. Due to their significantly lower permittivity, they can be clearly distinguished from their inorganic counterparts, like silicon and gallium arsenide. This has some important consequences for the character of the excited states as well as their dynamics. In the following, the excitonic processes in organic semiconductors will be introduced mainly based on the textbooks *Electronic Processes in Organic Semiconductors* by Köhler and Bässler [38] and *Principles of Fluorescence Spectroscopy* by Lakowicz [39]. Details on the quantum mechanical treatment of excited states in organic molecules can be found for example in the textbook *Molecular Quantum Mechanics* by Atkins [40].

2.1.1 Molecular Orbitals

In order to understand why (some) organic molecules have very favorable properties for optoelectronic applications, it is instructive to review the distribution of electrons in a carbon atom. In the ground state, atomic carbon has six electrons and is in a $1s^2 2s^2 2p_x^1 2p_y^1$ configuration, meaning that two electrons are in a 1s orbital, two in a 2s orbital, and the remaining two in two of the three $2p_x$, $2p_y$ and $2p_z$ orbitals. Importantly, the molecular binding of carbon relies not only on the two electrons in the 2p orbitals, but also on the electrons in the 2s orbital leading to 4 valence electrons. This is the case, since the energy that is released when carbon forms a molecular bond exceeds the energy difference between the 2s and the 2p orbitals. The bond formation, therefore, leads to strong mixing of the 2s and 2p orbitals which is also referred to as *orbital hybridization*. This hybridization is a key property of carbon atoms and, as discussed below, one of the main reasons for the advantageous electro-optical properties of organic molecules.

A small organic molecule on which the hybridization of molecular orbitals and their effect on the optical band gap can be explained well is ethene (C_2H_4). Figure 2.1 depicts the molecular orbital formation along with a simple energy level diagram for this molecule. Here, three binding partners are involved for each

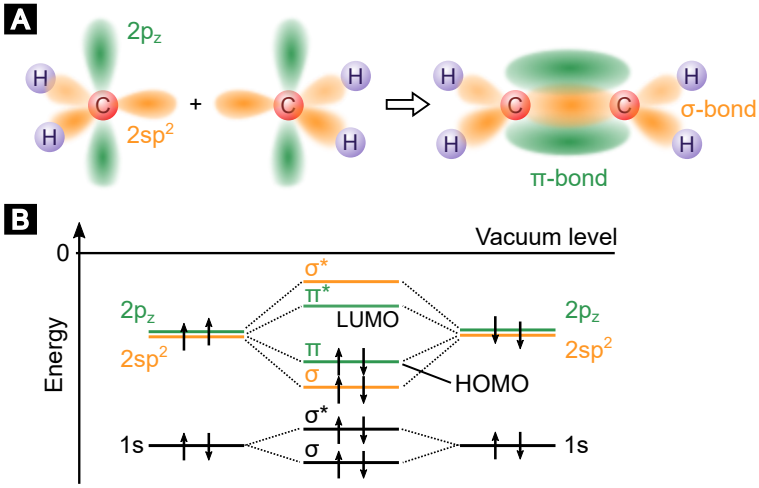

FIGURE 2.1: (A) Scheme of the molecular orbitals for ethene to illustrate σ- and π-bond formation. (B) Corresponding energy level diagram of ethene. Only the orbitals of the carbon-carbon interaction are shown (the two $2sp^2$ hybrid orbitals forming σ orbitals with hydrogen are left out). After Atkins [40].

carbon atom (two hydrogen atoms and one carbon atom) and therefore also three $2sp^2$ hybrid orbitals are formed via linear combinations (mixing) of the 2s orbital with the $2p_x$ and $2p_y$ orbitals. The electron in those single occupied hybrid orbitals can be paired with an electron from the hydrogen's 1s orbital or by the $2sp^2$ orbital of the other carbon atom. In both cases, the resulting bond is called a σ-bond, which is characterized by a maximum electron density in between the bonding partners and symmetry of the orbital with respect to rotation around the bond axis. While the formation of the σ-orbital can be seen as constructive interference between the two involved wavefunctions of the atomic orbitals, the anti-bonding σ^*-orbitals can be considered as destructive interference with a concomitant nodal plane in between the bonding atoms. Already intuitively, it can be recognized that due to the efficient screening of the nuclei's Coulomb repulsion, σ-orbitals are significantly stabilized in comparison to the involved atomic orbitals, while σ^*-orbitals, where the repulsion between the nuclei is not

screened, lie close to the vacuum level. Quantum mechanically this splitting of bonding and anti-bonding orbitals mainly depends on the resonance integral, which quantifies the interaction of the overlapping atomic orbitals with one of the nuclei. The second type of valence bond that is formed in ethene (but also characteristic for conjugated systems) is a π-bond. The corresponding π-orbital is formed by the two $2p_z$ orbitals of the carbon atoms leading to a maximum of the electron density above and below the molecular axis (see Figure 2.1A). Therefore, π-orbitals contribute little to the attractive force between the nuclei, but due to the reduced resonance interaction also a smaller energetic splitting between π and π^* applies. Especially the last point is an important property of π-orbitals and is utilized for organic semiconductor applications (*vide infra*).

Now that the formation of molecular orbitals has been briefly discussed using ethene as an example, it will be considered which of its orbitals are filled or empty. As shown in Figure 2.1B, in the ground state of ethene only the bonding σ-orbital (formed from the two $2sp^2$ orbitals) is filled while the anti-bonding σ^*-orbital remains empty, leading to a strong covalent bond between the carbon atoms. Additionally, the bonding π-orbital is filled and forms the highest occupied molecular orbital (HOMO) while the next higher orbital, a π^*-orbital, takes on the role of the lowest unoccupied molecular orbital (LUMO). Those two *frontier orbitals* play a critical role in electrical and optical processes. For ethene, the lowest-lying optical transition is a $\pi \rightarrow \pi^*$ transition. Typical energy values of $\pi \rightarrow \pi^*$ transitions lie in the range of 2 eV to 3 eV ($\sim$ 400 nm to 600 nm), nicely matching the visible wavelength region. Furthermore, typical energetic positions of the π^*-LUMO (-2 eV) and the π-HOMO (-5 eV) are well suited for charge injection due to a moderate energy difference to the work functions of typical electrode material. In contrast, if the σ and σ^* orbitals form the frontier orbitals, e.g., a molecule without π-conjugation (like ethane with $2sp^3$ hybridization of the two carbon atoms), optical transitions are in the vacuum-UV range and charge injection from electrodes is hampered by the low lying σ-HOMO (near -8 eV) and high σ^*-LUMO (close to the vacuum level).

2.1.2 Excited States

In the previous section, optical transitions were introduced in the simple picture where one electron of the HOMO gets promoted to the LUMO by absorption of a photon with energy corresponding to the energy difference of the frontier orbitals. However, this picture neglects electron-correlation effects like Coulomb and spin interactions (the latter interactions are discussed in Section 2.1.3). A possible way, to account for these correlation effects is by describing the excited state as a linear combination of different electron configurations. This concept is illustrated in Figure 2.2 for the ground state as well as for the first and second excited state. While the energetic position of the ground state can be accurately described by only a single electron configuration, for the excited states a mixing of different configurations has to be considered. For instance, the first excited state of organic molecules (S_1) can usually be described by a 80 % to 95 % contribution of the configuration with one electron in the LUMO and one electron in the HOMO. The remaining 5 % to 20 % are contributed by multiple other configurations, like the ground-state configuration or by a configuration with one electron in the HOMO+1 and one electron in the LUMO. Since this mixing is an effective description of the exciton formation, i.e., a Coulomb-bound electron-hole pair, the resulting energy of the excited state is always smaller than the involved dominant orbital transition (by the exciton binding energy). For organic semiconductors, exciton binding energies are typically large (at least several 100 meV), which is a consequence of the relatively strongly-bound carbon valence electrons and concomitant low dielectric constant ($\varepsilon_r < 4$). The large exciton binding energy of organic semiconductors is connected to a small mean displacement between the electron and hole (< 1 nm). Corresponding electron-hole pairs are referred to as *Frenkel excitons*. This is an important difference to inorganic semiconductors where the high dielectric constant ($\varepsilon_r \approx 11$) leads to an efficient screening of the Coulomb interaction between electron and hole. Hence, exciton binding energies for inorganic semiconductors are substantially lower (typically below the thermal energy at room temperature of 25 meV) with mean electron-hole distances up to 10 nm and are referred to as *Wannier-Mott excitons*. Since in this thesis only organic semiconductors are studied, the term *exciton* will refer to Frenkel excitons.

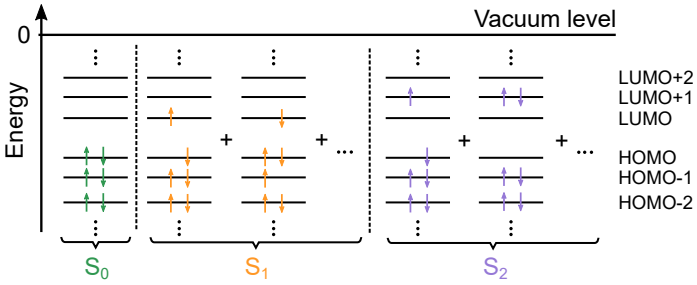

FIGURE 2.2: Schematic illustrating the configuration interaction. While the ground state (S_0) is associated only with a single configuration the first (S_1) and second (S_2) excited states are formed via linear combinations of multiple configurations. After Köhler and Bässler [38].

2.1.3 Spin States

Elementary particles like electrons and photons carry a spin which is an intrinsic form of angular momentum and has a significant impact on the energetic position of excited states, their dynamics, as well as on optical transitions. Electrons are particles with half-integer spin, meaning that a measurement of the electron spin in the (arbitrary) z-direction leads to an outcome of either $s_z = -1/2\hbar$ or $s_z = 1/2\hbar$. The magnetic spin quantum number m_s defines the corresponding electron states ($m_s = \pm 1/2$). As a side note, in total four quantum numbers are needed to specify an electronic state. Next to the spin quantum number, the other three quantum numbers were already used for labeling the molecular orbitals in Section 2.1.1. For instance the $2p_z$ orbital, where the principal quantum number $n = 2$, the angular quantum number $l = 1$ (denoted by p) and the magnetic quantum number $m_l = 0$ (denoted by the subscript z).

Returning to spin states, the amount of possible m_s values is responsible for the name of the corresponding spin state. As already indicated, for the unpaired electron two m_s values are possible and therefore it is referred to as *doublet state*. For multi-electron systems, like organic molecules, the total molecular spin is dependent on the individual spin components of each electron. However, since filled orbitals are always occupied by paired electrons with opposite spin (a

consequence of the Pauli principle) the total molecular spin $\mathbf{S}$ is determined only by electrons in singly occupied orbitals and can be calculated via addition of the unpaired electron spin vectors $\mathbf{s}_i$. Here, the absolute value of $\mathbf{S}$ is specified by the total spin quantum number S (which can be determined from the eigenvalues $S(S+1)\hbar^2$ of $\hat{\mathbf{S}}^2$, where $\hat{\mathbf{S}}$ is the spin angular momentum operator). In analogy to the case of a single electron, the total magnetic spin quantum number M_s can take on values reaching from $-S,-(S-1),...,S$, which are $2S+1$ combinations also referred to as *multiplicity* of the spin system. For instance, an exciton (two unpaired electrons) can either be described by $S=0$ or $S=1$, corresponding to antiparallel or parallel alignment of the spin vectors, respectively. For the $S=0$ state only $M_s=0$ is possible (multiplicity of one) which is therefore labeled as a *singlet state*. In contrast, for the $S=1$ state three distinct values of the magnetic spin quantum number are possible ($M_s=-1,0,+1$) corresponding to a multiplicity of three. Spin states with $S=1$ are therefore referred to as *triplet states*. In Figure 2.3 singlet and triplet states of a two-electron system are visualized, where the magnetic field leads to a defined z-direction and precession of the spins around this axis.

In the following, spin-state properties that are essential for this work are summarized. First of all, due to the exchange energy triplet states always lie at lower energies in comparison to singlet states with the same electron configuration. As a side note, this property is also the basis of Hund's rule of maximum multiplicity and leads to the triplet ground state of the unbound H_2C radical (looking back at Figure 2.1). Along this line, a prominent example of an organic molecule in a triplet ground state is molecular oxygen, with two unpaired electrons in degenerate π_x^* and π_y^* orbitals. However, usually, all electrons of the ground state configuration of organic molecules are paired and therefore organic molecules are in most cases in a singlet ground state.

Second, the total angular momentum (that is the sum of the spin and orbital momenta of the electrons) is a conserved quantity. The possibility of any transition between excited states taking place is therefore dependent on the changes in the spin and orbital momenta of the initial and final state of the transition and is one important aspect in determining the absorption cross-section as well as emission intensity of any optical (but also non-radiative) transition. These different transition processes of excited states as well as their probabilities will be discussed in the following section.

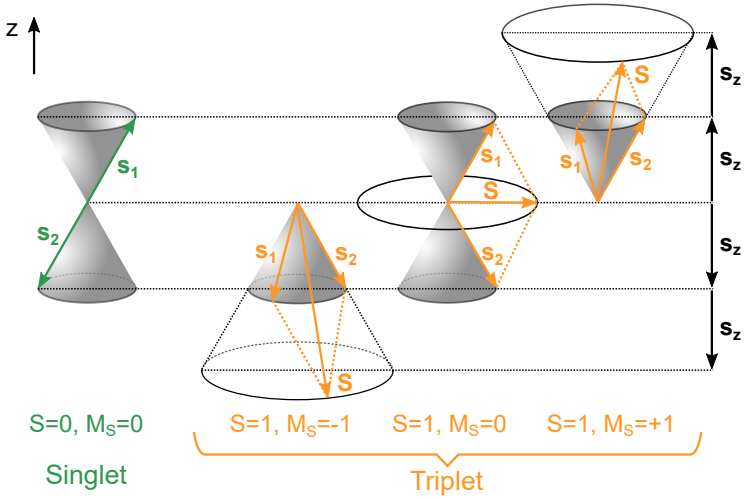

FIGURE 2.3: Precession of the spin vectors $\mathbf{s}_i$ of a coupled two-electron system (exciton) in a magnetic field in the z-direction. The total spin of the system is denoted as $\mathbf{S}$. Dependent on the alignment of the individual electron spins $\mathbf{s}_i$, either a singlet or a triplet state is formed. After Gerson and Huber [41].

2.1.4 Intramolecular Excited-State Processes

Before turning to the discussion of transitions between excited states the vibronic sub-structure is shortly introduced. Atomic nuclei are not at fixed positions but rather oscillate around an equilibrium position with a certain vibration frequency ω and associated vibrational energy $(n+(1/2))\hbar\omega$, with the number of excited quanta n. The different oscillating atoms constituting the molecule form a system of coupled oscillators which can be described by a set of normal modes each with an own sequence of energy eigenvalues. Those state manifolds form the vibrational substructure of each electronic state. As a side note, each vibrational level is further split into rotational sub-levels, which are not discussed in more detail here since their energetic splitting is usually smaller than the line width of the vibronic transitions. Typical vibrational quanta are in the range

of 100 meV to 300 meV and therefore organic molecules are usually in their vibrational ground state at room temperature ($k_B T \approx 26\,\text{meV}$).

The Jablonski diagram shown in Figure 2.4 illustrates the vibrational levels for the singlet (S_i) and triplet levels (T_i) of the molecule along with the most common intramolecular excited-state transitions. The probabilities of these transitions can be calculated by employing Fermi's golden rule with the perturbing Hamiltonian being the nuclear kinetic energy operator or the dipole operator, depending on whether it is a non-radiative or radiative transition, respectively, and the (approximated) molecular wavefunction given by the multiplication of the electronic, spin and vibrational wavefunctions ($\psi_{\text{total}} = \psi_{\text{el}}\psi_{\text{spin}}\psi_{\text{vib}}$). Such calculation results in a couple of general rules for intramolecular excited-state processes that will be introduced in the following.

First of all, transitions between states with different spin multiplicity, e.g., intersystem crossing (non-radiative) or phosphorescence (radiative), are in principle forbidden as a consequence of angular-momentum conservation. However, these transitions may become increasingly likely as the degree of spin-orbit coupling (SOC) increases. This mechanism describes the possibility that a change in the spin momentum can be compensated by a respective change in the orbital momentum of the molecule, e.g., by a $\sigma^* - \pi^*$ orbital mixing. Due to the in general small angular momenta of molecular orbitals in organic semiconductors, SOC is usually weak and transitions involving a spin multiplicity change are significantly less likely (typically by a factor of 1×10^{-6} and less) than their counterparts of transitions within the same spin manifold. As a side note, this situation can be significantly altered by heavy metal doping for instance by lanthanides with occupied f-orbitals (orbital quantum number l=3), as well as by a special design of frontier orbitals as will be discussed in Section 2.3 in the context of TADF molecules.

Next, non-radiative transitions between electronic states will be discussed. These are either internal conversion or intersystem crossing depending on whether the spin multiplicity is preserved or changed during the transition, respectively. During these isoenergetic transitions, the higher-lying electronic state with low vibrational energy transitions to a lower-lying electronic state with high vibrational energy. The probability of such a transition scales with the square of the vibronic wavefunction overlap (Franck-Condon factor) multiplied

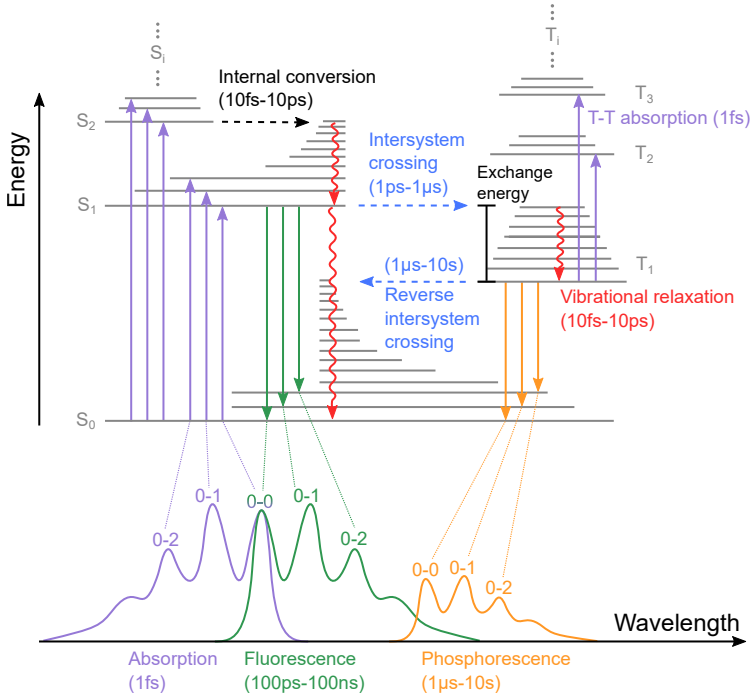

FIGURE 2.4: Jablonski diagram indicating the singlet and triplet manifold accompanied by arrows indicating most prominent transitions. Optical transitions are sketched with solid arrows, non-radiative horizontal (isoenergetic) transitions with dashed arrows and non-radiative vertical transitions with wavy arrows. The diagram is accompanied by schematic absorption and emission spectra. The indicated time-scales of the processes are meant as typical order-of-magnitude values and are based on Lakowics [39] and Köhler and Bässler [38]. The Jablonski diagram is drawn after McGlynn *et al.*[42].

by a term containing the electronic coupling (accounts for example for SOC). Furthermore, it can be shown that the rate of a non-radiative transition, k_{nr}, is exponentially decreasing with the energy gap between the two involved electronic states (both in the vibrational ground state) which is quantified by the well-known energy gap law:

$$k_{nr} \sim \exp\left(-\gamma \frac{\Delta E}{\hbar\omega_M}\right), \tag{2.1}$$

where $\hbar\omega_M$ is the vibrational quanta of the highest frequency mode and γ a term that is dependent on molecular parameters. As a result, for organic molecules, where the S_1-S_2 gap is typically smaller than 1 eV, non-radiative transitions dominate for higher excited states and therefore optical transitions like $S_2 \rightarrow S_0$ or $T_2 \rightarrow T_1$ are usually not observed in an emission spectrum. Importantly, non-radiative transitions are usually followed by fast vibrational relaxation due to the thermalization of the different vibrational modes of the molecule, as well as irreversible dissipation of vibrational energy to the environment both on a time-scale of about 1 ps. This leads to *Kasha's rule*, which empirically states that radiative transitions occur only from the S_1 (fluorescence) and T_1 (phosphorescence) towards the singlet ground state, and these radiative transitions will be discussed below.

For radiative transitions, the action of the dipole operator in Fermi's golden rule on ψ_{spin} and ψ_{vib} can typically be neglected. This is the case, since i) the transition of an electronic state (caused by the absorption or emission of a photon) occurs on time-scales too short for the atomic nuclei to react (Born-Oppenheimer approximation), and ii) the magnetic component of the electromagnetic field of the photon is too small to interact with the spin of the electron. Consequently, only the effect of the dipole operator on ψ_{el} has to be considered, and the corresponding factor is called the *electric factor*. The other two factors, *vibration factor*, and *spin factor* are simply obtained by the overlap integral of the initial and final states of the vibration and spin wave functions.

The magnitude of the electric factor is usually stated by the oscillator strength of the transition, which states the probability (with values reaching from zero to one) that the transition occurs compared to a single electron in a 3D harmonic potential well. The oscillator strength can in principle be determined by the

measurement of the extinction coefficient of the transition, but there are three important components that determine its order of magnitude. First of all, the symmetry of the two involved wavefunctions defines whether the oscillator strength can be different from zero. The dipole operator is of an odd symmetry under spatial inversion and therefore the wavefunctions of the final and initial state have to be of different parity in order to yield a non-vanishing integral. However, since the ground state wavefunction of most organic molecules is of even parity the excited state of the optical transition needs to be of odd parity, which leads to important selection rules of optical transitions (e.g., Laporte rules for centrosymmetric molecules). Second, the oscillator strength depends on the transition dipole moment and will be large in case the involved orbitals are well extended along its direction. Third, an appreciable wavefunction overlap is required between the two involved states of the transition to yield a high oscillator strength. In summary, those restrictions render $\pi \rightarrow \pi^*$ transitions usually with a high (0.01 to 1) oscillator strength since they are often symmetry allowed, and the frontier orbitals are well extended and well overlapping. In contrast, charge-transfer (CT) states where the frontier orbitals are localized on different sub-units of the molecule exhibit a significantly smaller oscillator strength.

Now that the electric factor was introduced, the spin and vibrational factors will shortly be discussed. As already indicated, for the spin factor not to be zero, a mixing between singlet and triplet excited state manifold via SOC is required. For the vibrational factor, it is decisive how much the eigenmodes are altered during the electronic transition. Usually, higher excited electronic states have an increased contribution of anti-bonding orbitals and therefore the distance of the equilibrium positions of two oscillating nuclei will be increased (displaced oscillator potential) and the frequency reduced (distorted oscillator potential). Dependent on this shift and distortion of the oscillator potentials, which can be quantified by the so-called *Huang-Rhys-parameter*, the intensity of the optical transitions will vary for different vibrational transitions. For example in the sketched absorption and emission spectrum in Figure 2.4 where the $S_1 \rightarrow S_0$ $0-0$ transition has decreased intensity in comparison to the $S_1 \rightarrow S_0$ $0-1$ transition as a result of the vibrational factor.

2.1.5 Electronic Coupling Between Molecules

So far no coupling between molecules was considered and the discussed emission and absorption spectra can therefore typically only be observed in the gas phase of the molecule (at sufficiently low pressures). In the condensed phase, i.e., solution, glass, or film, organic molecules are in close proximity to each other. Therefore, the electronic coupling between the molecules has a considerable influence on the energy levels of the ground and excited states and thus on the emission and absorption spectra. In the following, the coupling between the two molecules will be discussed to illustrate this effect.

The ground state energy E_g of two interacting molecules is given by [43]:

$$E_g = E_1 + E_2 + D, \tag{2.2}$$

where E_1 and E_2 are the individual ground state energies of the non-interacting molecules and D corresponds to the (negative) polarization energy arising from a van-der-Waals interaction. If one of the two molecules is in an excited state, an additional term appears, which leads to a splitting of the total excited state energy and is referred to as *resonance interaction* (β). The total energy of the molecular system is therefore given by [43]:

$$E_{\pm} = E_1^* + E_2 + D' \pm \beta, \tag{2.3}$$

where D' represents again the polarization energy of the excited system, with $|D'| > |D|$ for non-polar molecules.

Depending on the magnitude of the resonance energy, two cases (with continuous transition) are differentiated. For β in the range of 100 meV, the two coupled identical molecules are referred to as *dimer*. Here, the equilibrium distance between the molecules stays nearly unchanged between the ground and excited states, and a vibrational structure of the absorption and emission spectra can still be present. For significantly higher resonance interactions (several 100 meV) the excited molecules reorientate in order to optimize their interaction and are referred to as *excimer* (excited dimer). As a consequence of the significant relaxation towards the "excited" equilibrium distance between the molecules, no vibrational structure can be observed in the emission spectrum.

Before turning to example cases of dimer or excimer formation, a short general remark is made for chromophores in an amorphous environment, i.e., an organic thin film. As already indicated by Equations 2.2 and 2.3, the polarization effect of a molecule on its surrounding, here described by D and D', leads to inhomogeneous line broadening of the emission and absorption spectrum for an ensemble of identical molecules due to the difference in the individual local environments.

Returning to the discussion of two coupled molecules, two limiting cases will be introduced in the following, which are J- and H-aggregates. Here, the treatment will be based on the point-dipole approximation, meaning that an effective transition dipole moment is used for each of the interacting molecules, requiring that the distance between the chromophores is large in comparison to their individual size. An in-depth analysis for smaller distances that includes extended charge distributions is for example given by Gierscher and Park [44]. Figure 2.5 illustrates the aggregate formation where the transition dipole moments of the coupled molecules depend on the vector sum of the individual molecules' transition dipole moments (with absolute value μ).

For H-aggregates the molecules are arranged in a coplanar, stacked manner. Here, the lower excited state E_- carries no transition dipole moment due to anti-parallel alignment of the individual dipole moments, while E_+ carries a dipole moment of 2μ. Therefore, the absorption spectrum of H-aggregates shifts hypsochromically with increasing coupling strength between the molecules, and emission is strongly suppressed due to relaxation to the E_- state subsequent to optical excitation. In contrast, J-aggregates, where the molecules are arranged in a collinear and parallel fashion, and both emission and absorption involve the low lying E_- state with a total dipole moment of 2μ. Please note that in real films often an arbitrary orientation between the individual dipoles prevails and therefore the $E_- \rightarrow E_0$ and $E_+ \rightarrow E_0$ transitions both have a finite oscillator strength and the absorption spectrum can be split into a doublet.

In terms of applications, the often high oscillator strength of the $E_- \rightarrow E_0$ transition for J-aggregates can be employed for OLEDs [45, 46], while the increased lifetime (only given by the non-radiative decay rate) of E_- is beneficial for OPV applications [47, 48]. Importantly, the scaling of the polarization energy and the resonance interaction with distance r between the molecules are

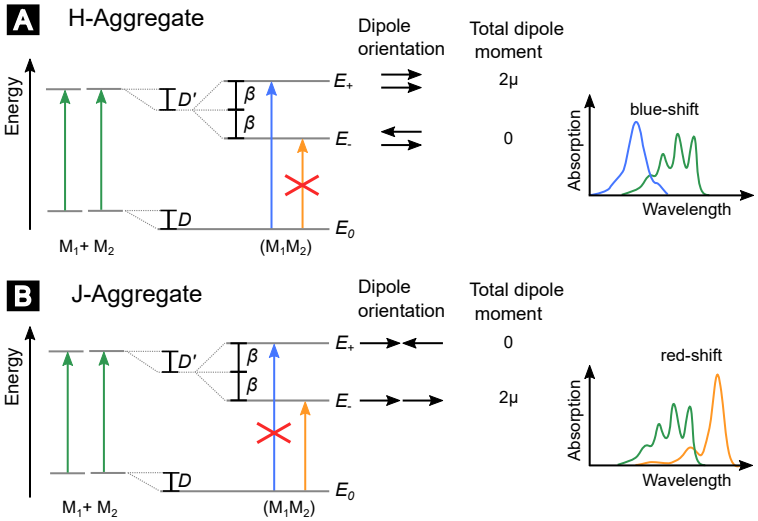

FIGURE 2.5: Schematic illustration of the ground and excited state energies for two electronically coupled identical molecules in H-aggregate configuration (A) and for J-Aggregate configuration (B). For both cases the ground and excited state of two uncoupled molecules are indicated on the left and the characteristic change in the absorption spectrum for two strongly coupled molecules is sketched on the right. After [38, 43].

different. While D and D' scale with $1/r^6$ (as a result of dipole-induced dipole coupling), β decreases exponentially with r since here the overlap of the charge density with either molecule is decisive for the magnitude of β. Therefore, small values of β (as usually desired for OLEDs) can be engineered by optically inert but sterically demanding side groups in order to shield the chromophore from resonance interactions with its surrounding.

2.2 Exciton Transport in Organic Semiconductors

Mainly dependent on the morphology of the organic semiconductor, exciton transport can either be dominated by coherent or incoherent transport. The former case applies to high-quality molecular crystals where the coupling strength between molecules exceeds the energetic variation between the sites [49]. Here, macroscopic Bloch functions and a resulting exciton band can be used to describe the wave-like exciton transport in analogy to the energy bands in inorganic semiconductors. However, in the predominant number of cases (and also in this work) transport in organic semiconductors is dominated by energetic disorder and exciton-phonon scattering, which leads to short dephasing times of excitons with respect to their lifetimes. As a result, exciton transport is incoherent and restricted to subsequent hops from one localized state to another, which can be treated as a 3D random walk in the absence of a gradient, e.g., due to temperature or concentration.

Incoherent exciton transport can be either based on a radiative or non-radiative transfer mechanism. For a radiative transfer (also referred to as *trivial transfer*) the energy donating site (*donor*) emits a photon that gets reabsorbed by the energy accepting site (*acceptor*). This type of transfer requires efficient emission and absorption, as well as a small Stokes shift. A characteristic for samples with an efficient trivial transfer is a red-shifted emission spectrum since the probability of reabsorption is increased for photons from the high-energy side of the emission spectrum. However, non-radiative transfer due to quantum chemical coupling between donor and acceptor is the prevailing case for dense organic media and therefore also of special importance for this work. Here, two different transfer mechanisms can be differentiated depending on the dominating coupling term (as derived from Fermi's golden rule). In case the Coulomb term dominates, that is, a dipole-dipole interaction, the transfer is referred to as *Förster resonance energy transfer* (FRET), while in case the exchange term dominates the transfer is referred to as *Dexter energy transfer* (DET). Both cases are schematically illustrated in Figure 2.6 and will be further specified in the following two subsections.

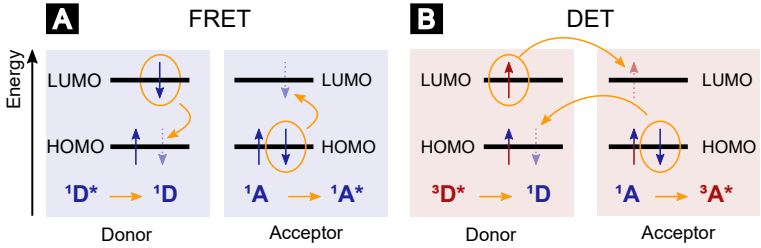

FIGURE 2.6: Exciton transport mechanisms in organic semiconductors. Schematic illustration of a Förster resonance energy transfer (FRET) for a singlet exciton (A), and a Dexter energy transfer (DET) of a triplet exciton (B).

2.2.1 Förster Resonance Energy Transfer

The Förster mechanism describes the transfer of energy between a dipole-dipole-coupled donor-acceptor system. In case the distance r between donor and acceptor is large in comparison to their sizes the point-dipole approximation can be used and the transfer rate of the FRET process, k_{FRET}, can be expressed as [50]:

$$k_{\mathrm{FRET}} = \frac{1}{\tau_{\mathrm{D}}^{0}} \left(\frac{R_0}{r} \right)^6, \tag{2.4}$$

where R_0 is the Förster radius and τ_{D}^{0} the lifetime of the pristine excited donor state (without the presence of acceptor sites). The Förster radius defines the distance between donor and acceptor at which the probability for a transfer is equal to the spontaneous decay of the excited donor state, with typical values in the range of 1 nm to 4 nm [38, 51]. For the calculation of R_0 the following equation can be used:

$$R_0^6 = \frac{9 f^2 \ln 10}{128 \pi^5 N_{\mathrm{A}} n^4} \eta \Omega, \tag{2.5}$$

with the orientation factor f, the refractive index n, the photoluminescence quantum yield (PLQY) of the donor η (see section 3.2.2), the Avogadro constant N_{A} and the spectral overlap integral Ω. Here, the orientation factor f describes the relative orientation between the two transition dipoles and can take on values between zero (perpendicular orientation) and two (collinear arrangement). For

samples where the orientation of dipole moments is isotropic, e.g., amorphous films or solutions, an average orientation factor of $f^2 = 2/3$ is used. Another important parameter for FRET is the spectral overlap integral Ω between the emission spectrum of the donor and the absorption spectrum of the acceptor. Ω is defined as:

$$\Omega = \int_0^\infty \varepsilon_A(\lambda) f_D(\lambda) \lambda^4 d\lambda, \tag{2.6}$$

with the molar decadic coefficient of the acceptor's extinction ε_A and f_D the normalized emission spectrum, i.e., $\int_0^\infty f_D(\lambda) d\lambda = 1$.

Please note that usually only the transfer of singlet excitons can be described by Förster theory since the spin multiplicity of donor and acceptor is individually conserved during this process. However, strong mixing of the singlet and triplet state manifold in organometallic compounds can lead to some degree of Förster-type triplet exciton transfer [52, 53].

2.2.2 Dexter Energy Transfer

Dexter-type transfer relies on the exchange of two electrons between the donor and acceptor. From the LUMO of the excited donor, an electron is transferred to the LUMO of the acceptor, while an electron from the HOMO of the acceptor is transferred to the singly occupied HOMO of the donor. This process, therefore, requires concurrent LUMO-LUMO and HOMO-HOMO overlap of donor and acceptor, which is an important prerequisite for the discussion of exciton transfer in TADF molecules as laid out in Chapter 5.

The requirement for wavefunction overlap leads to an exponential dependence of the transfer rate k_{DET} with distance r between donor and acceptor and based on Dexter's theory on electron-exchange is given by [54]:

$$k_{\mathrm{DET}} = J \exp\left(-\frac{2r}{L}\right). \tag{2.7}$$

Here, J is the product of the normalized spectral overlap integral and a factor related to the specific orbital interaction, while L stands for the effective Bohr radius. The exponential dependence restricts Dexter-type transfer usually to distances below 1 nm. Furthermore, since the Coulomb term usually dominates

for singlet excitons and vanishes for triplet excitons, it can be concluded that FRET transfer prevails for singlet excitons while Dexter transfer prevails for triplet excitons.

2.2.3 Exciton Diffusion

Now that the incoherent transfer processes of excitons in organic semiconductors were introduced, this section summarizes how a series of incoherent hops can be described by macroscopic quantities. In the absence of an external gradient, e.g., temperature or concentration, a series of incoherent exciton hops can be treated as a random-walk [55]. Importantly, this random-walk is "memoryless", meaning that the next hop is only dependent on the current position of the exciton but independent of its history. Analogous to a Brownian particle, this leads to a mean square displacement $|l^2|$ of the exciton that increases linearly with time t:

$$|l^2| = 2ZDt, \tag{2.8}$$

where Z corresponds to the dimensionality of the system and D is the diffusion constant of the particle. As a side note, critical for this treatment is that the probability distribution function for Förster and Dexter transfer and also the waiting times are not heavy-tailed, i.e., their moments are finite. This situation is for example not given when the excitons are trapped for a significant amount of time (heavy-tailed waiting times) leading to subdiffusion, i.e., $|l^2| \sim t^{\alpha}$ with $\alpha < 1$ [56, 57]. Along this line, a deviation from Gaussian distributed energetic disorder towards a heavy-tailed distribution also leads to subdiffusive exciton transport [58]. However, despite these rather specific cases, exciton motion in disordered organic semiconductors can usually be well described within the framework of normal diffusion ($\alpha = 1$). Accordingly, the analysis of exciton diffusion throughout this thesis builds upon the validity of Fick's laws of diffusion.

Please note that Equation 2.8 can also be used to determine an exciton diffusion constant if the transfer rates and corresponding distances between sites are known. For this purpose, the equation can be rearranged to:

$$D = \frac{1}{2Z}\xi\Delta x^2, \tag{2.9}$$

where ξ is the hopping frequency and Δx the distance between neighboring sites. This equation will for example be employed in Section 3.5 where it is used to determine the diffusion constant of singlet and triplet excitons based on the calculated transition probabilities to surrounding sites. Here, the factor $\xi \Delta x^2$ is replaced by a sum of all possible transitions (see Equation 3.19).

Often rather the exciton diffusion length l_D than the diffusion constant D is specified in the literature. Both quantities can be converted into each other using the exciton lifetime τ and Equation 2.8. Typical values of singlet diffusion lengths lie in the range of 2 nm to 20 nm [59, 60]. However, higher values can be reached for samples with well-aligned transition dipole moments [61], but with a fundamental upper limit at 230 nm [24]. This limit of the singlet diffusion length is a consequence of the Förster transfer mechanism, where a high transition dipole moment μ leads, on the one hand, to an increase in the transfer rate ($k_{\mathrm{FRET}} \sim \mu^4$), but on the other hand, to a decrease in the exciton lifetime ($\tau \sim \mu^{-2}$). Notably, this limit is only valid for incoherent singlet exciton transport, while for coherent singlet exciton transport in highly ordered structures diffusion length in the μm range can be realized [62–64].

In contrast, for triplet excitons, no fundamental limit for the exciton diffusion length exists. Here, the big difference in triplet lifetimes, as well as the strong dependence of the exchange coupling with the distance between molecules, leads to a wide scattering of triplet diffusion length between samples. As a result, for many amorphous organic semiconductors, the triplet diffusion length is similar to those of the singlet exciton and often lies in the range of 10 nm to 20 nm [65]. Long triplet diffusion length in the micrometer range can frequently be observed in samples with optimized wavefunction overlap between adjacent sites (molecular crystals, metal-organic frameworks, etc.). For example, 4 μm along one crystal axis of rubrene single crystals [66], 1 μm to 4 μm in a ladder-type conjugated polymer [67], and 1.6 μm in an anthracene-based metal-organic framework (MOF) [68].

There exists a wide range of different experimental methods to determine exciton diffusion length. Of special importance for this work are photoluminescence (PL) quenching experiments that can be further divided into volume [69, 70] and bilayer quenching experiments [71, 72]. The former method will be used

in several places of this work and is further specified in the context of a Stern-Volmer (SV) analysis in Section 3.4. Bilayer quenching experiments will be used in Chapter 6 in order to reveal the anisotropy in exciton diffusion in an anthracene-based SURMOF. Alternative approaches for the measurement of exciton diffusion length can for example rely on exciton-exciton annihilation [23, 73, 74], microwave conductivity [75], or electro-optical measurements [76]. Moreover, long-range triplet transport that exceeds the Abbe limit can in some cases also be directly observed by means of optical microscopy [66, 77].

2.3 Thermally Activated Delayed Fluorescence

This section introduces the underlying exciton processes of TADF OLEDs from a photophysical perspective. However, an introduction to this topic from a device perspective is for example given by Ostroverkhova [78] and an industrial perspective by Arjona-Esteban and Volz in *Highly Efficient OLEDs* [36].

2.3.1 Overview

As a consequence of the different spin multiplicities between singlet and triplet states, three out of four charge recombination events lead to triplet excitons in an OLED [79]. The resulting challenge of including the usually non-emissive triplet excitons in the light-emission process to obtain an efficient device has engaged scientists already for several decades. Since the development of the first efficient OLED by Tang and VanSlyke in 1987 [26], where the conversion efficiency between generated excitons and emitted photons (internal quantum efficiency (IQE)) was still fundamentally limited to 25 % due to the exclusive harvest of singlet excitons, several strategies for the inclusion of triplet excitons were developed in the following decades [80–82]. In the late 90s, a major breakthrough was achieved by the discovery that third-row transition metal complexes, especially those based on Ir^{3+}, Pr^{2+} and Os^{2+}, exhibit efficient SOC, and are potent triplet emitters [83]. In these materials, efficient intersystem crossing (ISC) of singlet excitons paired with the radiative $T_1 \rightarrow S_0$ transition leads to internal PLQYs that can reach 100 % [29]. These materials

are still state-of-the-art emitters of red and green OLEDs [84]. However, the utilization of phosphorescence-based emission for light-emitting devices has some undesirable aspects. Beyond the commercial challenge of the expensive noble-metal doping, technical challenges include the relatively broad emission spectra of phosphorescent emitters and insufficient stability of blue-emitting phosphorescent OLEDs for commercial applications [85–88].

An alternative class of molecules that allows the harvesting of both singlet and triplet excitons are thermally activated delayed fluorescence (TADF) molecules. They have been extensively studied due to their potential to outcompete phosphorescent emitters, at least within the elusive deep blue emission. These molecules are typically characterized by a small energy gap (ΔE_{ST}) between the lowest-excited singlet and triplet excitonic states. Consequently, triplet excitons (whose emission is negligible) can convert to the singlet state (whose emission is significant) by reverse intersystem crossing (RISC) [89]. The so-allowed harvesting of triplet excitons for emission enables the construction of OLEDs with internal PLQYs close to 100 % [90, 91]. To date, red, green, and blue TADF-based OLEDs have been realized with external quantum efficiencies exceeding 25 % [92–94].

Before turning to the mechanistic details of TADF, it is briefly placed in a historic context. Delayed fluorescence was discovered as early as 1929 by Perrin [95] and further investigated by Parker *et al.* using the dye eosin and therefore named *E-type delayed fluorescence* [89, 96]. Parker and coworkers described the TADF process as a thermally-activated transition between the lowest and a higher vibronic triplet state, followed by RISC to a resonant singlet vibronic state [96]. As a consequence, the connected RISC rate is (to a first approximation) proportional to the energy gap between the first excited singlet and triplet state ΔE_{ST}. Since for a long time, no molecules were discovered with sufficiently low ΔE_{ST} to be used in a light-emitting device, E-type delayed fluorescence got little attention in the literature. However, this situation changed drastically in 2009 when a breakthrough by Adachi *et al.* was achieved by employing a Sn^{4+}–porphyrin complex with efficient RISC for the construction of the first OLED with E-type delayed fluorescence [97]. Following the idea of reducing the exchange energy for a small ΔE_{ST}, Adachi and coworkers demonstrated the first all-organic TADF based OLEDs in 2012 with internal PLQYs already exceeding 90 % [90]. Since they used the term *TADF* in those

pioneering works, this terminology was adopted in the following throughout the entire OLED literature.

As already indicated, efficient harvesting of triplet excitons in TADF molecules requires a small exchange energy, i.e., a small ΔE_{ST}, comparable to the available thermal energy at room temperature (26 meV). The common strategy to reduce ΔE_{ST} is to spatially separate LUMO and HOMO. This can be achieved by a CT-state formation, which reduces the exchange energy due to a diminished wavefunction overlap between the electrons occupying the frontier orbitals. However, a vanishing orbital overlap also leads to a vanishing oscillator strength (see Section 2.1.4) and therefore efficient TADF emitters have to compromise between both aspects. Three distinct classes of materials satisfy those criteria best and already lead to efficient active layers in light-emitting devices [36]. These are: i) organo-transition metal compounds (mainly based on Cu^+) with metal-to-ligand charge-transfer (MLCT) states [98]; ii) purely organic molecules consisting of electron-donating (D) and accepting (A) units, thereby forming intramolecular charge-transfer (ICT) states [99]; iii) exited complexes (intermolecular D-A systems) with intermolecular CT states [100]. Even though this thesis will focus on the photophysics of ICT molecules, a short distinction between the three material classes as outlined below is instructive.

Excited complexes, often named in analogy to excimers (as introduced in Section 2.1.5) as *exciplexes* are from a photophysical perspective quite similar to ICT molecules. The main difference is an increased morphological inhomogeneity and an often not negligible contribution of fluorescence stemming from triplet-triplet annihilation (P-type fluorescence) [101–103]. However, there is a distinct difference between those purely organic systems and the organo-transition metal compounds, namely the degree of SOC. For the latter, SOC between the MLCT states leads to high ISC (k_{ISC}) and RISC (k_{RISC}) rates in comparison to the fluorescence decay rate k_{FL}, i.e., k_{ISC} and $k_{RISC} \gg k_{Fl}$. Therefore, the TADF process can here be described as a quasi-equilibrium between singlet and triplet states given by ΔE_{ST} and the Boltzmann distribution, leading to a good approximation of the fluorescence decay by a mono-exponential function [104]. For the organic systems, SOC is not sufficient to explain k_{ISC} and k_{RISC} and a second-order effect based on vibronic coupling has to be considered (*vide infra*) [31]. Consequently, for organic systems, k_{ISC} and k_{FL} are usually of similar magnitude and lie in the inverse nanosecond range, while k_{RISC} lies in

the inverse microsecond range. As a result, a kinetic model is needed for organic molecules in order to describe the fluorescence decay and will be introduced in Section 2.3.2.

Let us now turn to the mechanistic details of TADF in ICT molecules, whose photophysical investigation is one of the main parts of this work. It should be noted, that the precise mechanism behind RISC in ICT molecules is still under debate, even though a clearer picture has emerged in the last few years. For the description, multiple excited states of different character have to be considered, i.e., local excitations (LEs) of donor and acceptor and CT states. Figure 2.7 depicts one of the benchmark TADF molecules accompanied by a Jablonski diagram with the most prominent excited states. The molecular structure depicted in Figure 2.7A illustrates the characteristic nearly orthogonal A and D units. Such an alignment efficiently decouples the electron and hole and leads to effectively isoenergetic ^{1}CT and ^{3}CT states [106]. The quasi-degeneracy of the CT states plays an important yet subtle role in efficient RISC. When using Fermi's golden rule to calculate k_{RISC} the values are 5 to 6 orders of magnitudes too low, even when considering the weakly allowed $^3\mathrm{LE} \rightarrow {}^1\mathrm{CT}$ transition [107, 108]. A solution to this fundamental problem was put forward by Gibson *et al.* by considering spin-vibronic coupling up to second order in the nonadiabatic coupling elements, i.e., by a treatment beyond the Born-Oppenheimer approximation [31], and is now most widely accepted in literature [36]. This second-order SOC is a two-step mechanism and involves (dependent on the system at least) three strongly coupled states of different character [31, 105]. On a timescale significantly faster than RISC, the large vibronic coupling between a ^{3}LE and ^{3}CT state promotes equilibrium formation between both states and is followed by the rate-determining nonadiabatic mechanism [31]. This second-order vibronic coupling between ^{1}CT and ^{3}CT is mediated by the ^{3}LE state (either a local triplet on the donor $^3\mathrm{LE_D}$ or acceptor $^3\mathrm{LE_A}$) [31, 105, 109]. The latter coupling is strong in the case of D-A molecules since the CT states are nearly degenerate and therefore possess significant vibrational overlap [105]. Notably, the vibrational modes between the D and A units (torsional rocking) seem to be critical for efficient coupling [36].

Now that the spin-vibronic mechanism responsible for efficient SOC in ICT molecules was explained, some conclusions that are important for this work are summarized. First, the energy gap that has to be overcome thermally is

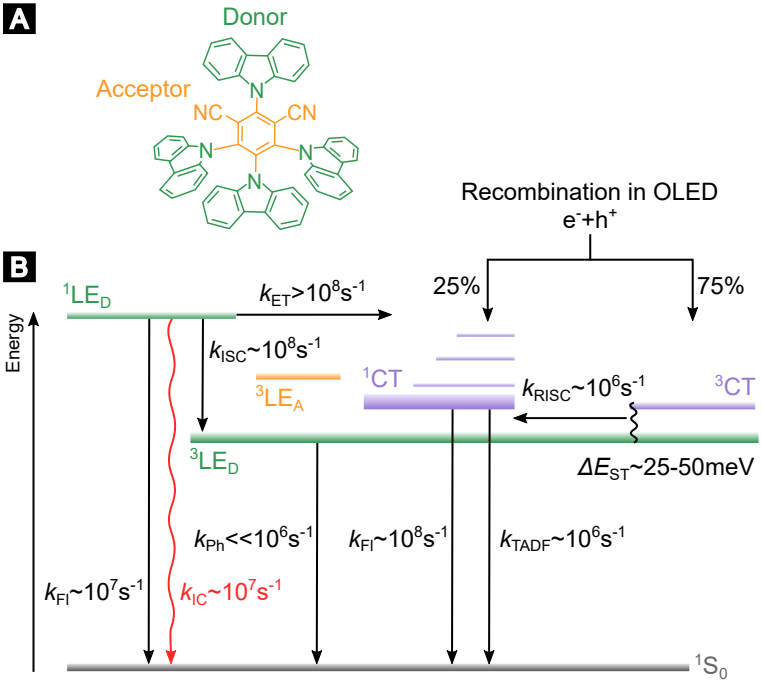

FIGURE 2.7: (A) Schematic of the benchmark TADF molecule 4CzIPN. (B) Generic Jablonski diagram of ICT-TADF molecules after Monkman [36]. Please note that to properly explain the underlying TADF mechanism, spin, electronic, and vibrational dynamics must be considered, which in principle cannot be adequately represented by a simple ladder-of-states diagram [105].

determined by the energetic position of the ^{3}LE with reference to the CT states. However, due to screening of the Coulomb interactions the energetic position of CT states is strongly dependent on the local environment, while the position of the ^{3}LE is nearly unaffected. Therefore, k_{RISC} and k_{ISC} rates of ICT molecules critically dependent on the host polarity and rigidity. Here, an increase in polarity (rigidity) stabilizes (destabilizes) CT states [80, 110]. Consequently, the judicious choice of the host is an important aspect in fine-tuning TADF based active layers [111]. Second, it should be noted that the excited state formation differs between photoexcitation by a laser and electric excitation in a device. In OLEDs, electrons (holes) are directly injected into the LUMO (HOMO) on the acceptor (donor) unit. This circumvents additional non-radiative losses that can occur during electron transfer (ET) from ^{1}LE to ^{3}LE subsequent to photoexcitation. Consequently, significantly higher IQE values are often observed in a device compared to PLQY values measured in an integrating sphere [112].

2.3.2 Reaction-Diffusion Equations of TADF Emitters

In this section, the reaction-diffusion equation for singlet and triplet excitons in TADF materials is established. Two special solutions to the equations are determined and are used at a later point to verify the results of a Monte Carlo (MC) simulation, as well as to simulate PL kinetics as a function of PL quencher concentration (see Section 3.5 and 5.3.2, respectively).

Before turning to the theoretical model, a few remarks are made to explain its basic premises. As laid out in the previous section, RISC rates are quite sensitive to the local environment of the emitter which can lead to a broad distribution of RISC rates in an amorphous thin film. However, such energetic disorder is not explicitly included in the following model (but could be approximated using effective rates). Furthermore, all processes are assumed to be linear in the triplet and singlet concentrations. The model is therefore only valid for pure TADF systems with negligible contribution of P-type fluorescence. Last but not least, incoherent exciton transport which can be described by Fick's second law is assumed (see also Section 2.2.3).

The reaction-diffusion equation for isotropically diffusing singlet and triplet excitons with concentration $c_\mathrm{s}(\boldsymbol{x},t)$ and $c_\mathrm{t}(\boldsymbol{x},t)$ and which can transition into one another and be generated at different positions $\boldsymbol{x}$ and times t, is given by:

$$\frac{\partial}{\partial t}c_\mathrm{s} = \left(D_\mathrm{s}\nabla^2 - k_\mathrm{s}\right)c_\mathrm{s} + k_\mathrm{RISC}\cdot c_\mathrm{t} + G_\mathrm{s}, \tag{2.10a}$$

$$\frac{\partial}{\partial t}c_\mathrm{t} = \left(D_\mathrm{t}\nabla^2 - k_\mathrm{t}\right)c_\mathrm{t} + k_\mathrm{ISC}\cdot c_\mathrm{s} + G_\mathrm{t}. \tag{2.10b}$$

Here, quantities connected to singlets and triplets are labeled with subscripts s and t, respectively. The first two terms on the right of the equation describe the diffusion and decay, the third term ISC between the two states and the last term the generation of excitons by a function $\boldsymbol{G}(\boldsymbol{x},t)$. The decay rates of singlet and triplet excitons are interconnected by $k_\mathrm{s} = k_\mathrm{r}^\mathrm{s} + k_\mathrm{nr}^\mathrm{s} + k_\mathrm{ISC}$ and $k_\mathrm{t} = k_\mathrm{r}^\mathrm{t} + k_\mathrm{nr}^\mathrm{t} + k_\mathrm{RISC}$, respectively.

Temporal Part of Equation 2.10

First, a solution to Equation 2.10 is considered that does not account for the diffusion part of the equation, i.e., a solution for a system without a spatial gradient in the singlet and triplet concentrations. As initial conditions a singlet concentration greater than zero and a triplet concentration of zero is chosen without generation at later times. This corresponds to a measurement of the PL kinetics after pulsed excitation. In this case, the system of partial differential equations reduces to a system of ordinary linear partial differential equations, which can be written in matrix form as:

$$\frac{\partial}{\partial t}\begin{pmatrix} c_\mathrm{s} \\ c_\mathrm{t} \end{pmatrix} = \begin{pmatrix} -k_\mathrm{s} & +k_\mathrm{RISC} \\ +k_\mathrm{ISC} & -k_t \end{pmatrix}\begin{pmatrix} c_\mathrm{s} \\ c_\mathrm{t} \end{pmatrix}. \tag{2.11}$$

By determination of the eigenvalues and eigenvectors a general solution can be constructed. Together with initial conditions $c_\mathrm{s}(0) = 1$ and $c_\mathrm{t}(0) = 0$ and requiring that the solution is bounded for $t \to \infty$, the special solution becomes:

$$\begin{pmatrix} c_\mathrm{s} \\ c_\mathrm{t} \end{pmatrix} = -\alpha\begin{pmatrix} C_1 \\ 1 \end{pmatrix}e^{-k_\mathrm{PF}t} + \alpha\begin{pmatrix} C_2 \\ 1 \end{pmatrix}e^{-k_\mathrm{DF}t}. \tag{2.12}$$

Here,

$$k_{\mathrm{PF}} = \frac{1}{2}\left(k_{\mathrm{s}} + k_{\mathrm{t}} + \sqrt{k_{\mathrm{s}}^2 - 2k_{\mathrm{s}}k_{\mathrm{t}} + 4k_{\mathrm{RISC}}k_{\mathrm{ISC}} + k_{\mathrm{t}}^2}\right)$$

and

$$k_{\mathrm{DF}} = \frac{1}{2}\left(k_{\mathrm{s}} + k_{\mathrm{t}} - \sqrt{k_{\mathrm{s}}^2 - 2k_{\mathrm{s}}k_{\mathrm{t}} + 4k_{\mathrm{RISC}}k_{\mathrm{ISC}} + k_{\mathrm{t}}^2}\right)$$

are the prompt and delayed fluorescence decay rates and $C_1 = (k_{\mathrm{t}} - k_{\mathrm{PF}})/k_{\mathrm{ISC}}$, $C_2 = (k_{\mathrm{t}} - k_{\mathrm{DF}})/k_{\mathrm{ISC}}$ and $\alpha = k_{\mathrm{ISC}}/(k_{\mathrm{PF}} - k_{\mathrm{DF}})$.

The time evolution of the singlet concentration (given by 2.12) is directly proportional to the observed fluorescence transient. It should be noted, that for organic TADF molecules $k_{\mathrm{RISC}} < k_{\mathrm{t}} \ll k_{\mathrm{s}}$ and therefore $k_{\mathrm{PF}} \approx k_{\mathrm{s}}$.

Diffusion Part of Equation 2.10

Second, the diffusion part of Equation 2.10 is studied in further detail. Here, the steady state solution for the problem of constant generation of singlet excitons at the origin is targeted as the boundary condition. Experimentally, this corresponds to generating excitons with an infinitely tightly-focused continuous-wave optical source and observing the concentration of triplets and singlets as a function of radius from this origin. The equation then is spherically symmetric and can be written as:

$$\frac{1}{r^2}\frac{\partial}{\partial r}r^2\frac{\partial}{\partial r}\begin{pmatrix} c_{\mathrm{s}} \\ c_{\mathrm{t}} \end{pmatrix} = \begin{pmatrix} \frac{k_{\mathrm{s}}}{D_{\mathrm{s}}} & -\frac{k_{\mathrm{RISC}}}{D_{\mathrm{s}}} \\ -\frac{k_{\mathrm{ISC}}}{D_{\mathrm{t}}} & \frac{k_{\mathrm{t}}}{D_{\mathrm{t}}} \end{pmatrix}\begin{pmatrix} c_{\mathrm{s}} \\ c_{\mathrm{t}} \end{pmatrix}. \tag{2.13}$$

By substitution of $\boldsymbol{c} = \boldsymbol{u}/r$ with $\partial \boldsymbol{c}/\partial r = 1/r \cdot \partial \boldsymbol{u}/\partial r - \boldsymbol{u}/r^2$ and $\partial^2 \boldsymbol{c}/\partial r^2 = 1/r \cdot \partial^2 \boldsymbol{u}/\partial r^2 - 2/r^2 \cdot \partial \boldsymbol{u}/\partial r + 2\boldsymbol{u}/r^3$ this equation can be further simplified to:

$$\frac{\partial^2}{\partial r^2}\begin{pmatrix} u_{\mathrm{s}} \\ u_{\mathrm{t}} \end{pmatrix} = \begin{pmatrix} \frac{k_{\mathrm{s}}}{D_{\mathrm{s}}} & -\frac{k_{\mathrm{RISC}}}{D_{\mathrm{s}}} \\ -\frac{k_{\mathrm{ISC}}}{D_{\mathrm{t}}} & \frac{k_{\mathrm{t}}}{D_{\mathrm{t}}} \end{pmatrix}\begin{pmatrix} u_{\mathrm{s}} \\ u_{\mathrm{t}} \end{pmatrix}. \tag{2.14}$$

The general solution to this system of second order differential equations can easily be constructed by determination of the eigenvalues and eigenvectors of its first order counterpart. For our case, a special solution can be found using the

boundary conditions $u_s(0) = 1$ and $u_t(0) = 0$ (given only singlets are created by the optical excitation at the origin) and further requiring the solution to be bounded for $t \to \infty$:

$$\begin{pmatrix} u_s \\ u_t \end{pmatrix} = \beta_1 \boldsymbol{\nu_1} e^{-\lambda_1 r} + \beta_2 \boldsymbol{\nu_2} e^{-\lambda_2 r}. \tag{2.15}$$

In the following, the eigenvalues $\lambda_{1/2}$, the prefactors $\beta_{1/2}$ as well as the two components of the eigenvectors $\boldsymbol{\alpha}_{1/2}$ will be stated. For the sake of clarity, the substitutions $a = \frac{k_s}{D_s}$, $b = \frac{k_{RISC}}{D_s}$, $c = \frac{k_{ISC}}{D_t}$ and $d = k_t/D_t$ were made. The two eigenvalues read:

$$\lambda_{1/2} = \frac{1}{\sqrt{2}} \sqrt{\mp\sqrt{a^2 - 2ad + 4bc + d^2} + a + d}. \tag{2.16}$$

The two components of the first eigenvector ν_1 are:

$$\nu_1(1) = \frac{\left(\sqrt{a+d-\sqrt{a^2+4bc-2ad+d^2}}\right)\left(-a+d+\sqrt{a^2+4bc-2ad+d^2}\right)}{\sqrt{2}c\left(-a-d+\sqrt{a^2+4bc-2ad+d^2}\right)}, \tag{2.17a}$$

$$\nu_1(2) = \frac{\sqrt{2(a+d-\sqrt{a^2+4bc-2ad+d^2})}}{-a-d+\sqrt{a^2+4bc-2ad+d^2}}, \tag{2.17b}$$

and of the second eigenvector ν_2:

$$\nu_2(1) = \frac{a-d+\sqrt{a^2+4bc-2ad+d^2})}{\sqrt{2}c\left(a+d+\sqrt{a^2+4bc-2ad+d^2}\right)}, \tag{2.18a}$$

$$\nu_2(2) = \frac{-\sqrt{2}}{\sqrt{a+d+\sqrt{a^2+4bc-2ad+d^2}}}. \tag{2.18b}$$

The two prefactors $\beta_{1/2}$ (which are determined using the two boundary conditions $u_s(0) = u_s^0$ and $u_t(0) = u_t^0$) are given by:

$$\beta_1 = \frac{u_s^0 - \beta v_2(1)}{v_1(1)} v_1(2), \tag{2.19a}$$

$$\beta_2 = \frac{u_t^0 - u_s^0 v_1(2)}{v_2(2)v_1(1) - v_2(1)v_1(2)}. \tag{2.19b}$$

The implications of Equation 2.15 will be further discussed in Section 3.5 and used here to verify a stochastic approach in simulating exciton motion between TADF emitters.

2.3.3 Hyperfluorescence

Even though substantial progress was made within the last years towards highly efficient, color pure, and stable TADF emitters, some key challenges remain to be solved in order to make TADF technology market-ready. Those challenges include the reduction of *roll-off* (decreasing external quantum efficiency at high charge carrier densities), a further increased lifespan of devices, as well as decreasing the bandwidth of the typically broad CT emission of TADF OLEDs [36]. The former two are connected to the long exciton lifetimes leading to a rapid increase in exciton density as a function of driving voltage, which, in turn, promotes bimolecular processes, like triplet-polaron or triplet-triplet annihilation [113, 114]. The resulting high-excited transient states subsequent to an annihilation event are known to expedite degradation of the emitters [115, 116].

A promising approach to tackle those issues was proposed by Nakanotatni *et al.* [37] and has been termed *hyperfluorescence technique* (also known as *TADF-assisted fluorescence*) [117, 118]. As illustrated in Figure 2.8 this approach entails additional doping with fluorescent molecules (F-dopants) to the host matrix, and use these to accept energy from the TADF molecules and emit it. By judicious choice of F-dopants, also referred to as *hyperfluorescence acceptors*,

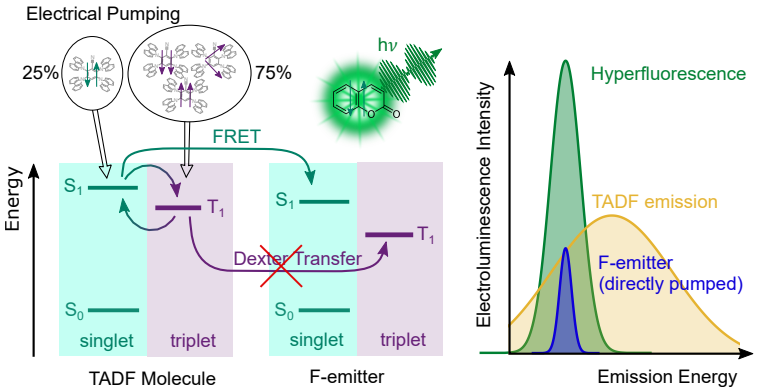

FIGURE 2.8: Schematic to illustrate the concept of an F-doped-TADF OLED, also referred to as *hyperfluorescence OLED*.

both the emission bandwidth and the excited-state lifetimes can be significantly reduced [119, 120].

In hyperfluorescence active layers both singlet and triplet excitons will primarily be formed on the TADF donors (doping concentration of F-dopants $\ll$ concentration of TADF dopants). It is then desired that singlet excitons are transferred to a hyperfluorescence acceptor, whereas corresponding triplet exciton transfer is suppressed (as it would create very-long lived dark states on the hyperfluorescence acceptors). An important factor in reaching such unmatched transfer is an increased transfer efficiency of singlet excitons (relative to triplet excitons) from TADF molecules to the hyperfluorescence acceptors. Since the transfer mechanism for singlet excitons is FRET, a good spectral overlap between the emission spectrum of the TADF molecule and the absorption spectrum of the F-dopant is essential (see Section 2.2.1). Furthermore, DET of triplet excitons could be prevented by sterically protected F-dopants, or by using TADF molecules with a small triplet diffusion length in comparison to the singlet diffusion length. The interplay between those parameters with regard to the device efficiency will be assessed in Chapter 5.

2.4 Metal-Organic Frameworks

Metal-organic frameworks (MOFs) are a new class of crystalline materials that appeared in the late 1990s. Research on these frameworks has gained enormous momentum in the following years due to a wide range of potential applications, including optoelectronics [25, 121, 122], catalysis [123], gas storage [124], chemical sensing [125] and biomedicine [126]. The success of this material class is based on the tremendous flexibility in the constituents' size, shape, and functionality with to date almost 100 000 different MOFs being reported in the Cambridge Structural database [127]. These fascinating networks are porous compounds with large surface areas that are built up from metal-based centers (*secondary building blocks*) linked by organic ligands (*linkers*). Beyond the relative ease in selecting metal centers and organic linkers to enable certain functionalities, also the doping of the pores (before or during application) adds additional versatility. Figure 2.9A depicts a scheme of a cubic MOF that is built from ditopic linkers, that is, linkers with two bonding ends (usually two carboxyl groups). However, due to the various types of linkers (ranging from di- to dodecatopic) MOFs can, in general, be found with a broad range of symmetries [128].

Surface-Anchored Metal-Organic Frameworks

In order to exploit the full potential of MOFs for optoelectronic devices, it is important to be able to control the orientation and size of the crystal grains and to create high-quality interfaces to the adjacent layers. However, this is a challenging task, since MOFs are typically nano- or microcrystalline powders and in case they are coated from solution onto a substrate they usually form polycrystalline films without a common orientation of the crystal grains [123]. Consequently, a lot of effort was put into finding a solution on how to grow a MOF directly on a substrate with a predefined crystal orientation [129]. These efforts resulted in a new class of MOFs that are grown in an epitaxial fashion onto functionalized surfaces and are referred to as *surface-anchored metal-organic frameworks* (SURMOFs) [130]. For the functionalization of the surface and anchoring of the MOF different strategies exist depending on the substrate

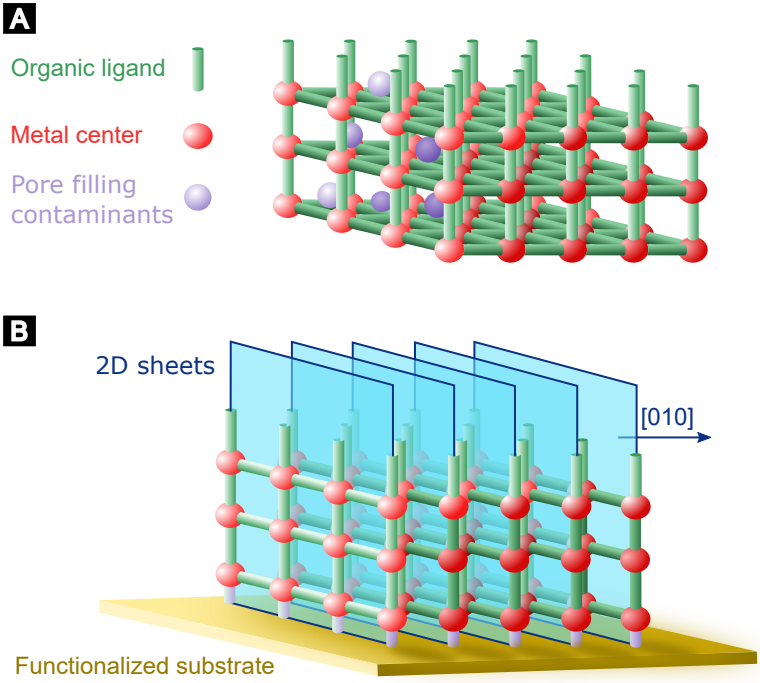

FIGURE 2.9: (A) Schematic drawing of a cubic metal-organic framework (MOF). (B) Sketch of a surface-anchored metal-organic framework (SURMOF) from the SURMOF-2 class. Here, the SURMOF is comprised of vertical 2D sheets that are stacked forming a tetragonal unit cell typically with P4 symmetry.

and the building unit's chemistry. Frequently used techniques include the usage of a self-assembled monolayer (SAM) that is coated on top of the substrate [131], as well as an oxygen plasma treatment of substrates with a native oxide layer to form hydroxyl groups [132]. Throughout this thesis, the former strategy is employed.

Special attention in this work is given to the SURMOF-2 class, a isoreticular MOF series, which is characterized by stacked two-dimensional (2D) sheets as depicted in Figure 2.9B. Here, the 2D sheets are formed by ditopic linkers bonded between two paddle-wheel type secondary building units (metal nodes) by their carboxylic acid groups [130]. The length of the linkers sets the distance to neighbors in the same sheet, while the distance between (010) planes is typically about 0.6 nm for various types of linkers [23, 130, 133]. A versatile method to deposit such SURMOF thin films is liquid-phase epitaxy, which can be employed using either a spin-, spray- or dip-coating approach, as well as a flow automation strategy [129]. Common to these approaches is the cyclic use of solutions containing linkers, rinsing agents, and secondary building units. Section 3.1.3 gives a detailed description of the spin coating process of SURMOFs, which corresponds to the method used within this thesis.

3

Methods

This chapter gives an overview of the experimental setups and techniques employed in the course of this work. In the first part, the sample preparation is discussed. Second, utilized steady-state and time-resolved spectroscopy techniques are presented, followed by a brief description of a Stern-Volmer analysis, which is useful in experimentally accessing exciton diffusion length. Last but not least, a stochastic approach of simulating the exciton motion in organic semiconductors, a Monte Carlo simulation, that is frequently used throughout this thesis is discussed in further detail.

3.1 Sample Preparation

Three different methods were employed to prepare the samples utilized within this thesis and are summarized in the following.

3.1.1 TADF Emitter in Degassed Solution

The samples employed in Chapter 4 were prepared by the present author and Rebekka V. Schneider by dissolving TADF emitter molecules in chloroform ($c = 5 \times 10^{-4}\,\mathrm{mol\,l^{-1}}$). The solutions were encapsulated in 1 mm quartz cuvettes. Since the triplet excitons are efficiently quenched by triplet oxygen (the electronic ground state of the molecule), the solutions were treated with argon prior to each measurement. This treatment involved bubbling the inert gas through a needle with an opening at the bottom of the cuvette for about 30 min. This method of degassing solutions is frequently utilized in literature for TADF emitters [134, 135]. The chemical synthesis of the employed molecules was carried out by Rebekka V. Schneider, Fabian Hundemer and Daniel Hahn (see Acknowledgments in Chapter 4) and is described in detail by Franco *et al.* [136].

3.1.2 Spin Coating of TADF Thin-Films

The samples investigated in Chapter 5 were prepared by the present author and Lorenz Graf von Reventlow (see Acknowledgments in Chapter 5) from solution and spin coated on quartz substrates at a spin frequency of $2000\,\mathrm{min^{-1}}$. Tetrahydrofuran (THF) was used as a solvent for 2,4,5,6-tetra(9*H*-carbazol-9-yl)isophthalonitrile (4CzIPN) and 2,3,5,6-tetrakis(3,6-di-*tert*-butyl-9*H*-carbazol-9-yl)benzonitrile (4TCzBN) samples, and dichloromethane (DCM) as a solvent for quinolino[3,2,1-de]acridine-5,9-dione (DiKTa) samples. Solutions were prepared using a concentration of $3\,\mathrm{g\,l^{-1}}$. For each TADF molecule samples with different quencher (weight) concentration were spin coated. As a quencher, indene-C60 bisadduct (ICBA) was used for 4CzIPN and 4TCzBN, and [6,6]-Phenyl-C61-butyric acid methyl ester (PCBM) as a quencher for DiKTa. 4CzIPN and 4TCzBN were dispersed in 1,3-bis(*N*-carbazolyl)benzene (mCP) with a weight concentration of 20 % while DiKTa at a concentration of

1 %. The molecules 4CzIPN and 4TCzBN were purchased from Luminescence Technology Corp. (Lumtec) and Osilla Ltd., respectively. The synthesis of DiKTa was carried out by Subeesh Madayanad Suresh (see Acknowledgments in Chapter 5) and is described in detail by Hall *et al.* [137].

3.1.3 Spin Coating of SURMOF Thin-Films

The Zn-ADB-SURMOF-2 (Zn-ADB) and Zn-DPP-SURMOF-2 (Zn-DPP) samples used in Chapter 6 were fabricated by Ritesh Haldar from solution and spin-coated on SAM-functionalized quartz substrates. In order to promote the self-assembly of the SURMOF, ethanolic solutions of zinc acetate (1×10^{-3} mol1^{-1}) and organic linker (20×10^{-6} mol1^{-1}) were sequentially spin-coated onto the substrates in a layer-by-layer fashion. A spin coating frequency of 2000 min^{-1} was used. As organic linkers, the molecules ditopic carboxylate 4,4'-(anthracene-9,10-diyl)dibenzoate (ADB) and ((2,5-bis(butyl)-3,6-bis(4-carboxylicphneyl-4-yl)-2,5-dihydropyrrolo[3,4-c]pyrrole-1,4-dione (DPP) were used, while as metal nodes Zn based paddle-wheel units [138] were employed (see Figures 6.1 and 6.6 for chemical structures). After each coating step of the metal or linker solution, the samples were rinsed with ethanol to remove unreacted zinc acetate, organic linkers, or by-products from the surface. The thickness of the samples was controlled by the number of deposition cycles (one cycle is equivalent to spin coating one time the metal and linker solution). 40 cycles of deposition resulted in a film thickness of about 34 nm.

For all SURMOF samples under study, the crystallinity was ensured by XRD measurements using a Bruker D8-Advance diffractometer with a wavelength of 0.154 018 nm (see Acknowledgments in Chapter 6 for details on who contributed to these material characterizations). Figure 3.1 shows exemplary XRD spectra of pristine Zn-ADB and Zn-DPP. The distance d between the planes were calculated using the Bragg condition:

$$n\lambda = 2dsin(\theta), \tag{3.1}$$

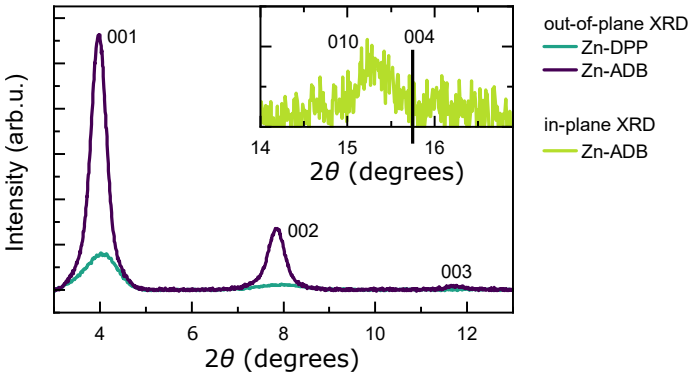

FIGURE 3.1: XRD spectrum of a Zn-ADB measured using a wavelength of $\lambda = 0.154\,018\,\text{nm}$. From these data, the distance between (001) and (100) planes was determined to 2.2 nm and the distance between (010) planes to 0.6 nm. The XRD measurements were performed by Ritesh Haldar.

where n is the order of diffraction and θ the glancing angle. Using the data shown in Figure 3.1 the distances between (001) and (100) planes were determined from out-of-plane measurements to 2.22 nm for Zn-ADB and 2.20 nm for Zn-DPP. The distance between the stacked 2D (010) planes was determined to 0.6 nm by an in-plane measurement and is equivalent for both SURMOFs (only shown for Zn-ADB in the Figure).

For the fabrication of mixed linker SURMOFs, the linker solution was prepared with different concentrations of the two linkers. The exact concentration of the two linkers in the spin-coated films was determined by dissolving the films again in DCM and measuring the optical attenuation of the pronounced absorption band of DPP at 500 nm.

Bilayer SURMOFs were fabricated by first spin-coating 25 cycles Zn-DPP as a bottom layer. In a second step, Zn-ADB was spin-coated on top for a various number of cycles.

3.2 Steady-State Spectroscopy Methods

3.2.1 Emission and Excitation Spectra

PL and excitation spectra were recorded using a spectrofluorometer (Varian Cary Eclipse) [139]. In this device, the sample is placed in-between two monochromators, one coupled to a xenon flash lamp as excitation source and the other one to a photomultiplier tube (PMT) as detector. In order to record a PL emission spectrum, the monochromator on the side of the light source is set to the desired excitation wavelength while the second monochromator scans the spectral emission range of the sample. For an excitation spectrum where the PL of the sample at a specific wavelength is tracked as a function of excitation wavelength, the second monochromator is set to a fixed position while the first monochromator scans the desired excitation range.

Alternatively, PL spectra were recorded using the variable laser output of an optical parametric oscillator (OPO) (see section 3.3.1) together with a fiber-coupled spectrometer (Avantes SensLine AvaSpec-ULS-RS-TEC). In this case, the sample was placed inside a vacuum chamber with pressures below 1×10^{-5} hPa. Scattered excitation light was blocked by a long-pass filter (Thorlabs FEL series) with a cut-on wavelength in between the spectral position of the laser and PL. Since these dielectric long-pass filters are using interference effects rather than absorption, the precise cut-on wavelength was selected by changing the angle of incidence (cut-on wavelength shifts to lower wavelength as a function of incident angle).

3.2.2 Photoluminescence Quantum Yield Measurements

An important benchmark for luminescent materials is the PLQY since it states the maximum efficiency that can be reached when the material is used as an active layer in a light emitting diode (LED). The PLQY η is defined by:

$$\eta = \frac{n_{\text{emitted}}}{n_{\text{absorbed}}}, \tag{3.2}$$

with number of emitted, n_{emitted}, and absorbed, n_{absorbed}, photons. To experimentally determine the PLQY of a material, the method of de Mello *et al.* was used throughout this thesis [140]. In this method, a spectrometer (Avantes AvaSpec-ULS2048x64TEC) is coupled to an integrating sphere (Labsphere) via an optical fiber (FP1000URT, Thorlabs). The employed integrating sphere is a hollow sphere with a diameter of 15 cm. Its inner surface is coated with Spectralon (a broadband diffuse reflecting material produced by Labsphere, Inc.) to distribute any incoming light isotropically over the sphere interior-surface. By measuring the number of photons N under a fixed solid angle Ω (e.g., given by the fiber), the total number of photons can be determined using:

$$N_{\text{total}} = \frac{4\pi N}{\Omega}. \tag{3.3}$$

Three separate measurements are required to measure the PLQY of a sample as it is illustrated in Figure 3.2. In measurement (A) the spectrum of the excitation source is measured by directing the excitation beam inside the empty integrating sphere. In measurement (B) and (C) the spectra of sample and excitation source are measured under direct and indirect excitation of the sample, respectively. The measured spectra were translated to the corresponding numbers of photons by multiplication of the spectra with a factor $\lambda/(hc)$, i.e. division by the photon energy, and subsequent integration over their spectral range. Note, that the spectrometer was irradiance calibrated using a calibration lamp (Ocean Optics HL-3P-CAL) leading to measured spectra that are proportional to a spectral intensity.

A simple way to estimate the PLQY of a sample is to use measurements (A) and (B) together with the following equation:

$$\eta \approx \frac{P_{\text{B}}}{L_{\text{A}} - L_{\text{B}}}. \tag{3.4}$$

Here, the integrated values of the PL and laser spectrum are denoted as P_{X} and L_{X}, respectively, together with the subscript X denoting the respective measurement. However, in this equation emission events are also counted stemming from absorption of photons that have previously been scattered at the integrating sphere (subsequent to reflection or transmission at the sample). In

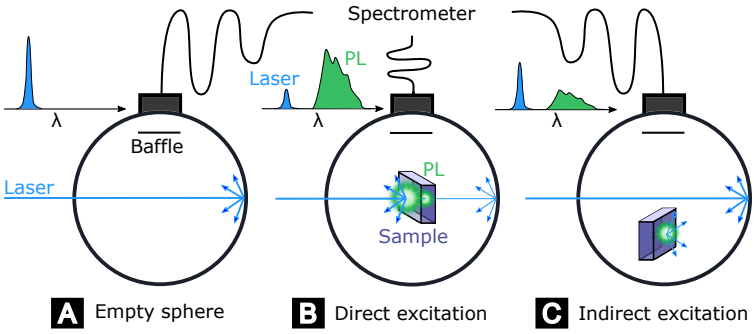

FIGURE 3.2: Scheme illustrating the three configurations of the integrating sphere used to determine the PLQY of a sample. (A) the sphere is empty; (B) the sample is in place and the excitation light is directed at the sample; (C) the sample is in place and the excitation light is directed onto the sphere wall. After de Mello *et al.* [140].

order to account for this fraction, measurement (C) is employed. In this case, the absorption A by the sample for a single interaction with the excitation light can be calculated by:

$$A = 1 - \frac{L_B}{L_C}. \tag{3.5}$$

The number of photons emitted by the sample in experiment (B) can be expressed as:

$$P_B = \eta L_A A + (1 - A) P_C. \tag{3.6}$$

Here, the first summand governs the emitted photons for which the connected absorption event was the first interaction of excitation light with the sample, while the second summand governs the emitted photons generated after absorption of light that has already had an interaction (reflection or transmission) with the sample. Rearranging Equation 3.6 leads to:

$$\eta = \frac{P_B - (1 - A) P_C}{L_A A}, \tag{3.7}$$

which is used to calculate the PLQY of the samples.

As an excitation source either a 375 nm LED (Thorlabs, LED375L) or a 405 nm continuous wave (CW) laser diode (Thorlabs, DL5146-101S) was utilized.

3.2.3 Ultraviolet-Visible Spectroscopy

Ultraviolet–visible spectroscopy (UV-Vis) absorption spectra were measured using a spectrophotometer (PerkinElmer LAMBDA 950 UV/Vis/Nir) [141] equipped with an integrated 150 mm integrating sphere coated with Spectralon. In this device, either a deuterium (for the ultraviolet range) or a tungsten halogen light source is used as an excitation source. The light sources are coupled to a double monochromator that is used to scan the illumination wavelength. Behind the monochromator, the light beam is split into a reference and a sample beam by a rotating reflective chopper wheel, which allows for compensation of light intensity fluctuations. The sample is placed in the center of the integrating sphere and is directly illuminated by the sample beam. The reference beam enters the integrating sphere off-centered such that light only reaches the sample via at least one scattering event at the integrating sphere's surface. For the detection of photons in the wavelength ranges 200 nm to 860 nm and 860 nm to 2500 nm a PMT and an InGaAs detector, respectively, are utilized.

The transmittance T is calculated according to:

$$T = \frac{I_{\text{sample},1} I_{\text{reference},0}}{I_{\text{sample},0} I_{\text{reference},1}}, \tag{3.8}$$

by using a measurement without sample ($I_{\text{sample},0}$ and $I_{\text{reference},0)}$) and a subsequent measurement with the sample inside the integrating sphere ($I_{\text{sample},1}$ and $I_{\text{reference},1)}$). The absorbance of the sample A can then be determined according to:

$$A = -\log_{10} T. \tag{3.9}$$

3.3 Time-Resolved Spectroscopy Methods

Within this work, both transient absorption as well as transient PL measurements were performed to gain insights on the exciton dynamics of the studied materials. For time-resolved PL measurements, three different setups were utilized: 1) A streak camera setup that was utilized if a sub-nanoseconds resolution was necessary, or if spectral shifts during PL decay had to be resolved; 2) An intensified charge-coupled device (ICCD) setup that was mainly used when TADF samples were studied since it allows for fast measurement of the ratio between prompt and delayed emissions; 3) A transient-absorption setup that was employed in case non-emissive species were probed. During all time-resolved measurements, the samples were held in a dynamic vacuum chamber with pressures below 1×10^{-5} hPa. For each time-resolved measurement, the fluence of the laser was determined by measuring spot size and pulse energy with a beam profiler (BC106N-VIS/M, Thorlabs) and an energy meter (LabMax, Coherent).

3.3.1 Streak Camera

A streak camera is used to measure ultrafast light phenomena (typically in the pico- to microsecond range) and, in combination with a spectrometer, provides intensity versus time versus wavelength information. The operating principle of a streak camera is sketched in Figure 3.3A. The luminescence of the sample is dispersed by a spectrometer and focused on the entrance slit of the streak camera. A set of lenses images the entrance slit onto the photocathode, where the incident light is converted to a number of electrons that is proportional to the incoming light intensity. The emitted electrons are accelerated parallel to the optical axis by an accelerating mesh and are passing a parallel plate capacitor. A temporally increasing high voltage is applied to the electrodes of the capacitor at a time synchronized with the incident light pulse. This ultra-fast temporal change in the voltage across the electrodes results in a high-speed sweep in which electrons are deflected in an increasing vertical direction depending on their arrival time. In this way, the timing information, when the electron entered the capacitor, is mapped to the vertical direction on the microchannel plate

(MCP). Precise control of the change in voltage at the capacitor enables a linear increase in time as a function of vertical position on the MCP. The MCP is responsible for the gain by multiplying the electrons several thousand times before they penetrate the phosphor screen. At the phosphor screen, the impact of the electrons leads to the emission of photons which are detected by a charge coupled device (CCD). All components in between photocathode and phosphor screen are embedded in a high vacuum tube also termed *streak tube*.

Figure 3.3B shows a sketch of the streak camera setup. The universal streak camera (C10910-02, Hamamatsu) with a S-1 photocathode (sensitivity range of 300 nm to 1600 nm) is coupled to a spectrometer (SpectraPro 300i, Acton). A mode-locked Ti:sapphire laser (Chameleon Ultra II, Coherent) with a repetition rate of 80 MHz and a pulse width of 140 fs is used as the excitation source for the sample. The variable wavelength (680 nm to 1080 nm) of the laser is extended by an OPO second-harmonic generation (SHG) system (Chameleon Compact OPO-Vis, Coherent). Within this system, the output of the laser can either be frequency doubled by a SHG unit or alternatively the 800 nm output can be used to pump the OPO with an optional SHG for the OPO signal beam. This combination of frequency doubling and frequency conversion by the OPO results in a broad tunable wavelength range from 340 nm to 1600 nm. The repetition rate of the laser can be reduced by a pulse picker, which is required for the measurement of PL lifetimes in the nanosecond and microsecond range and is employed in combination with the single-sweep unit (*vide infra*).

The employed streak camera can be utilized to measure time intervals in the range of 100 ps to 1 ms with a time resolution down to 1 ps. To cover those time intervals two distinct sweep units are required, a synchroscan and a single-sweep unit. The two sweep units contain the sweep electronics that are responsible for the generation of the voltage that is applied to the sweep electrodes. The synchroscan sweep unit (M10911-01, Hamamatsu) uses a sinusoidal voltage that is synchronized to the oscillator frequency of the mode-locked laser. The synchronization occurs via a photodiode (C1808-03, Hamamatsu) which is illuminated by a small fraction (i.e., 10 %) of the laser output together with a delay generator (C12270-01, Hamamatsu). The synchronization with the laser enables 80×10^6 experiments per second leading to a very good signal-to-noise ratio and measurement times often of “just” a couple of minutes. Another benefit of the synchroscan is the high time resolution down to 1 ps. However,

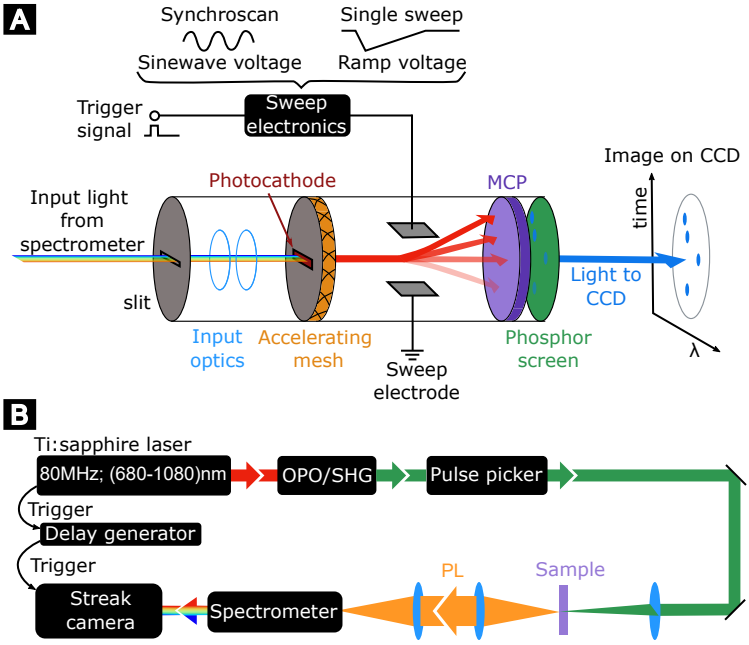

FIGURE 3.3: (A) operating principle of a streak camera based on *Guide to Streak Cameras* [142]. (B) sketch of the streak camera setup used within this thesis. A mode-locked Ti:sapphire laser is used to excite the sample. The wavelength of the laser can be tuned by an OPO-SHG system and the 80 MHz repetition rate decreased by a pulse picker. The PL of the sample gets dispersed by a spectrometer before the light enters the streak camera.

the maximum time interval (also termed *time base*) is limited to about 2 ns, since only the nearly linear range of the sinusoidal voltage (with time interval 12.5 ns) is used for the streak image. Another downside of the synchroscan unit can be the return sweep of the electrons in the second half period of the sweep voltage if the sample is still emitting light after about 5 ns subsequent to its excitation. Unlike the single-sweep unit presented below, the voltage of the MCP cannot be changed fast enough to prevent those electrons from the return sweep to contribute to the signal measured with the CCD, i.e., gating is not an option for the synchroscan unit.

The single-sweep unit (M10913-11, Hamamatsu) uses a ramp voltage to cover time bases in the range of 1.2 ns to 1 ms and time resolutions down to 20 ps. The unit is triggered by a delay generator (DG645, Stanford Research), which is in turn triggered by the internal clock (transistor-transistor logic (TTL) signal) of the mode-locked laser. The maximum sweep frequency of the single-sweep unit is 4 MHz, which makes it necessary to use the pulse picker to reduce the fundamental frequency of the laser by at least a factor of 20. The advantage of the lower repetition rate is not only the possibility to measure PL decay times in the nanosecond and microsecond range but as already indicated the possibility of gating the MCP. As such, the return sweep of the electron beam is never an issue when the single-sweep unit is employed.

The streak camera system was utilized throughout this work when spectral changes as a function of emission time were studied, as well as when a time-resolution below 1 ns was required to resolve certain photophysical processes. In part, the studies on the Zn-ADB SURMOF posed exactly these requirements, making streak camera measurements an important element of Chapter 6.

3.3.2 Time-Correlated Single Photon Counting

Time-correlated single-photon counting (TCSPC) is an alternative approach to measure PL kinetics and decay times. Figure 3.4 shows a sketch of the TCSPC setup used in this work, which will be briefly characterized in the following.

The diode controller starts the experiment by triggering the LED (NanoLED, Horiba), as well as the counter of the timing electronics (Single Photon Detection Module, FluoroHub). The light pulse of the LED excites the sample and a

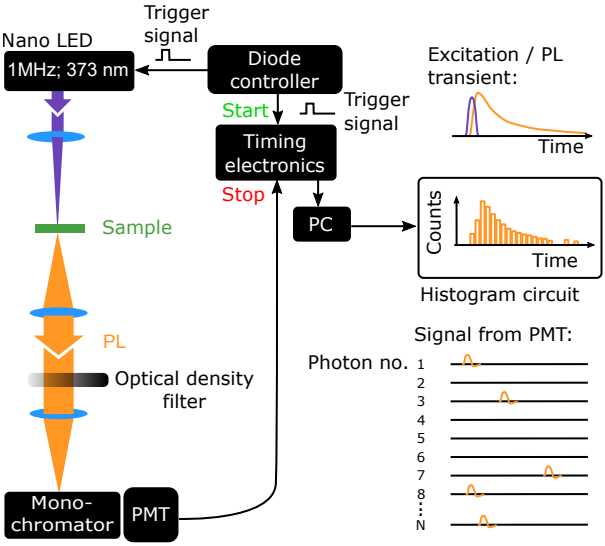

FIGURE 3.4: Schematic of the TCSPC setup used in this work. The diode controller simultaneously triggers the LED and the timing electronics to start the counter. The light pulse of the LED excites the sample and the PL is detected by a PMT that is coupled to a monochromator. The electric pulse generated by the PMT stops the counter of the timing electronics. The measured time interval is stored in a histogram before the measurement is repeated. Below 5 % of the experiments lead to a detection of a photon at the PMT as indicated by the schematic in the bottom right corner.

predefined wavelength range of the PL passes a monochromator and is detected by a PMT (PPD-650, Horiba). Once the signal of the PMT reaches the timing electronics the counter is stopped and the measured time interval stored in a histogram. This experiment is repeated many times until the histogram has the shape of a continuous function (usually over at least two to three orders of magnitude). It should be noted, that the dead time of the timing electronics after an event was counted lies in the time range of several 100 ns and therefore only one photon per excitation pulse can be detected . Furthermore, the high time resolution in the range of 0.1 ns of TCSPC measurements is reached by employing the steep rising edge of the electric pulses generated by the PMT in order to stop the counter of the timing electronics. Overlapping electronic pulses resulting from photons penetrating the PMT at similar times would therefore be detected as a single photon, even if the dead time of the electronics would be shorter. As a consequence, it must be assured that the probability of detecting more than one photon within one excitation period is sufficiently low (otherwise the PL transient will appear skewed towards shorter times). In practice, this is achieved by selecting a detection rate that is below 5 % of the repetition rate of the excitation source, either by adjusting the slit width of the monochromator or alternatively by an optical density filter that attenuates the excitation source or the PL. This means that in the majority of the experiments no photon is detected at all.

In case only one single species is emitting, the gained PL transient is proportional to its concentration. If multiple species with overlapping spectra are emitting, the PLQY of each species must be considered to determine their concentrations based on the PL transient. Within this work, TCSPC measurements were preferred to streak camera measurements in case only a specific wavelength of emission was studied.

3.3.3 Intensified Charge-Coupled Device

An ICCD is used to measure PL spectra of a sample within predefined time intervals after excitation. An ICCD consists of an image intensifier tube connected in series to a CCD. The image intensifier tube is similar in construction to the streak tube of a streak camera, with the main difference being the absence of the sweep electrodes and the accelerating mesh (see Figure 3.3A). Photons

that enter the ICCD are focused on a photocathode. The emitted photoelectrons are accelerated along the optical axis by a potential difference between the photocathode and the MCP. The electrons multiplied by the MCP impinge on a phosphor screen and the released photons are detected by a CCD.

The time resolution of the ICCD is introduced by controlling the gain of the device as a function of time. For fast switching (nanosecond range) between high and low gain, the potential difference between MCP and photocathode is altered from positive to negative values (in the range of $\pm 100\,\mathrm{V}$). In this way, emitted electrons from the photocathode can only reach the MCP in the desired time window. At slower gating ($> 100\,\mathrm{ns}$), the much higher potential applied across the MCP (typically up to 1000 V) can also be controlled.

Figure 3.5 shows a sketch of the ICCD setup. A Q-switched laser (picolo 1, InnoLas) with variable repetition rate (throughout this work a repetition rate of 5 kHz was used) and a wavelength of either 532 nm (second harmonic) or 355 nm (third harmonic) is employed to excite the sample. By using an interchangeable dichroic mirror that transmits the laser wavelength, but reflects the PL, the same lens is used to focus the excitation light on the sample and to collimate the emitted PL. The PL is coupled into an optical fiber which is connected to a spectrometer (SP-2358, Acton). The spectrometer is in turn coupled to the ICCD (PI-MAX4:1024f-HR, Teledyne Princeton Instruments). The timing electronics for gating the ICCD is triggered by the internal clock of the Q-switched laser. The smallest gate width of the system is 3 ns.

The ICCD setup was mainly used to study the exciton diffusion of TADF molecules (Chapter 5). Here, the advantage over the streak camera and TCSPC setup is the flexible gate width. It is beneficial in measuring PL transients that have decay components that differ in lifetime by several orders of magnitude, e.g., the prompt PL (nanosecond range) and the delayed PL of TADF molecules (microsecond range).

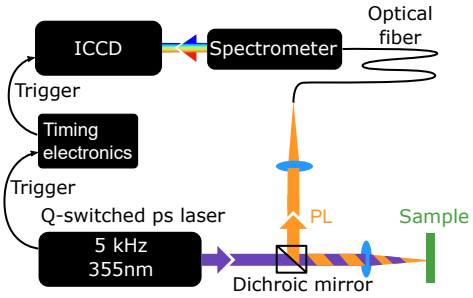

FIGURE 3.5: Schematic of the ICCD setup used within this work. A Q-switched laser is used to excite the sample through a dichroic mirror that transmits the 355 nm photons of the laser. The PL of the sample is reflected by the dichroic mirror and coupled into an optical fiber that is connected to the spectrometer-ICCD system. The ICCD is triggered by the internal clock of the laser.

3.3.4 Transient Absorption Spectroscopy

The underlying concept of transient absorption spectroscopy (TAS) is to investigate how the interaction between a probe pulse and a sample changes when the sample was previously excited by a pump pulse. The variable delay between the pump and probe beams allows for tracking those changes (which are attributable to the dynamics of the excited states) as a function of time. Figure 3.6 depicts the TA setup used in this thesis and will be introduced in the following.

Probe pulses are generated by white-light continuum generation (WLG) in a sapphire crystal using the output of a femtosecond amplifier (Spitfire Pro XP, SpectraPhysics). The femtosecond amplifier delivers a train of 800 nm laser pulses with a pulse width below 120 fs at a repetition rate of 1 kHz. The WLG process is based on multiple higher-order nonlinear processes acting together to cause severe spectral broadening of the pump beam [143]. Precise positioning of the 3 mm sapphire crystal relative to the focal plane of the lens in front of the crystal is a prerequisite for stable WLG. Therefore, the sapphire crystal is mounted on a linear translation stage (PT1, Thorlabs) allowing for translation with micrometer precision along the optical axis. In addition, the crystal can be rotated to ensure that the laser beam enters perpendicular to its front surface

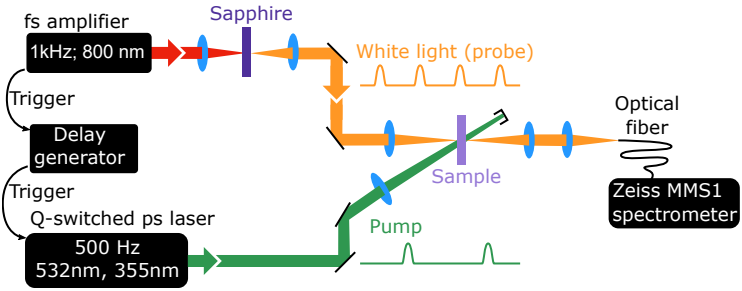

FIGURE 3.6: Schematic overview of the TAS setup. The white-light is generated by a sapphire crystal excited by 800 nm femtosecond pulses. These probe pulses are spatially overlapped on the sample with pump pulses generated by a Q-switched laser at half the frequency of the femtosecond amplifier repetition rate. A fiber-coupled spectrometer is used to detect the white-light pulses transmitted through the sample.

and a variable neutral-density filter (NDL-10C-2, Thorlabs) is used to adjust the power of the laser. Behind the sapphire crystal, a hot mirror is placed to damp the remaining 800 nm laser light, which would saturate the detector.

Pump pulses are generated by a Q-switched pump laser (picolo-1 MOPA, InnoLas Laser GmbH) with a fundamental wavelength of 1064 nm and variable repetition rate up to 5 kHz. A built-in harmonic generator module allows for conversion of the fundamental wavelength to 532 nm and 355 nm by a temperature-controlled lithium triborate (LBO) non-linear crystal. The Q-switched laser is electronically triggered by TTL pulses and synchronized to half the repetition rate of the femtosecond amplifier. The time delay between the probe and the pump pulses, as well as halving the frequency is introduced by a delay generator (DG535, Stanford Research Systems).

Pump and probe beams are focused on the sample and spatial overlap between both beams is verified. The diameter of the pump beam is chosen at least one order of magnitude wider than the probe beam to ensure an approximately constant excitation density over the probed region. For the detection a fiber-coupled spectrometer (MMS1, Zeiss) is used, whose pixel values are read out at

a frequency of 1 kHz. Throughout this work, only the change in transmission of the probe beam was measured (in contrast to a TAS reflection measurement). Two adjacent measurements, one of the excited and one of the unexcited sample, are used to calculate the TAS transmission signal $\Delta T/T$ for a given delay t_0 as:

$$\Delta T/T(\lambda, t_0) = \frac{T_{\text{on}}(\lambda, t_0) - T_{\text{off}}(\lambda)}{T_{\text{off}}(\lambda)}, \tag{3.10}$$

where T_{on} is the transmission of the excited and T_{off} of the unexcited sample. Further details on the software that was used to process the TAS data can be found elsewhere [144].

Using the cross-section $\sigma(\lambda)$ and the density of the species $N(t)$, as well as the thickness of the sample d, the contribution of a single species to the $\Delta T/T$ can be expressed as:

$$\Delta T/T(\lambda, t_0) = N(t)\sigma(\lambda)d. \tag{3.11}$$

In a TAS measurement three different signal types are usually differentiated: i) ground state bleach; ii) stimulated emission and iii) induced-absorption, which are summarized in Figure 3.7. As a side comment, in this work only organic samples together with low excitation fluences (<50 nJ cm^{-2}) were employed and therefore other features in the TAS spectrum that are frequently observed for inorganic semiconductors, e.g., changes in the refractive index or bandgap as a function of excitation density, are not discussed. Furthermore, all measurements were conducted with linear pump and probe polarizations and under the magic angle (54.7°) offset between them. This offset ensures that the measured dynamics are connected to changes in the excited state population and not (also) due to rotations of the probed transition dipole moments.

Ground State Bleach

A positive contribution to the signal occurs when the ground state of the sample is depopulated due to the creation of excited states by the pump pulse. This positive contribution to the $\Delta T/T(\lambda)$ is restricted to spectral regions where

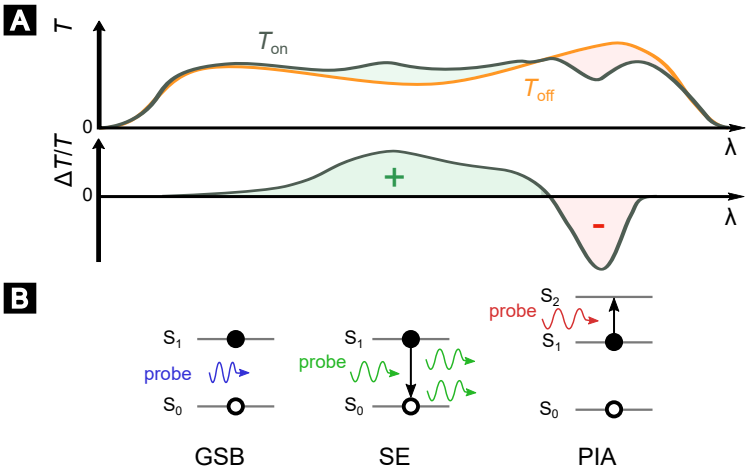

FIGURE 3.7: Schematic of possible features in a TAS spectrum. (A) Measured white-light spectrum with and without pump together with the resulting $\Delta T/T$ signal. (B) Overview of the excitonic processes that can be linked to the $\Delta T/T$ signal shown in (A). A positive $\Delta T/T$ is either attributed to a ground state bleach (GSB) or stimulated emission (SE), while a negative signal is attributed to photoinduced absorption (PIA).

the UV-Vis absorption spectrum of the sample is greater than zero. The spectrum of the ground state bleach is given by the ground state absorption of the chromophores that support the excited states.

Stimulated Emission

The radiative transitions of the sample can be stimulated by photons of the probe pulse that are in resonance with the transition. This process leads to an increase in T_{on} and therefore to a positive $\Delta T/T(\lambda)$. The spectral shape and kinetic of the stimulated emission spectrum is determined by the excited species present and can usually be correlated to a time-resolved PL kinetic, i.e., correlated to a streak camera measurement.

Photoinduced Absorption

A negative contribution to $\Delta T/T$ occurs when the excited species present absorb light. The transitions of the excited state species lie in general at different spectral positions than the optical transitions from the ground state, thus PIA spectra are characteristic of the excited states involved. Please note that optical transitions between the first excited triplet and higher-lying triplet states often carry a non-negligible oscillator strength and therefore PIA signals are very useful in probing triplet state kinetics (which are often not accessible by time-resolved PL measurements).

3.4 Stern-Volmer Analysis

A Stern-Volmer (SV) analysis is a frequently used tool to investigate fluorescence quenching phenomena [39, 145]. In such quenching analyses, two fundamentally different quenching processes must first be distinguished, static and dynamic quenching. In the first case the quencher forms a non-emissive complex with the fluorophore prior to excitation, that is, for quenched fluorophores, the emissive species is never formed during or subsequent to photoexcitation. Consequently, the fluorescence lifetime of the sample stays unchanged, and only the relative PL intensity changes as a function of quencher concentration. In contrast, for dynamic quenching, the emissive excited state is formed and subsequently quenched during its lifetime. Therefore, a hallmark of dynamic quenching is a reduction of this lifetime with increasing quencher concentration. In this thesis, only dynamic fluorescence quenching experiments are performed, and here again only those that can be referred to as *collisional quenching experiments*. As a side note, in literature collisional and dynamic quenching are often used as synonyms, however, in principle only all collisional quenching experiments are dynamic but not vise versa, e.g., a chromophore that is conjugated with a FRET acceptor (quencher) will exhibit a decreased fluorescence lifetime even though there is no relative (diffusive) motion between emitter and acceptor involved [146]. Along this line, the TADF-oligomer conjugates (T-oligomers) introduced in Chapter 4 fall into this category. Here, the inherently

dynamic FRET from oligomer to TADF core leads to dynamic quenching of the oligomer's fluorescence without any diffusive motion involved in this process.

Collisional quenching experiments can be employed to either extract diffusion constants of the quenching species, the fluorophore or of the exciton's motion [65, 147]. In general, such collisional quenching experiments of an excited fluorophore species F and a quenching species Q can be described by the following kinetic scheme [148, 149]:

$$\mathrm{F}^* + \mathrm{Q} \underset{k_\mathrm{d}}{\overset{k_{-\mathrm{d}}}{\leftrightarrows}} (\mathrm{F}^*\mathrm{Q}) \xrightarrow{k_\mathrm{a}} \mathrm{P}^*, \tag{3.12}$$

with $(\mathrm{F}^*\mathrm{Q})$ being a transient intermediate during the collision before the irreversible reaction product P^* (e.g., the excited quencher) is formed. Please note that for the case of exciton diffusion, the excited fluorophore F^* on the left-hand side of the equation is generally different from the one forming the intermediate state. The associated rates in Equation 3.12 are the bimolecular rate k_d for the formation of encounter pairs (directly connected to the diffusion constant of F or Q), and the monomolecular rates $k_{-\mathrm{d}}$ and k_a connected to their disappearance. For purely diffusion-controlled quenching $k_\mathrm{a} \gg k_{-\mathrm{d}}$ applies, which is also an important assumption for the validity of the Smoluchowski model employed throughout this thesis (*vide infra*). Furthermore, the fluorophore and quencher are assumed to be at fixed positions (at least within the lifetime of the exciton) and therefore the bimolecular rate is considered to be associated only with the motion of the exciton. This said, the decay rate $k([Q])$ of the fluorophore as a function of quencher concentration $[Q]$ can be described by:

$$k([Q]) = k_r + k_{nr} + k_Q[Q], \tag{3.13}$$

with k_r being the radiative, k_{nr} the non-radiative decay rate of the fluorophore without any quencher present, and k_Q the bimolecular quenching rate (here equal to k_d). The rate k_Q can then be used to calculate the diffusion constant of the exciton employing the Smoluchowski equation. Therefore, the task of determining the diffusion constant of the emissive species in diffusion-controlled quenching experiments reduces to the determination of k_Q.

In a SV analysis, k_Q is effectively extracted using the slope of the following linear function in $[Q]$, which is obtained by forming the ratio of the quenched and unquenched PL rates:

$$\frac{k([Q])}{k(0)} = 1 + \frac{k_Q}{k_r + k_{nr}}[Q] = 1 + K[Q]. \tag{3.14}$$

Assuming that the quenching rate k_Q is constant in time and independent of the quencher concentration, Equation 3.14 leads to a straight line with slope $k_Q/(k_r + k_{nr})$, usually referred to as the SV constant K. The reciprocal of the SV constant labels the quencher concentration at which 50 % of the fluorescence is quenched.

Employing the Smoluchowski equation the diffusion length (and hence the diffusion constant) can be extracted by:

$$l_{\mathrm{D}} = \sqrt{\frac{6K}{4\pi R}}, \tag{3.15}$$

where R is the interaction radius given by the radius of the exciton plus the radius of the quenching species. Notably, the Smoluchowski model assumes an infinite quenching rate at the contact distance R [39, 150]. This must be taken into account, for example, in the design of the MC simulation, such that when the exciton approaches the quencher, the quenching rate has to dominate the other possible hopping or decay rates of the exciton.

The SV plot can also deviate from a straight line, depending on the underlying mechanism that mediates the quenching process. Figure 3.8 summarizes frequently observed quenching mechanisms (and combinations) and their impact on the SV plot. Please mind, that the ordinate is labeled here as $\mathrm{F}_0/\mathrm{F} - 1$ to better differentiate the different quenching mechanisms. However, for fully diffusion-controlled quenching, employing fluorescence intensities (or PLQY values) is equivalent to a rate-based SV plot.

Concave-down SV plots can be observed when only a fraction of the quenchers are accessible for the excitons, e.g., due to quencher aggregation (see Chapter 6), or when some fluorophores are protected from quenching [39]. In contrast, concave-up SV plots are characteristic for combined static (e.g., complexion)

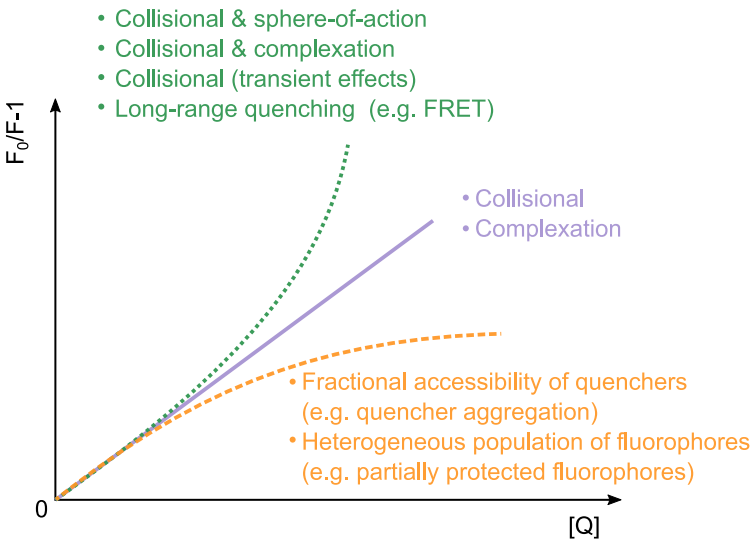

FIGURE 3.8: Generic SV plots based on the fluorescence intensity. Dependent on the mechanism that mediates quenching SV plots might deviate from the linear expression. The different cases are extracted from Lakowicz [39] and Gehlen [145].

and dynamic quenching. Remarkably, this sometimes also applies to situations of apparent static quenching (no changes in lifetimes), where the underlying quenching mechanism is nevertheless dynamic in nature. This can be the case especially if the extent of quenching is large. Here, each quencher is surrounded by a sphere with volume V in which the escape probability of a photo-excited exciton is virtually zero and is referred to as *sphere-of-action quenching*. The presence of a sphere-of-action leads to higher terms in $[Q]$ [39]:

$$\frac{\mathrm{F}}{\mathrm{F}_0} = (1 + K[Q]) \exp\left(V N_\mathrm{A}[Q]\right), \tag{3.16}$$

where N_A is Avogadro's constant. Another example for concave-up SV plots is also observed when the quenching process is not fully diffusion-controlled

but also reaction controlled ($k_a \sim k_{-d}$). In this case, and in contrast to the Smoluchowski or diffusion-limited model, the reduced reaction probability leads to transient quenching effects, since steady-state is not instantaneously achieved after excitation [149]. Last but not least, if the overall quenching has significant contributions from interactions stemming from distances that are greater than R (e.g., FRET-based quenching), the SC plot also deviates from a straight line and is again concave upward [150, 151].

In Chapter 5 the SV analysis is further developed to determine the diffusion length of non-emissive triplet states in TADF molecules.

3.5 Monte Carlo Simulation

A well-established method to simulate transport phenomena in organic semiconductors is a MC simulation [152–155]. The stochastic core principle of MC simulations can be conveniently implemented for organic semiconductors due to the in most cases good approximations of exciton localization to single molecules (no wave functions needed) and the random nature of hopping (diffusive transport) of the excited states. Within this work MC simulations were used to model the singlet and triplet exciton diffusion between TADF emitters, as well as singlet exciton diffusion in a SURMOF (Chapter 5 and Chapter 6, respectively). Since the development of the MC simulation is equivalent in both cases, the approach is only discussed for the TADF molecules in further detail below.

3.5.1 Simulation Method for TADF Molecules

For the TADF molecules the goal was to simulate PL quenching experiments as well as hyperfluorescence systems. In the two cases, TADF molecules had to be dispersed in a host matrix together with changing concentrations of a PL quencher or fluorescence acceptors (F-dopants), respectively. Figure 3.9 gives an overview of the different molecule types used in the simulation. The molecules were randomly placed (taking into account their predefined concentrations) on a cubic lattice with a lattice constant of 1 nm. In order to

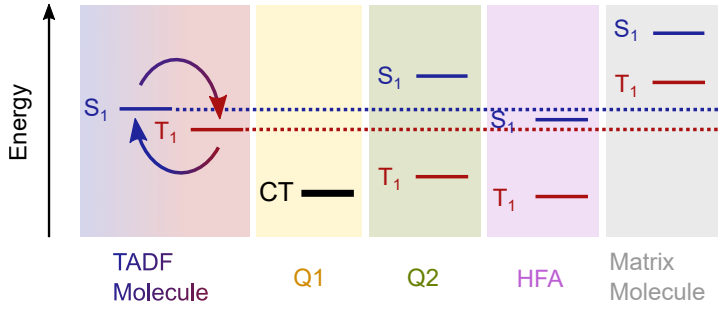

FIGURE 3.9: Schematic of the alignment of energy levels of the different molecules used in the simulations. The different depicted energy levels are the first excited singlet (S_1), the first excited triplet (T_1) and a charge transfer state (CT). Reprinted with permission from Jakoby *et al.* [56].

reduce the computation time of the simulations, all molecules of the same type were assumed to be isoenergetic, and periodic boundary conditions were utilized in all directions of the lattice. Hopping rates of singlet excitons were calculated using Förster theory, while of triplet excitons by employing Dexter theory (see Section 2.2). An excited state was introduced on a TADF molecule at a random position within the simulated volume. Optical pumping was mimicked by starting with 100 % in a singlet state, and electrical pumping by starting with 75 % in a triplet and 25 % in a singlet state. Two random numbers were generated to determine the lifetime of the state (employing inverse transform sampling and the exponential lifetime distribution of the state) and how the excited state will decay (i.e., radiative, non-radiative, ISC, or RISC). Until the lifetime of the exciton is reached, it propagates through the matrix by hopping, as described in the following. If ISC occurs, a new set of random numbers is selected for the lifetime of the new spin state and the decay mechanism. This continues until the exciton decays. At each ISC event the root mean square (RMS) displacement of the state relative to point of its creation (either injection or a previous ISC event) is recorded in a histogram. Additionally, the total RMS displacement of the exciton from injection until radiative or non-radiative decay, as well as its total lifetime are added to histograms. If the exciton undergoes radiative recombination, the counter for emitted photons is increased by one.

Here, emission events that include at least one cycle through the triplet state are counted separately from states that directly undergo radiative decay. These two counter values could then be used to calculate the prompt and delayed PLQY of the system by dividing them by the total number of excited states (sequentially) introduced to the system. The spatial histograms were binned into linear spaced bins with a width of 0.25 nm, while the temporal histograms were binned in 10 000 logarithmically spaced bins in the range of 1 ps to 10 ms.

3.5.2 Monte Carlo Step

The MC step of the simulation is based on the Direct Method of Gillespie [156], shortly introduced in the following. In a first step, a list of all possible hopping rates ξ_{ij} from the current position i to neighboring TADF and acceptor molecules j is determined. Second, two random numbers X_1 and X_2 are drawn from the uniform distribution in the unit interval, and a hop with rate ξ_{ik} is selected by the first random number:

$$\sum_{j=1}^{k-1} \xi_{ij} < X_1 \sum_{j=1}^{j_{\max}} \xi_{ij} \leq \sum_{j=1}^{k} \xi_{ij}. \tag{3.17}$$

The second random number is used to calculate the waiting time Δt for this hop, using inverse transform sampling:

$$\Delta t = -\frac{\ln(X_2)}{\sum_{j=1}^{j_{\max}} \xi_{ij}}. \tag{3.18}$$

In order to decrease the runtime of the simulation, the search for new hops to TADF molecules is stopped once the rate of the last added hop is less than 1 % of the fastest rate and defines $j_{\max}$.

3.5.3 Verification

The results of the MC simulation were verified by comparison with analytic solutions of the reaction-diffusion equation detailed in Section 2.3.2. Here, the

simulated system was comprised only of TADF molecules. The decay rates (k_r^S, k_{nr}^S, k_{ISC}, k_r^t, k_{nr}^t and k_{RISC}) were selected in accordance to one of the benchmark TADF molecules 2,3,5,6-tetra(9H-carbazol-9-yl)benzonitrile (4CzBN) [157]. The diffusion length for singlet excitons (selected via R_0) was set to 26 nm for the total lifetime of the exciton (including cycling) and the triplet diffusion length was varied (via J) between the simulations. Figure 3.10 compares the analytic solution with the MC simulation. In Figure 3.10A the time evolution of the system (by spatial integration over all excitons) is depicted for an initial condition of a singlet concentration greater zero and a triplet concentration of zero (at $t = 0$). The MC simulation was carried out for 1×10^7 simulated excitons. In Figure 3.10B the spatial solution for a constant injection rate of singlet excitons at the origin is depicted once quasi steady state is reached. Please note that in Figure 3.10B the solutions are plotted as concentrations times radius, since in this case the data can be described by biexponential functions (see Section 2.3.2).

The diffusion constants of singlet and triplet excitons (needed for the analytic solution in Figure 3.10B) were calculated based on the hopping rates ξ_{ij} from an arbitrary site i to all other sites j, and the distances x_{ij}^2 by using the following equation (see also Section 2.2.3):

$$D_i = \frac{1}{6} \sum_{j=1}^{j_{max}} \xi_{ij} \Delta x_{ij}^2. \tag{3.19}$$

For both cases, namely the spatial and temporal evolution of the singlet and triplet excited states, the MC simulation agrees well with the analytic solution of the system. As a side note, an interesting aspect of the spatial solution is that the excited-state profiles cannot be described by the diffusion of a single state with an 'average' diffusion constant. This signifies that for correctly describing such a system, a full consideration of both singlet and triplet states with their associated diffusion constants is necessary. Furthermore, the uniqueness of the diffusion in TADF films, wherein transport happens both in the singlet and triplet state, is clearly visible in this special solution to the reaction-diffusion equation.

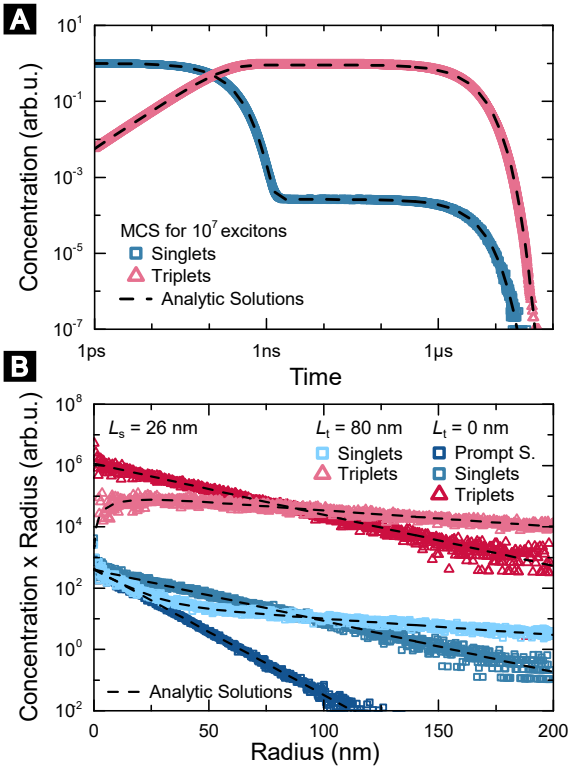

FIGURE 3.10: Comparison between the analytic solution and the MC simulation. The results of the MC simulation are shown after 10^7 simulated excitons. (A) Time evolution of spatially integrated singlet and triplet concentrations. (B) Spatial distribution of singlet and triplet excitons generated with a constant rate at the origin. Data are shown for a singlet diffusion length (with cycling) of 26 nm and a triplet diffusion length of either 0 nm or 80 nm. Adapted with permission from Jakoby *et al.* [56].

4

Increasing the Absorption Cross-Section of TADF Emitters

Beyond their application in active layers of OLEDs, TADF materials are also promising candidates to act as photonic markers. The long lifetime of the delayed luminescence of TADF molecules, usually in the microsecond range [158], can easily be separated by a time-gated measurement from potential background emission. This applies especially to biological systems since no naturally-occurring compounds exhibit such long-lived emission at room temperature. However, a problem that needs to be addressed to increase the applicability of TADF materials as photonic markers is their small absorption cross-section due

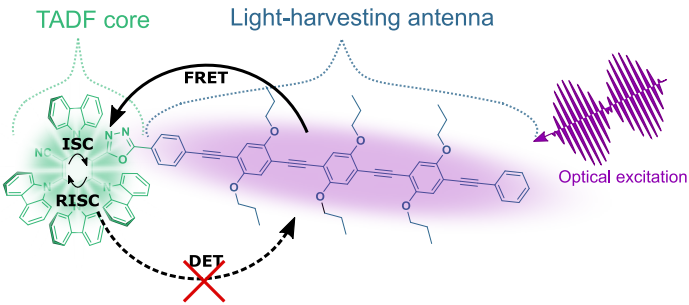

FIGURE 4.1: Schematic illustrating the concept of combining a strongly-absorbing oligomer antenna with a TADF active core in order to yield a bright photonic marker with delayed fluorescence.

to the CT nature of their absorption band [159, 160]. This chapter establishes the photophysics of T-oligomers, where the oligomer acts as a strongly-absorbing antenna feeding energy to the TADF core (see Figure 4.1). The studies show that the energy transfer between the oligomer and TADF core has good efficiency for all studied TADF-oligomer combinations, but for longer antenna the delayed fluorescence is turned off. This latter effect can be attributed to a decrease in the RISC rate. Interestingly, the transfer of the triplet CT state to the lower-lying triplet state on the oligomer is inefficient, and not responsible for the turn-off of the delayed fluorescence. Even though this finding precludes the use of the studied TADF-oligomer systems as photonic markers, the suppressed triplet transfer between the TADF core and the oligomer is still an encouraging finding for future research in this direction. Along this line, the finding of suppressed triplet motion in these TADF compounds was also the basis for further investigations on the limited triplet mobility in TADF molecules as laid out in Chapter 5.

Acknowledgements and Contributions

This chapter is based on the publication:

- O. Franco, M. Jakoby, R. V. Schneider, F. Hundemer, D. Hahn, B. S. Richards, S. Bräse, M. A. R. Meier, U. Lemmer, and I. A. Howard, "Sen-sitizing TADF absorption using variable length oligo(phenylene ethynylene)antennae," *Front. Chem.*, vol. 8, 126, 2020. [136]

The work was carried out within the SFB 1176 (project A4). O. Franco performed the steady-state absorption and PL experiments as well as the time-resolved PL experiments. The present author performed the simulation of the PL transients and the transient absorption experiments and analysis (work related to Figures 4.4-4.6) with the guidance of I. A. Howard. R. V. Schneider, F. Hundemer, and D. Hahn synthesized the T-oligomers (**T1**, **T3**, and **T5**) with the guidance of M. A. R. Meier and S. Bräse. The manuscript was conceptualized by O. Franco, the present author, and I. A. Howard. All authors participated in the discussion and writing of the manuscript.

One of the important contributions of the present author to this manuscript was the discovery of suppressed triplet motion in the studied TADF-oligomer conjugates. This finding inspired the present author to investigate in detail the exciton motion between TADF molecules, which led to the central findings of this thesis (as outlined in Chapter 5). In order to highlight this progression of the work, this thesis also opens with the results on the T-oligomers.

4.1 Energy Transfer within TADF-Oligomer Conjugates

The first step in designing a molecule that possesses a strong absorption band together with TADF functionality is a suitable selection of a TADF-active and a strongly absorbing chromophore. In order to promote efficient transfer of singlet excitons from the antenna to the TADF chromophore, good spectral overlap between the emission spectrum of the antenna and the absorption spectrum of the TADF chromophore has to be assured (see Section 2.2.1). That is, strong

absorption of the antenna in resonance with the energy of the TADF CT band (assuming a small Stokes shift of the antenna). With those prerequisites in mind, as antennae rod-like monodisperse oligo(phenylene ethynylene)s (OPEs) were selected, which allow for an easy adjustment of the emission (and absorption edge) energy by changing the length of the oligomer. As TADF-active unit a modified 4CzIPN molecule **T**, where one of the cyano acceptor groups was replaced by an oxadiazole-phenylene group to allow for coupling with the OPEs, was chosen. Here, 4CzIPN was used since it is one of the benchmark TADF molecules with pronounced green delayed fluorescence [90]. For further details on the chemical synthesis of **T** and the oligomers please refer to Hundemer *et al.* [161] and Schneider *et al.* [162], respectively. The T-oligomers were studied in degassed chloroform as described in Section 3.1.1.

Three different lengths of the OPEs (monomer, trimer, and pentamer) were coupled to **T**, forming the T-oligomers **T1**, **T3** and **T5**. In Figure 4.2 the absorption and emission spectra of **T** to **T5** together with those of the corresponding OPEs are shown accompanied by the molecular structure of the different compounds. The OPEs have a pronounced absorption band, which is centered around 390 nm for **OPE1**. As expected from $\pi - \pi^*$ transitions with enhanced conjugation, the increasing oligomer chain length leads to a bathochromic shift of the absorption edge as well as an increase in the oscillator strength. Accordingly, for the **OPE3** and **OPE5** the center of the absorption band of the $\pi - \pi^*$ transition shifts to around 410 nm and 425 nm, respectively. When comparing those spectra of the OPEs with those of the corresponding T-oligomers their similarity is clearly noticeable. The only distinct difference is the additional absorption feature for the T-oligomer centered around 290 nm, which can be attributed to the carbazole (Cz) building blocks of the TADF core. This Cz absorption feature was used to normalize the absorption spectra of **T1** to **T5**, which allowed accurate comparison of the absorption cross-sections at longer wavelengths between the four compounds. For all T-oligomer, the absorption of the $\pi - \pi^*$ transition of the antennae dominates the absorption spectrum in the range of 340 nm to 480 nm with a significantly higher cross-section than the CT absorption band of **T** present in the same spectral range. Furthermore, the increase of the oscillator strength relative to the Cz absorption is clearly visible, as well as an increasing bathochromic shift for longer antenna lengths. The T-oligomers absorption in the range of 340 nm to 480 nm can therefore be mainly attributed to the $\pi - \pi^*$

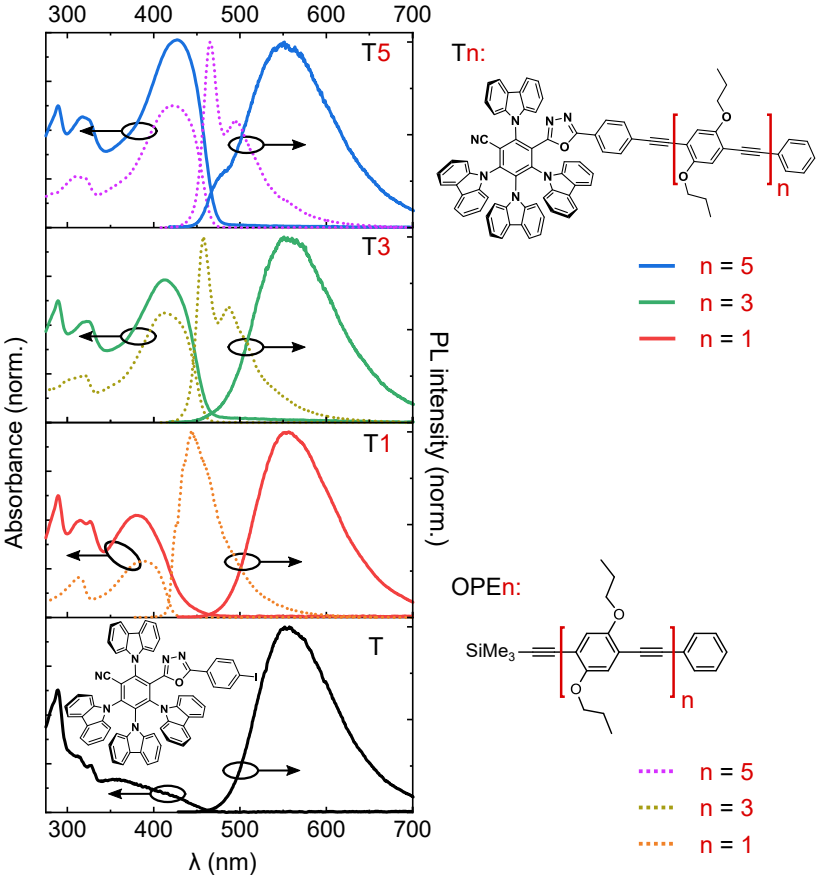

FIGURE 4.2: UV-Vis and PL spectra of the investigated compounds in chloroform ($c \leq 5 \times 10^{-4}$ mol l^{-1}) together with the chemical structures on the right. The spectra of **T** and the T-oligomers are plotted with thick solid lines, while the spectra of the corresponding OPEs are drawn in fine dashed lines. The absorption spectra of **T** and the T-oligomers were normalized to the peak around 290 nm that corresponds to the absorption band of Cz, whereas the spectra of the OPEs were normalized to the maximum value of **OPE5**. Steady-state PL and UV-Vis measurements conducted by Olga Franco. Adapted with permission from Franco *et al.* [136].

transition of the antennae. This signifies that the coupling to an OPE antenna is an effective way to introduce a strong absorption band to the TADF molecule. Furthermore, from these data, it can be concluded that for **T5** the OPE has sufficient length that its $\pi - \pi^*$ transition is in resonance with the CT absorption of the TADF chromophore.

Now that the strong absorption of the T-oligomers in the spectral region about 340 nm to 480 nm is verified, the energy transfer between the antennae and the TADF core of the molecule is studied. For this, the steady-state PL spectra of the T-oligomer and OPE were recorded under 355 nm excitation and are plotted in Figure 4.2. The peak positions of the emission spectra of the antennae shift bathochromically with increasing oligomer chain length from about 440 nm for **T1** to 465 nm for **T5**. In sharp contrast, the PL spectra of the T-oligomer remain essentially constant and are centered together with the PL spectrum of **T** around 560 nm irrespective of the oligomer chain length. Since the majority of photons at 355 nm are absorbed by the antennae, this agreement between the PL spectra suggests that the emission occurs from the same state and that this state is located on the TADF core. Thus, this observation signifies energy transfer between the oligomer chain and the TADF building block of the molecules. Only for **T5** a small high-energy shoulder of the PL spectra indicates that a minority of excitons are not transferred from the antennae to the TADF core within their lifetimes. However, since this shoulder only accounts for a minor contribution to the overall emission and under consideration of the TAS results (*vide infra*), the steady-state absorption and PL data indicate efficient energy transfer from the antenna to the TADF core. Therefore, in all cases, there is sufficient overlap of the antennae's emission spectra with the CT absorption of the core to promote efficient FRET of singlet excitons from oligomer to TADF core.

4.2 Impact of the Oligomer on the RISC Rate

In the previous section it was shown, that the T-oligomer represent good candidates for TADF-based markers due to their high absorption cross-section in the blue and near-UV region and since their emission is dominated by the TADF core. Now that these two aspects were established, the time-resolved PL

emission was studied in further detail. Specifically, the changes in the prompt and delayed decay rate were examined for the different oligomer chain lengths. Figure 4.3 depicts the PL transients of **T** and the T-oligomers. It is directly evident that the delayed component of the PL is significantly reduced from **T** to **T1** and that no delayed PL could be detected with the sensitive ICCD setup for compounds **T3** and **T5**. The PL kinetics were fitted with biexponential functions. The corresponding rates and amplitudes are stated in Table 4.1. The fraction of delayed fluorescence relative to the total emitted PL, χ_D, was determined from the prompt PL lifetime τ_P, the delayed PL lifetime τ_D and the respective amplitudes A_P and A_D via the relationship:

$$\chi_D = \frac{\tau_D}{A_P/A_D\,\tau_P + \tau_D}. \tag{4.1}$$

While for the sample **T** about 40 % of the emission is due to delayed fluorescence, for the **T1** sample only 5 % is emitted with the delayed lifetime. These results are clearly negative for the targeted application of photonic markers with strong absorption and delayed emission. However, in the following the mechanism that turns off the delayed fluorescence for the T-oligomers is studied in further detail and provides interesting insights on how to design molecules for the intended application.

The most straightforward hypothesis for the turn-off of the delayed fluorescence with increasing oligomer chain length would be a triplet exciton transfer from the TADF core to the lower-lying triplet state on the oligomer. The singlet energies of the TADF core and OPE antennae are similar, while the singlet-triplet gap of the oligomers is around 0.7 eV [163, 164], whereas it is only about 0.24 eV for the TADF core [165]. Therefore, triplet exciton transfer should be energetically favored and would efficiently quench the delayed PL of T-oligomers. Here, the trapped triplet state on the oligomer would return to the singlet ground state by non-radiative ISC (followed by fast vibrational relaxation). However, as will be laid out in the following, this energy transfer process is not pronounced for the T-oligomers most likely due to a sterically shielded LUMO on the TADF core (*vide infra*).

A qualitative argument that the transfer of triplet excitons from the TADF core to the antenna is not a dominant process can be deduced from Figure 4.3. The energy transfer of triplet excitons from the TADF core to the oligomer chain

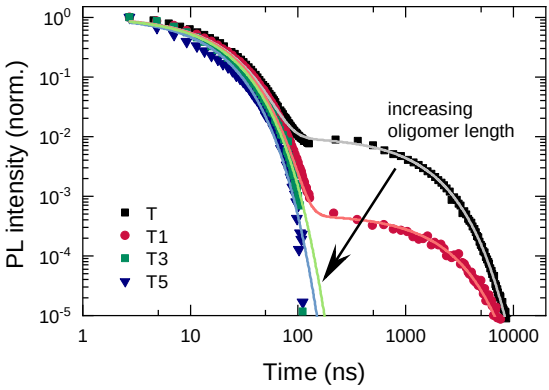

FIGURE 4.3: PL kinetics of the four investigated T-oligomers in deoxygenated chloroform ($c = 5 \times 10^{-4}\,\mathrm{mol\,l^{-1}}$). Lifetimes and amplitudes of the biexponential fits are stated in Table 4.1. Time-resolved PL measurements conducted by Olga Franco. Reprinted with permission from Franco *et al.* [136].

would only effect the non-radiative decay rate of triplet excitons on the TADF core, while all other decay rates (of singlet and triplet excitons) should stay the same. Therefore, the photo-generated singlet excitons would populate the triplet state with the same yield and the initial triplet population would stay untouched. This would lead to a similar amplitude of the delayed PL kinetics of the different T-oligomers. However, this does not fit to the observed data, since the amplitude of the delayed PL of **T1** is strongly reduced in comparison to the one of **T**. Along this line, the increase in the non-radiative decay rate of the triplet exciton would decrease the delayed lifetime (since the average amount of singlet-triplet cycles would be reduced). However, this is also not in accordance with the observed data, since the delayed lifetime increases from 1.2 µs to 1.7 µs between the sample **T** and **T1**. An alternative hypothesis for the lack of delayed emission is a reduction in the RISC rate induced by the oligomer. This decrease would lead to an increase of the delayed lifetime (as the average time for one singlet-triplet cycle would increase) while decreasing

TABLE 4.1: Prompt and delayed lifetimes (τ_P and τ_D, respectively) determined from the biexponential fits shown in Figure 4.3. The ratio between the delayed and total emission, χ_D, was calculated from the determined lifetimes and amplitudes (A_P and A_D) as described in the text.

	τ_P (ns)	τ_D (µs)	A_P/A_D	χ_D
T	16	1.2	1×10^2	0.40
T1	16	1.7	2×10^3	0.05
T3	15	-	-	0
T5	14	-	-	0

the amplitude of the delayed PL. Consequently, such a change in the RISC rate might be in accordance with the observed data. In the following, this will be investigated quantitatively by using an analytic model for the PL transients.

For modeling the PL kinetics the solution to the rate equations of the system (see Equation 2.11) is used. As a first step, the kinetics of **T** are fitted by using parameters in accordance with literature values of 4CzIPN [90, 166], with slight adjustments due to the minor changes of the molecular structure (slight increase in k_r^s, k_{ISC} and k_{nr}^t). Second, the determined rates are used as a reference for modeling the PL kinetic of **T1**. Here, two different models are employed; 1) the triplet transfer model, where the non-radiative decay rate (of triplet excitons) is used as a free parameter, 2) the decreased RISC model, where the RISC rate is used as a free parameter to fit the kinetics of **T1**. Figure 4.4 shows the PL kinetics of the samples **T** and **T1** accompanied by the model functions (reference and one for each model). The used rates for the three model functions are summarized in Table 4.2.

The data of **T1** could not be fitted using the triplet transfer model. Here, in Figure 4.2 the model function is shown for a doubled non-radiative triplet decay rate, which would correspond to a triplet exciton transfer, i.e., quenching efficiency, of 33 %. However, the addition of this additional loss channel does

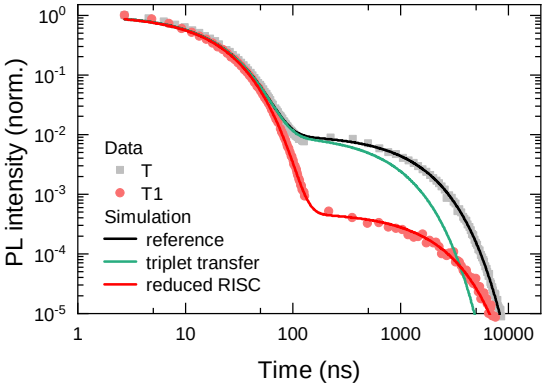

FIGURE 4.4: Simulated PL kinetics for the reference, triplet transfer, and reduced RISC models described in the text. The reference and reduced RISC models agree with the observed data for **T** and **T1**, respectively. The triplet transfer model does not agree with the observed data. The parameters used for the three models are summarized in Table 4.2. Adapted with permission from Franco *et al.* [136].

TABLE 4.2: Parameters used for the simulation of the PL transients shown in Figure 4.4.

	reference (T)	triplet transfer	decreased RISC
$k_s^r + k_s^{nr}$	1.3×10^7	1.3×10^7	1.3×10^7
k_{ISC}	3.9×10^7	3.9×10^7	3.9×10^7
k_{RISC}	6.0×10^5	6.0×10^5	3.0×10^4
$k_t^{nr} + k_t^Q$	6.0×10^5	1.2×10^6	6.0×10^5

not lead to a significant reduction of the initial delayed PL around 100 ns and is therefore not in accordance with the observed PL kinetic for **T1**.

In contrast, the RISC model accurately describes the measured kinetic when using a RISC rate that is reduced by a factor of 20. A reduction of the RISC rate as a function of oligomer chain length is therefore in accordance with the observed data, while an increasing transfer of triplet excitons to the lower-lying triplet state of the oligomer is not. This observation will be further substantiated in the following section using TAS.

4.3 Impact of the Oligomer on the CT-LE Resonance

TAS is used to further substantiate the hypothesis of a decreasing RISC rate with increasing oligomer chain length, as well as for studying the dynamics of the intermediate photo-excited states. Latter analysis leads to the conclusion that the CT state is becoming off-resonant with the ^{3}LE state for longer oligomer lengths which turns off the delayed emission.

TAS data were collected by measuring the change in transmission $\Delta T/T$ in the spectral region 520 nm to 880 nm induced by a previous pump pulse with a wavelength of 800 nm. A fluence-dependent measurement was used to ascertain

that the kinetics shown below (with a fluence of 20 nJ cm^{-2}) are due to linear processes only and that the sample did not degrade during the investigation.

Figure 4.5 depicts three measured TAS surfaces of the sample **T**, **T1** and **T5**. For all samples the determined TAS surface is negative, meaning that photo-induced absorption (PIA) features are dominating the TAS spectra in the observed wavelength region. Here, two distinct features can be directly distinguished for **T** and **T1**. An PIA band centered around 800 nm which is rising with the instrumental response function (IRF) and decays biexponentially with the same decay rates as the PL kinetics of the two samples (see Table 4.1). The second feature is centered around 600 nm with a rise time corresponding to the prompt decay lifetime ($\tau = 16$ ns) and reaching its maximum after about 100 ns. Further analysis of the data matrices confirms that only two distinct excited states are responsible for the TAS surface of **T** and **T1**. For both samples the data matrix has rank 2, meaning that the data matrix (minus noise) can be expressed by the outer product of a $2 \times X_1$ matrix S and a $X_2 \times 2$ matrix T, where X_1 corresponds to the number of data values along the spectral axis, while X_2 to the amount along the time axis. In contrast, the TAS surface of sample **T5** possesses only a single feature, which is centered around 800 nm and has a rise time of 14 ns corresponding to the PL lifetime of **T5**. Accordingly, the rank of the data matrix of **T5** is only 1.

Figure 4.6 shows two plots of the TAS kinetics at the two already highlighted wavelengths regions. In Figure 4.6A the TAS kinetics are integrated in the spectral range of 550 nm to 650 nm and are accompanied by the prompt PL transient of **T**. It is clearly evident that the PIA feature of **T** and **T1** rises with a similar rate constant as the PL transient decays. Figure 4.6B shows the integrated TAS kinetics in the spectral range of 750 nm to 850 nm accompanied by biexponential fits. In this wavelength region the difference in the PL kinetics between samples **T**, **T1** and **T5** is most pronounced. While the TAS kinetics of **T** and **T1** rise with the IRF this is not the case for **T5**, where the PIA feature rises with an inverse rate constant of 14 ns. The fitting parameters used for the three fits are summarized in Table 4.3. The prompt PL lifetimes were used as fixed parameters with the same values as determined from the PL kinetics (see Table 4.1).

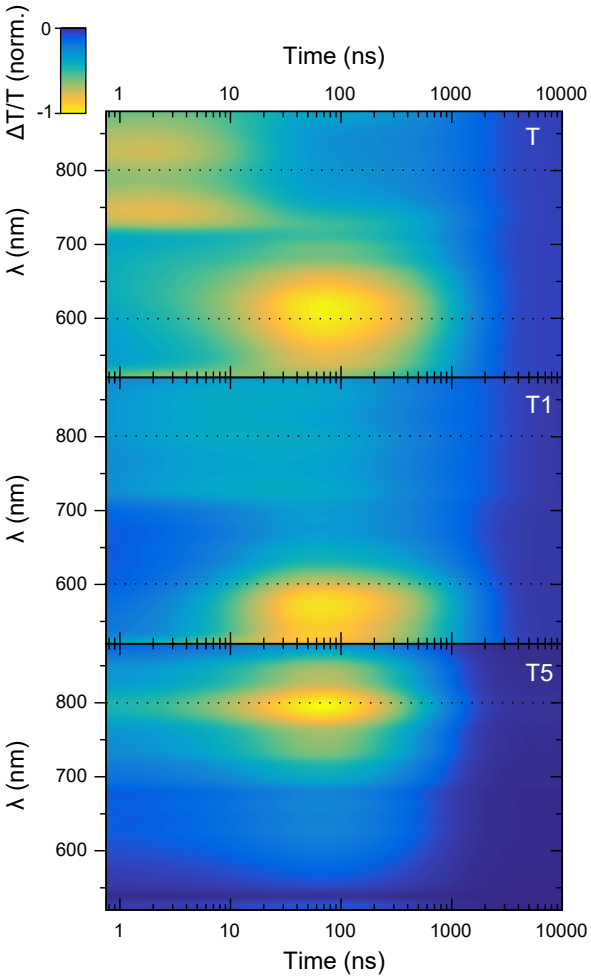

FIGURE 4.5: TAS contour maps of **T**, **T1**, and **T5**. The black dashed lines correspond to the positions of the kinetics shown in Figure 4.6. Reprinted with permission from Franco *et al.* [136].

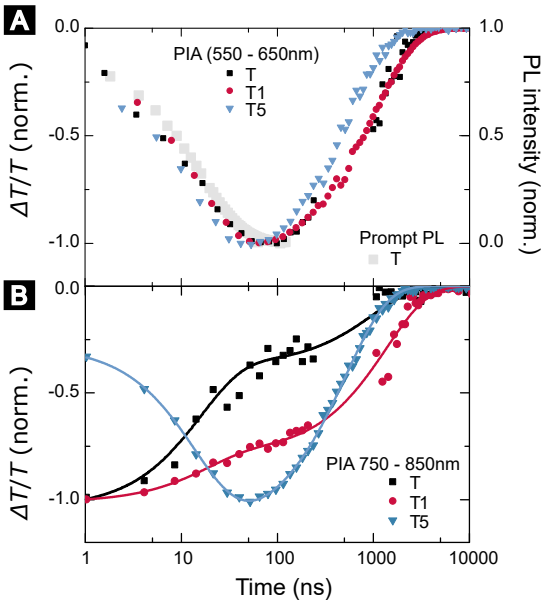

FIGURE 4.6: TAS kinetics of **T**, **T1**, and **T5** for the integrated wavelength regions 550 nm to 650 nm (A) and 750 nm to 850 nm (B). Adapted with permission from Franco *et al.* [136].

Before turning to a detailed discussion of the mechanism that is responsible for the lack of delayed emission, it will be shown that the TAS data is in accordance with the analysis of the PL kinetics, i.e., that triplet exciton transfer from the TADF core to the oligomer chain is not a dominant process for neither of the samples. Triplet exciton transfer from the TADF core to the oligomer chain should be most pronounced in **T5** due to the bathochromic shift of the first excited triplet level with increasing oligomer chain length. This triplet exciton transfer should be connected to a rise of a new spectral feature after ISC that corresponds to the excited-state absorption of the oligomer triplet, while the initial PIA feature of the TADF core ^{3}CT state should disappear. However, this does not fit to the observed TAS surface for **T5**. As already mentioned, for **T5** only a single excited state is responsible for the entire TAS. This state cannot be attributed to an oligomer triplet state for the following reasons. First, the signal is already present immediately after excitation with a signal height of about 25 %. It is not possible that such a significant amount of the population already transferred to the oligomer within such a short time (sub-nanosecond range). Second, the subsequent rise time of the signal corresponds to the prompt PL decay lifetime (14 ns) and therefore the state responsible for the PIA feature is directly populated from the CT singlet state of the TADF core and not from ^{3}CT. Third, the lifetime of the PIA feature would be multiple orders of magnitude too low for triplet lifetimes usually observed for the oligomers studied. For example, the triplet lifetime of poly(p-phenylene ethynylene) powder samples at room temperature was determined to 200 µs by Partee *et al.*[167]. He and his coworkers utilized triplet-triplet annihilation and the resulting delayed emission to determine the triplet lifetime. In independent pulse radiolysis measurements, this finding was further substantiated [168, 169].

Therefore, based on the above arguments, it can be excluded that the TAS surface of **T5** is due to a triplet exciton on the oligomer. Further, it can be assumed that if such a triplet state would be present, it would also be detected in the studied wavelength region, as poly(p-phenylene ethynylene) triplet excitons show a strong PIA feature at 780 nm [170]. Thus, the TAS measurements provide further evidence that the energetically favorable transition of the ^{3}CT from the TADF core to the oligomer is not significant for the T-oligomers.

Now that the consensus between the PL and TAS measurements was verified, the TAS data is examined in further detail. Based on the detailed TAS study of

TABLE 4.3: Prompt and delayed lifetimes (τ_P and τ_D, respectively) determined from the biexponential fits shown in Figure 4.6B.

	τ_P (ns)	τ_D (µs)	A_P	A_D
T	16	1.2	−0.67	−0.37
T1	16	1.7	−0.26	−0.77
T5	14	0.7	0.84	−1.1

4CzIPN by Hosokai *et al.* the PIA band at 600 nm that grows in within the first 100 ns can be attributed to a local triplet state (^{3}LE) on the phtalonitrile core of the molecules [157]. This signature of the ^{3}LE is only observed for **T** and **T1**, even though it is hypsochromically shifted to 550 nm for **T1**. This shift of the PIA band is most likely the consequence of a shift in the ^{3}LE energy level between **T** and **T1**. For **T5**, this PIA band is absent which indicates that the ^{3}LE is either not populated at all or significantly shifted in energy. The congruence of the prompt PL decay and the growth of the PIA for **T** and **T1**, highlighted earlier, reinforces the conclusion that the species responsible for the PIA feature is populated directly from the CT singlet state via ISC (see Figure 4.6A).

For 4CzIPN the energetic resonance between ^{3}LE and the CT states is assumed to be a crucial part for efficient RISC [110, 171]. In this association, the ^{3}CT can transfer to the CT singlet state via the aid of the local triplet intermediate, since ISC between a localized and a CT state is quantum-mechanically less strictly forbidden in comparison to a CT-CT ISC process (see also Section 2.3). Accordingly, it was observed that the presence of an PIA band that grows in with the prompt PL lifetime and can be associated with the ^{3}LE state is critical for efficient RISC [157]. The presence of the PIA for **T** and **T1** around 600 nm indicates that the ^{3}CT efficiently mixes with the ^{3}LE state in these two samples, i.e., that the ^{3}LE state is populated. However, in **T1** this PIA feature is slightly less dominant (and spectrally shifted) with respect to the 800 nm feature and not present for **T5**, indicating that the ^{3}LE is less populated with increasing oligomer

chain length. The TAS data provide therefore evidence that the oligomer chain disturbs the ^{3}LE-^{3}CT resonance and, as a direct consequence, turns off RISC and thus delayed fluorescence. This hypothesis will be further substantiated by the analysis of the second PIA feature centered around 800 nm, which is present in all three samples.

The PIA feature around 800 nm can be assigned to a reduced electron density on the Cz units of 4CzIPN, since it closely resembles the PIA for Cz^+ cations [172, 173]. The Cz^+ formation, in turn, indicates CT state formation between the donor (Cz) and acceptor (phtalonitrile). The TAS signature of Cz^+ is present for all times for the three samples, with differences only in the intensity of the feature.

For **T** this PIA feature decreases more than 50 % within the prompt PL decay lifetime (see Figure 4.6B) even though the triplet yield of **T** is about 75 %. This indicates that the PIA feature at 800 nm connected to CT formation is reduced for triplet excitons in comparison to singlet excitons, which, in turn, can be explained by a mixing of the ^{3}LE state with the ^{3}CT state. As already mentioned, the ^{3}LE state is located mainly on the phtalonitrile and therefore, if in resonance with the ^{3}CT state, reduces the PIA at 800 nm, which is connected to Cz^+ formation. This explanation is also in accordance with the work by Etherington and coworkers, who recognized that the PIA attributed to the ^{3}CT state varies depending on the mixing of the ^{3}CT and ^{3}LE state [110].

For **T1**, the PIA connected to Cz^+ decreases only by about 70 % within the first 100 ns, but the triplet yield stays approximately untouched between the samples **T** and **T1**, as indicated by the same prompt PL lifetimes. This, in turn, means that the CT character of the triplet state has increased for **T1**, which fits the argument of a reduced population of the ^{3}CT for longer oligomer chains. For **T5**, the PIA kinetics are noticeably different. Here, the PIA feature increases with the same rate as the prompt PL. Even though the physical mechanism causing this increase in the strength of the PIA can not be derived from the data with certainty, it is consistent with strong CT formation and a lack of ^{3}LE population. Given that recent research showed that the torsional rocking modes of the Cz groups surrounding the phtalonitrile core are essential for efficient coupling between ^{3}CT and ^{3}LE state [31], those modes might be somewhat suppressed, e.g., due to steric hindrance, once an OPE is attached.

In summary, also the PIA feature around 800 nm provides evidence that the CT gets stabilized relative to the ^{3}LE with increasing oligomer chain length. Accordingly, RISC is turned off since the state mediating between both spin manifold, ^{3}LE, is successively less populated with increasing oligomer chain length. Last but not least, it should be noted that an energetic shift in the CT manifold, i.e., a stabilization of the LUMO by the oligomer, is not considered since no spectral shift in the prompt and delayed (**T** and **T1**) emission was observed (see Figure 4.2).

4.4 Conclusion

This chapter investigated the photophysics of a sequence of molecules composed of a TADF core conjugated to a OPE antenna with different lengths. The study was an attempt to increase the absorption cross-section of the weakly absorbing TADF molecules while retaining the delayed PL emission on the microsecond scale. The combination of a high absorption cross-section together with delayed emission would be a desired property of optical markers. This is the case since it would allow for low excitation intensities together with background-free detection of the delayed emission. Positive with respect to this application were the UV-Vis measurements, which showed that the molar extinction coefficient can be increased by a factor of five by an OPE of suitable length. Along this line, efficient energy transfer from the antenna to the TADF core could be verified by steady-state PL measurements. However, time-resolved PL measurements revealed that the delayed emission was significantly attenuated for shorter antennae and turned off for longer antennae, which is clearly negative in terms of applying these materials for photonic markers with delayed emission. Based on time-resolved PL measurements a reduction in the RISC rate could be identified as the origin in the reduction of the delayed emission. A detailed TAS study further revealed that the CT character of the triplet state increases with increasing oligomer chain length. This could be attributed to a reduced mixing of the ^{3}CT and ^{3}LE state, most likely due to an energetic shift of the ^{3}LE or a change in vibronic coupling due to the presence of the oligomer antenna.

In summary, this pioneering work of designing strong delayed PL emitters based on TADF core-antenna combinations provides some promising directions, but

further work is required, especially to fully understand how RISC rates can be maintained upon the addition of the antenna. In this regard, dynamic density-functional theory (DFT) calculations could be very valuable to understand the energetic shifts and changes in vibronic couplings of the intermediate species once an antenna is attached. Furthermore, such simulations would be helpful for the screening process of more promising TADF core-antenna combinations.

However, the surprising finding that the energetically favorable Dexter energy transfer of triplet excitons from the TADF core to the oligomer chain is not responsible for the loss of delayed emission also triggered further investigations of exciton motion between TADF molecules. In this sense, the investigation of this chapter can be considered particularly essential for this thesis in drawing attention to the unique exciton transport processes of TADF molecules. The next chapter focuses on TADF exciton transport along with the question if the orthogonal nature of LUMO and HOMO in organic TADF molecules restrict the Dexter energy transfer of triplet excitons.

5

Exciton Motion between TADF Emitters

In the context of OLEDs that allow for the harvest of both singlet and triplet excitons while also emitting with a high color purity, the strategy of combining a TADF donor with a hyperfluorescence acceptor (F-dopant) is attracting significant attention. For this strategy to work, the excitons generated on the TADF molecules must arrive at the acceptor only when in their excited singlet state. The arrival of excitons in the triplet state at the acceptor is deleterious to device performance and must be suppressed (see Figure 5.1). Here, two approaches are particularly promising to enable such spin-sensitive harvest. On the one hand, one could employ sterically protected F-dopants that inhibit short-range Dexter-type transfer of triplet excitons to the acceptor. On the other hand, one

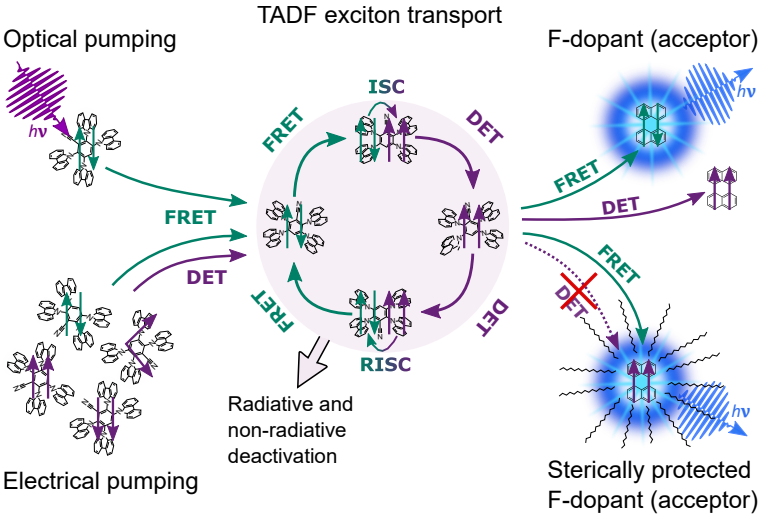

FIGURE 5.1: Schematic of exciton motion in a hyperfluorescence OLED. Singlets can migrate by Förster resonant energy transfer (FRET) between adjacent TADF molecules and fluorescent dopants (F-dopants), or undergo intersystem crossing (ISC) to a triplet state. Triplets either migrate by Dexter type energy transfer (DET) between neighboring TADF molecules and F-dopants (loss mechanism) or reverse intersystem crossing into a singlet state (RISC). Adapted with permission from Jakoby *et al.* [56].

could purposefully control the ratio between singlet and triplet exciton motion between TADF molecules. Possibly, if the triplet diffusion length is small compared to the singlet diffusion length, the triplet exciton transfer to the acceptor could already be sufficiently suppressed. Therefore, to evaluate this association, it is important to distinguish both singlet and triplet diffusion lengths in TADF molecules, especially in the context of an hyperfluorescence device.

This chapter first demonstrates that it is possible to accurately extract triplet diffusion length by a Stern-Volmer (SV) type analysis, overcoming limitations in the pioneering studies on exciton diffusion in organic TADF molecules. Second, this chapter demonstrates that arrival in the singlet state and suppression

of triplet exciton trapping at acceptors can be achieved in common TADF materials that suppress inter-TADF-molecule triplet motion while allowing singlet exciton motion. In the benchmark materials 4CzIPN and 4TCzBN, it is shown that the singlet diffusion lengths are (9.1 ± 0.2) and (12.8 ± 0.3) nm, whereas the triplet diffusion lengths are at least an order of magnitude lower in each case. Theoretical results confirm that the lack of overlap between the shielded lowest unoccupied molecular orbitals hinders triplet motion between TADF chromophores in such molecular architectures. Although this cause of triplet motion suppression does not occur in molecular architectures based on alternating HOMO/LUMO patterns that rely on complementary electron resonance effects (e.g., DiKTa), triplet diffusion is nevertheless suppressed when such molecules are dispersed in a matrix material at a concentration low enough to suppress aggregation (which they are in device architectures). Furthermore, a MC simulation establishes that steric protection of F-dopants leads to a negligible increase in the singlet harvesting efficiency as long as triplet motion is suppressed. Conclusively, a small triplet diffusion length, achievable through molecular design and sufficient dispersion, is sufficient for allowing efficient singlet harvesting from TADF molecules by standard fluorescence acceptors. This accurate understanding of triplet diffusion is critical for the design of hyperfluorescence OLED emitter layers based on TADF donors and fluorescence acceptors.

Acknowledgements and Contributions

This chapter is based on the following two publications:

- M. Jakoby, S. Heidrich, L. Graf von Reventlow, C. Degitz, S. Madayanad Suresh, E. Zysman-Colman, W. Wenzel, B. S. Richards, and I. A. Howard, "Method for accurate experimental determination of singlet and triplet exciton diffusion between thermally activated delayed fluorescence molecules," *Chem. Sci.*, vol. 12, pp. 1121–1125, 2021. [174]

The idea and experimental design were conceived by the present author and I. A. Howard. The present author conducted the experimental measurements, the preparation of DiKTa samples, as well as the derivation and verification of the SV analysis for TADF molecules with the guidance of I. A. Howard and

B. S. Richards. S. Heidrich and C. Degitz performed the density functional theory calculations with the guidance of W. Wenzel. L. Graf von Reventlow prepared the 4CzIPN and 4TCzBN films. S. Madayanad Suresh synthesized the molecule DiKTa with the guidance of E. Zysman-Colman. The manuscript was conceptualized by the present author and I. A. Howard. All authors participated in the discussion and writing of the manuscript.

- M. Jakoby, B. S. Richards, U. Lemmer, and I. A. Howard, "Investigations of singlet and triplet diffusion in thermally activated delayed-fluorescence emitters: Implications for hyperfluorescence," *Phys. Rev. B*, vol. 100, 045303, 2019. [56]

The idea and the design of the Monte Carlo simulation were conceived by the present author and I. A. Howard. The simulation was written by the present author with the assistance of I. A. Howard and applied to exciton motion between TADF emitters, as well as hyperfluorescence OLEDs active layers. The manuscript was conceptualized by the present author and I. A. Howard. All authors participated in the discussion and writing of the manuscript.

5.1 Method for Determination of Singlet and Triplet Diffusion Lengths

This section derives an equation that allows the accurate determination of the triplet diffusion length based on time-resolved PL measurements of a series of samples with varying quencher concentrations. The starting point are the coupled rate equations that were already introduced in Section 2.3.2 and are rewritten here for reasons of clarity:

$$\frac{\partial}{\partial t}\begin{pmatrix} c_\mathrm{s} \\ c_\mathrm{t} \end{pmatrix} = \begin{pmatrix} -k_\mathrm{s} & +k_\mathrm{RISC} \\ +k_\mathrm{ISC} & -k_\mathrm{t} \end{pmatrix}\begin{pmatrix} c_\mathrm{s} \\ c_\mathrm{t} \end{pmatrix}. \tag{5.1}$$

Here, c_s and c_t are the singlet and triplet excited-state concentrations, while k_s and k_t, the singlet and triplet decay rates, are given by:

$$k_\mathrm{s/t}([Q]) = k^r_\mathrm{s/t} + k^{nr}_\mathrm{s/t} + k^Q_\mathrm{s/t}[Q] + k_\mathrm{ISC/RISC}. \tag{5.2}$$

These expressions differ from the previously discussed rate equations only in the additional term $k^{Q}_{s/t}[Q]$, which represents a quenching rate that scales linearly with the concentration of a quenching molecule distributed randomly through the film, $[Q]$. The diffusion lengths can be extracted through a SV analysis, wherein the SV constant $K_{s/t}[Q]$ is defined by (see Section 3.4):

$$K_{s/t}[Q] = \frac{k_{s/t}([Q])}{k^{0}_{s/t}} - 1, \tag{5.3}$$

where $k^{0}_{s/t}$ is $k_{s/t}([Q])$ when $Q = 0$ (the unquenched singlet or triplet lifetime). Employing the Smoluchowski equation, the following relation between the SV constant $K_{s/t}$ and the diffusion length for the singlet or triplet excitons $l_{s/t}$ can be derived [39]:

$$l_{s/t} = \sqrt{\frac{6K_{s/t}}{4\pi R}}, \tag{5.4}$$

where R is the interaction radius. The interaction radius depends, in turn, on the radius of the quenching species and the exciton. As a side note, for TADF molecules two types of quencher can be employed. A triplet only and a CT quencher that quenches singlet and triplet excitons with similar rates (see Figure 3.9). Here, the focus will be put on the latter case, since it allows the extraction of both singlet and triplet exciton diffusion lengths with one measurement series.

For singlet excitons, the SV constant (and therefore the singlet diffusion length during a single pass through the singlet excitonic state) can be easily experimentally determined by measuring the quenching of the prompt luminescence as a function of quencher concentration:

$$K_{s}[Q] = \frac{k_{P}([Q])}{k^{0}_{P}} - 1, \tag{5.5}$$

where k_P is the measured fluorescence decay rate. Please note, this assumes that $k_{RISC} \ll k_s$ and therefore $k_s \approx k_P$ which is almost always true for organic TADF molecules [89].

For triplet excitons, the SV constant $K_t[Q]$ is given by:

$$K_t[Q] = \frac{k_t([Q])}{k_t^0} - 1 = \frac{k_{RISC} + k_t^{nr} + k_t^Q[Q]}{k_{RISC} + k_t^{nr}} - 1. \tag{5.6}$$

However, this equation can not directly be employed for the extraction of the triplet diffusion length since the triplet decay rate $k_t([Q])$ (sum of the non-radiative, RISC and quenching rate) is not directly accessible by any optical experiment. Therefore, this equation needs to be further adjusted to be solely dependent on easily observable experimental quantities in order to be useful in determining the triplet diffusion length of organic TADF emitters.

Using the reverse and inter-system crossing efficiencies ϕ_{RISC} and ϕ_{ISC}, respectively, the total PLQY of a TADF molecule can be denoted by the following expression:

$$\eta_{total} = \eta_P \underbrace{\sum_{n=0}^{\infty} (\phi_{ISC}\phi_{RISC})^n}_{\langle n \rangle} = \frac{\eta_P}{1 - \phi_{ISC}\phi_{RISC}}, \tag{5.7}$$

with the prompt PLQY η_P and the average number of passes through the singlet state $\langle n \rangle$. Solving for k_t (using $\phi_{ISC/RISC} = k_{ISC/RISC}/k_{s/t}$) leads to:

$$k_t = \frac{k_{ISC} k_{RISC} \eta_{total}}{\eta_D k_s}, \tag{5.8}$$

with the delayed PLQY $\eta_D = \eta_{total} - \eta_P$. Inserting Equation 5.8 in Equation 5.6 and again using $k_s \approx k_P$ yields:

$$K_t[Q] = \frac{\chi_D^0}{\chi_D([Q])} \frac{k_P^0}{k_P([Q])} - 1. \tag{5.9}$$

Here, $\chi_D = \eta_D/\eta_{total}$ is the fraction of delayed over the overall emission.

All quantities of Equation 5.9 can now be easily measured by time-resolved spectroscopy methods, and the triplet diffusion length in a single pass through the triplet state can be determined.

For reasons of clarity and to better illustrate the developed approach, Equations 5.5 and 5.9 can be re-expressed in terms of integral areas under the PL kinetics. For this, the data is first normalized. Second, given the mono-molecular decays, the delayed and prompt lifetimes can be found by the integral areas under the respective portions of the curve (labeled A and B). In this case, Equation 5.5 can be rewritten as:

$$K_s[Q] = \frac{A_0}{A([Q])} - 1, \tag{5.10}$$

and Equation 5.9 as:

$$K_t[Q] = \frac{A+B}{A_0+B_0}\frac{AB_0}{A_0B} - 1. \tag{5.11}$$

Figure 5.2 illustrates how time-resolved PL data as a function of quencher concentration should then be analyzed. Here, the quenching of the PL kinetics was analytically simulated using the solution to the rate equations of the system for $K_s/K_t = 5$ (see Section 5.3.2 for further details).

Equations 5.10 and 5.11 allow the singlet and triplet diffusion lengths to be easily determined through two integrals. As a side note, since $k_D \ll k_P$, area A can usually be well approximated by a simple integral over the prompt time range of the PL kinetic. Furthermore, in case the PL transient is not comprised of two mono-exponential functions, e.g., due to inhomogeneities in the film, an average decay rate has to be determined and Equation 5.9 has to be considered.

It should be noted that the above analysis leads to the extraction of the diffusion length during one cycle through the respective exciton. That is, the diffusion lengths within the lifetimes $1/k_s^0$ and $1/k_t^0$ for singlet and triplet excitons, respectively. In order to determine the total diffusion length that the excited state moves during all cycles through the singlet or triplet state, the diffusion length for a single pass in a state has to be multiplied by the square root of the average number of passes through the state. The number of passes through a state (assuming the excited-state enters that state once) is given by $\langle n \rangle = (A_0 + B_0)/A_0$.

In the following, a short remark is made for the case when only triplet excitons are quenched, for example by using a triplet only quencher. In this case,

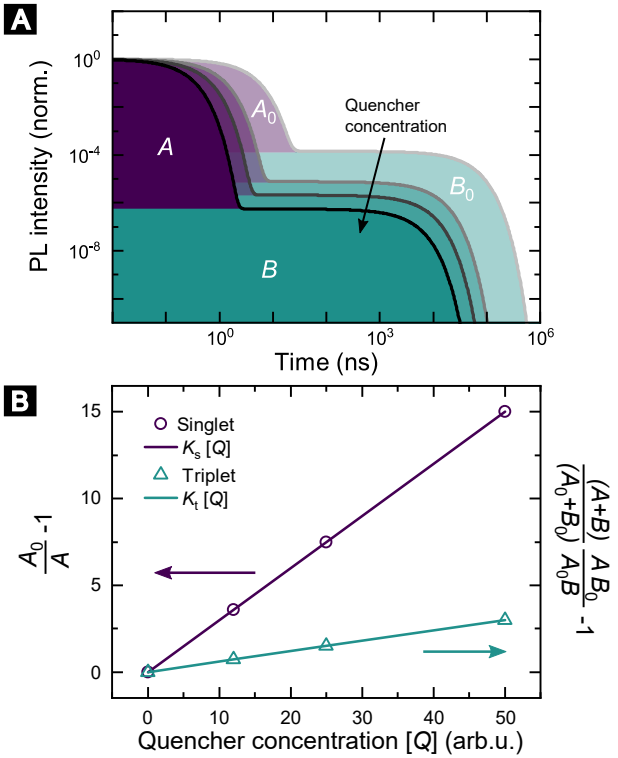

FIGURE 5.2: Methodology of determining singlet and triplet diffusion lengths between TADF molecules. (A) Simulated PL kinetics based on Equation 5.1 for four different quencher concentrations. (B) SV plot for singlet and triplet excitons based on Equation 5.10 and 5.11 using the indicated areas shown in (A). Reprinted with permission from Jakoby *et al.* [174].

Equation 5.11 reduces to:

$$K_t[Q] = \frac{A_0 + B}{A_0 + B_0}\frac{B_0}{B} - 1, \tag{5.12}$$

which is equivalent to:

$$K_t[Q] = \left(\frac{B}{B_0} - 1\right)\frac{1}{\langle n\rangle}. \tag{5.13}$$

This equation demonstrates that the derived SV equation reduces again to the standard form if a triplet-only quencher is used. Here, the determined SV constant for triplet excitons will be by a factor $\langle n\rangle$ increased, and therefore already includes spin cycling. This aspect is discussed again during the analytical verification of the method, where B and B_0 are expressed as k_D and k_D^0, respectively. It should be stressed that this equivalence is only valid as long singlet excitons do not contribute to the quenching.

5.2 Alternative Approach Based on Quenching of Delayed Decay Rate

In principle, it is also possible to determine the triplet diffusion length by measuring the prompt and delayed decay rate. In this case, however, the ISC and RISC rates would also be required (*vide infra*), which makes this approach poorly applicable in practice. Furthermore, it should be noted that the quenching of the delayed decay rate is not directly correlated to the triplet diffusion length.

The delayed lifetime is given by (see Section 2.3.2):

$$k_\mathrm{D} = \frac{1}{2}\left(k_\mathrm{s} + k_\mathrm{t} - \sqrt{k_\mathrm{s}^2 - 2k_\mathrm{s}k_\mathrm{t} + 4k_\mathrm{RISC}k_\mathrm{ISC} + k_\mathrm{t}^2}\right). \tag{5.14}$$

Solving for k_t leads to:

$$k_\mathrm{t} = \frac{k_\mathrm{D}^2 - k_\mathrm{D}k_\mathrm{s} - k_\mathrm{RISC}k_\mathrm{ISC}}{k_\mathrm{D} - k_\mathrm{s}}, \tag{5.15}$$

which can be inserted in Equation 5.6 to yield:

$$K_t[Q] = \left(\frac{k_D^2 - k_D k_s - k_{RISC} k_{ISC}}{k_D^0 - k_D^0 k_s^0 - k_{RISC} k_{ISC}}\right)\left(\frac{k_D^0 - k_s^0}{k_D - k_s}\right) - 1. \tag{5.16}$$

Considering the magnitudes of the different rates in Equation 5.16 for organic TADF molecules ($k_D \ll k_s$), Equation 5.16 can be further simplified to:

$$K_t[Q] \approx \frac{k_D k_s + k_{RISC} k_{ISC}}{k_D^0 k_s^0 + k_{RISC} k_{ISC}} \frac{k_s^0}{k_s} - 1. \tag{5.17}$$

As such, the quenching efficiency, i.e., the triplet SV constant, can in general not be well approximated using solely the fraction k_D/k_D^0. This finding will be discussed further in Section 5.6.

5.3 Verification of the Method

In the following, the validity of the presented approach in extracting singlet and triplet diffusion lengths of organic TADF molecules (see Sections 5.1 and 5.2) will be verified by a MC simulation as well as by an analytic approach.

5.3.1 Monte Carlo Simulation

The details of the MC simulation used for this verification are described in Section 3.5, but important constants and parameters are stated again for reasons of clarity. The decay rates were chosen in accordance with the molecule 4CzBN [157]. The diffusion length of singlet excitons was kept fixed at 7.4 nm (or 18.1 nm including singlet-triplet cycling), which is a value on par with the experimental results in Section 5.4, but also with standard singlet diffusion lengths in organic materials [59, 60]. The triplet exciton diffusion length was changed in the range of 0 nm to 55 nm by adjusting J in the Dexter transfer model equation, while the effective Bohr radius was kept fixed at $L = 0.2$ nm (compare Section 2.2.2) [175]. This lead to typical triplet transfer rates between 1 nm (center-to-center) displaced molecules in the range of $0\,\mathrm{ns}^{-1}$ to $2.1\,\mathrm{ns}^{-1}$ [176]. Each set

of singlet and triplet diffusion lengths was simulated for 20 different quencher concentrations in the range of 0 nm^{-3} to 0.032 nm^{-3} and the simulation of each quencher concentration was based on 1×10^4 excitons. It was assumed that singlet and triplet excitons are quenched with similar rates, in order to emulate CT quenchers. Here, transfer rates of excitons adjacent to a CT quencher were selected as 1 ps^{-1} to ensure a diffusion-limited quenching process, and are also on par with typical rates for CT formation including PCBM [177].

Figure 5.3 illustrates such data set for a triplet diffusion length of 26 nm and singlet diffusion length of 18.1 nm. Using the normalized singlet concentration kinetics (that are equivalent to the PL transients), SV plots for singlet and triplet excitons can be determined via the derived Equations 5.10 and 5.11, respectively.

Figure 5.4 depicts the SV plots for different triplet diffusion lengths in the range of 0 nm to 55 nm. In Figure 5.4A the SV plots for singlet excitons are shown. As expected, all simulated data lie on a single straight line irrespective of the set triplet diffusion length. This signifies that triplet diffusion does not interfere with the extraction of the singlet diffusion length when utilizing a standard SV analysis based on the prompt fluorescence of organic TADF molecules.

Figure 5.4B shows the SV plots for triplet excitons based on the approach presented in Section 5.1. Here, the extracted data lie on straight lines that have an increasing slope with increasing triplet diffusion length. As shown further below, these slopes can be accurately correlated to the right triplet diffusion lengths (selected as the simulation parameter).

Please note that the abscissa in the SV plots for singlet and triplet excitons is restricted to a quencher concentration of 0.01 nm^{-3} (in contrast to the PL kinetics shown in Figure 5.3). At higher concentrations, the data of longer triplet diffusion lengths started to be dominated by noise due to the limited number of simulated excitons (1×10^4). In addition, the data points begin to deviate from straight lines at higher concentrations, which can be attributed to an increasing contribution of sphere-of-action quenching, i.e., the breakdown of diffusion-limited quenching [39]. Furthermore, the exponential dependence of the quenching rate as a function of distance also leads to an upwards bend of the SV equation [150]. Looking back at Figure 5.3, this is also the most likely

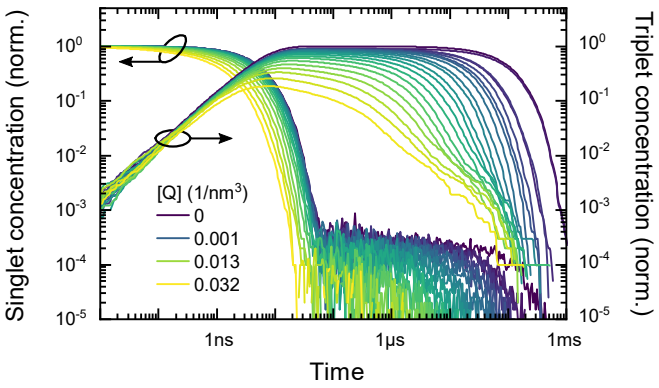

FIGURE 5.3: Sample data set for a triplet diffusion length of 26 nm and singlet diffusion length of 18.1 nm. From these singlet concentration data, the SV plots shown in Figure 5.4 are extracted.

explanation regarding the deviation of triplet concentrations from biexponential functions for high quenching concentrations.

The SV constants extracted from the plots shown in Figure 5.4 (not all simulated data are shown for reasons of clarity) were used to calculate singlet and triplet diffusion lengths by using Equation 5.4 and were compared to the set values of the simulation. In Figure 5.5 this comparison is illustrated by plotting the extracted (singlet and triplet) diffusion lengths as a function of the set triplet diffusion lengths. The extracted singlet diffusion lengths should therefore correspond to a straight line with an intersection with the abscissa at 18.1 nm and a slope of zero (the singlet diffusion lengths was kept fixed for all simulations). The triplet diffusion lengths should yield a straight line through the origin with slope one. As clearly shown in Figure 5.5, the extracted values meet those criteria by scattering around those expected values. Accordingly, this indicates the validity of Equations 5.10 and 5.11 for the determination of singlet and triplet diffusion lengths of organic TADF molecules.

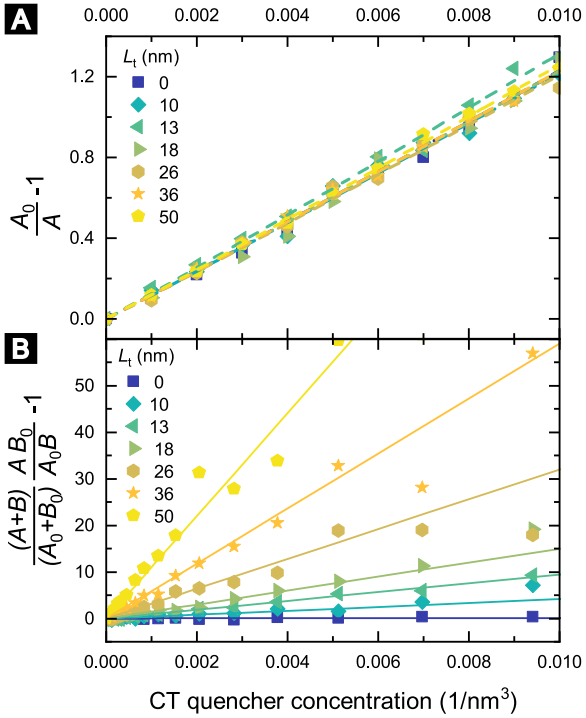

FIGURE 5.4: SV plots extracted from MC simulations for singlet excitons (A) and triplet excitons (B). For the SV analyisis with a triplet diffusion length of 26 nm the corresponding data are shown in Figure 5.3.

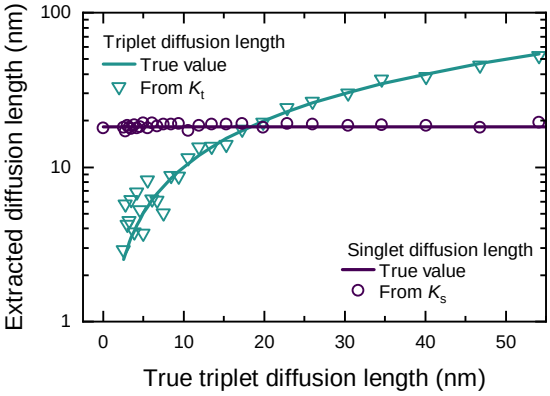

FIGURE 5.5: Extracted diffusion lengths of singlet and triplet excitons using an MC simulation and SV plots based on Equations 5.10 and 5.11. The diffusion length of the singlets was kept fixed at 18.1 nm throughout all simulations, while the triplet diffusion length was employed as simulation parameter. Adapted with permission from Jakoby *et al.* [174].

5.3.2 Analytic Approach

In the analytical approach to verify the novel SV method for organic TADF molecules, the rate equations of the system are employed (see Equation 5.1) to determine k_s and χ_D as a function of quencher concentration. This can be done by linearly increasing $k^Q_{s/t}[Q]$ in the analytic solution to the rate equations (see Equation 2.12). Figure 5.6A depicts the simulated transients for three different scenarios: i) singlet only quenching with $K_s = 0.3$ and $K_t = 0$; ii) singlet and triplet quenching with $K_s = 0.3$ and $K_t = 0.06$; iii) triplet only quenching with $K_s = 0$ and $K_t = 0.06$. In a real experiment and diffusion-limited quenching, these scenarios can be either attributed to selective quenchers, or to selective diffusion of the excitons. The simulated kinetics are labeled based on the quenching efficiencys (QEs) of singlet and triplet excitons, defined by $1 - k^0_{s/t}/k_{s/t}$. Notably, in case triplet excitons are not quenched, the delayed kinetics

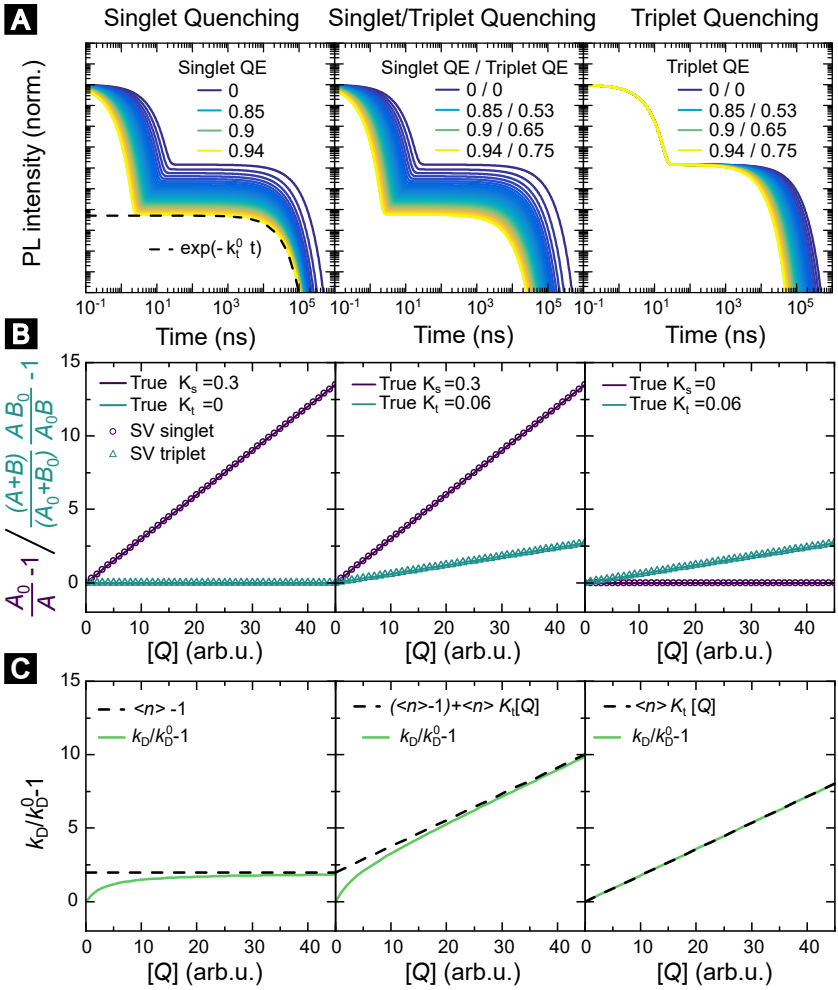

FIGURE 5.6: (A) Simulated PL kinetics for the molecules 4TCzBN for three different quenching scenarios. (B) SV plots extracted from the simulated PL kinetics in (A) by using the equations written at the ordinate and accompanied by linear functions with slopes corresponding to the true $K_{s/t}$ values. (C) SV plots using the standard SV equation based on k_P and k_D. Adapted with permission from Jakoby *et al.* [174].

converge to an asymptote described by a mono-exponential function with decay rate k_t^0. This is the case, since the averaged number $\langle n \rangle$ of passes through the triplet state of excitons contributing to delayed emission, i.e., excitons with at least one ISC event, approaches one with increasing $[Q]$ (see Equation 5.7).

As a side note, the kinetics would be identical for other K_s and K_t values as long as their ratio is unchanged. Accordingly, in the SV plots discussed below, due to the scalable $[Q]$, only the relationship between K_s and K_t is actually important. However, the previously mentioned K values are used in the following and can be seen as an explicit example without loss in generality. The PL kinetics shown in Figure 5.6A together with Equation 5.10 and 5.11 (or similarly Equation 5.17) are utilized to determine the SV plots shown in B. As evidenced by the Figure, both singlet and triplet quenching are accurately described within these SV analyses.

Last but not least, Figure 5.6C depicts SV plots in case the standard SV expression is applied to the delayed decay rate. Interestingly, for all cases, the slope of the asymptote corresponds to the SV constant for triplets (including cycling), and in case singlet excitons also contribute to the quenching, the interception with the ordinate is given by one minus the average number of complete singlet-triplet cycles $\langle n \rangle$. However, as long as singlet quenching is present, approximating the triplet quenching efficiency by $1 - k_D^0/k_D$ leads to significant deviation in the extracted triplet diffusion length. This is especially true if the analysis is carried out at low quencher concentrations, but dependent on the number of cycles $\langle n \rangle$ also for high quenching efficiencies ($> 90\,\%$) as long as a linear regression through the origin is used to extract K_t. In light of a real experiment, a strategy of employing the standard SV expression for high quencher concentration might additionally be problematic due to an increasing amount of static quenching that needs to be accounted for [39]. As an alternative, the use of a triplet-only quencher to extract the triplet diffusion length can also be a good approach, as shown in Figure 5.6C. However, such an approach would have the downside that two sample series would have to be fabricated to extract singlet and triplet diffusion lengths. This would also introduce additional uncertainties in the extraction of the ratio between singlet and triplet diffusion lengths, e.g., by the uncertainties in the interaction radii or quencher concentrations. Given that especially the ratio of both diffusion lengths is crucial for the simulation of hyperfluorescence devices (*vide infra*),

the reliance on CT quenchers, where both diffusion lengths can be evaluated using the same sample set, seems to be particularly advantageous.

5.4 Experimental Study of Exciton Motion

Now that the new method was introduced and verified by simulation and theory, it is demonstrated using three benchmark TADF molecules, 4CzIPN, 4TCzBN and DiKTa. The electron-accepting molecules ICBA or PCBM are employed as PL quenchers, which act as CT quenchers and therefore quench both singlet and triplet excitons with similar transfer rates. For the measurement of the PL kinetics, an intensified charge-coupled device (ICCD) and/or a streak camera were utilized. The organic TADF molecules were dispersed in a host matrix of mCP to prevent aggregation of the molecules. For 4CzIPN and 4TCzBN a guest concentration of 20 wt% was used, which is on the high side for the active layer of OLEDs involving those molecules [178], in order to determine an upper bound of the triplet diffusion length in devices. However, due to the tendency of DiKTa to aggregate at mCP concentration of 80 % the guest concentration was lowered to 1 wt% for the DiKTa thin films. Further details on the sample preparation can be found in Section 3.1.2.

Figures 5.7 and 5.8 show the raw data of time-resolved PL measurements of the TADF molecules with various quencher concentrations. The data were analyzed according to Equations 5.10 and 5.11. The area A and B were approximated by integration over the prompt and delayed fraction of the PL kinetics, respectively. As already mentioned, this approximation works well for organic TADF molecules since $k_P \ll k_D$. In Figure 5.9 the extracted SV plots are shown alongside the molecular structures of the three TADF molecules. The resulting diffusion lengths l_D and diffusion constants D are summarized in Table 5.1. The upper limits in Table 5.1 are determined by using the upper bound of the deviation from the mean value of K_t. However, for all studied molecules a triplet diffusion length of 0 nm is well within the error bounds of the experimental data. As a side note, the slightly negative mean of K_t for 4TCzBN could be the result of relaxation processes leading to a small overestimation of the singlet exciton quenching within the delayed lifetime. However, before turning to a detailed discussion of the results and placing them into the context of other

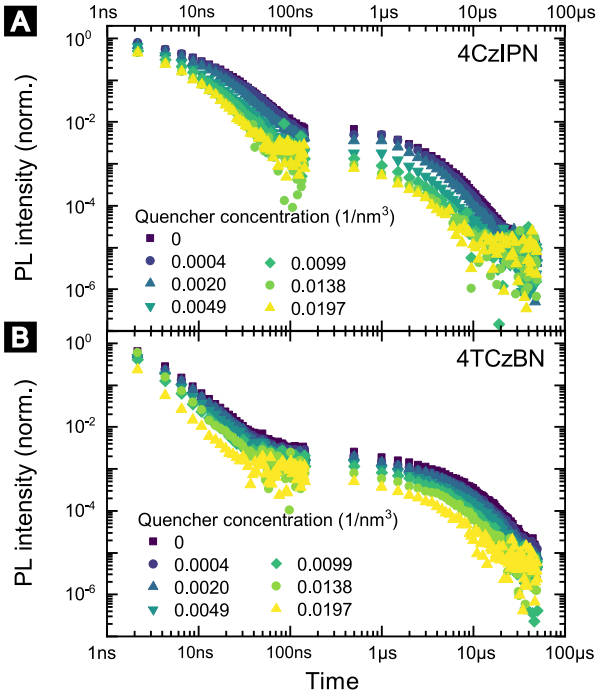

FIGURE 5.7: PL transients of the 4CzIPN (A) and 4TCzBN (B) quenching series excited at 355 nm and recorded with an ICCD camera. Reprinted with permission from Jakoby *et al.* [174].

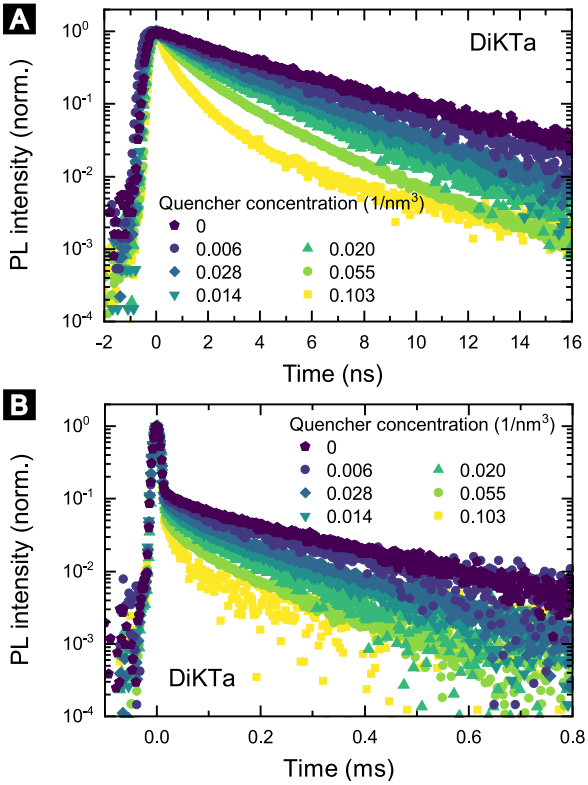

FIGURE 5.8: PL transients of the DiKTa quenching series excited at 343 nm. (A) PL transients extracted from a streak image with a time base of 20 ns. (B) PL transients taken from a streak image with a time base of 1 ms. Reprinted with permission from Jakoby *et al.* [174].

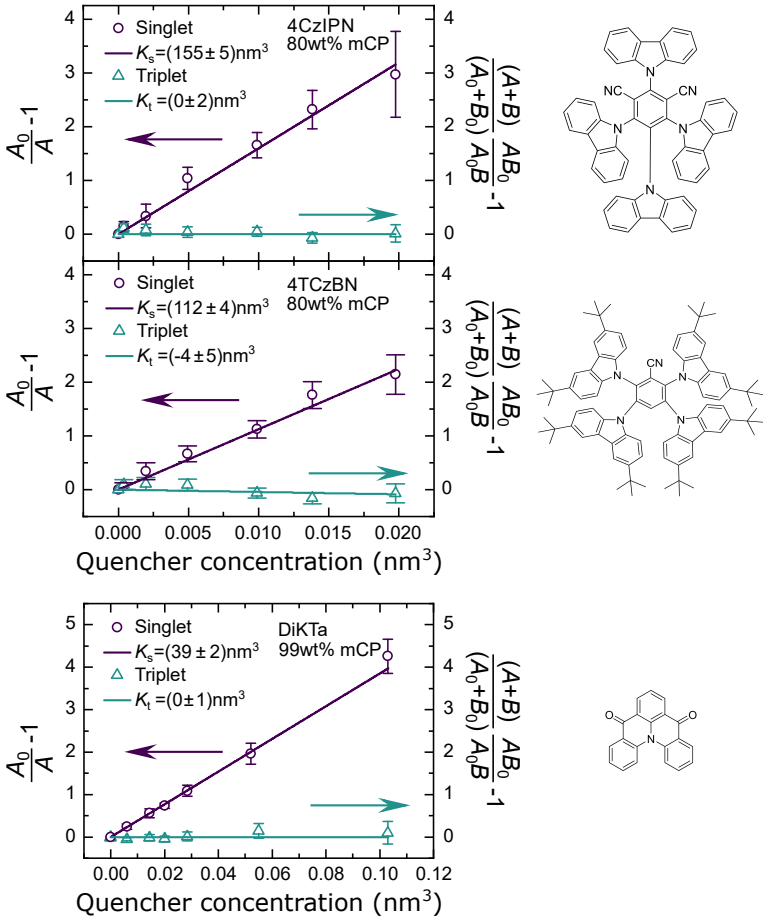

FIGURE 5.9: SV plots of the TADF molecules 4CzIPN, 4TCzBN and DiKTa accompanied by molecular structures. Adapted with permission from Jakoby *et al.* [174].

TABLE 5.1: Singlet and triplet diffusion lengths and constants for a single cycle and the total number of cycles through the respective state within the lifetime of the exciton. The data is extracted from the linear fits shown in Figure 5.9. The determined diffusion parameters correspond to films in which the TADF molecules are dispersed in an mCP host matrix (20 wt% for 4CzIPN and 4TCzBN and 1 wt% for DiKTa). Reprinted with permission from Jakoby *et al.* [174].

	Singlet Excitons		
	single l_D (nm)	total l_D (nm)	D_s (cm^2/s)
4CzIPN	8.6 ± 0.2	9.1 ± 0.2	$(1.0 \pm 0.1) \times 10^{-5}$
4TCzBN	7.3 ± 0.2	12.8 ± 0.3	$(2.9 \pm 0.2) \times 10^{-5}$
DiKTa	4.3 ± 0.2	8.3 ± 0.3	$(7.3 \pm 0.5) \times 10^{-6}$
	Triplet Excitons		
	single l_D (nm)	total l_D (nm)	D_t (cm^2/s)
4CzIPN	< 1.0	< 1.2	$< 6 \times 10^{-10}$
4TCzBN	< 0.7	< 1.0	$< 8 \times 10^{-10}$
DiKTa	< 0.7	< 1.3	$< 2 \times 10^{-11}$

exciton diffusion studies found in the literature, the results are first verified by means of density functional theory (DFT) simulations.

5.5 Verification by Density-Functional Simulations

DFT simulations were employed to verify the vanishing contribution of triplet exciton motion to the overall diffusion lengths, as found in the previous section. Details on these DFT simulations can be found elsewhere [174], but important aspects are briefly summarized in the following. As a first step, morphologies are generated in a volume of 16x16x16 nm^3 employing force field methods to emulate physical vapor deposition. For the calculation of the triplet transfer rates, the 10 most centered molecules are used (to avoid periodic boundary conditions) and the transfer rates are computed in accordance with Marcus theory between the 45 possible combinations. All other molecules, except the two selected, are estimated as partial charges and represent the molecular environment in the DFT calculations. Due to the structural similarity of 4TCzBN and 4CzIPN the simulations were restricted to the molecules 4TCzBN and DiKTa.

Figure 5.10A depicts the determined Dexter transfer rates as a function of the distance between the interacting molecules for a film that includes only TADF molecules. The highest occurring rate in the simulation for 4TCzBN was $267\,s^{-1}$ with a center-of-mass distance between the interacting molecules of 1.4 nm. This rate can be used to determine an upper bound of the triplet diffusion constant, assuming that between each neighboring molecule this transfer rate and distance would apply (see Section 2.2.3). This leads to an upper bound of the triplet diffusion constant of $1 \times 10^{-12}\,cm^2\,s^{-1}$. However, for the chosen 20 wt% concentration that is also used in devices, the average distance between molecules increases to about 2 nm. Therefore, the triplet diffusion length in such mixed films is likely to be even significantly lower.

In comparison to 4TCzBN, the highest occurring rate in the pure DiKTa film was significantly higher with $7.24 \times 10^8\,s^{-1}$ for a center-to-center separation of 0.43 nm. The resulting upper bound of the diffusion constant is $2 \times 10^{-7}\,cm^2/s$. However, when simulating a film comprised of a mixture between DiKTa and

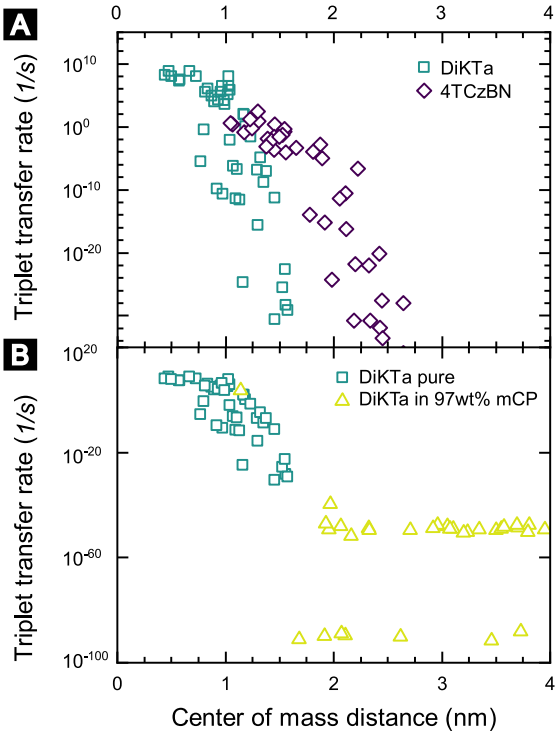

FIGURE 5.10: (A) Determined Dexter transfer rates for the molecules DiKTa and 4TCzBN in pure TADF films. (B) Comparison of the triplet transfer rates of a pure DiKTa film also shown in (A) with a mixture of DiKTa and 97 wt% mCP. Please note that due to numeric artifacts (rounding of small numbers) the rates for the mixed morphology are mainly centered around $1 \times 10^{-50}\,\mathrm{s}^{-1}$ and $1 \times 10^{-90}\,\mathrm{s}^{-1}$, but the determined values can be seen as upper bounds. The DFT simulations were performed by Shahriar Heidrich. Adapted with permission from Jakoby *et al.* [174].

97 wt% mCP, only one of the 45 molecular-pair combinations let to a non-vanishing rate with a value of $4.74 \times 10^3\,\mathrm{cm}^2/\mathrm{s}$ and a separation of 1.1 nm, and an upper bound of $1 \times 10^{-11}\,\mathrm{cm}^2/\mathrm{s}$ for the triplet diffusion constant. However, considering the probability of the occurrence of such a non-vanishing rate, the diffusion constant is again likely to be much smaller than this upper boundary.

The electron-exchange-based triplet transfer requires the transfer of a hole and an electron from the energy donating molecule to the energy accepting molecule (see Section 2.2.2), therefore, it is instructive to also compare electron and hole transfer rates to detect possible restrictions of the transfer due to a single species. Figure 5.11 compares charge-transfer rates for the two studied molecules in pure films. For DiKTa both electron and hole transfer rates are of similar magnitude with values up to $2 \times 10^{14}\,\mathrm{s}^{-1}$. In contrast, the charge-transfer rates for 4TCzBN are considerably smaller and in addition, electron transfer rates are 3 to 4 orders of magnitude lower than the corresponding transfer rates of holes. Accordingly, the highest occurring rate of electron transfer is $2 \times 10^{12}\,\mathrm{s}^{-1}$ while for holes only $1 \times 10^{9}\,\mathrm{s}^{-1}$.

The fast charge-transfer for DikTa in comparison to 4TCzBN can be attributed to the molecular structure. The planar DiKTa molecules easily stack and form molecular aggregates [137], which, in turn, leads to high charge-transfer rates. Furthermore, such stacking leads to a comparable amount of overlap between the LUMOs and HOMOs of the interacting molecules [137, 179]. Therefore, similar transfer rates of electrons and holes can be expected, matching the results of the DFT simulation. In comparison, 4TCzBN is much less susceptible to aggregation due to the spherical shape and the additional steric protection by the tert-butyl substituents [180]. Furthermore, the LUMO is centered mainly on the inlying benzonitrile and is therefore well protected from interacting with the LUMO of a second molecule, especially a second 4TCzBN molecule. In contrast, the HOMO is located on the outer carbazole units and possesses an increased probability of wavefunction overlap with a second molecule. This nicely aligns with the DFT calculations, where a suppressed hole transfer between these molecules in comparison to the electron transfer was found. Consequently, the negligible triplet transport in 4TCzBN can be attributed to the restricted LUMO-LUMO overlap. However, in light of the experimental results, where also a negligible triplet diffusion length was found for 4CzIPN, the finding

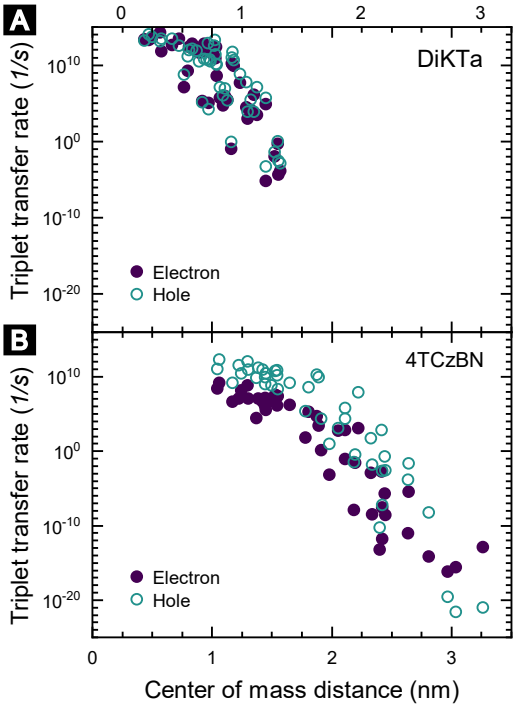

FIGURE 5.11: Determined electron and hole transfer rates of DiKTa (A) and 4TCzBN (B). The DFT simulations were performed by Shahriar Heidrich. Adapted with permission from Jakoby *et al.* [174].

of restricted triplet motion seems to be rather general for TADF molecules with outer lying donor units, at least for those with structural similarity to 4TCzBN.

Figure 5.12 summarizes the findings of this section, i.e., restricted triplet diffusion in typical OLED active layers doped with donor-acceptor molecules like 4TCzBN or DiKTa. While in the former case restricted LUMO-LUMO overlap was identified as the cause, in the latter case the high inter-molecular spacings between TADF molecules (to prevent aggregation) are responsible.

5.6 Discussion

Before discussing the implications of the preceding findings for a hyperfluorescence device, these findings will first be put into the context of literature. To begin with, the extracted singlet and triplet diffusion lengths and the underlying methods for their determination are discussed. In literature, three other experimental diffusion studies on exciton motion in TADF thin films can be found. In the following, these studies will be compared to the results of this thesis.

In each of the three exciton diffusion studies found in literature, the molecule 4CzIPN is included, and therefore it will be the focus of the discussion. In the publication by Yurash *et al.* diffusion lengths were extracted by bulk quenching experiments similar to the ones performed in this thesis, but with the difference that pure films of 4CzIPN (without host) were used [166]. The extracted diffusion lengths of Yurash and coworkers for a single occurrence of the state are 7.9 nm for singlet and 2.8 nm for triplet excitons. While the singlet diffusion length agrees rather well with the value determined here (8.6 nm) the triplet diffusion length is significantly higher in comparison to the value determined in this thesis (< 1 nm). The slightly increased value of singlet excitons might be due to an aggregation-induced decrease in the PLQY of the films employed by Yurash *et al.* [90, 166]. In contrast, for triplet excitons, an increased exchange coupling due to the smaller average distance between 4CzIPN in the pure TADF films employed by Yurash and coworkers might explain the deviation. However, in light of the results of the DFT simulations discussed in Section 5.5, where a vanishing triplet diffusion length was determined for the structural similar molecule 4TCzBN, an overestimation of the triplet diffusion length by Yurash

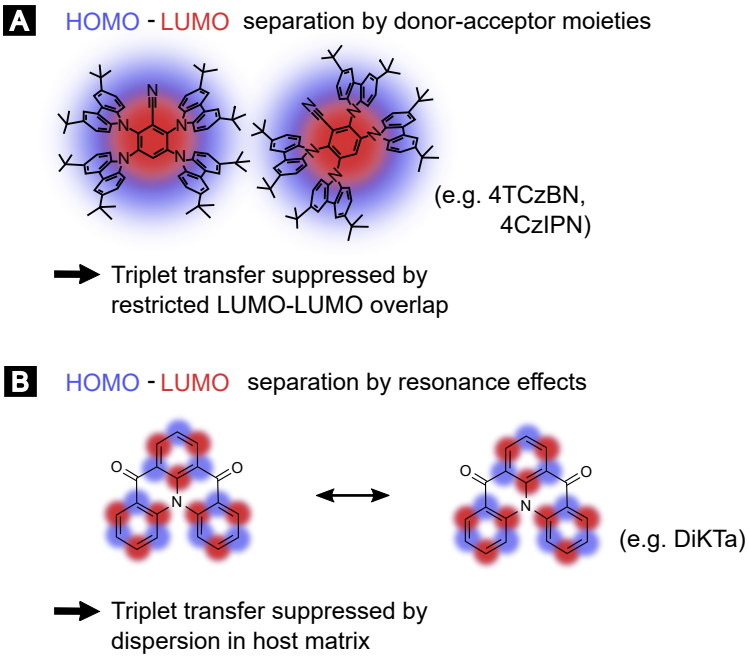

FIGURE 5.12: Schematic of exciton motion in TADF based devices. (A) suppressed triplet transfer as a result of the molecular architecture restricting the LUMO-LUMO overlap for two donor-acceptor type molecules like 4TczBN or 4CzIPN. (B) suppressed triplet transfer due to a highly dispersion (to prevent aggregation) for electron resonance based TADF molecules. Adapted with permission from Jakoby *et al.* [174].

et al. has to be considered. An indication for such overestimation is given by the approach Yurash and coworkers have chosen in determining the triplet diffusion length. This approach involves approximating the quenching efficiency of triplet excitons by $1 - k_{\mathrm{D}}^{0}/k_{\mathrm{D}}$. The so determined quenching efficiencies are used to extract triplet diffusion length based on an MC simulation that fits these quenching efficiencies (by varying D_t). However, as laid out in Figure 5.6, as well as in Section 5.2, such an approach leads in general to an overestimation of the triplet diffusion length, especially considering that for 4CzIPN the singlet diffusion length is significantly higher than the triplet diffusion length.

Another exciton diffusion study on 4CzIPN was performed by Menke and Holmes, who used bilayer structures to extract both singlet and triplet diffusion lengths [176]. Hole-accepting hexacarbonitrile (HATCN) was used as the quenching layer [176, 181], while 4CzIPN was dispersed in various concentrations in *p*-bis(triphenylsilyl)benzene as the emission layer [176]. Utilizing sample series with varying thickness of the emission layer (one series for each 4CzIPN concentration) the total exciton diffusion lengths, including motion both in the singlet and triplet states, were extracted as a function of 4CzIPN concentration. The contribution of singlet and triplet excitons to this overall diffusion length was determined using Förster theory. Here, the theoretically calculated singlet diffusion length was employed together with the total diffusion length, to deduce the contribution of triplet motion (by fitting J of the Dexter-type coupling). For 20 wt% 4CzIPN in HATCN, a singlet diffusion length of about 1.5 nm and a triplet diffusion length of about 5.3 nm were determined. In light of the results of this chapter and also considering the results on the singlet diffusion length of Yurash *et al.* the most likely explanation of the deviation is an underestimated FRET radius by Menke and Holmes [166, 176].

Last but not least, a third exciton diffusion study was performed by Niwa *et al.* and this study aligns well with the finding of this chapter of a vanishing triplet diffusion length for 4CzIPN [182]. Niwa and coworkers determined triplet diffusion constants for various doping concentrations of 4CzIPN in mCP based on a low-temperature triplet-triplet annihilation (TTA) study. Based on the TTA coefficient they determined a triplet diffusion constant of only about $1 \times 10^{-13}\,\mathrm{cm^2\,s^{-1}}$ for 10 % 4CzIPN in mCP (at 6 K) [182]. This value is more than two orders of magnitudes lower than the one determined in section 5.4. This is reasonable, as the lower concentration (10 %) of 4CzIPN, as well as

the lower temperature used by Niwa et al. is likely to decrease the diffusion constant. Furthermore, the determined experimental value in this thesis is an upper bound based on the experimental accuracy.

In addition to the publication by Niwa *et al.* [182], other experimental findings found in the literature also indicate negligible triplet diffusion in TADF emitters with a molecular structure similar to the one of 4CzIPN and 4TCzBN. First of all, it was demonstrated in a recent comparison of experimental device characteristics and kinetic MC simulations that in a hyperfluorescence device based on 4CzIPN-Me as sensitizer, triplet transport to fluorescent dopants is a negligible loss channel [183]. Moreover, in the context of conjugated molecular crystals, Narushima *et al.* recently showed that even though the stacked molecules have a good LUMO-LUMO overlap, the very small overlap between adjacent HOMOs leads to a very small diffusion constant for triplet excitons ($3 \times 10^{-9}\,\mathrm{cm^2\,s^{-1}}$) [184]. Along these lines, the negligible triplet diffusion lengths of 4CzIPN and 4TCzBN are supported by the findings presented in Chapter 5, where attaching phenylene ethynylene based oligomers to a 4CzIPN core did not lead to quenching of the triplet state on the TADF core by the lower-lying triplet state on the oligomer.

5.7 Implications for an Hyperfluorescence OLED

In hyperfluorescence OLEDs, fluorescent molecules (F-dopants) are added as a second dopant to the host matrix and are used to accept energy from the TADF molecules and emit it. Such an OLED design strategy is a promising approach to increase the value of TADF based OLEDs. By judicious choice of F-dopants and TADF sensitizer, the net radiative rate can be significantly increased, which, in turn, shortens the overall excited-state lifetime and ultimately increases device lifespan. Furthermore, the narrower bandwidth of the fluorescence acceptor leads to a higher color purity [37, 117]. In hyperfluorescence devices low F-dopant concentrations in comparison to TADF sensitizers have to be employed in order to prevent exciton formation of dark triplet states on the F-dopants. Consequently, most created excitons will have to diffuse between TADF molecules in order to reach a fluorescence acceptor. Once an F-dopant is neared, the exciton can either transfer by FRET if it is in the singlet state,

or by Dexter transfer if it is in the triplet state. While the former process is desired and leads to an emissive singlet state on the F-dopant, the latter process results in a long-lived dark state on the fluorescence acceptor and is detrimental to device performance. Intuitively, the Dexter transfer from TADF sensitizer to fluorescence acceptor can either be suppressed by a high singlet diffusion in comparison to the triplet diffusion length or alternatively by encasing the F-dopants in a shielding sheath of inert side-chains to keep TADF molecules far enough away to selectively suppress the short-range Dexter transfer. This raises the question of whether triplet transport in TADF molecules can be desirable to increase hyperfluorescence OLED efficiencies? On the one side, the improved triplet diffusion could help excitons to reach the fluorescence acceptor molecules. On the other side, mobile triplet excitons are also more likely to be trapped by fluorescence acceptors.

Herein, this section investigates how a changing ratio between singlet and triplet diffusion lengths impacts the singlet harvesting-efficiency of protected and unprotected F-dopants in a hyperfluorescence active layer. For this purpose, the MC simulation, that was introduced in Section 3.5, is employed and the required rates are chosen again in accordance with the TADF molecule 4CzBN [157]. Moreover, in these simulations, the excitons were initialized at 25 % as singlet and 75 % as triplet excitons in order to emulate electrical excitation in an OLED. Sterically protected emitters were mimicked by predefining all positions within a radius of 1.75 nm around an F-dopant as inert matrix molecules. The average distance between TADF molecules was set to 1.7 nm and the concentration of F-dopants changed between simulations in the range of 0 % to 7 % relative to the total doping concentration of TADF molecules and F-dopants. The FRET radius between TADF molecules was selected as $R_0 = 2\,\text{nm}$, leading to a singlet diffusion length on par with the experimental results in Section 5.4 (7.4 nm). Between TADF sensitizer and fluorescence acceptors, $R_0 = 3.35\,\text{nm}$ was chosen, a reasonable assumption for well-matched FRET donor-acceptor pairs [38, 51]. The Dexter rates from TADF molecule towards an adjacent unprotected F-dopant was selected to be $4.5\,\text{ns}^{-1}$ and towards a protected F-dopant to $2 \times 10^{-4}\,\text{ns}^{-1}$, while between TADF molecules a value of 0 and $0.2\,\text{ns}^{-1}$ was used for no triplet motion and a triplet diffusion length of 7.4 nm, respectively.

Figure 5.13 depicts the simulated data for these two triplet motion scenarios. The best performance in terms of a singlet exciton quantum yield on the F-

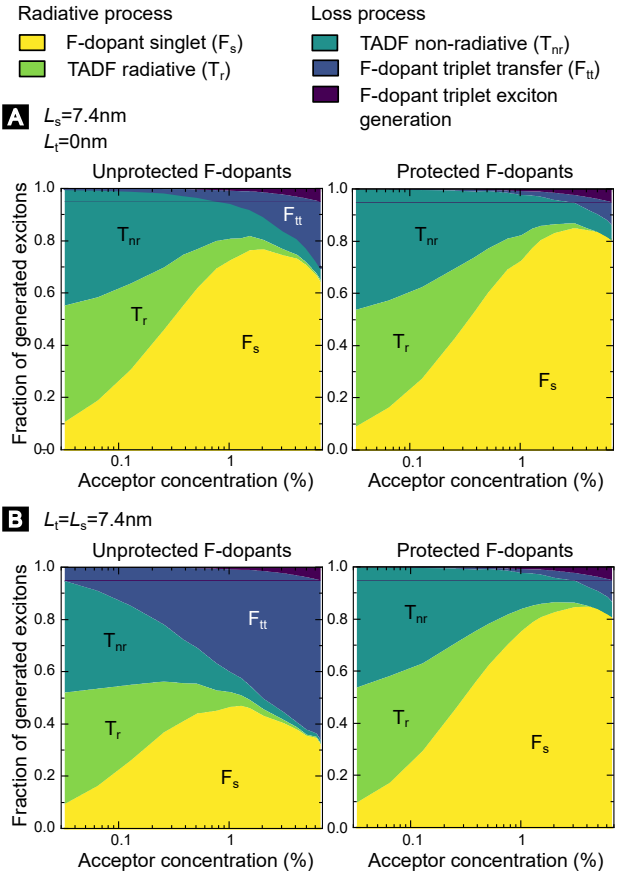

FIGURE 5.13: Simulation of active layers of hyperfluorescence OLEDs, comparing efficiencies of architectures with unprotected and sterically protected F-dopants. The abscissa corresponds to F-dopant concentration relative to the total number of dopants (TADF molecules and F-dopants). Two different triplet motion scenarios where simulated for a singlet diffusion length of $L_s = 7.4\,\text{nm}$: i) no triplet motion; ii) triplet diffusion length equal to the singlet diffusion length. The internal quantum yields of the active layers are given by F_s+T_r assuming the F-dopant's PLQY to be 100 %.

dopants (harvesting efficiency) is achieved by active layers including sterically-protected F-dopants. Here, a maximum harvesting efficiency of 84 % is reached irrespective of the triplet diffusion length. In contrast, for the unprotected fluorescence acceptors, triplet transport has a strongly deleterious effect on the harvesting efficiency. Without triplet motion, still 77 % of the excitons reach the F-dopants in a singlet state. However, once triplet motion is turned on, the maximum harvesting efficiency is reduced to only 46 %. The optimum doping concentration for protected emitters lies at about 3 % to 4 % and shifts to slightly lower values for unprotected emitters (2 % with and 1 % without triplet motion). Please note, in these simulations, it was assumed that the likelihood for recombination of electron and hole on a TADF molecule in comparison to recombination on the fluorescence acceptor is solely dependent on the relative doping concentration. However, the steric protection of F-dopants might shift this ratio towards TADF molecules, which, in turn, would shift the optimum doping concentration to slightly higher values. The same applies if the protected F-dopants suppress triplet transfer entirely. These two aspects are substantiated by Figure 5.14, where the harvesting efficiency is plotted when all excitons are initialized on TADF molecules and triplet transfer to protected F-dopants is completely suppressed. Here, the harvesting efficiency exceeds 90 % for the protected emitters at a concentration of 5 % and reaches 80 % for unprotected emitters at an optimum concentration of 2 %. Figure 5.14 further substantiates that the harvesting efficiency is independent of the triplet diffusion constant as long as triplet transfer to the F-dopants is suppressed. Here, the different triplet diffusion lengths were simulated by changing the Dexter coupling between TADF molecules (see Section 5.3.1).

As already indicated, an important motivation for research on hyperfluorescence OLEDs is to achieve a short overall exciton lifetime in the active layer. For the simulated case of 4CzBN, the initial average exciton lifetime is 29 µs. In the simulation including protected emitters, the turnover time from charge recombination to photon emission decreases to about 4 µs, independent of the triplet diffusion length. For the case of unprotected emitters and immobile triplets, the turnover time is further decreased to 2.8 µs. These results signify that: i) the hyperfluorescence approach is an effective method in substantially decreasing exciton dwell times in the active layer; ii) a beneficial aspect of a hyperfluorescence approach involving unprotected F-dopants in conjunction

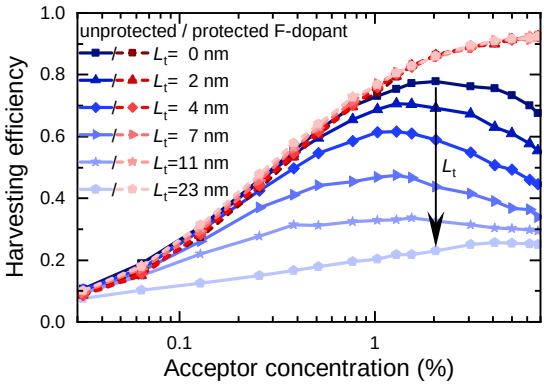

FIGURE 5.14: Singlet harvesting efficiency as a function of F-dopant concentration. Here, losses connected to direct exciton formation on F-dopants are neglected. Furthermore, protected F-dopants are assumed to suppress 100 % of triplet transfer in contrast to Figure 5.13. Red data points correspond to sterically protected emitters, while blue data points correspond to unprotected emitters. In both cases, a set of different triplet diffusion lengths is shown, while the singlet diffusion length is kept constant at 7.4 nm. Adapted with permission from Jakoby *et al.* [56].

with immobile triplet excitons can be a further decreased exciton lifetime in the active layer. This latter aspect can be attributed to a slight reduction in the FRET transfer rates introduced by the steric protection.

In summary, this section demonstrated that there exist two pathways towards reaching high-efficiency hyperfluorescence. The first is to suppress triplet transfer to the fluorescence acceptors by developing appropriate steric protection, as already discussed in literature [185]. However, a second pathway, which is nearly as efficient, is to suppress the motion of triplets between TADF molecules. In light of the experimental results presented at the beginning of this chapter, where TADF molecules with suppressed triplet motion were detected, the second pathway seems to be a very promising approach towards highly efficient hyperfluorescence OLEDs.

5.8 Conclusion

This chapter presented a method on how to accurately determine singlet and triplet diffusion lengths and constants based on easily accessible experimental data. Moreover, it demonstrated that this approach overcomes limitations in the pioneering studies on exciton diffusion in organic TADF molecules (especially studies on 4CzIPN). The developed approach was employed to extract exciton diffusion lengths of 4CzIPN, 4TCzBN, and DiKTa based on time-resolved PL measurements. The experiments revealed the novel insight that triplet diffusion in TADF molecules can be extremely limited, which was further supported by DFT calculations. For 4CzIPN and 4TCzBN a restricted LUMO-LUMO overlap could be identified as the underlying cause for restricted triplet motion, while for DiKTa the low doping concentrations in the matrix (to prevent aggregation) suppressed the electron exchange between TADF molecules. Based on those findings, an MC simulation was designed to illustrate how precise knowledge of exciton diffusion lengths can be utilized in optimizing hyperfluorescence active layers, e.g., to determine the optimum doping concentrations of TADF molecules and fluorescence acceptors. Furthermore, it was shown that limited triplet diffusion is highly favorable for hyperfluorescence device architectures. These findings open up a new pathway to optimize hyperfluorescence OLEDs. Besides utilizing sterically protected emitters, the selection of TADF molecules with vanishing triplet diffusion length is a promising alternative. In light of the experimental results of restricted triplet motion for TADF molecules with similar structural design as 4CzIPN, the recently observed high efficiencies in hyperfluorescence systems without sterically protected emitters might be explained [37, 186–188]. Furthermore, it can be noted that the discussion of singlet and triplet motion in the context of hyperfluorescence can be easily transferred to white OLEDs, where partial singlet exciton transfer for example between blue-emitting TADF molecules and yellow emitting F-dopants is desired [189].

6

Exciton Transport in Zn-ADB-SURMOF-2

An important parameter for the design of light-harvesting materials is the ratio between the exciton diffusion and absorption length. For efficient devices, a value above one is desired to ensure that the majority of generated excitons can reach an interface where charge separation takes place. Due to the in general small diffusion lengths ($< 20\,\mathrm{nm}$) of singlet excitons in disordered organic semiconductors, the field of organic photovoltaics has turned to bulk-hetero junctions with eutectic mixtures of donor and acceptor molecules [19, 60, 65, 190, 191]. This approach keeps distances between the point of excitation and the next donor-acceptor interface sufficiently low but has the downside of additional exciton or polaron trapping in poorly interconnected donor or acceptor areas

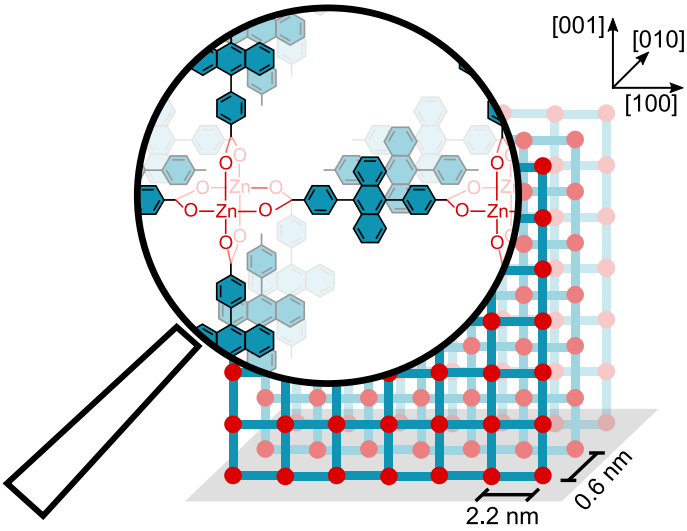

FIGURE 6.1: Architecture of the Zn-ADB-SURMOF-2. The Zn-based paddle-wheel type secondary building units and the ADB linkers are sketched in red and blue, respectively. For reasons of clarity, the paddle-wheel units are only drawn in the first layer of the magnified scheme.

(islands, etc.). The design of a solution-processable organic semiconductor with sufficiently high singlet diffusion length ($\gg$100 nm) enabling the return to planar devices is therefore still desirable.

A promising material class that might be able to fulfill those needs are SURMOFs [129]. In particular, the sheet-like Zn-SURMOF-2 structure recently received special recognition in literature [130]. Up-conversion structures [192, 193], solar cells [188], TADF based OLEDs [194], as well as long-range triplet exciton transport [23] have already been demonstrated. In this chapter, it will be shown that the Zn-ADB-SURMOF-2 (Zn-ADB), depicted in Figure 6.1, has further promising characteristics: i) Two different photoexcited states are present in the Zn-ADB, one monomer-related, the other excimer-related; ii) By using two linkers, one acting as a FRET donor while the other one acting as a FRET acceptor, an efficient energy harvesting network can be

built; iii) The defined orientations and positions of the chromophores facilitate long-range singlet transport. In specific it is shown, that the tetragonal unit cell of the SURMOF-2 structure leads to an anisotropic diffusion tensor for the excimer-related exciton, with the preferred direction of motion along the axis where intermolecular distances are smallest ([010]-direction). In contrast, this anisotropic exciton motion is less pronounced for the monomer-related excited state.

Acknowledgements and Contributions

This chapter is based on the publication:

- R. Haldar*, M. Jakoby*, A. Mazel, Q. Zhang, A. Welle, T. Mohamed, P. Krolla, W. Wenzel, S. Diring, F. Odobel, B. S. Richards, I. A.Howard, and C. Wöll, "Anisotropic energy transfer in crystalline chromophore assemblies," *Nat. Commun.*, vol. 9, no. 1, 4332, 2018. [61]

R. Haldar and C. Wöll came up with the idea of synthesizing a SURMOF with efficient FRET between two linkers. The experiments on the different layer stacks to extract the anisotropic diffusion tensor were conceived by the author and I. A. Howard. The chemical synthesis of the SURMOFs was conducted by R. Haldar with the guidance of C. Wöll. A. Mazel and S. Diring carried out the DPP linker synthesis. Q. Zhang and W. Wenzel planned the Force Field calculations and Q. Zhang carried out the calculations. A. Welle, T. Mohamed, and P. Krolla helped with material characterizations. PL, absorption, streak camera, and lifetime experiments were performed by the author. The data analysis of these experiments was performed by the author with support from Ian A. H. and B. S. Richards. The manuscript was conceptualized by R. Haldar and the present author. All authors participated in the discussion and writing of the manuscript.

*authors contributed equally

6.1 Excited States in Zn-ADB-SURMOF-2

Zn-ADB is assembled from Zn-based paddle-wheel type secondary building units and ADB linkers forming an array of stacks of square type 2D sheets. As can be seen in Figure 6.1 this arrangement leads to 1D stacks of the linker chromophores in [010] direction, with small nearest neighbor intermolecular distances of 0.6 nm, while in [100] and [001] direction distances of 2.2 nm apply (see Section 3.1.3). This ordered and therefore also anisotropic arrangement of chromophores has an intriguing impact on the excited-state dynamics. Additionally, the rotational freedom of the anthracene unit of the ADB linker inside Zn-ADB has an important influence on the excited states, which will be discussed in the following subsection.

6.1.1 Impact of the Rotational Motion of ADB Linkers on the Photo-Excited States

In order to shed light on the excited-state dynamics of Zn-ADB the arrangement of chromophores inside Zn-ADB was studied in further detail. As a first step, absorbance and PL spectra of ADB in ethanol and after assembly into the SURMOF were recorded and are plotted in Figure 6.2. For the linker in ethanol the emission spectrum is featureless and centered around 2.85 eV, while the absorption spectrum reveals four vibronic transitions located at 3.15 eV, 3.32 eV, 3.49 eV and 3.67 eV. For Zn-ADB both spectra, absorption, and emission show a significant bathochromic shift from solution to Zn-ADB. The absorption spectrum shifts by about 0.053 eV to the red, while the PL spectrum by about 0.18 eV. Additionally, the PL spectrum of ADB possesses a shoulder at 2.75 eV and the vibrational features of the absorption spectrum are distorted. Taking the 0-1 vibronic peak at 3.32 eV as a reference, the 0-0 feature is reduced, while the 0-2 feature is increased for the Zn-ADB in comparison to the linker in ethanol.

The absorption spectrum of the ADB linker in ethanol aligns well with the absorption spectrum of anthracene found in literature [39], signifying that the benzoate units of the molecule have a negligible impact on the LUMO and HOMO and with it on the optical properties of the chromophore. The changes of the emission and absorption spectra for Zn-ADB can be attributed to increased

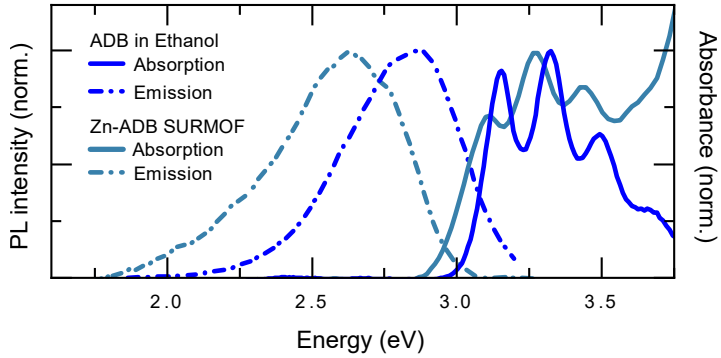

FIGURE 6.2: Absorption and PL spectra of ADB in ethanol ($0.02\,\mathrm{mol\,cm^{-3}}$) and of Zn-ADB. The PL spectra are normalized to the peak intensity of the 0-1 vibronic transition. A photon energy of 3.26 eV was used for the excitation of the samples.

intermolecular interactions of the chromophores due to the close stacking. These interactions can be, dependent on the intermolecular distances of the interacting molecules, either due to Coulomb interactions or due to electron exchange interactions. For the latter type, the intermolecular distance of 0.6 nm is still slightly large for efficient coupling [195, 196]. For the Coulomb interaction, the relative orientation of the $S_0 - S_1$ transition-dipoles of the chromophores is most important to qualitatively describe the changes in absorption and emission. For the ADB linker this transition dipole moment is aligned parallel to the p_z-orbitals of the carbon atoms [197]. Based on the simplified scheme in Figure 6.1, J-aggregates would be expected inside the Zn-ADB. However, J-aggregates typically possess small stokes-shifts, pronounced 0-0 oscillator strength, as well as a red-shifted absorption and emission spectrum [38, 198]. While the bathochromic shift of the PL and absorption spectra of the SURMOF could be explained by the formation of J-aggregates, the reduction in the intensity of the 0-0 vibronic peak is not matching to this assignment [38, 199].

To better understand this apparent deviation, a closer look at the orientation of the linkers inside Zn-ADB is necessary. For this purpose, optimized potential for

liquid simulation (OPLS) were performed considering the structural constraints in Zn-ADB. As shown in Figure 6.3, the energy-optimized geometry of the ADB linkers was found to be in a rotated state of the anthracene units relative to the (010) planes. The angle θ between (010) planes and the anthracene unit was found to be 47.7° for the lowest internal energy configuration of the system. This angle corresponds to distances between adjacent anthracene units in the stacking direction of 0.42 nm.

Additionally, the OPLS data reveals that the potential surface of the rotation of chromophores has a rather shallow minimum. At room temperature within $k_BT \approx 2.4\,\mathrm{kJ\,mol^{-1}}$ rotations from 42° to 51° can be realized. However, taking the bathochromic shift of $0.18\,\mathrm{eV} = 17.4\,\mathrm{kJ\,mol^{-1}}$ of the PL as a reference for feasible rotations, the ADB units can rotate by 24° to 57°, which would reduce the nearest-neighbour intermolecular anthracene distance to 0.34 nm. At this small distance, Dexter type coupling becomes important for aromatic systems and excited dimers (excimers) are likely to be formed [195, 200, 201].

6.1.2 Monomer and Excimer Excitonic State Dynamics

In order to gain a better understanding of the excimer formation inside Zn-ADB, time-resolved PL spectra were recorded. Figure 6.4 shows a streak camera image of the first 1.5 ns of PL emission of the SURMOF. The sample was excited using the mode-locked Ti:sapphire laser setup (see Section 3.3.1) with a photon energy of 3.26 eV and a fluence of $16\,\mathrm{nJ\,cm^{-2}}$. The streak image reveals that the peak position of the PL spectrum shifts to the red with increasing time after excitation. During the time of excitation, the emission is centered around 2.7 eV, while after 1500 ps it is centered at 2.5 eV. This shift indicates that there are at least two different emissive species with distinct PL spectra and lifetimes present in the sample.

A detailed analysis of the streak image further indicates that the data matrix (minus noise) has rank 2, pinpointing that there are two emissive species present in Zn-ADB. As a consequence, the data matrix can be expressed by the multiplication of a $2 \times X_1$ matrix S and a $X_2 \times 2$ matrix T, where X_1 corresponds to the number of pixels along the energy axis, while X_2 to the number of pixels along the time axis of the streak image. To determine the spectra (matrix S)

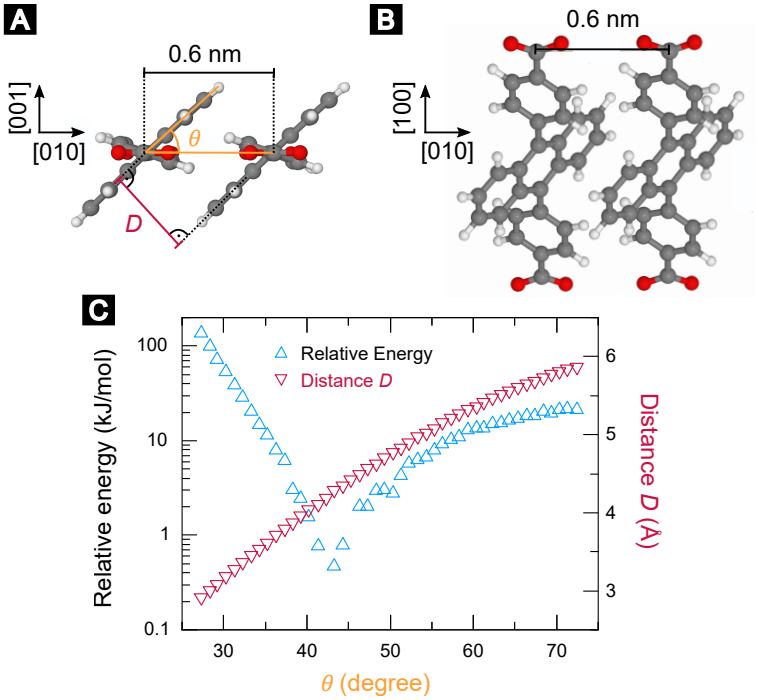

FIGURE 6.3: Results of the force-field simulations conducted by Quiang Zang. (A) and (B) show a top and side view, respectively, of two neighboring anthracene units in the minimum energy geometry. Please mind that [100] and [001] are equivalent due to the C4 symmetry along [010]). θ is defined as the angle between the (010) planes and the plane that bisects the carbon atoms of anthracene. (C) Energy change relative to the minimum energy geometry at $\theta = 47.7°$ and anthracene-anthracene distance D plotted against the relative degree of rotation of the anthracene units θ. Please note that the point of minimum energy is not part of the plot due to the logarithmic y-axis.

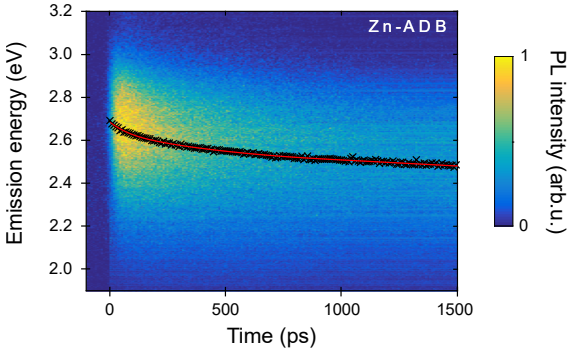

FIGURE 6.4: Streak image of the Zn-ADB SURMOF excited at 3.26 eV. The peak position of the PL spectrum at each time step is marked by a black cross. As a guide to the eye, these peak values are fitted by a spline fit shown in red. Adapted with permission from Haldar *et al.* [61].

and PL transients (matrix T) of the two species, the method of multivariate curve resolution together with a constrained alternating least squares algorithm (MCR-ALS) was used [202]. Both matrices were constrained to be positive. The resulting transients and PL spectra of the two species are shown in 6.5A and B, respectively. The spectra reveal, that there is one species with a featureless PL spectrum centered around 2.58 eV and a second energetically higher lying species with a PL spectrum centered around 2.81 eV. The spectral position and shape of the energetically lower-lying state match nicely with PL spectra of excimers of interacting anthracene molecules [195, 196, 203]. Therefore, this state is from now on referred to as “excimer”, while the energetically higher lying state is referred to as “excited monomer”. This assignment will be underpinned further in the following.

For this purpose, the gained PL kinetics and PL spectra of the two species will be studied in further detail. As clearly evidenced by Figure 6.5A, the excimer’s PL transient does not rise with the IRF in contrast to the PL transient of the excited monomer. This observation is the first indication for an energy transfer from the monomer species to the excimer. In order to verify this association, the two PL kinetics are model by a set of coupled rate equations. For a system

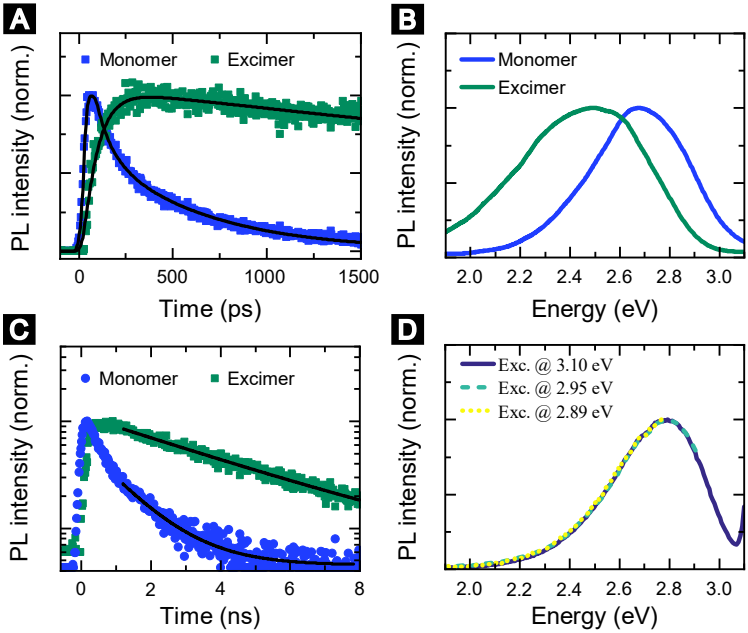

FIGURE 6.5: (A) and (C) PL transients of the excited monomer and excimer state for a 2 ns and 10 ns time base, respectively. The PL transients are fitted by biexponential deconvolution fits (black solid lines). (B) PL spectra of the donor and excimer state. The PL transients and emission spectra in (A), (B), and (C) have been determined from two streak images with different time bases, using a multivariate curve resolution fit together with a constrained alternating least squares algorithm. Note the linear intensity axis in (A) for better visibility of the increased rise time of the excimer state, in contrast to the log scale in (C). (D) PL spectra of Zn-ADB upon excitation with different photon energies. Adapted with permission from Haldar *et al.* [61].

with two components, where one feeds energy to the other and both states can also transition to the ground state, the coupled rate equations read:

$$\frac{\partial}{\partial t}c_{\mathrm{M}} = -k_{\mathrm{M}}c_{\mathrm{M}}, \tag{6.1a}$$

$$\frac{\partial}{\partial t}c_{\mathrm{E}} = -k_{\mathrm{E}}c_{\mathrm{E}} + k_{\mathrm{M}}c_{\mathrm{M}}. \tag{6.1b}$$

Here, c_{M} and c_{E} are the excited monomer and excimer concentrations, while k_{M} and k_{E} are their decay rates, respectively. Solving these coupled linear differential equations using the boundary conditions $c_M(0) = 1$ and $c_E(0) = 0$ (a consequence of the MCR-ALS approach is an ambiguous relative amplitude of the transients and therefore normalized transients were fitted) leads to:

$$c_{\mathrm{M}} = e^{-k_{\mathrm{M}}t}, \tag{6.2a}$$

$$c_{\mathrm{E}} = \frac{k_{\mathrm{M}}}{k_{\mathrm{M}} + k_{\mathrm{E}}}e^{-k_{\mathrm{E}}t} - \frac{k_{\mathrm{M}}}{k_{\mathrm{M}} + k_{\mathrm{E}}}e^{-k_{\mathrm{M}}t}. \tag{6.2b}$$

This solution was convoluted with the IRF of the streak camera and fitted to the kinetics shown in Figure 6.5A. However, since the excited monomer related PL transient was not well represented by a monoexponential a second exponential was added to the Equation 6.2a (*vide infra*). Furthermore, to improve the fitting quality the excimer PL lifetime was fixed to 4.0 ns. This value was determined using a second streak image with an increased time base of 10 ns. Figure 6.5C depicts the PL transients of both states which have been extracted by means of MCR-ALS from the streak image with 10 ns time base. Using mono exponential fits the long-lived lifetimes of the excimer (4.0 ns) and excited monomer (1.2 ns) were determined. A summary of the extracted lifetimes is given in Table 6.1.

The additional PL lifetime of the excited monomer in comparison to the proposed model (Equation 6.2a) can be justified by considering the polydispersity of the sample with crystal sizes below 140 nm [23, 133]. Therefore, many grain boundaries are present in the sample where excimer formation is aggravated. Additionally, since an activation energy is required for rotational configurations where excimer formation is enabled (see Section 6.1.1), the concentration of

TABLE 6.1: Extracted lifetimes of the fits shown in Figure 6.5 (A) and (C). While τ_1 is extracted from a monoexponential fit of the transients shown in Figure 6.5 (C), τ_2 and τ_3 are extracted using a biexponential reconvolution fit to the transients shown in Figure 6.5 (A).

	Monomer	Excimer
τ_1 (ns)	1.2 ± 0.1 ($\approx 20\,\%$)	4.0 ± 0.2 (decay)
τ_2 (ps)	570 ± 30 ($\approx 30\,\%$)	
τ_3 (ps)	80 ± 4 (50 %)	80 ± 4 (rise)

excimer and excited monomer should follow a Boltzmann distribution, and a complete transfer of population is therefore not expected. As a consequence, the presence of an additional decay lifetime of the monomer species can be expected. However, calculating the two fractions of both concentrations is beyond the scope of this work, since neither state is in thermal equilibrium after excitation.

The determined lifetimes suggest that about 50 % of the monomer excited states transfer to become excimer states with an inverse rate of 80 ps. In the β-form of anthracene crystals, this transfer time is much shorter at about 150 fs [195]. This divergence can be attributed to the different type of packing of the anthracene chromophores in Zn-ADB in comparison to the bulk anthracene crystals. Furthermore, the endothermic process of ADB rotation could explain this increased transfer time. That excess energy is needed for the process of excimer formation (i.e., in form of thermalization after photoexcitation) can be demonstrated by excitation energy-dependent PL measurements. As can be seen in Figure 6.5D, by shifting the excitation energy along the absorption edge of Zn-ADB, no shift in the PL can be observed suggesting an unchanged ratio of excited monomer and excimer states. This signifies that the excimer does not absorb light and excess energy is needed for its formation. Therefore, the excimer is always created through the excited monomer state.

Now that the two distinct excited states of Zn-ADB are established, the next section turns to studying the energy transfer of both states to a second energy

accepting linker (DPP). Here it will be shown that both states can efficiently transfer energy to this energy accepting linker.

6.2 Design of a Donor-Acceptor SURMOF

The design of a SURMOF based on two linkers, each with distinct functionality, was already established by Oldenburg *et al.* [133]. Here, he and his coworkers showed that the dilution of an emissive ADB linker with an optically-inert linker can be used to control the internal PLQY of the SURMOF. Based on this excellent groundwork, a donor-acceptor SURMOF was designed by replacing the inert linker with a FRET acceptor. The restrictions of similar intramolecular distances between the two carboxyl groups for both linkers, as well as good spectral overlap of the absorption spectrum of the acceptor with the emission spectrum of ADB led to the linker DPP. Figure 6.6 shows a schematic of the donor-acceptor SURMOF, with ADB acting as FRET donor (sensitizer) and DPP as FRET acceptor (emitter). For the studies presented in the upcoming sections, the concentration of DPP inside Zn-ADB was changed in the range of 0 % to 4 % relative to the total number of linker sites.

In the following subsection, FRET between both linkers is studied in solution as well as after both linkers are incorporated into Zn-ADB. Here, it will be shown that the SURMOF structure facilitates the energy transfer between the linkers. In the second subsection, the distinct transfer efficiencies of the excited monomer and excimer excited states towards the acceptor will be established.

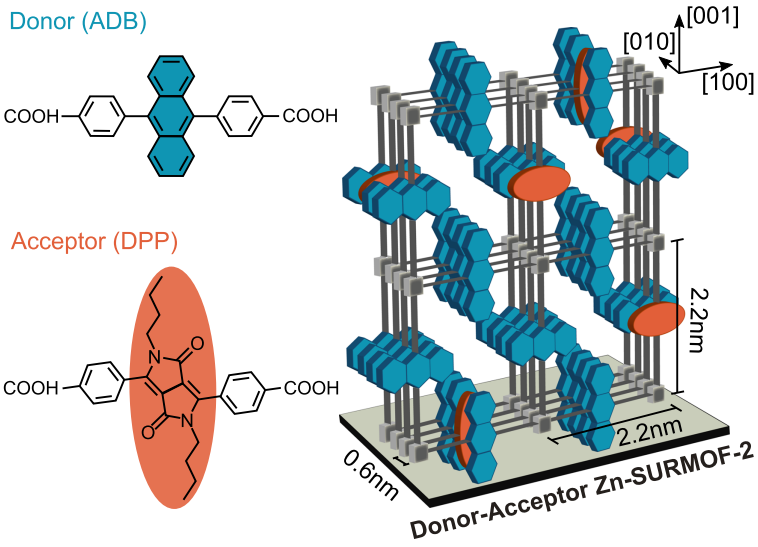

FIGURE 6.6: Architecture of the donor-acceptor Zn-ADB SURMOF. On the left side the individual linkers used to construct the mixed-linker SURMOF are shown, while on the right side a schematic of the fabricated SURMOF is depicted. Adapted with permission from Haldar *et al.* [61].

6.2.1 Energy Transfer between ADB and DPP

As a starting point to study the energy transfer between ADB and DPP inside Zn-ADB, the spectral overlap between the donor emission and acceptor absorption spectra is analyzed. Figure 6.7A shows the PL spectra of Zn-ADB and ADB and DPP in ethanol accompanied by the absorption spectrum of DPP. Please note that the emission spectrum of ADB in ethanol and Zn-ADB were already discussed in Section 6.1.1 and are just shown here again for reasons of clarity. The emission spectrum of DPP peaks at 2.2 eV with an additional shoulder at 2.10 eV, while the absorption spectrum has a featureless band centered around 2.6 eV aligning well with the Zn-ADB emission spectrum. As a side note, it was chosen to show the DPP absorption in ethanol since only small doping

concentrations of the Zn-ADB were used throughout this study. However, an aggregation-induced spectral shift of the absorption band centered around 2.6 eV for DPP in ethanol and a pristine SURMOF build with DPP linkers only (Zn-DPP) showed no significant spectral shift (shift below 0.05 eV and compare also Figure 6.7A and B).

The absorption and emission spectra of DPP coincide well with other spectra of diketopyrrolepyrrole derivatives found in literature [204, 205]. The intense absorption feature at 2.6 eV arises from a $\pi - \pi^*$ transition, mainly localized on the lactame unit of the linker [204]. The excellent overlap of this absorption feature with the emission spectrum of Zn-ADB, which is a requirement for efficient FRET, gives a first indication that ADB and DPP linkers form a well-tailored FRET system inside Zn-ADB. Notably, the bathochromic shift of the ADB emission spectrum due to excimer formation is clearly of benefit with regard to the spectral overlap (see Figure 6.7A).

A commonly used tool to investigate the presence of energy transfer between two molecules is an excitation spectrum. Here, the PL emission of the acceptor is tracked while the excitation energy is swept across the absorption spectra of the donor. Figure 6.7B depicts the excitation spectra of three (0.1 %, 0.8 % and 3.9 %) mixed-linker SURMOF structures measured by detecting emitted photons at 2.0 eV. To simplify comparison, the spectra are accompanied by an excitation spectrum of pristine Zn-DPP, as well as the absorption spectrum of Zn-ADB. In the range of 2.9 eV to 3.5 eV the excitation spectra of the doped samples follow the absorption spectrum of Zn-ADB in the range of 2.9 eV to 3.5 eV. Here, also the vibronic features of the Zn-ADB absorption spectrum are visible in the excitation spectra. Given that the excitation spectrum tracks the PL emission of the DPP linkers, these data clearly indicate the presence of energy transfer from ADB towards DPP.

In the range of 2.2 eV to 2.8 eV the excitation spectra of the three doped samples follow the excitation spectrum of the pristine Zn-DPP sample. In this spectral range, the DPP linkers are directly excited (compare also Figure 6.7A). Notably, such a direct excitation (at 2.6 eV) results in a significantly reduced emission intensity in comparison to an excitation via ADB (at 3.2 eV). For instance, the DPP emission is by a factor of 30 reduced when comparing direct with indirect excitation for the 0.1 % sample. This factor reduces to 13 and 8 for the 0.8 %

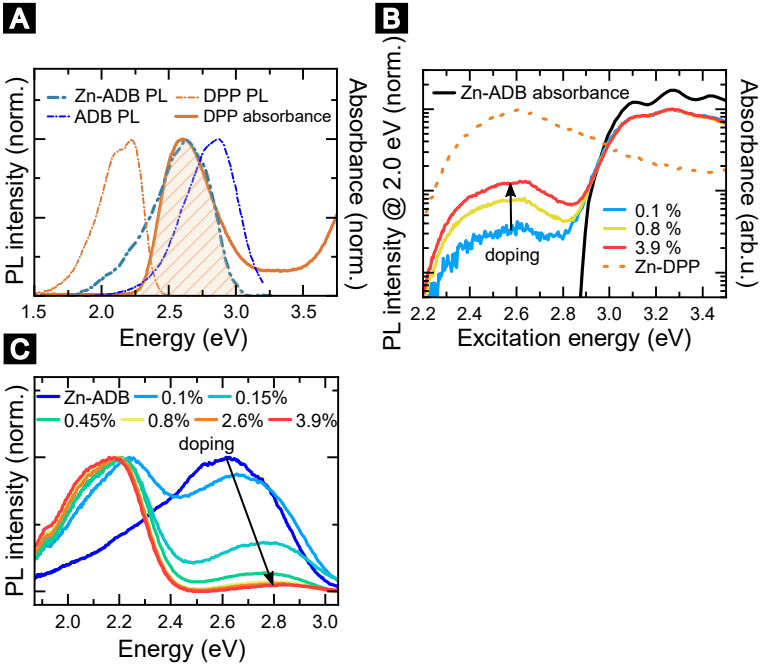

FIGURE 6.7: (A) PL spectra of ADB and DPP in ethanol (0.02 mol cm^{-3}) and Zn-ADB. These three PL spectra are accompanied by the absorption spectrum of DPP in ethanol. The spectral overlap of the absorption of DPP and the PL of Zn-ADB is shaded in orange. (B) Normalized excitation spectra of doped Zn-ADB and pristine Zn-DPP accompanied by the absorption spectrum of Zn-ADB. (C) Normalized PL spectra of Zn-ADB for different doping concentrations of DPP (excitation at 3.26 eV). Adapted with permission from Haldar *et al.* [61].

and 3.9 % sample, respectively. Especially the factor 30 of the 0.1 % doped sample, signifies the efficient transfer of energy from ADB to DPP.

In order to further characterize the energy transfer from ADB to DPP, the PL spectra of the doped Zn-ADB are compared to the one of pristine Zn-ADB. These spectra are shown in Figure 6.7C. Notably, with increasing doping concentration the PL of Zn-ADB is more and more quenched due to the energy transfer between both linkers. Additionally, spectral shifts of the PL of both ADB and DPP can be observed. The PL spectrum of ADB shifts hypsochromically from the pristine sample to the 3.9 % sample from 2.62 eV to 2.84 eV. In contrast, the PL peak of DPP shifts bathochromically from 2.24 eV to 2.18 eV. As will be further discussed in the next section, the bathochromic shift of the DPP PL spectrum can be connected to the aggregation of the DPP linker inside the SURMOF. The hypsochromic shift of the PL indicates increased quenching of the excimer in comparison to the monomer excited state. These data therefore signifies that both excited species of the Zn-ADB have to be considered to accurately describe the energy transfer between ADB and DPP inside the SURMOF.

6.2.2 Energy Transfer Efficiencies of Excimer and Excited Monomer State to DPP

As indicated at the end of the previous subsection, to fully understand the energy transfer between ADB and DPP inside the SURMOF the two distinct excited states of the Zn-ADB have to be considered. In Figure 6.10A the PL spectra of these two states are shown together with the absorption spectrum of DPP. The PL spectra of both states have a significant spectral overlap with the absorption of DPP. A FRET energy transfer of both states towards DPP can therefore be expected. In order to resolve from which state(s) the energy is migrating towards DPP, time-resolved PL measurements were utilized. Figure 6.8 compares the streak image of pristine Zn-ADB and a 0.1 % doped sample for the first 200 ps of emission. In the spectral range where the acceptor PL is dominating (1.9 eV to 2.2 eV), a slow rise in comparison to Zn-ADB is clearly visible. Taking this observation as a starting point, samples with different amounts of DPP doping were analyzed at different emission energies to determine the contribution of

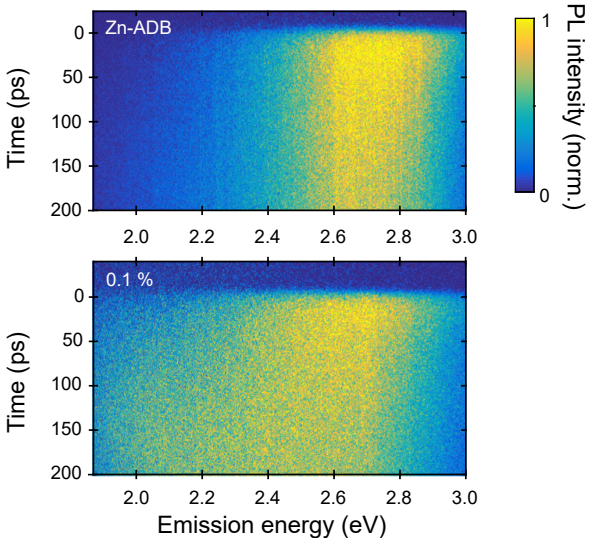

FIGURE 6.8: Two streak camera images of pristine Zn-ADB (A) and doped Zn-ADB with 0.1 % DPP (B). The samples were excited at 3.26 eV. Adapted with permission from Haldar *et al.* [61].

each of the two excited states to the energy transfer to DPP. For this purpose, the different transfer rates of the system were determined. An overview of these rates can be found in the excited state scheme in Figure 6.9.

In order to study the energy transfer between the monomer excited state and DPP, the rise time of the acceptor PL was determined at time scales below 250 ps. For this, the streak images were integrated in the range of 1.91 eV to 2.07 eV to yield PL transients reassembling mainly the PL of the acceptor. Figure 6.10C depicts the corresponding transients. The rise times of these PL kinetics were extracted using biexponential fits, with a rising and a decaying component (see Equation 6.2). By subtraction of the fluorescence decay rate k_{M} from the determined rise times, the transfer rate of the excited monomer to DPP $k_{\mathrm{MA}}^{\mathrm{T}}$ was extracted. With increasing quencher concentration (0 % to 3.9 %), the

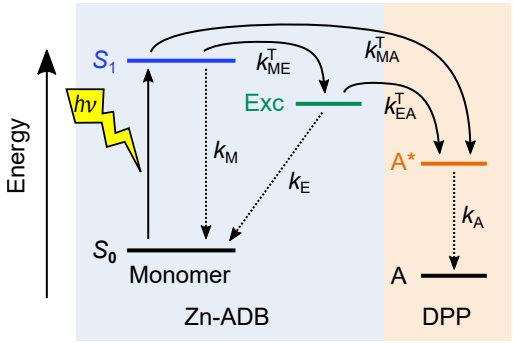

FIGURE 6.9: Scheme of the excited state dynamics of the mixed-linker donor-acceptor SURMOF-2 structures. Adapted with permission from Haldar *et al.* [61].

rise times shorten from 83 ps to 47 ps, indicating an increasing transfer rate $k^{\mathrm{T}}_{\mathrm{MA}}$ from the excited monomer to the acceptor.

The transfer rates $k^{\mathrm{T}}_{\mathrm{EA}}$ between the excimer and DPP were assessed using PL transients at 2.6 eV that were measured using a TCSPC setup. The transients were fitted by biexponential fits with the faster decay rate connected to the excited monomer state (above $0.8\,\mathrm{ns}^{-1}$) and the second slower decay rate connected to the excimer state. From the second decay rate, the transfer rate $k^{\mathrm{T}}_{\mathrm{EA}}$ was determined by subtracting k_{A}. A summary of all determined rates for the samples with different quencher concentrations can be found in Table 6.2.

Using the transfer rates between both states and DPP, the corresponding transfer efficiencies were determined using in case of the excimer (and in the same fashion for the excited monomer):

$$\eta_{\mathrm{T}} = \frac{k^{\mathrm{T}}_{\mathrm{EA}}}{k^{\mathrm{T}}_{\mathrm{EA}} + k_{\mathrm{E}}}. \tag{6.3}$$

The calculated transfer efficiencies are shown in Figure 6.10B. For the excited monomer, the transfer efficiencies increase to about 40 % and for the excimer state to about 73 % before reaching a plateau at a doping concentration of

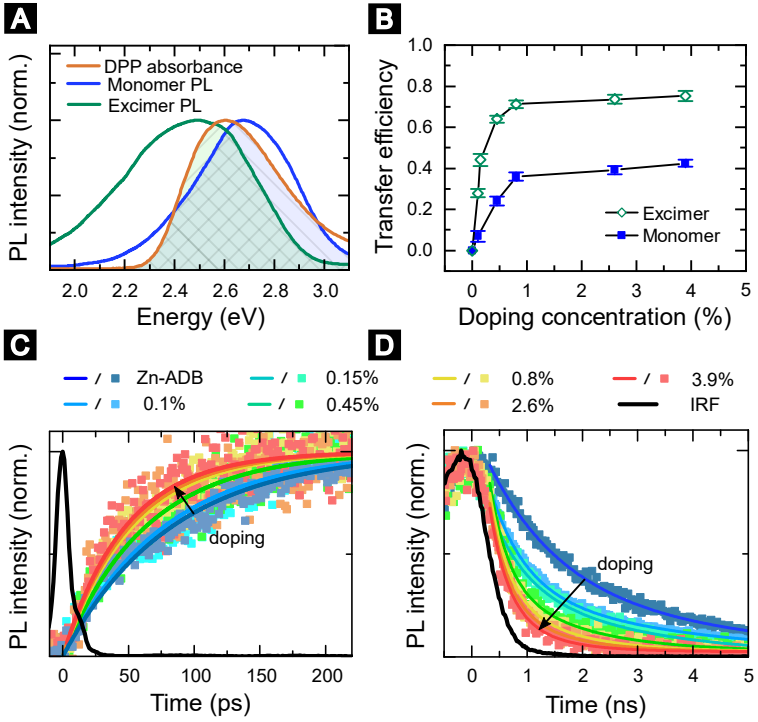

FIGURE 6.10: (A) PL spectra of the excimer and excited monomer (both acting as sensitizers) together with the absorption of the emitter DPP. The emission spectra were determined using a multivariate curve resolution fit as discussed in Section 6.1.2. The spectral overlap between the absorption of DPP and PL of the monomer and excimer is shaded in blue and green, respectively. (B) The efficiency of the excited states quenching as a function of DPP doping concentration. The quenching efficiencies for the monomer excimer state and excimer were calculated using the fits shown in (C) and (D), respectively. The error bars are determined by propagating the uncertainties of the fits. (C) PL rise of the DPP emission at 1.98 eV and (D) PL decay of the excimer at 2.6 eV for different DPP doping concentrations. The black lines represent the instrument response function (IRF). Adapted with permission from Haldar *et al.* [61].

TABLE 6.2: Extracted decay rates of the fits shown in Figure 6.5 (A) and (C). While $k_M + k_{MA}^T$ are extracted from the fits shown in Figure 6.5 (C), $k_E + k_{EA}^T$ are extracted using a biexponential reconvolution fit to the transient shown in Figure 6.5 (D).

	Monomer		Excimer	
	(measured)		(measured)	
DPP (%)	$k_M + k_{MA}^T$ (ns^{-1})	k_{MA}^T (ns^{-1})	$k_E + k_{EA}^T$ (ns^{-1})	k_{EA}^T (ns^{-1})
0	12.1	0	0.25	0
0.1	13.0	0.9	0.32	0.07
0.15			0.45	0.20
0.45	15.9	3.8	0.70	0.45
0.8	18.9	6.8	0.87	0.62
2.6	19.9	7.8	0.95	0.70
3.9	21.1	9.0	1.04	0.79

about 1 %. The higher quenching efficiencies of the excimer in comparison to the excited monomer align well with the already discussed blue shift of the steady-state PL with increasing doping concentration (see Figure 6.7C). That the quenching efficiencies reach a plateau for doping concentration above 1 % can be explained by a non-uniform distribution of DPP linkers for higher doping concentrations. In these cases, the DPP linkers tend to aggregate in the Zn-ADB SURMOF leading to an effectively reduced doping concentration. This DPP linker aggregation is supported by the redshift of the acceptor PL (see Figure 6.7C).

The plot of the quenching efficiencies (Figure 6.10B) demonstrates that both states are mobile inside the SURMOF and are feeding energy to the acceptor. However, before studying the diffusion lengths of both states the FRET energy

transfer is characterized in further detail by determining the FRET radii of both states for a transfer towards DPP.

6.2.3 FRET Radii of Excimer and Excited Monomer

In order to quantitatively describe the energy transfer from donor (ADB) to acceptor (DPP), the Förster radii for the monomer and excimer are estimated in the following. This constant quantifies the separation of donor and acceptor at which the transfer rate is equal to the photoluminescence decay rate (without quencher sites present). The FRET radius of each of the excited states was determined as described in Section 2.2.1. The experimental data required for these calculations have already been presented in the previous sections, but will be referred to again below to specify the procedure for determining the FRET radii. First of all, the PL spectra of the two states and the absorption spectrum of DPP shown in Figure 6.10A, are used together with the extinction coefficient of DPP ($34\,200\,\mathrm{l\,mol^{-1}\,cm^{-1}}$) [206], to calculate the overlap integrals Ω_M and Ω_E. These overlap integrals become $\Omega_\mathrm{M} = 1.1 \times 10^{-13}\,\mathrm{l\,mol^{-1}\,cm^3}$ and $\Omega_\mathrm{E} = 0.9 \times 10^{-13}\,\mathrm{l\,mol^{-1}\,cm^3}$ for the excited monomer and the excimer, respectively. Using a refractive index of $n = 1.39$ [207] and $f^2 = 0.6$ these overlap integrals translate to Förster radii of $8.4\eta_\mathrm{M}^{1/6}$nm and $8.1\eta_\mathrm{E}^{1/6}$nm for monomer and excimer, respectively. As a side note, the chosen value for the dipole orientation factor corresponds to a random distribution of dipoles, e.g., in solution. However, due to the low activation energy for the rotation of anthracene units around their bond axes (see Figure 6.3), this value was also used here. Furthermore, small deviations in the square of the dipole orientation factor have in principle a small impact on the determined FRET radius due to the power of 6 dependence.

For the last step in calculating the FRET radii, the PLQY values of the monomer η_M and excimer state η_E are required. For this purpose, the PLQY values were estimated using the following equation:

$$\eta_\mathrm{total} = \eta_\mathrm{M} + \eta_\mathrm{E}\eta_\mathrm{ME}^\mathrm{T}. \tag{6.4}$$

Here, η_total is the overall PLQY of Zn-ADB and $\eta_\mathrm{ME}^\mathrm{T}$ the transfer efficiency from excited monomer to excimer. The overall PLQY η_total was determined

to be 4.9 % using an integrating sphere and the method described in Section 3.2.2. In order to separate the contribution of excimer and excited monomer to η_{total}, a PL kinetic as well as the emission spectra of both states were employed. The required PL kinetic is extracted at 2.48 eV from the streak image with a time base of 10 ns (see Figure 6.5C), while as PL spectra those shown in Figure 6.5B are utilized. By fitting the kinetic with a biexponential fit and using the spectrally weighted amplitudes and PL lifetimes, the contribution of the excimer state to the overall photon emission was estimated to $\phi_{\text{E}} \approx 77\,\%$. The PLQY of the excimer η_{E} was then calculated using:

$$\eta_{\text{E}} = \frac{\eta_{\text{total}}\,\phi_{\text{E}}}{\eta_{\text{ME}}^{\text{T}}}. \tag{6.5}$$

With a transfer efficiency $\eta_{\text{ME}}^{\text{T}}$ of 50 % (see Section 6.1.2) the PLQY values become $\eta_{\text{E}} \approx 7.5\,\%$ and $\eta_{\text{M}} \approx 1.2\,\%$ for excimer and excited monomer, respectively. These PLQY values can now be utilized to determine the FRET radii of both states (for a FRET transfer towards DPP), which become 4.9 nm and 4.1 nm for excimer and excited monomer, respectively.

The estimated R_0 values are slightly higher then for most common organic donor acceptor systems, where R_0 usually lies in the range of 1 nm to 4 nm [38, 51]. However, also higher values have been demonstrated, e.g., 6.5 nm for polyfluorene copolymers [208], 7 nm for colloidal nanocrystal polymer host systems [209] or 5.4 nm for tetraphenylporphyrin-Doped Poly(9,9-dioctylfluorene) [210].

The determined FRET radii of both states are utilized in the following section to estimate the diffusion constants of both states.

6.3 Exciton Dynamics in Zn-ADB SURMOF

The expectation that exciton diffusion is not isotropic in the crystalline material was the basis for the selection of a set of quenching experiments that could unravel a possible anisotropy of exciton motion. As the first step, a SV analysis was carried out using a series of Zn-ADB films with different doping concentrations of DPP to determine the number of sites visited on average by each

exciton. The obtained findings were used as constants for simple Monte Carlo simulations, which allowed the estimation of the diffusion lengths for different motion scenarios of the excitons. In order to determine the correct motion scenario, quenching-layer experiments were carried out to extract the exciton diffusion lengths in the direction perpendicular to the film surface ([001]). In this way, it could be shown that the excimer state motion is reduced to motion between sheets (i.e., along [010]).

6.3.1 Stern-Volmer Analysis and Exciton Motion Scenarios

To determine the average number of jumps to individual linker sites that each exciton undertakes within its lifetime, a SV analysis was utilized. Here, the determined transfer rates of the monomer-related exciton and excimer (see Table 6.2B) are plotted in units of the unquenched fluorescence decay rate as a function of the quencher concentration. These two SV plots are depicted in Figure 6.11. The slopes of the two plots (i.e., the SV constants) are connected to the diffusion lengths via the Smoluchovski equation [39], while the inverses of the slopes state the concentration at which half of the excited states transfer to the acceptor (compare also Section 3.4). The SV constants of both states were determined to be $102\,\mathrm{nm}^3$ and $485\,\mathrm{nm}^3$ for monomer and excimer, respectively. Considering the packing of the ADB linkers inside the SURMOF ($0.69\,\mathrm{nm}^{-3}$) these values can be translated to average numbers of visited linkers per excitation [211]. This approximation is based on the following notion. The SV constant states the volume that can be attributed to each quencher when 50 % of the excitons reach a quenching site. Consequently, each exciton visits approximately a number of unique linker sites that correspond to half of this volume. Here, such an analysis neglects a final potentially long-range FRET transfer from donor to acceptor but provides a framework to qualitatively compare the excited state's motion. Within this treatment the excited monomer and the excimer visit within their lifetimes in average 35 and 167 unique hopping sites, respectively.

The average numbers of hopping sites were used as constants for MC simulations, where the simulation parameter was the relative change in intermolecular coupling for different lattice directions (*vide infra*). These changes in coupling lead to different motion scenarios, which are not meant to reproduce the photophysics of this system in full accuracy, but rather demonstrate how

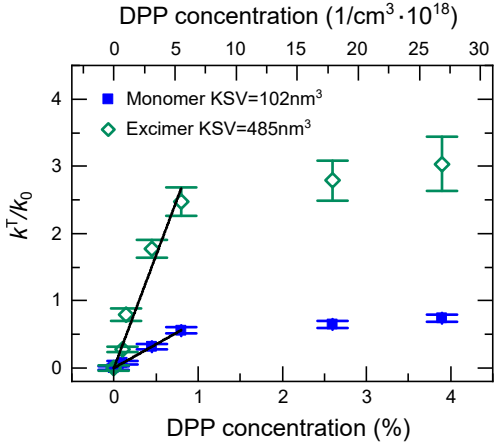

FIGURE 6.11: SV plot of the Zn-ADB doped with different concentrations of DPP. The plot is based on the transients shown in Figures 6.10 (C) and (D). The doping concentrations are stated in units of cm^{-3} (top x-axis) and in % (bottom x-axis). Adapted with permission from Haldar *et al.* [61].

an anisotropy of exciton diffusion impacts the effective diffusion length. The three simulated motion scenarios are: i) isotropic diffusion with transfer rates scaling as $1/l^2$ (where l is the separation of neighboring sites); ii) anisotropic diffusion-based on FRET (rates scaling with $1/r^6$); iii) 1D diffusion in [010] direction (vanishing transfer rates in [100] and [001] directions).

For the MC simulation, the molecules were placed on an isoenergetic tetragonal lattice with the lattice parameter corresponding to Zn-ADB. In the case of the isotropic diffusion simulations, only nearest neighbor hops were considered. For the simulations based on FRET transfer and 1D motion, a cut-off radius of 2.5 nm was selected. The rates between molecules were scaled as such that the averaged number of visited sites within the lifetime of the monomer and excimer was 35 and 167, respectively.

Figure 6.12 summarizes the MC simulation results of the three motion scenarios for the excited monomer and excimer. Here, the diffusion lengths determined for different lattice directions (based on the average of 10000 simulations) are

stated alongside a possible trajectory of the corresponding motion scenario. In Figure 6.12A, the trajectory of the excimer is shown for the case of an isotropic diffusion constant. Such a motion scenario results in a RMS displacement of 4 nm and 7 nm for the excited monomer and excimer, respectively. In Figure 6.12B, the trajectory of the excimer is shown for FRET-based transport (without considering the orientation factor of the coupling dipoles). The orientation factor κ changes its value from 4 for a collinear arrangement over 1 for a parallel arrangement to 0 in case the inner product of the dipole moments is zero. However, including κ in the simulations would have only a small effect on the determined diffusion lengths, since the rates between movement between and along sheets already differ by a factor of about 3000. In case of FRET-based transfer, the diffusion lengths along [010] are 13 nm and 29 nm, while in [100] and [001] only 1 nm and 3 nm for excited monomer and excimer, respectively. In the last scenario, shown in Figure 6.12C, the case of pure 1D diffusion is considered, resulting in diffusion lengths of 11 nm and 49 nm for monomer and excimer, respectively.

The expectation regarding the motion scenarios is that the excited monomer will follow the FRET transfer motion scenario, possibly with small deviations due to the small distance in the [010] direction and the possible breakdown of the point-dipole approximation, leading to further increased coupling in [010] direction. For the excimer, 1D diffusion is expected since a FRET-type motion is not possible due to the vanishing absorption cross-section of this state. Consequently, the transfer must be based on Dexter type coupling which should be strongly suppressed in [100] and [001] due to the big (2.2 nm) inter-molecular distances in these directions.

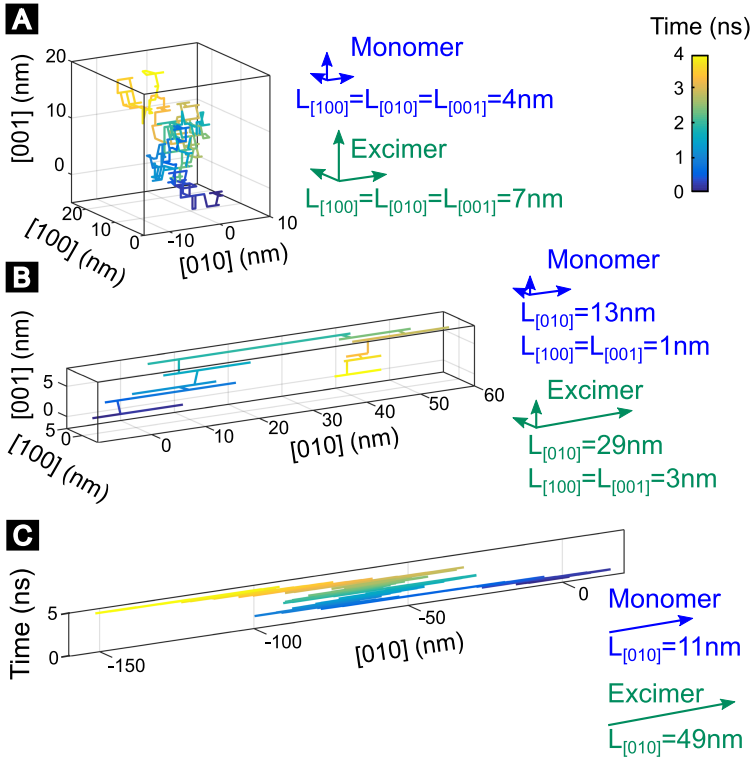

FIGURE 6.12: Summary of the Monte Carlo simulations of the excimer and excited monomer. Based on the SV analysis the number of unique visited linker sites is estimated to 35 for the monomer for the excimer to 167. Depending on the motion scenario of the excitons this translates to different effective diffusion lengths inside the SURMOF. (A) isotropic 3D diffusion, (B) anisotropic 3D diffusion rates scaling as $1/r^6$ with hopping distance in the tetragonal lattice, and (C) 1D diffusion in which only energy transfer in [010] is considered. Adapted with permission from Haldar *et al.* [61].

6.3.2 Anisotropic Motion of Excimer State

In order to determine which of the in the previous section presented motion scenario is closest to reality, a bilayer quenching experiment was designed to probe the exciton diffusion length in [100] direction. However, in the cause of the measurement, it turned out, that this approach was not accurate enough to differentiate the small differences in the diffusion lengths in [001] direction for the monomer excited state (for the three motion scenarios those are 0 nm, 1 nm and 4 nm). Hence, the focus of this section will lie on analyzing the different motion scenarios for the excimer state.

The bilayer quenching experiments were based on a sample series of two stacked layers: a spray-coated quenching layer of doped Zn-ADB with 2.6 % DPP and a pristine Zn-ADB layer deposited on top with varying thickness d. The choice of a doped instead of a pure Zn-DPP film was made to circumvent any aggregation-induced effects of the acceptor DPP, as well as to keep acceptor diffusion into the Zn-ADB layer at a minimum. Six different layer thicknesses d were spray-coated on top of the quenching layer.

The quenching efficiencies of the excimer were determined by measuring the quenched PL lifetimes using a TCSPC setup. The PL spectra of the samples were collected at 2.75 eV, where both excimer and monomer are emitting. To separate the PL components of monomer and excimer a biexponential reconvolution fit was used to determine the lifetimes of monomer and excimer state. Figure 6.13 shows the measured data accompanied by the biexponential fits. The extracted lifetimes and amplitudes are summarized in Table 6.3. Please note that the monomer lifetime is partially restricted by the IRF of the TCSPC setup.

The quenching efficiency Q_{E} of the excimer PL was calculated according to

$$Q_{\mathrm{E}} = 1 - k_{\mathrm{E}}/(k_{\mathrm{E}} + k_{\mathrm{EA}}^{\mathrm{T}}), \tag{6.6}$$

with the quenched excimer PL decay rate $k_{\mathrm{E}} + k_{\mathrm{EA}}^{\mathrm{T}}$ and the PL rate of a pristine film k_{E}. To further analyze the determined quenching efficiencies of the samples with different d, two possible quenching scenarios had to be differentiated: i) exciton generation in the pristine top layer and subsequent transfer to the bottom layer followed by quenching by an acceptor; ii) exciton generation in the mixed bottom quenching layer followed by quenching at an acceptor. In

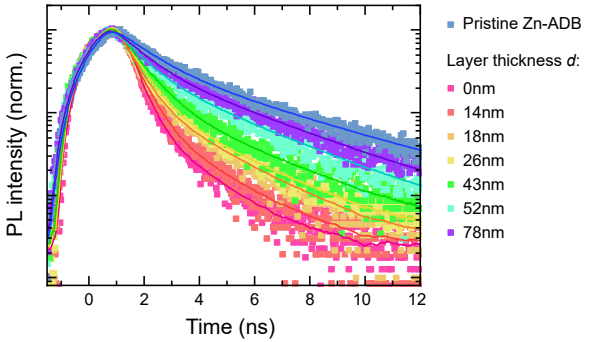

FIGURE 6.13: PL transients of the donor excitons at 2.75 eV for various thicknesses of the donor layer on top of the 2.6 % doped Zn-ADB layer. Each transient is accompanied by a biexponential reconvolution fit. Adapted with permission from Haldar *et al.* [61].

order to separate these two contributions to the overall quenching efficiency of the excimer, the following equation was used:

$$Q_{\text{total}} = f_{\text{B}} Q_{\text{B}} + (1 - f_{\text{B}}) \eta_{\text{T}\to\text{B}} Q_{\text{B}}, \tag{6.7}$$

with the fraction of the bottom layer thickness in comparison to the total film thickness f_{B}, the quenching efficiency of the bottom layer Q_{B} and the transfer efficiency of excitons from the top to the bottom layer $\eta_{\text{T}\to\text{B}}$.

To model the transfer efficiency $\eta_{\text{T}\to\text{B}}$ of the excimer and to extract the diffusion length in [100] direction a one-dimensional diffusion formula was used, assuming no gradient of the exciton density in planes parallel to the surface (for all samples under study, the absorption length was much bigger than the layer thickness) [212]:

$$\frac{\partial n(x,t)}{\partial t} = D \frac{\partial n(x,t)^2}{\partial x^2} - \frac{n(x,t)}{\tau} - k_F n(x,t) + G(x,t). \tag{6.8}$$

Here, n(x,t) is the exciton density perpendicular to the donor-acceptor interface, and G(x,t) the exciton generation rate at position x and time t. The first term

TABLE 6.3: Extracted decay rates of the fits shown in Figure 6.5 (A) and (C). While $k_M + k_{MA}^T$ are extracted from the fits shown in Figure 6.5 (C), $k_E + k_{EA}^T$ are extracted using a biexponential reconvolution fit to the transient shown in Figure 6.5 (D).

	Monomer		Excimer
d (nm)	$k_M + k_{MA}^T$ (ns^{-1})	Amplitude %	$k_E + k_{EA}^T$ (ns^{-1})
0	2.87	0.99	0.69
16	1.97	0.97	0.54
25	1.58	0.96	0.46
30	1.40	0.94	0.41
50	1.19	0.91	0.35
60	1.11	0.83	0.32
90	1.03	0.79	0.30
Zn-ADB	0.86	0.78	0.24

on the right governs the diffusion of excitons with a Diffusion constant D, the second term the monomolecular decay of excitons with decay rate $1/\tau$, the third quenching at an acceptor, and the last term the generation of excitons by the laser. The quenching process is assumed to be based on long-range FRET with a rate of k_F given by:

$$k_F = \frac{\pi}{6} c_A \tau R_0^6 x^3, \tag{6.9}$$

where c_A is the acceptor density and R_0 the FRET radius.

At the donor-acceptor interface instantaneous quenching of excitons while at the air film interface reflection and no quenching of excitons is assumed. These

two boundary conditions are included in the equations by requiring:

$$n(x=0) \stackrel{!}{=} 0, \tag{6.10a}$$

$$\frac{\partial n(x=d)}{\partial x} \stackrel{!}{=} 0, \tag{6.10b}$$

accounting for the quenching and non-quenching interface, respectively. The 1D-continuity equation was solved numerically for different FRET radii R_0, diffusion constants D, and layer thicknesses d, to find the best fit to the measured quenching efficiency of the excimer PL. Figure 6.14A depicts the experimentally determined quenching efficiencies together with the theoretically predicted curves. The experimental data quickly drop from 68 % to 20 % for layer thicknesses in the range of 0 nm to 78 nm. The theoretical curves are plotted in case of no exciton diffusion along [001] as a yellow surface for FRET radii in the range of 4.5 nm to 5.5 nm. These solutions align well with the measured data and are also in accordance with the estimated FRET radius of 4.9 nm for the excimer (see Section 6.2.3). In contrast, the simulations of an isotropic diffusion length of 7 nm for FRET radii in the range of 4.5 nm to 5.5 nm are not consistent with the experimental data (see green surface in Figure 6.14A).

Thus, the comparison between theory and the experimental data indicates that the excimer diffuses preferentially along the stacking direction of the anthracene chromophores, i.e., in [010] direction (compare Figure 6.14B). Considering the results of Section 6.1, this 1D diffusion of the excimer state can be associated with enhanced electronic coupling between the stacked anthracene chromophores, which promotes a delocalization of the electronic excitation along [010] direction. Based on the simple MC simulations in Section 6.3.1, 1D diffusion length of 49 nm would apply. However, this analysis neglected that the last long-range FRET hop towards the acceptor will in most cases not be along the preferred 1D direction of the exciton motion inside pristine Zn-ADB. Therefore, the real diffusion length will be somewhat lower, and more refined theoretical calculations are needed to verify this finding.

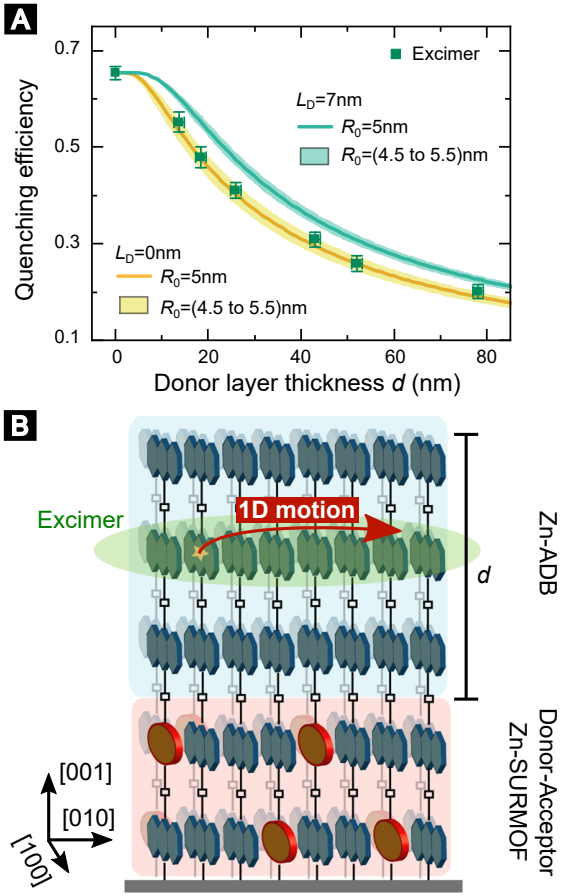

FIGURE 6.14: (A) Schematic illustration of the bilayer structure and the anisotropic energy transfer path of the excimer. (B) Quenching efficiencies extracted from the biexponential fits to the PL transients shown in Figure 6.13 as a function of donor layer thickness d. The error bars are determined by propagating the uncertainties of the biexponential fits. The experimental data is accompanied by solutions to Equation 6.8 for two different motion scenarios (isotropic and 1D diffusion).

6.4 Conclusion

In this chapter, the presence of two excited singlet states in the Zn-ADB SURMOF were established, an excited state localized to single anthracene chromophores and a delocalized excimer-like state. The two states can be distinguished by their different PL lifetimes and energies. The excimer-like state is attributed to the rotational freedom of the anthracene units and the subsequent change in the coupling of adjacent molecules. Furthermore, it was demonstrated that both states are mobile and can efficiently transfer energy to a FRET acceptor that is incorporated inside the SURMOF. By correlating a bulk quenching and a bilayer quenching experiment it could be shown that the energy transfer of the excimer state is largely restricted in the crystallographic [010] direction. Basic theoretical considerations suggest that the 1D motion of the excimer state has a diffusion length of about 49 nm. Even though this diffusion length might be somewhat overestimated due to the last long-range FRET hop towards DPP, this is an exciting finding in light that the excimer states' absorption cross-section is essentially zero and therefore its transport is not based on dipole-dipole interactions, i.e., FRET-based hopping. Consequently, the exciton transport of the excimer state has to rely solely on wavefunction overlap between adjacent chromophores (Dexter-type transport). In this context, it would therefore be interesting to examine whether the motion of the excimer is (partly) due to coherent transport. Suggestions on how such experiments could look like will be given in the following chapter.

7

Conclusion and Outlook

This thesis investigated the unique exciton transport properties of organic TADF emitters as well as of an anthracene-based SURMOF. These studies were targeted at three specific application areas. These are photonic-markers, organic light-emitting diodes, as well as photovoltaics. In the following, the most important results in each of these areas are discussed and an outlook is given.

7.1 Towards Background-Free Photonic Markers

TADF emitters are not only interesting to study in the context of an OLED, but also for applications as photonic markers. The long fluorescence lifetime in the microsecond range allows detection of the emission without capturing the background fluorescence of other chromophores in the sample. However, to increase the value of TADF emitters as photonic markers, high external quantum yields are desired, which TADF molecules usually do not possess due to the CT nature of their absorption band. In order to tackle this issue, a modified 4CzIPN molecule (acting as TADF emitter) was conjugated with oligo(phenylene ethynylene) (OPE) of various lengths (acting as light-harvesting antennae). As anticipated, the antennae transferred virtually all energy to the lower-lying singlet state on the TADF core of the molecule. However, an unfortunate finding was that for longer antennae, which are desired for higher absorption cross-sections, the delayed fluorescence was turned off. Interestingly, this turn-off was attributed to a decrease in the RISC rate and not to a transfer of the triplet state from the TADF core to the lower-lying triplet state on the OPE. Here, on the one hand, the most likely explanation for this decrease in the RISC rate is a suppression of the vibronic modes responsible for the coupling between LE and CT states. On the other hand, the restricted triplet transfer from TADF core to oligomer is most likely a consequence of a reduced LUMO-LUMO overlap between both constituents. This latter aspect was verified by triplet motion studies between 4CzIPN emitters as laid out in the next section. The finding that the TADF emission is not quenched by the presence of the lower-lying triplet state on the oligomer is certainly encouraging for further research in this direction.

Outlook

In light of current research showing that strong vibronic coupling between singlet and triplet states is essential for efficient RISC in organic TADF molecules, several guidelines can be followed for further work in the direction of TADF based photonic markers. For 4CzIPN in particular, the dynamic torsional rocking of the donor groups surrounding the acceptor group seem

to be important vibronic modes to couple localized and CT states [31]. This efficient coupling is in turn an important prerequisite for efficient RISC [31]. For this reason, it would be interesting to find out if this mode is somewhat suppressed, e.g., due to steric hindrance, once an OPE is attached to 4CzIPN. To this end, Raman spectroscopy could be employed in order to compare the magnitude and energetic position of the torsional rocking mode of D and A units about the N-C bond. Here, an energetic shift with respect to the typical position (31 meV) or a lower intensity could substantiate the claim that this molecular vibration is suppressed once the OPE is attached [36]. Along these lines, time-dependent DFT calculations that go beyond the Born-Oppenheimer approximation are a promising tool for judicious selection of well-matched TADF-antenna pairs. In these simulations, it could be verified that the vibronic modes that are essential for efficient RISC stay active, once both components are merged, while modes that promote non-radiative transitions remain suppressed. In conclusion, although this research needs to be further progressed in order to obtain powerful TADF-based markers, compliance with the above-mentioned guidelines promises a rapid achievement of this goal in the future.

In parallel to the investigations on TADF-based photonic markers, systems based on rare-earth coordination polymers were investigated as possible alternatives in the course of this work [213] (see Appendix **??** for submitted version of this manuscript). Even though the actual discussion of these compounds is beyond the scope of this thesis, a short outlook of this work for background-free photonic markers is given as a comparison to TADF based markers. Figure 7.1 depicts the investigated compound that is composed of rare-earth metal centers and carboxylated 4,4'-diphenyl-2,2'-bipyridine ligands. In contrast to the also investigated anthracene-based SURMOF, here, no long-range order is present and the metal centers primarily serve the purpose of suppressing molecular vibrations as well as increasing spin-orbit coupling (SOC). This suppression of molecular vibrations together with increased SOC leads to long-lived phosphorescence of the organic ligands ($\tau = 76\,\mathrm{ms}$) at room temperature. Compared to standard TADF emitters, this lifetime is about three orders of magnitudes longer and would allow for convenient detection of the photonic marker's PL kinetic through simple camera systems, e.g., from a smartphone [213, 214]. Furthermore, next to the orange phosphorescence in the millisecond range, the studied coordination polymer exhibits blue fluorescence in the nanosecond and

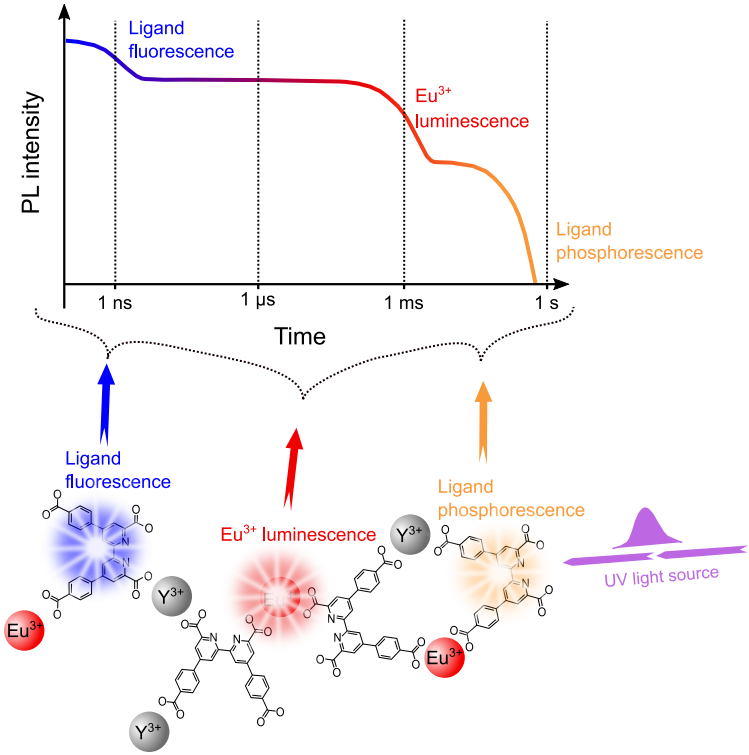

FIGURE 7.1: Background-free photonic marker based on rare-earth coordination polymer with persistent luminescence. From Jakoby *et al.* [213].

red europium emission in the microsecond range. These three emission bands with lifetimes in the nanosecond, microsecond, and millisecond ranges make this coordination polymer a unique photonic marker of interest, for example in the context of advanced anti-counterfeiting tags [215]. However, a challenge that still needs to be addressed is the rather low PLQY of the ligands' emission (1 %). A suitable starting point to tackle this issue is to decrease the high degree of energetic disorder caused by the varying local environments for individual ligands (and rare-earth ions) of this rather amorphous compound. Designing metal-organic frameworks with defined structures and similar ligands would therefore be a promising route to increase the low PLQY of the ligands in the future.

7.2 Towards Hyperfluorescence OLEDs

In a hyperfluorescence OLED, the matrix forming the active layer is codoped with fluorescence emitters and TADF molecules. Here, the TADF molecules serve the purpose of converting generated triplet excitons to singlet excitons and sensitizing the fluorescence acceptor once being in a singlet excited state. However, in order to suppress electron-hole recombination on fluorescence acceptors, where 75 % of the recombination events would lead to dark triplet states, the doping concentration of the fluorescence acceptors has to be kept low in comparison to TADF molecules. Consequently, excitons formed on TADF molecules have to be efficiently funneled to the F-dopants while being in a singlet state. Two promising design strategies can be employed to achieve the selective harvest of singlet excitons by the F-dopants. The first approach involves sterically protected emitters that selectively suppress short-range Dexter transfer of triplet electrons. The second approach, as established in this thesis, is to rely on TADF molecules with restricted triplet exciton diffusion. This approach is particularly promising since some TADF molecules inherently suppress triplet motion due to their molecular design, that is, a restricted LUMO-LUMO overlap between adjacent molecules. Such restricted triplet motion, as found in TADF molecules like 4CzIPN or 4TCzBN, is an important result of this thesis. These findings are based on a method developed in this work to accurately determine the singlet and triplet exciton diffusion lengths of organic

TADF molecules. Considering that this method is based only on standard experimental data, it could be of broad use for the TADF OLED community in order to obtain accurate parameters that allow physical modeling of device performance. Consequently, this might be an important step towards optimized hyperfluorescence devices that can provide color-pure OLEDs with reduced efficiency roll-off at high driving voltages.

Outlook

This thesis focused on the experimental investigation of TADF molecules in which the central acceptor unit is surrounded by four electron-donating building blocks (e.g., 4CzIPN), as well as on a planar molecule where both LUMO and HOMO are sterically unprotected (DiKTa). However, in both cases, triplet motion was suppressed. In the first case due to a sterically protected LUMO, while in the second case due to a high dispersion in the host matrix to prevent aggregation. In the future, it would be interesting to investigate triplet motion of TADF molecules beyond these two limiting cases. Figure 7.2 shows three examples of organic TADF molecules that would be worth studying to extend the results of this thesis to other TADF molecule structures. Above all, these are the frequently used butterfly-shaped D-A-D TADF molecules [216], as well as molecules comprised only of one donor and acceptor unit [217]. In addition, Hall and coworkers recently synthesized Mes_3DiKTa, a modified version of DiKTa in which three orthogonal mesityl groups inhibit aggregation-induced quenching up to a doping concentration of 30 wt%. Here, it would be interesting to investigate if triplet motion at high doping concentrations is turned on, or if the steric protection by the mesityl groups also prevents triplet motion.

Besides those rather fundamental studies of TADF molecules, future work should utilize the gained insights on exciton motion to design real hyperfluorescence devices. Here, as a first step, it would be interesting to verify the simulated results, where negligible triplet diffusion was a key in obtaining high efficiencies, on a real hyperfluorescence active layer. In such a study, for example a set of TADF molecules that exhibit a changing ratio of singlet and triplet diffusion lengths could be employed in conjunction with suitable fluorescence acceptors. However, critical for a correct correlation between triplet motion and harvesting efficiency would be a careful consideration of the changing singlet diffusion

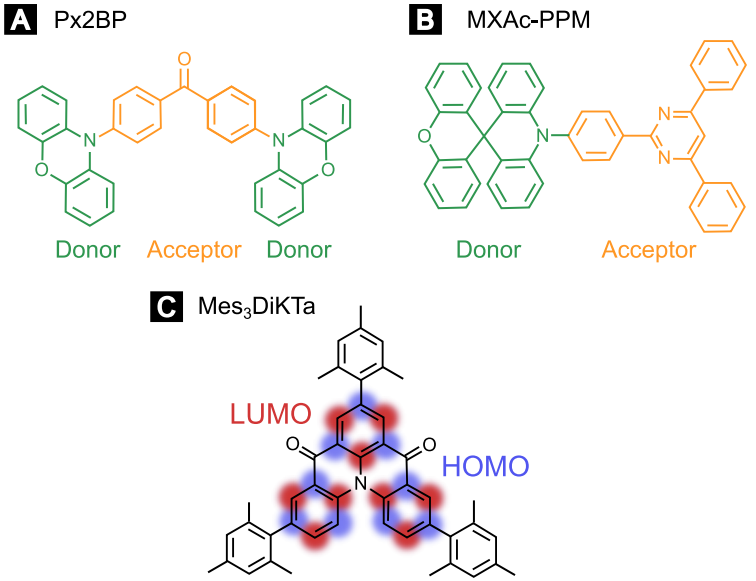

FIGURE 7.2: TADF molecules with different structural motifs, whose comparison would be interesting within a future triplet motion study of TADF molecules. These structures include butterfly shaped D-A-D molecules (A) [216], simple D-A molecules (B) [217] and sterically protected TADF molecules based on electron resonance effects [137].

lengths, as well as of the FRET radii between different donor-acceptor pairs. A promising alternative approach could therefore be, to stick to a single TADF molecule that exhibits appreciable triplet motion at high doping concentration and study the harvesting efficiency as a function of TADF doping concentration. It might then be possible, to correlate the optimum TADF doping concentration to the onset of triplet motion. Subsequent to such studies on the active layer of hyperfluorescence devices, the ultimate goal should be to further verify the results on real electronically pumped devices. This is especially important due to the changing ratio in the initial singlet and triplet populations. Consequently, it can be expected that detrimental processes induced by triplet motion are more significant in an electrically pumped device.

7.3 Towards SURMOF-Based Solar Cells

Efficient solar cells that are based on a planar device structure require an exciton diffusion length that exceeds the absorption length of the active layer. While this goal is easily met in silicon-based solar cells, it remains a long-standing objective for organic photovoltaics. In the typically amorphous organic active layers, absorption length are usually in the range of 100 nm to 1000 nm and exciton diffusion lengths are $\ll 20$ nm. However, since the exciton diffusion length often exceeds the absorption length in molecular single crystals, crystalline chromophore assemblies (such as SURMOFs) are very interesting to study in this context.

In this thesis, the singlet exciton motion in a Zn-ADB SURMOF was investigated. In this hybrid compound, organic ADB linkers and Zn-based metal centers form 2D sheets that are stacked perpendicular to the substrate with an inter-sheet distance of 0.6 nm. The porosity of the SURMOFs allows the anthracene chromophores to rotate around the bond axis that the linker forms with the two metal centers, thereby further reducing the inter-chromophore spacing. In the equilibrium position, this distance is 0.42 nm, which is still slightly large for strong inter-molecular coupling that could promote an extended wavefunction. In accordance, after excitation, a localized monomer excited state is formed which emits at a center wavelength of about 440 nm. However, within the first 80 ps subsequent to excitation, 50 % of the excited

monomers relax into a lower-lying excimer state with PL emission centered around 480 nm. The excimer formation is attributed to a rotated equilibrium position of the chromophores once being in an excited state, leading to a decreased inter-chromophore distance accompanied by stronger coupling between chromophores. Based on the available energy (stokes shift between monomer and excimer emission) in conjunction with force-field simulations, the new equilibrium position exhibits an inter-chromophore distance of only 0.34 nm, which is suitable for excimer formation. Furthermore, an exciton diffusion study reveals that the excimer motion is restricted to the [010] direction (stacking direction of the sheets), which also signifies the increased inter-chromophore coupling in the stacking direction. A first estimation of the 1D diffusion length, where the last long-range FRET hop towards the acceptor is neglected, leads to a value of about 49 nm for the excimer state. For the monomer excited state, the small diffusion length perpendicular to the substrate independent of the underlying motion scenario prevented detection of anisotropic diffusion. However, the tetragonal unit cell of the SURMOF makes a FRET-based scenario most likely in which the monomer diffuses about 13 nm in [010] direction and about 1 nm in [100] and [001] directions.

The finding of the long diffusion length of the excimer is particularly interesting since it has a vanishing absorption cross-section and thus the underlying diffusion mechanism cannot be based on dipole-dipole (FRET) interactions. Consequently, the excimer motion is either based on incoherent Dexter type transfer or could also be (partially) coherent in nature as indicated by the significant energetic relaxation from monomer to excimer state. Efficient singlet transfer that does not rely on FRET is a promising finding for further investigations in this regard. Here, the limit of the singlet exciton diffusion length of 230 nm applicable to incoherent FRET-based hopping can be exceeded [24].

Outlook

Additional work in the direction of exciton motion in Zn-ADB should further investigate the transfer mechanism of the excimer state, as well as verify its diffusion length based on a different methodology. For the first point, it would be instructive to measure the anisotropy of the excimer's motion using polarization-dependent TA measurements. This would be a promising approach

in determining the dephasing time of the excimer state, which could give an indication if the excimer's motion is partially coherent. Along this line, a low-temperature study of the diffusion length of the excimer would be an interesting path to investigate whether the dephasing is mainly caused by scattering on phonons. For the second point, a fluence-dependent study of the PL kinetics might enable the extraction of an excimer-excimer annihilation coefficient, which, in turn, allows the determination of the excimer's diffusion length. Alternatively, quenching experiments based on CT quencher could increase the accuracy of the determined diffusion lengths of both monomer and excimer states. Here, for example HATCN could be doped inside the pores of the Zn-ADB for SV-type quenching experiments. Alternatively, an indium tin oxide (ITO) quenching layer could be used as a substrate on which the SURMOF is grown for different film thicknesses. Since in this case, no FRET transfer of the excitons to the quenching layer is possible, the accuracy of the determined diffusion length could be increased compared to the one determined in this work. Beyond such studies that may improve the accuracy in determining the diffusion length, it would be important to investigate the morphology of the film in further detail. Along this line, Adams *et al.* demonstrated in a palladium-porphyrin-based SURMOF-2 that is structural equivalent and prepared in the same fashion as Zn-ADB, that crystal grains are only about 100 nm in diameter [23]. Further, he and his coworker showed that the triplet diffusion length could theoretically reach several micrometers, but the exciton's motion in the real film was restricted to single crystal grains. Similarly, the bottleneck for the diffusion length of the excimer in Zn-ADB could also be the small grain sizes.

Ultimately, to exploit long singlet diffusion lengths in a SURMOF based device, also the direction of preferential exciton motion must be controlled. In the studied Zn-ADB SURMOF this preferential exciton motion aligns with the stacking direction of the chromophores and thus lies in a direction parallel to the substrate. However, to be beneficial for a device, this preferential direction of exciton motion would have to be perpendicular to the substrate. A promising route to change the direction of exciton motion inside SURMOF-2 structures would be to rely on pillar-type SURMOFs similar to the one presented by Gordillo *et al.* [218], or So *et al.* [219]. Here, the pillar linkers are employed to act as spacers between the 1D sheets, thereby enabling a rotated assembly of the SURMOF. Since the distance between the 2D layers can then be controlled by

the length of the pillar linkers, this approach provides additional capability to fine-tune the coupling between the chromophores and thus the exciton motion within the SURMOF.

References

[1] R. Croce and H. van Amerongen, "Natural strategies for photosynthetic light harvesting," *Nat. Chem. Biol.*, vol. 10, no. 7, pp. 492–501, 2014.

[2] G. D. Scholes, G. R. Fleming, A. Olaya-Castro, and R. van Grondelle, "Lessons from nature about solar light harvesting," *Nat. Chem.*, vol. 3, no. 10, pp. 763–774, 2011.

[3] J. M. Anna, G. D. Scholes, and R. van Grondelle, "A Little Coherence in Photosynthetic Light Harvesting," *Bioscience*, vol. 64, no. 1, pp. 14–25, 2013.

[4] I. Szabó, E. Bergantino, and G. M. Giacometti, "Light and oxygenic photosynthesis: energy dissipation as a protection mechanism against photo-oxidation," *EMBO Rep.*, vol. 6, no. 7, pp. 629–634, 2005.

[5] J. F. Allen and J. Forsberg, "Molecular recognition in thylakoid structure and function," *Trends Plant Sci.*, vol. 6, no. 7, pp. 317 – 326, 2001.

[6] J. Ye, K. Sun, Y. Zhao, Y. Yu, C. Kong Lee, and J. Cao, "Excitonic energy transfer in light-harvesting complexes in purple bacteria," *J. Chem. Phys.*, vol. 136, no. 24, 245104, 2012.

[7] T. Mirkovic, E. E. Ostroumov, J. M. Anna, R. van Grondelle, Govindjee, and G. D. Scholes, "Light Absorption and Energy Transfer in the Antenna Complexes of Photosynthetic Organisms," *Chem. Rev.*, vol. 117, no. 2, pp. 249–293, 2017.

[8] I. Oda, K. Hirata, S. Watanabe, Y. Shibata, T. Kajino, Y. Fukushima, S. Iwai, and S. Itoh, "Function of Membrane Protein in Silica Nanopores: Incorporation of Photosynthetic Light-Harvesting Protein LH2 into FSM," *J. Phys. Chem. B*, vol. 110, no. 3, pp. 1114–1120, 2006.

[9] X. Hu, A. Damjanović, T. Ritz, and K. Schulten, "Architecture and mechanism of the light-harvesting apparatus of purple bacteria," *Proc. Natl. Acad. Sci. U.S.A.*, vol. 95, no. 11, pp. 5935–5941, 1998.

[10] V. Sundström, T. Pullerits, and R. van Grondelle, "Photosynthetic Light-Harvesting: Reconciling Dynamics and Structure of Purple Bacterial LH2 Reveals Function of Photosynthetic Unit," *J. Phys. Chem. B*, vol. 103, no. 13, pp. 2327–2346, 1999.

[11] Bernanose, André, Comte, Marcel, and Vouaux, Paul, "Sur un nouveau mode d'émission lumineuse chez certains composés organiques," *J. Chim. Phys.*, vol. 50, pp. 64–68, 1953.

[12] D. Kearns and M. Calvin, "Photovoltaic Effect and Photoconductivity in Laminated Organic Systems," *J. Chem. Phys.*, vol. 29, no. 4, pp. 950–951, 1958.

[13] M. Koden, *History of OLEDs*. John Wiley & Sons, Ltd, 2016, ch. 1, pp. 1–11.

[14] C. W. Tang, "Two-layer organic photovoltaic cell," *Appl. Phys. Lett.*, vol. 48, no. 2, pp. 183–185, 1986.

[15] G. Yu, J. Gao, J. C. Hummelen, F. Wudl, and A. J. Heeger, "Polymer Photovoltaic Cells: Enhanced Efficiencies via a Network of Internal Donor-Acceptor Heterojunctions," *Science*, vol. 270, no. 5243, pp. 1789–1791, 1995.

[16] S. Liu, J. Yuan, W. Deng, M. Luo, Y. Xie, Q. Liang, Y. Zou, Z. He, H. Wu, and Y. Cao, "High-efficiency organic solar cells with low non-radiative recombination loss and low energetic disorder," *Nat. Photonics*, vol. 14, no. 5, pp. 300–305, 2020.

[17] L. Meng, Y. Zhang, X. Wan, C. Li, X. Zhang, Y. Wang, X. Ke, Z. Xiao, L. Ding, R. Xia, H.-L. Yip, Y. Cao, and Y. Chen, "Organic and solution-processed tandem solar cells with 17.3% efficiency," *Science*, vol. 361, no. 6407, pp. 1094–1098, 2018.

[18] National Renewable Energy Laboratory (NREL), "Best Research-Cell Efficiency Chart". URL: https://www.nrel.gov/pv/cell-efficiency.html (accessed November 20, 2020).

[19] M. Scharber and N. Sariciftci, "Efficiency of bulk-heterojunction organic solar cells," *Prog. Polym. Sci.*, vol. 38, no. 12, pp. 1929 – 1940, 2013, topical issue on Conductive Polymers.

[20] A. Polman, M. Knight, E. C. Garnett, B. Ehrler, and W. C. Sinke, "Photovoltaic materials: Present efficiencies and future challenges," *Science*, vol. 352, no. 6283, 2016.

[21] Q. Burlingame, C. Coburn, X. Che, A. Panda, Y. Qu, and S. R. Forrest, "Centimetre-scale electron diffusion in photoactive organic heterostructures," *Nature*, vol. 554, no. 7690, pp. 77–80, 2018.

[22] D. Venkateshvaran, M. Nikolka, A. Sadhanala, V. Lemaur, M. Zelazny, M. Kepa, M. Hurhangee, A. J. Kronemeijer, V. Pecunia, I. Nasrallah, I. Romanov, K. Broch, I. McCulloch, D. Emin, Y. Olivier, J. Cornil, D. Beljonne, and H. Sirringhaus, "Approaching disorder-free transport in high-mobility conjugated polymers," *Nature*, vol. 515, no. 7527, pp. 384–388, 2014.

[23] M. Adams, M. Kozlowska, N. Baroni, M. Oldenburg, R. Ma, D. Busko, A. Turshatov, G. Emandi, M. O. Senge, R. Haldar, C. Wöll, G. U. Nienhaus, B. S. Richards, and I. A. Howard, "Highly Efficient One-Dimensional Triplet Exciton Transport in a Palladium–Porphyrin-Based Surface-Anchored Metal–Organic Framework," *ACS Appl. Mater. Interfaces*, vol. 11, no. 17, pp. 15 688–15 697, 2019.

[24] S. R. Yost, E. Hontz, S. Yeganeh, and T. Van Voorhis, "Triplet vs Singlet Energy Transfer in Organic Semiconductors: The Tortoise and the Hare," *J. Phys. Chem. C*, vol. 116, no. 33, pp. 17 369–17 377, 2012.

[25] S. Wu, Z. Li, M.-Q. Li, Y. Diao, F. Lin, T. Liu, J. Zhang, P. Tieu, W. Gao, F. Qi, X. Pan, Z. Xu, Z. Zhu, and A. K.-Y. Jen, "2D metal–organic framework for stable perovskite solar cells with minimized lead leakage," *Nat. Nanotechnol.*, vol. 15, no. 11, pp. 934–940, 2020.

[26] C. W. Tang and S. A. VanSlyke, "Organic electroluminescent diodes," *Appl. Phys. Lett.*, vol. 51, no. 12, pp. 913–915, 1987.

[27] M. Koden, *OLED displays and lighting*. Chichester, UK Hoboken, NJ: John Wiley & Sons, 2016.

[28] M. A. Baldo, D. F. O'Brien, Y. You, A. Shoustikov, S. Sibley, M. E. Thompson, and S. R. Forrest, "Highly efficient phosphorescent emission from organic electroluminescent devices," *Nature*, vol. 395, no. 6698, pp. 151–154, 1998.

[29] C. Adachi, M. A. Baldo, M. E. Thompson, and S. R. Forrest, "Nearly 100% internal phosphorescence efficiency in an organic light-emitting device," *J. Appl. Phys.*, vol. 90, no. 10, pp. 5048–5051, 2001.

[30] G. Zhou, W.-Y. Wong, and X. Yang, "New Design Tactics in OLEDs Using Functionalized 2-Phenylpyridine-Type Cyclometalates of Iridium(III) and Platinum(II)," *Asian J. Chem.*, vol. 6, no. 7, pp. 1706–1727, 2011.

[31] J. Gibson, A. P. Monkman, and T. J. Penfold, "The Importance of Vibronic Coupling for Efficient Reverse Intersystem Crossing in Thermally Activated Delayed Fluorescence Molecules," *ChemPhysChem*, vol. 17, no. 19, pp. 2956–2961, 2016.

[32] S. Schmidbauer, A. Hohenleutner, and B. König, "Chemical Degradation in Organic Light-Emitting Devices: Mechanisms and Implications for the Design of New Materials," *Adv. Mater.*, vol. 25, no. 15, pp. 2114–2129, 2013.

[33] Q. Zhang, D. Tsang, H. Kuwabara, Y. Hatae, B. Li, T. Takahashi, S. Y. Lee, T. Yasuda, and C. Adachi, "Nearly 100% Internal Quantum Efficiency in Undoped Electroluminescent Devices Employing Pure Organic Emitters," *Adv. Mater.*, vol. 27, no. 12, pp. 2096–2100, 2015.

[34] T.-A. Lin, T. Chatterjee, W.-L. Tsai, W.-K. Lee, M.-J. Wu, M. Jiao, K.-C. Pan, C.-L. Yi, C.-L. Chung, K.-T. Wong, and C.-C. Wu, "Sky-Blue Organic Light Emitting Diode with 37% External Quantum Efficiency Using Thermally Activated Delayed Fluorescence from Spiroacridine-Triazine Hybrid," *Adv. Mater.*, vol. 28, no. 32, pp. 6976–6983, 2016.

[35] I. Lee and J. Y. Lee, "Molecular design of deep blue fluorescent emitters with 20% external quantum efficiency and narrow emission spectrum," *Org. Electron.*, vol. 29, pp. 160 – 164, 2016.

[36] H. Yersin, *Highly efficient OLEDs: Materials based on thermally activated delayed fluorescence*. Wiley-VCH, 2018.

[37] H. Nakanotani, T. Higuchi, T. Furukawa, K. Masui, K. Morimoto, M. Numata, H. Tanaka, Y. Sagara, T. Yasuda, and C. Adachi, "High-efficiency organic light-emitting diodes with fluorescent emitters," *Nat. Commun.*, vol. 5, 2014.

[38] A. Köhler and H. Bässler, *Electronic Processes in Organic Semiconductors - An Introduction*. New York: John Wiley & Sons, 2015.

[39] J. R. Lakowicz, *Principles of Fluorescence Spectroscopy*. Berlin Heidelberg: Springer Science & Business Media, 2007.

[40] P. W. Atkins and R. S. Friedman, *Molecular Quantum Mechanics*. New York, London: OUP Oxford, 2011.

[41] F. Gerson and W. Huber, *Physical Fundamentals of Electron Spin Resonances*. John Wiley & Sons, Ltd, 2004, ch. 1, pp. 3–9.

[42] S. McGlynn, T. Azumi, and M. Kinoshita, *Molecular Spectroscopy of the Triplet State*. Prentice-Hall, Englewood Cliffs, NJ., 1969.

[43] M. Kasha, H. R. Rawls, and M. A. El-Bayoumi, "The exciton model in molecular spectroscopy," *Pure and Applied Chemistry*, vol. 11, no. 3-4, pp. 371 – 392, 01 Jan. 1965.

[44] J. Gierschner and S. Y. Park, "Luminescent distyrylbenzenes: tailoring molecular structure and crystalline morphology," *J. Mater. Chem. C*, vol. 1, pp. 5818–5832, 2013.

[45] J. R. Tischler, M. S. Bradley, V. Bulović, J. H. Song, and A. Nurmikko, "Strong Coupling in a Microcavity LED," *Phys. Rev. Lett.*, vol. 95, 036401, 2005.

[46] Z. Zhao, S. Chen, J. W. Y. Lam, Z. Wang, P. Lu, F. Mahtab, H. H. Y. Sung, I. D. Williams, Y. Ma, H. S. Kwok, and B. Z. Tang, "Pyrene-substituted ethenes: aggregation-enhanced excimer emission and highly efficient electroluminescence," *J. Mater. Chem.*, vol. 21, pp. 7210–7216, 2011.

[47] A. Zitzler-Kunkel, M. R. Lenze, K. Meerholz, and F. Würthner, "Enhanced photocurrent generation by folding-driven H-aggregate formation," *Chem. Sci.*, vol. 4, pp. 2071–2075, 2013.

[48] N. J. Hestand and F. C. Spano, "Molecular Aggregate Photophysics beyond the Kasha Model: Novel Design Principles for Organic Materials," *Acc. Chem. Res.*, vol. 50, no. 2, pp. 341–350, 2017.

[49] J. Tsurumi, H. Matsui, T. Kubo, R. Häusermann, C. Mitsui, T. Okamoto, S. Watanabe, and J. Takeya, "Coexistence of ultra-long spin relaxation time and coherent charge transport in organic single-crystal semiconductors," *Nat. Phys.*, vol. 13, no. 10, pp. 994–998, 2017.

[50] T. Förster, "Zwischenmolekulare Energiewanderung und Fluoreszenz," *Ann Phys*, vol. 437, no. 1-2, pp. 55–75, 1948.

[51] U. Lemmer, A. Ochse, M. Deussen, R. Mahrt, E. Göbel, H. Bassler, P. Haring Bolivar, G. Wegmann, and H. Kurz, "Energy transfer in molecularly doped conjugated polymers," *Synth. Met.*, vol. 78, no. 3, pp. 289 – 293, 1996.

[52] G. D. Scholes, "Long-Range Resonance Energy Transfer in Molecular Systems," *Annu. Rev. Phys. Chem.*, vol. 54, no. 1, pp. 57–87, 2003.

[53] Y. Kawamura, J. Brooks, J. J. Brown, H. Sasabe, and C. Adachi, "Intermolecular Interaction and a Concentration-Quenching Mechanism of Phosphorescent Ir(III) Complexes in a Solid Film," *Phys. Rev. Lett.*, vol. 96, 017404, 2006.

[54] D. L. Dexter, "A Theory of Sensitized Luminescence in Solids," *J. Chem. Phys.*, vol. 21, no. 5, pp. 836–850, 1953.

[55] K. Feron, X. Zhou, W. J. Belcher, and P. C. Dastoor, "Exciton transport in organic semiconductors: Förster resonance energy transfer compared with a simple random walk," *J. Appl. Phys.*, vol. 111, no. 4, 044510, 2012.

[56] M. Jakoby, B. S. Richards, U. Lemmer, and I. A. Howard, "Investigations of singlet and triplet diffusion in thermally activated delayed-fluorescence emitters: Implications for hyperfluorescence," *Phys. Rev. B*, vol. 100, 045303, 2019.

[57] R. Metzler and J. Klafter, "The random walk's guide to anomalous diffusion: a fractional dynamics approach," *Phys. Rep.*, vol. 339, no. 1, pp. 1 – 77, 2000.

[58] S. M. Vlaming, V. A. Malyshev, A. Eisfeld, and J. Knoester, "Subdiffusive exciton motion in systems with heavy-tailed disorder," *J. Chem. Phys.*, vol. 138, no. 21, 214316, 2013.

[59] O. V. Mikhnenko, H. Azimi, M. Scharber, M. Morana, P. W. M. Blom, and M. A. Loi, "Exciton diffusion length in narrow bandgap polymers," *Energy Environ. Sci.*, vol. 5, pp. 6960–6965, 2012.

[60] R. R. Lunt, N. C. Giebink, A. A. Belak, J. B. Benziger, and S. R. Forrest, "Exciton diffusion lengths of organic semiconductor thin films measured by spectrally resolved photoluminescence quenching," *J. Appl. Phys.*, vol. 105, no. 5, 053711, 2009.

[61] R. Haldar, M. Jakoby, A. Mazel, Q. Zhang, A. Welle, T. Mohamed, P. Krolla, W. Wenzel, S. Diring, F. Odobel, B. S. Richards, I. A. Howard, and C. Wöll, "Anisotropic energy transfer in crystalline chromophore assemblies," *Nat. Commun.*, vol. 9, no. 1, 4332, 2018.

[62] J. R. Caram, S. Doria, D. M. Eisele, F. S. Freyria, T. S. Sinclair, P. Rebentrost, S. Lloyd, and M. G. Bawendi, "Room-Temperature Micron-Scale Exciton Migration in a Stabilized Emissive Molecular Aggregate," *Nano Lett.*, vol. 16, no. 11, pp. 6808–6815, 2016.

[63] A. T. Haedler, K. Kreger, A. Issac, B. Wittmann, M. Kivala, N. Hammer, J. Köhler, H.-W. Schmidt, and R. Hildner, "Long-range energy transport

in single supramolecular nanofibres at room temperature," *Nature*, vol. 523, no. 7559, pp. 196–199, 2015.

[64] Y. Wan, A. Stradomska, J. Knoester, and L. Huang, "Direct Imaging of Exciton Transport in Tubular Porphyrin Aggregates by Ultrafast Microscopy," *J. Am. Chem. Soc.*, vol. 139, no. 21, pp. 7287–7293, 2017.

[65] O. V. Mikhnenko, P. W. M. Blom, and T.-Q. Nguyen, "Exciton diffusion in organic semiconductors," *Energy Environ. Sci.*, vol. 8, pp. 1867–1888, 2015.

[66] P. Irkhin and I. Biaggio, "Direct Imaging of Anisotropic Exciton Diffusion and Triplet Diffusion Length in Rubrene Single Crystals," *Phys. Rev. Lett.*, vol. 107, 017402, 2011.

[67] M. Samiullah, D. Moghe, U. Scherf, and S. Guha, "Diffusion length of triplet excitons in organic semiconductors," *Phys. Rev. B*, vol. 82, 205211, 2010.

[68] J. Park, M. Xu, F. Li, and H.-C. Zhou, "3D Long-Range Triplet Migration in a Water-Stable Metal–Organic Framework for Upconversion-Based Ultralow-Power in Vivo Imaging," *J. Am. Chem. Soc.*, vol. 140, no. 16, pp. 5493–5499, 2018.

[69] A. Bruno, L. X. Reynolds, C. Dyer-Smith, J. Nelson, and S. A. Haque, "Determining the Exciton Diffusion Length in a Polyfluorene from Ultrafast Fluorescence Measurements of Polymer/Fullerene Blend Films," *J. Phys. Chem. C*, vol. 117, no. 39, pp. 19 832–19 838, 2013.

[70] G. J. Hedley, A. J. Ward, A. Alekseev, C. T. Howells, E. R. Martins, L. A. Serrano, G. Cooke, A. Ruseckas, and I. D. W. Samuel, "Determining the optimum morphology in high-performance polymer-fullerene organic photovoltaic cells," *Nat. Commun.*, vol. 4, no. 1, 2867, 2013.

[71] W. A. Luhman and R. J. Holmes, "Investigation of Energy Transfer in Organic Photovoltaic Cells and Impact on Exciton Diffusion Length Measurements," *Adv. Funct. Mater.*, vol. 21, no. 4, pp. 764–771, 2011.

[72] O. V. Mikhnenko, F. Cordella, A. B. Sieval, J. C. Hummelen, P. W. M. Blom, and M. A. Loi, "Temperature Dependence of Exciton Diffusion in

Conjugated Polymers," *J. Phys. Chem. B*, vol. 112, no. 37, pp. 11 601–11 604, 2008.

[73] A. Suna, "Kinematics of Exciton-Exciton Annihilation in Molecular Crystals," *Phys. Rev. B*, vol. 1, pp. 1716–1739, 1970.

[74] A. D. Poletayev, J. Clark, M. W. B. Wilson, A. Rao, Y. Makino, S. Hotta, and R. H. Friend, "Triplet Dynamics in Pentacene Crystals: Applications to Fission-Sensitized Photovoltaics," *Adv. Mater.*, vol. 26, no. 6, pp. 919–924, 2014.

[75] J. E. Kroeze, T. J. Savenije, M. J. W. Vermeulen, and J. M. Warman, "Contactless Determination of the Photoconductivity Action Spectrum, Exciton Diffusion Length, and Charge Separation Efficiency in Polythiophene-Sensitized TiO2 Bilayers," *J. Phys. Chem. B*, vol. 107, no. 31, pp. 7696–7705, 2003.

[76] P. Peumans, A. Yakimov, and S. R. Forrest, "Small molecular weight organic thin-film photodetectors and solar cells," *J. Appl. Phys.*, vol. 93, no. 7, pp. 3693–3723, 2003.

[77] P. Avakian and R. E. Merrifield, "Experimental Determination of the Diffusion Length of Triplet Excitons in Anthracene Crystals," *Phys. Rev. Lett.*, vol. 13, pp. 541–543, 1964.

[78] O. Ostroverkhova, *Handbook of Organic Materials for Optical and (Opto)Electronic Devices - Properties and Applications*. Amsterdam: Elsevier, 2013.

[79] M. A. Baldo, D. F. O'Brien, M. E. Thompson, and S. R. Forrest, "Excitonic singlet-triplet ratio in a semiconducting organic thin film," *Phys. Rev. B*, vol. 60, pp. 14 422–14 428, 1999.

[80] P. L. dos Santos, M. K. Etherington, and A. P. Monkman, "Chemical and conformational control of the energy gaps involved in the thermally activated delayed fluorescence mechanism," *J. Mater. Chem. C*, vol. 6, pp. 4842–4853, 2018.

[81] Y. Luo and H. Aziz, "Correlation Between Triplet–Triplet Annihilation and Electroluminescence Efficiency in Doped Fluorescent Organic Light-Emitting Devices," *Adv. Funct. Mater.*, vol. 20, no. 8, pp. 1285–1293, 2010.

[82] S. Reindl and A. Penzkofer, "Higher excited-state triplet-singlet intersystem crossing of some organic dyes," *Chem. Phys.*, vol. 211, no. 1, pp. 431 – 439, 1996.

[83] H. Yersin, *Triplet Emitters for OLED Applications. Mechanisms of Exciton Trapping and Control of Emission Properties*. Berlin, Heidelberg: Springer Berlin Heidelberg, 2004, pp. 1–26.

[84] M. Baldo, S. Forrest, and M. Thompson, *Organic electroluminescence*, Z. H. Kafafi, Ed. CRC Press, 2005.

[85] W. Song and J. Y. Lee, "Degradation Mechanism and Lifetime Improvement Strategy for Blue Phosphorescent Organic Light-Emitting Diodes," *Adv. Opt. Mater.*, vol. 5, no. 9, 1600901, 2017.

[86] S. Kim, H. J. Bae, S. Park, W. Kim, J. Kim, J. S. Kim, Y. Jung, S. Sul, S.-G. Ihn, C. Noh, S. Kim, and Y. You, "Degradation of blue–phosphorescent organic light–emitting devices involves exciton-induced generation of polaron pair within emitting layers," *Nat. Commun.*, vol. 9, no. 1, 1211, 2018.

[87] K. Goushi, R. Kwong, J. J. Brown, H. Sasabe, and C. Adachi, "Triplet exciton confinement and unconfinement by adjacent hole-transport layers," *J. Appl. Phys.*, vol. 95, no. 12, pp. 7798–7802, 2004.

[88] V. Sivasubramaniam, F. Brodkorb, S. Hanning, H. P. Loebl, V. van Elsbergen, H. Boerner, U. Scherf, and M. Kreyenschmidt, "Investigation of FIrpic in PhOLEDs via LC/MS technique," *Cent. Eur. J. Chem.*, vol. 7, no. 4, 836, 2009.

[89] F. B. Dias, T. J. Penfold, and A. P. Monkman, "Photophysics of thermally activated delayed fluorescence molecules," *Methods Appl. Fluoresc.*, vol. 5, no. 1, 012001, 2017.

[90] H. Uoyama, K. Goushi, K. Shizu, H. Nomura, and C. Adachi, "Highly efficient organic light-emitting diodes from delayed fluorescence," *Nature*, vol. 492, no. 7428, pp. 234–238, 2012.

[91] F. B. Dias, K. N. Bourdakos, V. Jankus, K. C. Moss, K. T. Kamtekar, V. Bhalla, J. Santos, M. R. Bryce, and A. P. Monkman, "Triplet Harvesting with 100% Efficiency by Way of Thermally Activated Delayed Fluorescence in Charge Transfer OLED Emitters," *Adv. Mater.*, vol. 25, no. 27, pp. 3707–3714, 2013.

[92] W. Zeng, H.-Y. Lai, W.-K. Lee, M. Jiao, Y.-J. Shiu, C. Zhong, S. Gong, T. Zhou, G. Xie, M. Sarma, K.-T. Wong, C.-C. Wu, and C. Yang, "Achieving Nearly 30% External Quantum Efficiency for Orange–Red Organic Light Emitting Diodes by Employing Thermally Activated Delayed Fluorescence Emitters Composed of 1,8-Naphthalimide-Acridine Hybrids," *Adv. Mater.*, vol. 30, no. 5, p. 1704961, 2018.

[93] B. S. Kim and J. Y. Lee, "Engineering of Mixed Host for High External Quantum Efficiency above 25% in Green Thermally Activated Delayed Fluorescence Device," *Adv. Funct. Mater.*, vol. 24, no. 25, pp. 3970–3977, 2014.

[94] T.-A. Lin, T. Chatterjee, W.-L. Tsai, W.-K. Lee, M.-J. Wu, M. Jiao, K.-C. Pan, C.-L. Yi, C.-L. Chung, K.-T. Wong, and C.-C. Wu, "Sky-Blue Organic Light Emitting Diode with 37% External Quantum Efficiency Using Thermally Activated Delayed Fluorescence from Spiroacridine-Triazine Hybrid," *Adv. Mater.*, vol. 28, no. 32, pp. 6976–6983, 2016.

[95] Perrin, Francis, "La fluorescence des solutions - Induction moléculaire. - Polarisation et durée d'émission. - Photochimie," *Ann. Phys.*, vol. 10, no. 12, pp. 169–275, 1929.

[96] C. Parker and C. Hatchard, "Triplet-singlet emission in fluid solutions. Phosphorescence of eosin," *J. Chem. Soc. Faraday Trans.*, vol. 57, pp. 1894–1904, 1961.

[97] A. Endo, M. Ogasawara, A. Takahashi, D. Yokoyama, Y. Kato, and C. Adachi, "Thermally Activated Delayed Fluorescence from Sn^{4+}−Porphyrin Complexes and Their Application to Organic Light

Emitting Diodes – A Novel Mechanism for Electroluminescence," *Adv. Mater.*, vol. 21, no. 47, pp. 4802–4806, 2009.

[98] G. U. Mahoro, J. Fernandez-Cestau, J.-L. Renaud, P. B. Coto, R. D. Costa, and S. Gaillard, "Recent Advances in Solid-State Lighting Devices Using Transition Metal Complexes Exhibiting Thermally Activated Delayed Fluorescent Emission Mechanism," *Adv. Opt. Mater.*, vol. 8, no. 16, 2000260, 2020.

[99] M. Y. Wong and E. Zysman-Colman, "Purely Organic Thermally Activated Delayed Fluorescence Materials for Organic Light-Emitting Diodes," *Adv. Mater.*, vol. 29, no. 22, 1605444, 2017.

[100] M. Sarma and K.-T. Wong, "Exciplex: An Intermolecular Charge-Transfer Approach for TADF," *ACS Appl. Mater. Interfaces*, vol. 10, no. 23, pp. 19 279–19 304, 2018.

[101] D. Graves, V. Jankus, F. B. Dias, and A. Monkman, "Photophysical Investigation of the Thermally Activated Delayed Emission from Films of m-MTDATA:PBD Exciplex," *Adv. Funct. Mater.*, vol. 24, no. 16, pp. 2343–2351, 2014.

[102] V. Jankus, C.-J. Chiang, F. Dias, and A. P. Monkman, "Deep Blue Exciplex Organic Light-Emitting Diodes with Enhanced Efficiency; P-type or E-type Triplet Conversion to Singlet Excitons?" *Adv. Mater.*, vol. 25, no. 10, pp. 1455–1459, 2013.

[103] P. L. dos Santos, F. B. Dias, and A. P. Monkman, "Investigation of the Mechanisms Giving Rise to TADF in Exciplex States," *J. Phys. Chem. C*, vol. 120, no. 32, pp. 18 259–18 267, 2016.

[104] M. J. Leitl, D. M. Zink, A. Schinabeck, T. Baumann, D. Volz, and H. Yersin, "Copper(I) Complexes for Thermally Activated Delayed Fluorescence: From Photophysical to Device Properties," *Top Curr Chem*, vol. 374, no. 3, 25, 2016.

[105] T. J. Penfold, F. B. Dias, and A. P. Monkman, "The theory of thermally activated delayed fluorescence for organic light emitting diodes," *Chem. Commun.*, vol. 54, pp. 3926–3935, 2018.

[106] C. M. Marian, "Spin–orbit coupling and intersystem crossing in molecules," *Wiley Interdiscip. Rev. Comput. Mol. Sci.*, vol. 2, no. 2, pp. 187–203, 2012.

[107] M. A. El-Sayed, "Spin—Orbit Coupling and the Radiationless Processes in Nitrogen Heterocyclics," *J. Chem. Phys.*, vol. 38, no. 12, pp. 2834–2838, 1963.

[108] B. T. Lim, S. Okajima, A. Chandra, and E. Lim, "Radiationless transitions in electron donor-acceptor complexes: selection rules for S1 $\rightarrow$ T intersystem crossing and efficiency of S1 $\rightarrow$ S0 internal conversion," *Chem. Phys. Lett.*, vol. 79, no. 1, pp. 22 – 27, 1981.

[109] P. Data, P. Pander, M. Okazaki, Y. Takeda, S. Minakata, and A. P. Monkman, "Dibenzo[a,j]phenazine-Cored Donor–Acceptor–Donor Compounds as Green-to-Red/NIR Thermally Activated Delayed Fluorescence Organic Light Emitters," *Angew. Chem. Int. Ed.*, vol. 55, no. 19, pp. 5739–5744, 2016.

[110] M. K. Etherington, J. Gibson, H. F. Higginbotham, T. J. Penfold, and A. P. Monkman, "Revealing the spin–vibronic coupling mechanism of thermally activated delayed fluorescence," *Nat. Commun.*, vol. 7, 13680, 2016.

[111] P. L. dos Santos, J. S. Ward, M. R. Bryce, and A. P. Monkman, "Using Guest–Host Interactions To Optimize the Efficiency of TADF OLEDs," *J. Phys. Chem. Lett.*, vol. 7, no. 17, pp. 3341–3346, 2016.

[112] F. B. Dias, J. Santos, D. R. Graves, P. Data, R. S. Nobuyasu, M. A. Fox, A. S. Batsanov, T. Palmeira, M. N. Berberan-Santos, M. R. Bryce, and A. P. Monkman, "The Role of Local Triplet Excited States and D-A Relative Orientation in Thermally Activated Delayed Fluorescence: Photophysics and Devices," *Adv. Sci.*, vol. 3, no. 12, 1600080, 2016.

[113] K. Masui, H. Nakanotani, and C. Adachi, "Analysis of exciton annihilation in high-efficiency sky-blue organic light-emitting diodes with thermally activated delayed fluorescence," *Org. Electron.*, vol. 14, no. 11, pp. 2721 – 2726, 2013.

[114] M. A. Baldo, C. Adachi, and S. R. Forrest, "Transient analysis of organic electrophosphorescence. II. Transient analysis of triplet-triplet annihilation," *Phys. Rev. B*, vol. 62, pp. 10 967–10 977, 2000.

[115] W. Song, T. Kim, J. Y. Lee, Y. Lee, and H. Jeong, "Investigation of degradation mechanism of phosphorescent and thermally activated delayed fluorescent organic light-emitting diodes through doping concentration dependence of lifetime," *J Ind Eng Chem*, vol. 68, pp. 350 – 354, 2018.

[116] S. R. Forrest, "Excitons and the lifetime of organic semiconductor devices," *Philos. Trans. Royal Soc. A*, vol. 373, no. 2044, 20140320, 2015.

[117] T. Furukawa, H. Nakanotani, M. Inoue, and C. Adachi, "Dual enhancement of electroluminescence efficiency and operational stability by rapid upconversion of triplet excitons in OLEDs," *Sci. Rep.*, vol. 5, no. 1, 8429, 2015.

[118] H. Abroshan, Y. Zhang, X. Zhang, C. Fuentes-Hernandez, S. Barlow, V. Coropceanu, S. R. Marder, B. Kippelen, and J.-L. Brédas, "Thermally Activated Delayed Fluorescence Sensitization for Highly Efficient Blue Fluorescent Emitters," *Adv. Funct. Mater.*, vol. 30, no. 52, 2005898, 2020.

[119] S. K. Jeon, H.-J. Park, and J. Y. Lee, "Highly Efficient Soluble Blue Delayed Fluorescent and Hyperfluorescent Organic Light-Emitting Diodes by Host Engineering," *ACS Appl. Mater. Interfaces*, vol. 10, no. 6, pp. 5700–5705, 2018.

[120] C.-Y. Chan, L.-S. Cui, J. U. Kim, H. Nakanotani, and C. Adachi, "Rational Molecular Design for Deep-Blue Thermally Activated Delayed Fluorescence Emitters," *Adv. Funct. Mater.*, vol. 28, no. 11, 1706023, 2018.

[121] J. Yu, Y. Cui, H. Xu, Y. Yang, Z. Wang, B. Chen, and G. Qian, "Confinement of pyridinium hemicyanine dye within an anionic metal-organic framework for two-photon-pumped lasing," *Nat. Commun.*, vol. 4, no. 1, 2719, 2013.

[122] I. Stassen, N. Burtch, A. Talin, P. Falcaro, M. Allendorf, and R. Ameloot, "An updated roadmap for the integration of metal–organic frameworks

with electronic devices and chemical sensors," *Chem. Soc. Rev.*, vol. 46, pp. 3185–3241, 2017.

[123] M. Yoon, R. Srirambalaji, and K. Kim, "Homochiral Metal–Organic Frameworks for Asymmetric Heterogeneous Catalysis," *Chem. Rev.*, vol. 112, no. 2, pp. 1196–1231, 2012.

[124] O. M. Yaghi, G. Li, and H. Li, "Selective binding and removal of guests in a microporous metal–organic framework," *Nature*, vol. 378, no. 6558, pp. 703–706, 1995.

[125] Y. Cui, Y. Yue, G. Qian, and B. Chen, "Luminescent Functional Metal–Organic Frameworks," *Chem. Rev.*, vol. 112, no. 2, pp. 1126–1162, 2012.

[126] P. Horcajada, T. Chalati, C. Serre, B. Gillet, C. Sebrie, T. Baati, J. F. Eubank, D. Heurtaux, P. Clayette, C. Kreuz, J.-S. Chang, Y. K. Hwang, V. Marsaud, P.-N. Bories, L. Cynober, S. Gil, G. Férey, P. Couvreur, and R. Gref, "Porous metal–organic-framework nanoscale carriers as a potential platform for drug delivery and imaging," *Nat. Mater.*, vol. 9, no. 2, pp. 172–178, 2010.

[127] A. Li, R. Bueno-Perez, S. Wiggin, and D. Fairen-Jimenez, "Enabling efficient exploration of metal–organic frameworks in the Cambridge Structural Database," *CrystEngComm*, vol. 22, pp. 7152–7161, 2020.

[128] H. Ghasempour, K.-Y. Wang, J. A. Powell, F. ZareKarizi, X.-L. Lv, A. Morsali, and H.-C. Zhou, "Metal–organic frameworks based on multicarboxylate linkers," *Coord. Chem. Rev.*, vol. 426, 213542, 2021.

[129] J. Liu and C. Wöll, "Surface-supported metal–organic framework thin films: fabrication methods, applications, and challenges," *Chem. Soc. Rev.*, vol. 46, pp. 5730–5770, 2017.

[130] J. Liu, B. Lukose, O. Shekhah, H. K. Arslan, P. Weidler, H. Gliemann, S. Bräse, S. Grosjean, A. Godt, X. Feng, K. Müllen, I.-B. Magdau, T. Heine, and C. Wöll, "A novel series of isoreticular metal organic frameworks: realizing metastable structures by liquid phase epitaxy," *Sci. Rep.*, vol. 2, no. 1, 921, 2012.

[131] S. Hermes, F. Schröder, R. Chelmowski, C. Wöll, and R. A. Fischer, "Selective Nucleation and Growth of Metal–Organic Open Framework Thin Films on Patterned COOH/CF3–Terminated Self–Assembled Monolayers on Au(111)," *J. Am. Chem. Soc.*, vol. 127, no. 40, pp. 13 744–13 745, 2005.

[132] Y.-H. Xiao, Z.-G. Gu, and J. Zhang, "Surface-coordinated metal–organic framework thin films (SURMOFs) for electrocatalytic applications," *Nanoscale*, vol. 12, pp. 12 712–12 730, 2020.

[133] M. Oldenburg, A. Turshatov, D. Busko, M. Jakoby, R. Haldar, K. Chen, G. Emandi, M. O. Senge, C. Wöll, J. M. Hodgkiss, B. S. Richards, and I. A. Howard, "Enhancing the photoluminescence of surface anchored metal–organic frameworks: mixed linkers and efficient acceptors," *Phys. Chem. Chem. Phys.*, vol. 20, pp. 11 564–11 576, 2018.

[134] K. Nasu, T. Nakagawa, H. Nomura, C.-J. Lin, C.-H. Cheng, M.-R. Tseng, T. Yasuda, and C. Adachi, "A highly luminescent spiro-anthracenone-based organic light-emitting diode exhibiting thermally activated delayed fluorescence," *Chem. Commun.*, vol. 49, pp. 10 385–10 387, 2013.

[135] H. Noda, H. Nakanotani, and C. Adachi, "Excited state engineering for efficient reverse intersystem crossing," *Sci. Adv.*, vol. 4, no. 6, 2018.

[136] O. Franco, M. Jakoby, R. V. Schneider, F. Hundemer, D. Hahn, B. S. Richards, S. Bräse, M. A. R. Meier, U. Lemmer, and I. A. Howard, "Sensitizing TADF Absorption Using Variable Length Oligo(phenylene ethynylene) Antennae," *Front. Chem.*, vol. 8, p. 126, 2020.

[137] D. Hall, S. M. Suresh, P. L. dos Santos, E. Duda, S. Bagnich, A. Pershin, P. Rajamalli, D. B. Cordes, A. M. Z. Slawin, D. Beljonne, A. Köhler, I. D. W. Samuel, Y. Olivier, and E. Zysman-Colman, "Improving Processability and Efficiency of Resonant TADF Emitters: A Design Strategy," *Adv. Opt. Mater.*, vol. 8, no. 2, 1901627, 2020.

[138] S. Vagin, A. K. Ott, and B. Rieger, "Paddle-Wheel Zinc Carboxylate Clusters as Building Units for Metal-Organic Frameworks," *Chem. Ing. Tech.*, vol. 79, no. 6, pp. 767–780, 2007.

[139] Agilent Technologies, Inc., "Cary Eclipse fluorescence spectrophotometer"(2016). URL: https://www.agilent.com/cs/library/usermanuals/public/1758.pdf (accessed July 10, 2020).

[140] J. C. de Mello, H. F. Wittmann, and R. H. Friend, "An improved experimental determination of external photoluminescence quantum efficiency," *Adv. Mater.*, vol. 9, no. 3, pp. 230–232, 1997.

[141] PerkinElmer, Inc., "High performance lambda spectroscopy accessories"(2007). URL: http://www.labsphere.com.cn/uploads/LambdaSpectroscopyBrochure.pdf (accessed July 10, 2020).

[142] Hamamatsu Photonics K.K., "Guide to streak cameras"(2008). URL: https://www.hamamatsu.com/resources/pdf/sys/SHSS0006E_STREAK.pdf (accessed July 10, 2020).

[143] A. Brodeur and S. L. Chin, "Ultrafast white-light continuum generation and self-focusing in transparent condensed media," *J. Opt. Soc. Am. B*, vol. 16, no. 4, pp. 637–650, 1999.

[144] M. Adams, "Triplet exciton transport in porphyrin-based surface-anchored metal-organic framework thin films," Ph.D. dissertation, Karlsruhe Institute of Technology (KIT), 2019.

[145] M. H. Gehlen, "The centenary of the Stern-Volmer equation of fluorescence quenching: From the single line plot to the SV quenching map," *J. Photochem. Photobiol. C*, vol. 42, 100338, 2020.

[146] N. Hildebrandt, C. M. Spillmann, W. R. Algar, T. Pons, M. H. Stewart, E. Oh, K. Susumu, S. A. Díaz, J. B. Delehanty, and I. L. Medintz, "Energy Transfer with Semiconductor Quantum Dot Bioconjugates: A Versatile Platform for Biosensing, Energy Harvesting, and Other Developing Applications," *Chem. Rev.*, vol. 117, no. 2, pp. 536–711, 2017.

[147] J. R. Lakowicz and G. Weber, "Quenching of fluorescence by oxygen. Probe for structural fluctuations in macromolecules," *Biochemistry*, vol. 12, no. 21, pp. 4161–4170, 1973.

[148] D. G. Truhlar, "Nearly encounter-controlled reactions: The equivalence of the steady-state and diffusional viewpoints," *J. Chem. Educ.*, vol. 62, no. 2, 104, 1985.

[149] M. A. Castanho and M. J. Prieto, "Fluorescence quenching data interpretation in biological systems: The use of microscopic models for data analysis and interpretation of complex systems," *Biochim. Biophys. Acta, Biomembr.*, vol. 1373, no. 1, pp. 1 – 16, 1998.

[150] B. Zelent, J. Kusba, I. Gryczynski, M. L. Johnson, and J. R. Lakowicz, "Time-resolved and steady-state fluorescence quenching of N-acetyl-l-tryptophanamide by acrylamide and iodide," *Biophys. Chem.*, vol. 73, no. 1, pp. 53 – 75, 1998.

[151] R. F. Pasternack, M. Caccam, B. Keogh, T. A. Stephenson, A. P. Williams, and E. J. Gibbs, "Long-range fluorescence quenching of ethidium ion by cationic porphyrins in the presence of DNA," *J. Am. Chem. Soc.*, vol. 113, no. 18, pp. 6835–6840, 1991.

[152] H. Bässler, "Charge transport in disordered organic photoconductors a monte carlo simulation study," *Phys. Status Solidi B*, vol. 175, no. 1, pp. 15–56, 1993.

[153] N. van der Kaap and L. Koster, "Massively parallel kinetic Monte Carlo simulations of charge carrier transport in organic semiconductors," *J. Comput. Phys.*, vol. 307, pp. 321 – 332, 2016.

[154] C. Groves, "Developing understanding of organic photovoltaic devices: kinetic Monte Carlo models of geminate and non-geminate recombination, charge transport and charge extraction," *Energy Environ. Sci.*, vol. 6, pp. 3202–3217, 2013.

[155] M. Scheidler, U. Lemmer, R. Kersting, S. Karg, W. Riess, B. Cleve, R. F. Mahrt, H. Kurz, H. Bässler, E. O. Göbel, and P. Thomas, "Monte Carlo study of picosecond exciton relaxation and dissociation in poly(phenylenevinylene)," *Phys. Rev. B*, vol. 54, pp. 5536–5544, 1996.

[156] D. T. Gillespie, "A general method for numerically simulating the stochastic time evolution of coupled chemical reactions," *J. Comput. Phys.*, vol. 22, no. 4, pp. 403 – 434, 1976.

[157] T. Hosokai, H. Matsuzaki, H. Nakanotani, K. Tokumaru, T. Tsutsui, A. Furube, K. Nasu, H. Nomura, M. Yahiro, and C. Adachi, "Evidence and mechanism of efficient thermally activated delayed fluorescence promoted by delocalized excited states," *Sci. Adv.*, vol. 3, no. 5, e1603282, 2017.

[158] Z. Yang, Z. Mao, Z. Xie, Y. Zhang, S. Liu, J. Zhao, J. Xu, Z. Chi, and M. P. Aldred, "Recent advances in organic thermally activated delayed fluorescence materials," *Chem. Soc. Rev.*, vol. 46, pp. 915–1016, 2017.

[159] R. S. Nobuyasu, Z. Ren, G. C. Griffiths, A. S. Batsanov, P. Data, S. Yan, A. P. Monkman, M. R. Bryce, and F. B. Dias, "Rational design of TADF polymers using a donor–acceptor monomer with enhanced TADF efficiency induced by the energy alignment of charge transfer and local triplet excited states," *Adv. Opt. Mater.*, vol. 4, no. 4, pp. 597–607, 2016.

[160] L. Yu, Z. Wu, G. Xie, W. Zeng, D. Ma, and C. Yang, "Molecular design to regulate the photophysical properties of multifunctional TADF emitters towards high-performance TADF-based OLEDs with EQEs up to 22.4% and small efficiency roll-offs," *Chem. Sci.*, vol. 9, pp. 1385–1391, 2018.

[161] F. Hundemer, L. Graf von Reventlow, C. Leonhardt, M. Polamo, M. Nieger, S. M. Seifermann, A. Colsmann, and S. Bräse, "Acceptor Derivatization of the 4CzIPN TADF System: Color Tuning and Introduction of Functional Groups," *ChemistryOpen*, vol. 8, no. 12, pp. 1413–1420, 2020.

[162] R. V. Schneider, K. A. Waibel, A. P. Arndt, M. Lang, R. Seim, D. Busko, S. Bräse, U. Lemmer, and M. A. R. Meier, "Sequence-definition in stiff conjugated oligomers," *Sci. Rep.*, vol. 8, no. 1, 17483, 2018.

[163] A. Köhler, J. S. Wilson, R. H. Friend, M. K. Al-Suti, M. S. Khan, A. Gerhard, and H. Bässler, "The singlet-triplet energy gap in organic and Pt-containing phenylene ethynylene polymers and monomers," *J. Chem. Phys.*, vol. 116, no. 21, pp. 9457–9463, 2002.

[164] A. Köhler and D. Beljonne, "The singlet–triplet exchange energy in conjugated polymers," *Adv. Funct. Mater.*, vol. 14, no. 1, pp. 11–18, 2004.

[165] Y. Pan, W. Li, S. Zhang, L. Yao, C. Gu, H. Xu, B. Yang, and Y. Ma, "High Yields of Singlet Excitons in Organic Electroluminescence through Two Paths of Cold and Hot Excitons," *Adv. Opt. Mater.*, vol. 2, no. 6, pp. 510–515, 2014.

[166] B. Yurash, H. Nakanotani, Y. Olivier, D. Beljonne, C. Adachi, and T.-Q. Nguyen, "Photoluminescence Quenching Probes Spin Conversion and Exciton Dynamics in Thermally Activated Delayed Fluorescence Materials," *Adv. Mater.*, vol. 31, no. 21, 1804490, 2019.

[167] J. Partee, E. L. Frankevich, B. Uhlhorn, J. Shinar, Y. Ding, and T. J. Barton, "Delayed Fluorescence and Triplet-Triplet Annihilation in π-Conjugated Polymers," *Phys. Rev. Lett.*, vol. 82, pp. 3673–3676, 1999.

[168] L. P. Candeias, J. Wildeman, G. Hadziioannou, and J. M. Warman, "Pulse Radiolysis–Optical Absorption Studies on the Triplet States of p-Phenylenevinylene Oligomers in Solution," *J. Phys. Chem. B*, vol. 104, no. 35, pp. 8366–8371, 2000.

[169] A. Monkman, H. Burrows, I. Hamblett, S. Navaratnam, U. Scherf, and C. Schmitt, "The triplet state of the ladder-type methyl-poly(p-phenylene) as seen by pulse radiolysis–energy transfer," *Chem. Phys. Lett.*, vol. 327, no. 1, pp. 111 – 116, 2000.

[170] A. M. Funston, E. E. Silverman, K. S. Schanze, and J. R. Miller, "Spectroscopy and Transport of the Triplet Exciton in a Terthiophene End-Capped Poly(phenylene ethynylene)," *J. Phys. Chem. B*, vol. 110, no. 36, pp. 17 736–17 742, 2006.

[171] E. W. Evans, Y. Olivier, Y. Puttisong, W. K. Myers, T. J. Hele, S. M. Menke, T. H. Thomas, D. Credgington, D. Beljonne, R. H. Friend *et al.*, "Vibrationally Assisted Intersystem Crossing in Benchmark Thermally Activated Delayed Fluorescence Molecules," *J. Phys. Chem. Lett.*, vol. 9, no. 14, pp. 4053–4058, 2018.

[172] M. Yamamoto, Y. Tsujii, and A. Tsuchida, "Near-infrared charge resonance band of intramolecular carbazole dimer radical cations studied by nanosecond laser photolysis," *Chem. Phys. Lett.*, vol. 154, no. 6, pp. 559 – 562, 1989.

[173] Y. Tsujii, A. Tsuchida, Y. Onogi, and M. Yamamoto, "Stabilization of carbazole radical cation formed in poly(N-vinylcarbazole) by charge delocalization," *Macromolecules*, vol. 23, no. 17, pp. 4019–4023, 1990.

[174] M. Jakoby, S. Heidrich, L. Graf von Reventlow, C. Degitz, S. M. Suresh, E. Zysman-Colman, W. Wenzel, B. S. Richards, and I. A. Howard, "Method for accurate experimental determination of singlet and triplet exciton diffusion between thermally activated delayed fluorescence molecules," *Chem. Sci.*, vol. 12, pp. 1121–1125, 2021.

[175] V. Grosshenny, A. Harriman, and R. Ziessel, "Electronic Energy Transfer Across Ethynyl-Bridged RuII/OsII Terpyridyl Complexes," *Angew. Chem. Int. Ed.*, vol. 34, no. 10, pp. 1100–1102, 1995.

[176] S. M. Menke and R. J. Holmes, "Exciton Transport in an Organic Semiconductor Exhibiting Thermally Activated Delayed Fluorescence," *J. Phys. Chem. C*, vol. 120, no. 16, pp. 8502–8508, 2016.

[177] G. Grancini, D. Polli, D. Fazzi, J. Cabanillas-Gonzalez, G. Cerullo, and G. Lanzani, "Transient Absorption Imaging of P3HT:PCBM Photovoltaic Blend: Evidence For Interfacial Charge Transfer State," *J. Phys. Chem. Lett.*, vol. 2, no. 9, pp. 1099–1105, 2011.

[178] B. Wex and B. R. Kaafarani, "Perspective on carbazole-based organic compounds as emitters and hosts in TADF applications," *J. Mater. Chem. C*, vol. 5, pp. 8622–8653, 2017.

[179] Y. Yuan, X. Tang, X.-Y. Du, Y. Hu, Y.-J. Yu, Z.-Q. Jiang, L.-S. Liao, and S.-T. Lee, "The Design of Fused Amine/Carbonyl System for Efficient Thermally Activated Delayed Fluorescence: Novel Multiple Resonance Core and Electron Acceptor," *Adv. Opt. Mater.*, vol. 7, no. 7, 1801536, 2019.

[180] D. Zhang, M. Cai, Y. Zhang, D. Zhang, and L. Duan, "Sterically shielded blue thermally activated delayed fluorescence emitters with improved efficiency and stability," *Mater. Horiz.*, vol. 3, pp. 145–151, 2016.

[181] H.-W. Lin, W.-C. Lin, J.-H. Chang, and C.-I. Wu, "Solution-processed hexaazatriphenylene hexacarbonitrile as a universal hole-injection layer

for organic light-emitting diodes," *Org. Electron.*, vol. 14, no. 4, pp. 1204 – 1210, 2013.

[182] A. Niwa, S. Haseyama, T. Kobayashi, T. Nagase, K. Goushi, C. Adachi, and H. Naito, "Triplet-triplet annihilation in a thermally activated delayed fluorescence emitter lightly doped in a host," *Appl. Phys. Lett.*, vol. 113, no. 8, 083301, 2018.

[183] S. Gottardi, M. Barbry, R. Coehoorn, and H. van Eersel, "Efficiency loss processes in hyperfluorescent OLEDs: A kinetic Monte Carlo study," *Appl. Phys. Lett.*, vol. 114, no. 7, 073301, 2019.

[184] K. Narushima, Y. Kiyota, T. Mori, S. Hirata, and M. Vacha, "Suppressed Triplet Exciton Diffusion Due to Small Orbital Overlap as a Key Design Factor for Ultralong-Lived Room-Temperature Phosphorescence in Molecular Crystals," *Adv. Mater.*, vol. 31, no. 10, 1807268, 2019.

[185] S. H. Han and J. Y. Lee, "Spatial separation of sensitizer and fluorescent emitter for high quantum efficiency in hyperfluorescent organic light-emitting diodes," *J. Mater. Chem. C*, vol. 6, pp. 1504–1508, 2018.

[186] S. H. Han, J. H. Jeong, J. W. Yoo, and J. Y. Lee, "Ideal blue thermally activated delayed fluorescence emission assisted by a thermally activated delayed fluorescence assistant dopant through a fast reverse intersystem crossing mediated cascade energy transfer process," *J. Mater. Chem. C*, vol. 7, pp. 3082–3089, 2019.

[187] S. Wang, Y. Zhang, W. Chen, J. Wei, Y. Liu, and Y. Wang, "Achieving high power efficiency and low roll-off OLEDs based on energy transfer from thermally activated delayed excitons to fluorescent dopants," *Chem. Commun.*, vol. 51, no. 60, pp. 11 972–11 975, 2015.

[188] J. Liu, W. Zhou, J. Liu, I. Howard, G. Kilibarda, S. Schlabach, D. Coupry, M. Addicoat, S. Yoneda, Y. Tsutsui, T. Sakurai, S. Seki, Z. Wang, P. Lindemann, E. Redel, T. Heine, and C. Wöll, "Photoinduced Charge-Carrier Generation in Epitaxial MOF Thin Films: High Efficiency as a Result of an Indirect Electronic Band Gap? (Angew. Chem. Int. Ed. 25/2015)," *Angew. Chem. Int. Ed.*, vol. 54, no. 25, pp. 7201–7201, 2015.

[189] W. Song, I. H. Lee, S.-H. Hwang, and J. Y. Lee, "High efficiency fluorescent white organic light-emitting diodes having a yellow fluorescent emitter sensitized by a blue thermally activated delayed fluorescent emitter," *Org. Electron.*, vol. 23, pp. 138 – 143, 2015.

[190] A. Lewis, A. Ruseckas, O. Gaudin, G. Webster, P. Burn, and I. Samuel, "Singlet exciton diffusion in MEH-PPV films studied by exciton–exciton annihilation," *Org. Electron.*, vol. 7, no. 6, pp. 452 – 456, 2006.

[191] G. Zhang, J. Zhao, P. C. Y. Chow, K. Jiang, J. Zhang, Z. Zhu, J. Zhang, F. Huang, and H. Yan, "Nonfullerene Acceptor Molecules for Bulk Heterojunction Organic Solar Cells," *Chem. Rev.*, vol. 118, no. 7, pp. 3447–3507, 2018.

[192] M. Oldenburg, A. Turshatov, D. Busko, S. Wollgarten, M. Adams, N. Baroni, A. Welle, E. Redel, C. Wöll, B. S. Richards, and I. A. Howard, "Photon Upconversion at Crystalline Organic–Organic Heterojunctions," *Adv. Mater.*, vol. 28, no. 38, pp. 8477–8482, 2016.

[193] M. Oldenburg, "Photon upconversion heterostructures made from surface-anchored metal-organic frameworks," Ph.D. dissertation, Karlsruhe Institute of Technology (KIT), 2019.

[194] R. Haldar, M. Jakoby, M. Kozlowska, M. Rahman Khan, H. Chen, Y. Pramudya, B. S. Richards, L. Heinke, W. Wenzel, F. Odobel, S. Diring, I. A. Howard, U. Lemmer, and C. Wöll, "Tuning Optical Properties by Controlled Aggregation: Electroluminescence Assisted by Thermally-Activated Delayed Fluorescence from Thin Films of Crystalline Chromophores," *Chem. Eur. J.*, vol. 26, no. 71, pp. 17 016–17 020, 2020.

[195] F. Lederer, F. Graupner, B. Maerz, M. Braun, and W. Zinth, "Excimer formation in 9,10-dichloroanthracene – Solutions and crystals," *Chem. Phys.*, vol. 428, pp. 82 – 89, 2014.

[196] S. Dey, P. Mondal, and S. P. Rath, "Aggregation-controlled excimer emission in an axial anthracene–Sn(iv)porphyrin–anthracene triad in the solid and solution phases," *New J. Chem.*, vol. 39, pp. 4100–4108, 2015.

[197] C. Quarti, D. Fazzi, and M. Del Zoppo, "A computational investigation on singlet and triplet exciton couplings in acene molecular crystals," *Phys. Chem. Chem. Phys.*, vol. 13, pp. 18 615–18 625, 2011.

[198] F. Panzer, H. Bässler, and A. Köhler, "Temperature Induced Order–Disorder Transition in Solutions of Conjugated Polymers Probed by Optical Spectroscopy," *The Journal of Physical Chemistry Letters*, vol. 8, no. 1, pp. 114–125, 2017.

[199] F. Würthner, T. E. Kaiser, and C. R. Saha-Möller, "J-Aggregates: From Serendipitous Discovery to Supramolecular Engineering of Functional Dye Materials," *Angew. Chem. Int. Ed.*, vol. 50, no. 15, pp. 3376–3410, 2011.

[200] C. Janiak, "A critical account on pi–pi stacking in metal complexes with aromatic nitrogen-containing ligands," *J. Chem. Soc., Dalton Trans.*, pp. 3885–3896, 2000.

[201] A. Hayer, V. de Halleux, A. Köhler, A. El-Garoughy, E. W. Meijer, J. Barberá, J. Tant, J. Levin, M. Lehmann, J. Gierschner, J. Cornil, and Y. H. Geerts, "Highly Fluorescent Crystalline and Liquid Crystalline Columnar Phases of Pyrene-Based Structures," *The Journal of Physical Chemistry B*, vol. 110, no. 15, pp. 7653–7659, 2006.

[202] A. de Juan and R. Tauler, "Multivariate Curve Resolution (MCR) from 2000: Progress in Concepts and Applications," *Crit. Rev. Anal. Chem.*, vol. 36, no. 3-4, pp. 163–176, 2006.

[203] M. Sugino, Y. Araki, K. Hatanaka, I. Hisaki, M. Miyata, and N. Tohnai, "Elucidation of Anthracene Arrangement for Excimer Emission at Ambient Conditions," *Crystal Growth & Design*, vol. 13, no. 11, pp. 4986–4992, 2013.

[204] Y. Farré, L. Zhang, Y. Pellegrin, A. Planchat, E. Blart, M. Boujtita, L. Hammarström, D. Jacquemin, and F. Odobel, "Second Generation of Diketopyrrolopyrrole Dyes for NiO-Based Dye-Sensitized Solar Cells," *J. Phys. Chem. C*, vol. 120, no. 15, pp. 7923–7940, 2016.

[205] M. Kaur and D. H. Choi, "Diketopyrrolopyrrole: brilliant red pigment dye-based fluorescent probes and their applications," *Chem. Soc. Rev.*, vol. 44, pp. 58–77, 2015.

[206] M. Grzybowski and D. T. Gryko, "Diketopyrrolopyrroles: Synthesis, Reactivity, and Optical Properties," *Adv. Opt. Mater.*, vol. 3, no. 3, pp. 280–320, 2015.

[207] E. Redel, Z. Wang, S. Walheim, J. Liu, H. Gliemann, and C. Wöll, "On the dielectric and optical properties of surface-anchored metal-organic frameworks: A study on epitaxially grown thin films," *Appl. Phys. Lett.*, vol. 103, no. 9, 091903, 2013.

[208] H. Wang, Y. Xu, T. Tsuboi, H. Xu, Y. Wu, Z. Zhang, Y. Miao, Y. Hao, X. Liu, B. Xu, and W. Huang, "Energy transfer in polyfluorene copolymer used for white-light organic light emitting device," *Org. Electron.*, vol. 14, no. 3, pp. 827 – 838, 2013.

[209] S. Kaufmann, T. Stöferle, N. Moll, R. F. Mahrt, U. Scherf, A. Tsami, D. V. Talapin, and C. B. Murray, "Resonant energy transfer within a colloidal nanocrystal polymer host system," *Appl. Phys. Lett.*, vol. 90, no. 7, 071108, 2007.

[210] T. Virgili, D. G. Lidzey, and D. D. C. Bradley, "Efficient Energy Transfer from Blue to Red in Tetraphenylporphyrin-Doped Poly(9,9-dioctylfluorene) Light-Emitting Diodes," *Adv. Mater.*, vol. 12, no. 1, pp. 58–62, 2000.

[211] H.-J. Son, S. Jin, S. Patwardhan, S. J. Wezenberg, N. C. Jeong, M. So, C. E. Wilmer, A. A. Sarjeant, G. C. Schatz, R. Q. Snurr, O. K. Farha, G. P. Wiederrecht, and J. T. Hupp, "Light-Harvesting and Ultrafast Energy Migration in Porphyrin-Based Metal–Organic Frameworks," *J. Am. Chem. Soc.*, vol. 135, no. 2, pp. 862–869, 2013.

[212] S. R. Scully and M. D. McGehee, "Effects of optical interference and energy transfer on exciton diffusion length measurements in organic semiconductors," *J. Appl. Phys.*, vol. 100, no. 3, 034907, 2006.

[213] M. Jakoby, C. Beil, P. Nazari, B. S. Richards, M. Seitz, A. Turshatov, and I. A. Howard, "Rare-earth coordination polymers with multimodal luminescence on the nano-, micro-, and milli-second time scales," *iScience*, vol. 24, no. 3, 102207, 2021.

[214] Y. Tao, K. Yuan, T. Chen, P. Xu, H. Li, R. Chen, C. Zheng, L. Zhang, and W. Huang, "Thermally activated delayed fluorescence materials towards the breakthrough of organoelectronics," *Adv. Mater.*, vol. 26, no. 47, pp. 7931–7958, 2014.

[215] S. Yang, B. Zhou, Q. Huang, S. Wang, H. Zhen, D. Yan, Z. Lin, and Q. Ling, "Highly Efficient Organic Afterglow from a 2D Layered Lead-Free Metal Halide in Both Crystals and Thin Films under an Air Atmosphere," *ACS Appl. Mater. Interfaces*, vol. 12, no. 1, pp. 1419–1426, 2020.

[216] S. Y. Lee, T. Yasuda, Y. S. Yang, Q. Zhang, and C. Adachi, "Luminous Butterflies: Efficient Exciton Harvesting by Benzophenone Derivatives for Full-Color Delayed Fluorescence OLEDs," *Angew. Chem. Int. Ed.*, vol. 53, no. 25, pp. 6402–6406, 2014.

[217] I. S. Park, H. Komiyama, and T. Yasuda, "Pyrimidine-based twisted donor–acceptor delayed fluorescence molecules: a new universal platform for highly efficient blue electroluminescence," *Chem. Sci.*, vol. 8, pp. 953–960, 2017.

[218] M. A. Gordillo, D. K. Panda, and S. Saha, "Efficient MOF-Sensitized Solar Cells Featuring Solvothermally Grown [100]-Oriented Pillared Porphyrin Framework-11 Films on ZnO/FTO Surfaces," *ACS Appl. Mater. Interfaces*, vol. 11, no. 3, pp. 3196–3206, 2019.

[219] M. C. So, G. P. Wiederrecht, J. E. Mondloch, J. T. Hupp, and O. K. Farha, "Metal–organic framework materials for light-harvesting and energy transfer," *Chem. Commun.*, vol. 51, pp. 3501–3510, 2015.